

**OBSERVATIONS OF THE CRAB  
NEBULA AND PULSAR IN THE OPTICAL  
AND  $\gamma$ -RAY BANDS WITH STACEE**

Pascal Fortin  
Department of Physics  
McGill University, Montreal  
September, 2005

A thesis submitted to McGill University  
in partial fulfillment of the requirements  
of the degree of Doctor of Philosophy

©Pascal Fortin, 2005



Library and  
Archives Canada

Bibliothèque et  
Archives Canada

Published Heritage  
Branch

Direction du  
Patrimoine de l'édition

395 Wellington Street  
Ottawa ON K1A 0N4  
Canada

395, rue Wellington  
Ottawa ON K1A 0N4  
Canada

*Your file* *Votre référence*  
*ISBN: 978-0-494-21645-3*  
*Our file* *Notre référence*  
*ISBN: 978-0-494-21645-3*

#### NOTICE:

The author has granted a non-exclusive license allowing Library and Archives Canada to reproduce, publish, archive, preserve, conserve, communicate to the public by telecommunication or on the Internet, loan, distribute and sell theses worldwide, for commercial or non-commercial purposes, in microform, paper, electronic and/or any other formats.

The author retains copyright ownership and moral rights in this thesis. Neither the thesis nor substantial extracts from it may be printed or otherwise reproduced without the author's permission.

#### AVIS:

L'auteur a accordé une licence non exclusive permettant à la Bibliothèque et Archives Canada de reproduire, publier, archiver, sauvegarder, conserver, transmettre au public par télécommunication ou par l'Internet, prêter, distribuer et vendre des thèses partout dans le monde, à des fins commerciales ou autres, sur support microforme, papier, électronique et/ou autres formats.

L'auteur conserve la propriété du droit d'auteur et des droits moraux qui protègent cette thèse. Ni la thèse ni des extraits substantiels de celle-ci ne doivent être imprimés ou autrement reproduits sans son autorisation.

---

In compliance with the Canadian Privacy Act some supporting forms may have been removed from this thesis.

Conformément à la loi canadienne sur la protection de la vie privée, quelques formulaires secondaires ont été enlevés de cette thèse.

While these forms may be included in the document page count, their removal does not represent any loss of content from the thesis.

Bien que ces formulaires aient inclus dans la pagination, il n'y aura aucun contenu manquant.

  
**Canada**

*À Réjean, Nicole et Mélanie...*

# Abstract

The Solar Tower Atmospheric Cherenkov Effect Experiment (STACEE) is an atmospheric Cherenkov telescope that detects cosmic  $\gamma$ -rays using the wavefront-sampling technique. STACEE uses the large mirror area of the National Solar Thermal Test Facility (NSTTF) to achieve an energy threshold below 200 GeV. This telescope was used to search for high-energy  $\gamma$ -ray emission from the Crab Nebula and pulsar. A statistical excess of  $4.07\sigma$  in the number of on-source events compared to off-source events was detected in 15 hours of on-source observing time, corresponding to an integral flux above the energy threshold ( $E_{thr} = 185 \pm 35$  GeV) of  $I(E > E_{thr}) = (2.5 \pm 0.6) \times 10^{-10}$  photons  $cm^{-2} s^{-1}$ . The observed flux is in agreement with the previous result obtained by STACEE-32 and consistent with the power law spectrum seen at higher energies. A special instrument was developed to make simultaneous observations of the Crab in the optical and  $\gamma$ -ray bands. Pulsed emission was detected in the optical band, demonstrating the accuracy of the barycentering and epoch folding analysis tools. After barycentering the arrival times and calculating the rotational phases of  $\gamma$ -ray events, no evidence for pulsed emission from the Crab pulsar was found. The upper limit on the pulsed fraction of the signal was 16.4% at the 99.9% confidence level. Unfortunately, neither the polar cap model, nor the outer gap model is excluded by this new upper limit.

# Résumé

Le télescope à effet Cherenkov atmosphérique STACEE détecte des rayons- $\gamma$  d'origine cosmique en utilisant la technique d'échantillonnage du front d'onde. STACEE utilise les miroirs du National Solar Thermal Test Facility (NSTTF) pour atteindre un seuil d'énergie sous 200 GeV. Ce télescope fut utilisé pour effectuer une recherche de rayons- $\gamma$  provenant de la Nébuleuse ainsi que du pulsar du Crabe. Un excès statistique de  $4.07\sigma$  du nombre d'événements sur source comparativement au nombre d'événements hors source fut détecté en 15 heures d'observation sur source, ce qui correspond à un flux intégral au dessus du seuil d'énergie ( $E_{thr} = 185 \pm 35$  GeV) de  $I(E > E_{thr}) = (2.5 \pm 0.6) \times 10^{-10}$  photons  $cm^{-2} s^{-1}$ . Ce flux concorde avec le résultat obtenu précédemment par STACEE-32 et est compatible avec le spectre en loi de puissance mesuré à plus hautes énergies. Un instrument spécial fut développé pour effectuer des observations simultanées du Crabe dans les bandes optique et  $\gamma$ . Une émission pulsée fut découverte dans la bande optique, ce qui démontre la précision des procédures de barycentrisation et du calcul de phase. Après la barycentrisation des temps d'arrivée et le calcul de phase des événements  $\gamma$ , aucune évidence d'émission pulsée n'est observée pour le pulsar du Crabe. La limite supérieure sur la fraction pulsée du signal fut de 16.4% à un niveau de confiance de 99.9%. Malheureusement, ni le modèle de la calotte polaire, ni le modèle de la cavité externe n'est exclu par cette nouvelle limite supérieure.

# Acknowledgements

I would like to thank my supervisor Ken Ragan for giving me the opportunity to join an exciting experiment in the field of  $\gamma$ -ray astrophysics. Working on a small experiment like STACEE was a remarkable learning experience as I had countless opportunities to participate to the development of the detector and contribute to the scientific analysis of the data. I would also like to thank my unofficial supervisor David Hanna for all his technical advice and for proof-reading drafts of this thesis.

None of this work would have been possible without the help of STACEE collaborators here at McGill and at other institutions in Canada and the U.S.. It was a pleasure working with them and I have good memories of collaboration meetings and data taking shifts in New Mexico.

I would like to thank Paul Mercure and Juan Gallego for keeping the computers and network running and for answering all my questions. Excellent system administrators are difficult to find and the Physics department at McGill is extremely lucky to have both Paul and Juan.

Writing this thesis was very much like running a long marathon. I am grateful to all my friends for their incredible moral support. Here at McGill, I would like to thank the STACEE and *pulsar* graduate students and postdocs. I would also like to thank my friends and amazing coaches from the McGill Triathlon Club. Your friendship and support were essential to keep me motivated and reach my goal of completing an Ironman.

I am grateful to my best friend Mélanie Renaud for all these years of camaraderie, and to my French soul mate Martine Bertrand for sharing the best times of my life. Finally, I want to thank my parents and sister for their unconditional love and support.

## Statement of original work

I first joined the STACEE collaboration in September of 1998 as a graduate student at McGill University. After completing a Master's degree on the 32-channel version of STACEE, I embarked on a Ph.D. degree in January of 2000 and continued working on the STACEE experiment. One of my first contributions as a Ph.D. student was to write a software driver and API for the digital trigger system. In September of 2000, I moved to New Mexico for an extended period of time (7 months), during which I helped upgrade the experiment to 48 channels, implemented and debugged the new digital trigger and DAQ systems, and spent countless nights running the experiment.

Given the small size of the STACEE collaboration (less than 20 collaborators), we all had to spend several weeks each year at the site running and calibrating the experiment. During these shifts, I actively contributed to the alignment of the individual heliostat facets and biasing of the heliostat pointing. The idea of using single photon statistics to measure the gain of the PMTs was initially proposed by Jim Hinton, but I adapted and perfected the technique for the FADCs. I am responsible for the techniques used to measure pulse slewing and timing resolution.

One of the most important contributions I made to this experiment was the PASS0 data reduction package. The first version of the code was used to perform an independent analysis of the Crab data obtained during the 1998-1999 season. I maintained the code for the last five years and updated it to reflect changes to the experiment.

I am entirely responsible for the design, implementation, and testing of the system used to search for pulsed emission from the optical Crab pulsar. I wrote the code used for the DAQ as well as the analysis code for barycentering, digital filtering, and pulse folding.

I also took an active role in the simulation sub-project by implementing fake optical sources as inputs to the `sandfield` simulation package. After Richard Scalzo's graduation, I became the official maintainer of the `sandfield` simulation package. I took full advantage of the computing environment in the physics department at McGill University and generated all the Monte Carlo results presented in this thesis.

# Contents

<b>Abstract</b>	<b>ii</b>
<b>Résumé</b>	<b>iii</b>
<b>Acknowledgements</b>	<b>iv</b>
<b>Statement of original work</b>	<b>v</b>
<b>I Gamma-Ray Astrophysics</b>	<b>1</b>
<b>1 A primer on <math>\gamma</math>-ray detection</b>	<b>2</b>
1.1 Early satellites . . . . .	2
1.2 A revolution in space . . . . .	6
1.2.1 The Compton Gamma Ray Observatory . . . . .	8
1.3 Future satellites . . . . .	11
1.4 Ground-based detectors . . . . .	12
1.4.1 Extensive Air Showers and Cherenkov radiation . . . . .	13
<b>2 Gamma-rays from the Crab</b>	<b>21</b>
2.1 A brief biography of the Crab . . . . .	21
2.2 High energy emission from the nebula . . . . .	25
2.3 High energy emission from the pulsar . . . . .	26
2.3.1 Pulsed emission models . . . . .	28
<b>II STACEE: A ground-based detector</b>	<b>33</b>
<b>3 Concept</b>	<b>34</b>
<b>4 STACEE optics</b>	<b>38</b>
4.1 Heliostats . . . . .	38
4.2 Secondary optics and cameras . . . . .	41
<b>5 STACEE electronics</b>	<b>47</b>
5.1 Photomultiplier tubes . . . . .	47

5.2	Trigger system . . . . .	49
5.3	Waveform digitizers (FADCs) . . . . .	52
5.4	Optical pulsar detection system . . . . .	52
<b>6</b>	<b>Calibration of STACEE electronics</b>	<b>56</b>
6.1	Calibration and monitoring of the PMT gains . . . . .	56
6.1.1	FADC Gain Inference Technique, <i>a.k.a.</i> FGIT . . . . .	57
6.1.2	Monitoring the gains with $\sigma^2/I$ method . . . . .	59
6.2	Timing residuals and timing resolution . . . . .	61
<b>7</b>	<b>Data reduction package: PASSO</b>	<b>67</b>
7.1	Event analysis . . . . .	67
7.2	Field brightness correction . . . . .	69
<b>8</b>	<b>Pulsar timing tools</b>	<b>73</b>
8.1	Epoch folding and barycentering . . . . .	73
8.2	Validation of the technique . . . . .	74
<b>9</b>	<b>Data quality cuts</b>	<b>80</b>
9.1	Detector malfunction cuts . . . . .	80
9.2	Atmospheric instability cuts . . . . .	80
9.2.1	Clouds and transient disturbances . . . . .	82
9.2.2	Frost and water condensation . . . . .	82
<b>10</b>	<b>Detector simulation and expected performance</b>	<b>86</b>
10.1	The CORSIKA air-shower simulation . . . . .	86
10.2	The sandfield optical simulation . . . . .	87
10.3	The elec electronics simulation . . . . .	88
10.4	Simulation parameters . . . . .	91
10.5	Effective areas and energy thresholds . . . . .	93
10.6	Cosmic ray event trigger rate . . . . .	97
10.7	Optical Crab Pulsar simulations . . . . .	98
10.7.1	Optical photons from the Crab Pulsar . . . . .	99
10.7.2	Optical response . . . . .	102
10.7.3	Electronics response . . . . .	102
<b>III</b>	<b>Data set and analysis</b>	<b>107</b>
<b>11</b>	<b>Optical data set</b>	<b>108</b>
11.1	Properties of the background noise . . . . .	109
11.2	Digital filtering . . . . .	114
11.3	Predicted pulse profile . . . . .	115
11.4	Analysis results . . . . .	118

<b>12 Gamma-ray data set</b>	<b>120</b>
12.1 Nebula analysis . . . . .	120
12.1.1 2002-2003 season . . . . .	121
12.1.2 2003-2004 season . . . . .	122
12.1.3 Integral Flux Results . . . . .	123
12.1.4 Estimating the systematic errors . . . . .	126
12.2 $\gamma$ -ray pulsar analysis . . . . .	129
<b>13 Summary of results and conclusions</b>	<b>132</b>
13.1 Future directions for STACEE . . . . .	134
13.2 Ground-based revolution . . . . .	135
<b>A Optical data set</b>	<b>138</b>
<b>B List of pairs and analysis results</b>	<b>140</b>
<b>C Upper limits using the method of Helene</b>	<b>144</b>
<b>D GNUCAP code</b>	<b>146</b>

# List of Figures

1.1	Schematic view of the Explorer XI $\gamma$ -ray detector . . . . .	4
1.2	First GRB detected by the Vela-4A satellite . . . . .	5
1.3	Diagram of the $\gamma$ -ray detector on COS-B . . . . .	7
1.4	2CG catalog of point sources detected by the COS-B telescope . . . . .	7
1.5	CGRO instruments: BATSE, OSSE, COMPTEL, and EGRET . . . . .	8
1.6	Distribution of GRBs detected by BATSE . . . . .	9
1.7	Schematic of the EGRET instrument . . . . .	10
1.8	The third EGRET catalog all-sky map . . . . .	11
1.9	Sky map of point sources detected above 250 GeV . . . . .	13
1.10	Shower size as a function of depth in the atmosphere . . . . .	14
1.11	Diagram of Cherenkov radiation shock front . . . . .	16
1.12	Cherenkov light yield as a function of energy and composition . . . . .	17
1.13	Lateral density profile of Cherenkov photons . . . . .	18
1.14	Lateral timing profiles for $\gamma$ -ray and proton showers . . . . .	19
1.15	Cherenkov images in the focal plane of an imaging telescope . . . . .	20
2.1	Multi-wavelength images of the Crab Nebula . . . . .	22
2.2	The first star chart showing the Crab Nebula . . . . .	23
2.3	Drawing of the Crab Nebula by William Parsons . . . . .	24
2.4	Nonthermal radiation of the Crab Nebula . . . . .	27
2.5	EGRET's pulse profile of the Crab pulsar above 100 MeV . . . . .	28
2.6	Pulsed $\gamma$ -ray fluxes and limits for the Crab pulsar . . . . .	29
2.7	Schematic diagram of the polar cap and outer gap models . . . . .	30
3.1	Aerial view of the NSTTF . . . . .	35
3.2	Conceptual design of the STACEE experiment . . . . .	37
4.1	Schematic diagram of an individual STACEE heliostat . . . . .	39
4.2	Drift scans on Iota Cancri . . . . .	40
4.3	Schematic diagram illustrating the concept of canting . . . . .	41
4.4	Schematic view of the solar tower . . . . .	42
4.5	Selection of the 64 STACEE heliostats . . . . .	43
4.6	Photo of the secondary optical system on the 260-level . . . . .	45
4.7	Schematic view of a STACEE PMT can assembly . . . . .	45
4.8	Photo and ray-tracing of a typical DTIRC used by STACEE . . . . .	46
4.9	Overall throughput of the STACEE optical system . . . . .	46

5.1	Schematic diagram of the STACEE electronics . . . . .	48
5.2	Rate versus threshold curve . . . . .	51
5.3	Sample FADC trace for a typical Cherenkov event . . . . .	53
5.4	Optical pulsar hardware . . . . .	54
5.5	Diagram of the band-pass filter circuit . . . . .	55
6.1	Schematic diagram of the laser calibration system . . . . .	57
6.2	Sample FADC trace for a single photoelectron pulse . . . . .	58
6.3	FGIT distributions of pulse charges . . . . .	60
6.4	Plot of $\sigma^2$ versus $I$ . . . . .	62
6.5	Distributions of timing residuals . . . . .	63
6.6	Timing resolution as a function of the pulse amplitude . . . . .	65
6.7	Comparison of the rise time for small and large pulses . . . . .	66
7.1	Sample FADC trace for a triggered event in PASS0 . . . . .	68
7.2	Excess event rate as a function of the characteristic current . . . . .	71
7.3	Excess event rate after padding as a function of the threshold . . . . .	72
8.1	CELESTE optical pulse profile of the Crab pulsar . . . . .	75
8.2	STACEE analysis of the CELESTE optical Crab pulsar data . . . . .	75
8.3	Pulse profile of pulsar PSR J2021+3651 . . . . .	76
8.4	Pulse profile of pulsar PSR 1639+36 with barycentering . . . . .	78
8.5	Pulse profile of pulsar PSR 1639+36 without barycentering . . . . .	79
9.1	Effect of clouds passing through the field of view of STACEE . . . . .	83
9.2	Effect of frost on the trigger rate . . . . .	85
10.1	Distribution of photons in the plane of the North secondary mirror . . . . .	89
10.2	Real and simulated traces . . . . .	90
10.3	Differential energy spectra for $p$ and ${}^4\text{He}$ . . . . .	92
10.4	Distribution of core positions for $\gamma$ -rays and $p$ . . . . .	94
10.5	Effective area curves along the trajectory of the Crab . . . . .	95
10.6	Effect of the analysis procedure on the effective areas . . . . .	96
10.7	Differential $\gamma$ -ray trigger rate as a function of energy . . . . .	98
10.8	Spectrum of the Crab Pulsar in the UV and optical . . . . .	100
10.9	Pulse profile of the Crab Pulsar in the optical band . . . . .	101
10.10	Simulation of the optical system for channel 66 . . . . .	103
10.11	Effective areas of the 3 optical channels . . . . .	104
10.12	Frequency-domain response of the filter circuit . . . . .	105
10.13	Power spectra and pulse profiles before and after the filters . . . . .	106
11.1	Sample trace of electronic noise with its frequency content . . . . .	110
11.2	Pulse profile of electronic noise after folding . . . . .	111
11.3	Sample trace and frequency content with noise from the night sky . . . . .	112
11.4	Pulse profile with night sky background noise . . . . .	113
11.5	Simulation of pulse profile with 120 Hz noise . . . . .	114
11.6	Frequency response of the notch-filter at 120 Hz . . . . .	116

11.7	Predicted pulse profile for the Crab pulsar with a notch-filter . . . . .	117
11.8	Predicted pulse profile with simulated signal and real background . . . . .	118
11.9	Pulse profile of the Crab pulsar in the optical band . . . . .	119
12.1	Overall detector response for $\gamma$ -rays . . . . .	125
12.2	Pulse profile for the Crab pulsar . . . . .	129
13.1	STACEE integral flux result . . . . .	133
13.2	Sky map of point sources detected above 250 GeV as of March 2005 . .	137

# List of Tables

9.1	Standard cuts . . . . .	81
10.1	Hour angle, azimuth, and elevation of EAS . . . . .	91
10.2	Predicted trigger rates compared to real data . . . . .	98
12.1	Livetime of 2002-2003 dataset after cuts . . . . .	122
12.2	Livetime of 2003-2004 dataset after cuts . . . . .	123
12.3	Results of the Crab Nebula analysis . . . . .	123
12.4	Sources of systematic uncertainty . . . . .	128
12.5	Results of search for pulsed emission from the Crab pulsar . . . . .	131
13.1	Summary of STACEE results for the Crab Nebula and pulsar . . . . .	133
A.1	Runlog summary for optical pulsar campaign . . . . .	139
B.1	Listing of pairs for the 2002-2003 season . . . . .	141
B.2	Listing of pairs for the 2003-2004 season . . . . .	143

# **Part I**

## **Gamma-Ray Astrophysics**

# Chapter 1

## A primer on $\gamma$ -ray detection

Considered by many authors to be the seminal paper in the field of  $\gamma$ -ray astronomy, Phillip Morrison's 1958 paper entitled "*On Gamma-Ray Astronomy*" [106] marked the beginning of a new era in the fields of cosmic ray research and astronomy. At the time, processes generating high energy charged particles were only studied through low energy channels: radio and polarized optical bands. Radiation detected in these bands is produced by secondary processes; high energy particles interacting with magnetic fields. Even though cosmic rays could be detected from the ground, the galactic and extra-galactic magnetic fields scramble the arrival direction of charged particles, such that their places of origin cannot be identified. Morrison pointed out that  $\gamma$  radiation in the few tenths MeV to 100's MeV would be directly related to high-energy and nuclear processes. He described physical processes which were expected to produce continuous and line spectra in the  $\gamma$ -ray range and suggested that  $\gamma$ -rays could be produced in solar flares and in the Crab Nebula, predictions that were later confirmed. He concluded his paper with the following statement: "*This note is intended mainly to attract to this problem the attention of those experimenters skilled in the required arts.*" Many detectors, both in space and ground-based, were commissioned during the next decades. The following sections highlight some of the key results from these experiments. For a more comprehensive review of the evolution of this field of research, the reader is invited to consult these excellent review articles [151, 113].

### 1.1 Early satellites

Above a few keV (X-rays), photons have so much energy that they cannot be focused by mirrors. Special techniques must be used to detect the energy lost by these photons when they interact with matter. At energies  $E \gtrsim 30$  MeV ( $\gamma$ -rays), photons predominantly lose

energy by  $e^+/e^-$  pair production. Detectors aboard satellites use the following generic technique to detect these  $\gamma$ -rays:

- Gamma-rays are first converted to  $e^+/e^-$  pairs as they pass through a piece of dense material, called a *target*, which is about one radiation length thick. This target is usually made of a high-Z material, e.g. lead (Pb), which offers a large cross-section for pair-production. The charged particles then lose energy in different parts of the detector and generate a trigger if certain conditions are met.
- Detectors located in space are constantly bombarded by charged particles (cosmic rays) that can initiate a response which is in many respects identical to that of a  $\gamma$ -ray. Given that the flux of cosmic rays is many orders of magnitude superior to the flux of  $\gamma$ -rays, they represent a significant source of background. For this reason, detectors are surrounded by a thin anticoincidence shield (usually made of plastic scintillator) which is viewed by sensitive light detectors. When charged cosmic rays pass through the anticoincidence shield, they lose energy by ionization and atomic excitation. The excited atoms in the plastic lose this energy by emitting photons which are detected by the light detectors. Contrary to cosmic rays,  $\gamma$ -rays can easily pass through the anticoincidence detector without losing energy. Hence, the anticoincidence shield acts as a veto against cosmic rays and is essential to maximize the sensitivity of the detector.
- In modern detectors, a tracking module is used to record the trajectory of the  $e^+/e^-$  pairs. This information is used to reconstruct the direction of the original  $\gamma$ -ray.
- Finally, the  $e^+/e^-$  pair is absorbed in a calorimeter where its energy is measured. The origin, energy, and time of the primary  $\gamma$ -rays are used to study the spatial distribution, spectra, and time variability of the  $\gamma$ -ray sky.

Launched on April 27, 1961, Explorer XI was the very first satellite dedicated to  $\gamma$ -ray astronomy [95]. The small  $\gamma$ -ray detector, which could fit in a college student's backpack, was built by William L. Kraushaar and George W. Clark from the Massachusetts Institute of Technology (MIT) and had an energy threshold of about 50 MeV (see figure 1.1). The  $\gamma$ -rays were converted to  $e^+/e^-$  pairs in a sandwich crystal scintillator made of alternate slabs of CsI and NaI, and the energy was measured by a Lucite Cherenkov counter. Unfortunately, problems with the power supply forced the end of operation after only a few months. Of the 127 events identified as  $\gamma$ -rays, 105 were produced in the earth's atmosphere, and the remaining 22 events came from a variety of directions in space. After

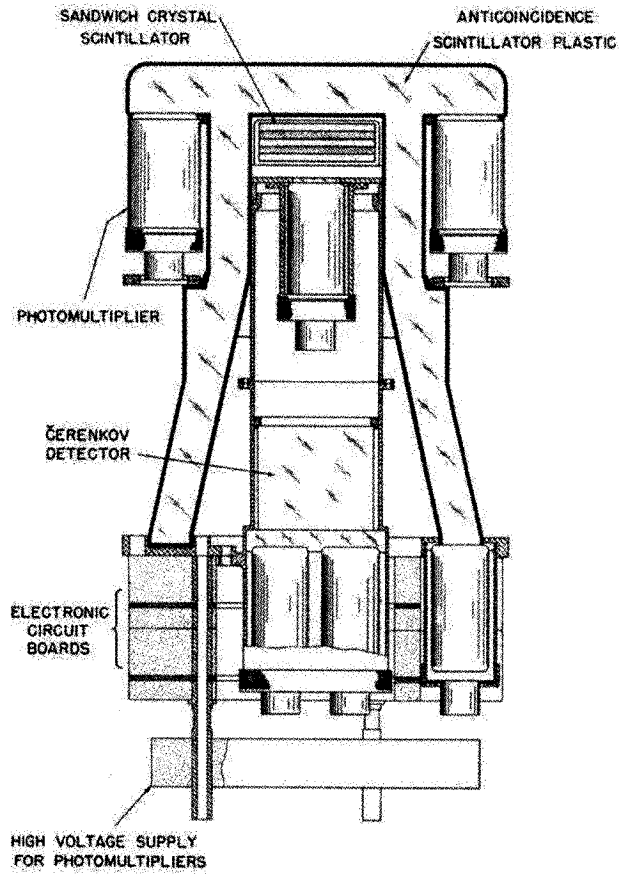


Figure 1.1: Schematic view of the Explorer XI  $\gamma$ -ray detector. The instrument is 20 inches high, 10 inches in diameter, and weighs about 30 pounds. Taken from [95]

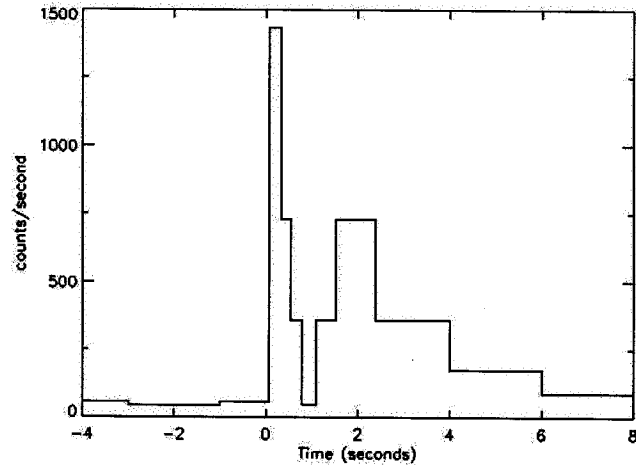


Figure 1.2: First GRB detected on July 2, 1967. The data plotted show a sudden increase in the count rate of the  $\gamma$ -ray instrument on board the Vela-4A satellite indicating a sudden flash of  $\gamma$ -rays. Taken from [141].

the Explorer XI mission, a number of  $\gamma$ -ray detectors flew on the OGO<sup>1</sup>, OSO<sup>2</sup>, Vela, and Russian Cosmos series of satellites. In 1967, the OSO-III satellite carried a  $\gamma$ -ray instrument that detected 621  $\gamma$ -ray events above an energy threshold of 50 MeV [35, 96]. The celestial distribution of the events was anisotropic, showing a concentration along the galactic equator and an extended region of higher intensity around the galactic center.

One of the most exciting discoveries in  $\gamma$ -ray astronomy was made in the late 1960s and early 1970s by detectors on board military defence satellites. The Vela (meaning *watchman* in Spanish) satellite series was designed to detect  $\gamma$ -rays from nuclear bomb testing in the vicinity of the Earth and monitor world-wide compliance with the 1963 nuclear test ban treaty. The satellites were launched in pairs and the technologies for detection improved with each series. The Vela 5-A/B and 6-A/B series had sufficient timing resolution to determine the direction of the triggered events with  $\sim 10$ -degree angular resolution. The analysis of 16 short bursts of  $\gamma$ -rays by scientists at the Los Alamos Scientific Laboratory excluded the Sun and Earth as possible sources and showed that the  $\gamma$ -ray events were of cosmic origin [93]. While looking back at older data from the Vela-4A/B satellites, scientists found an event that occurred on July 2, 1967 (see Figure 1.2) and which is now believed to be the first observed  $\gamma$ -ray burst (GRB) [141].

<sup>1</sup>Orbiting Geophysical Observatories

<sup>2</sup>Orbiting Solar Observatories

Advances in technologies developed at particle accelerators were soon incorporated into space-based detectors. The first satellite to use a spark chamber to track the trajectory of  $e^+/e^-$  pairs inside the detector was the second Small Astronomy Satellite (SAS-2) [43]. SAS-2 was launched on November 19 1972, and on June 8 1973, a failure of the low-voltage power supply ended the collection of data. Even though the mission lasted only seven months, it provided an exciting view of the high-energy Universe above 30 MeV [48]. SAS-2 showed that Galactic  $\gamma$ -radiation dominated the diffuse radiation along the entire Galactic plane and was most pronounced in the region of the Galactic center. A number of point sources were discovered, including the Crab Nebula (for which a significant fraction of the  $\gamma$ -ray signal was pulsed at the radio pulsar frequency) and Vela supernova remnant. The angular resolution of the telescope wasn't sufficient to associate the other sources with individual stars or stellar systems. Shortly after the SAS-2 mission ended, the European Space Agency (ESA) launched its own  $\gamma$ -ray mission, COS-B, on August 9, 1975 [16]. Initially planned for two years, the mission was extended successfully to 6 years and 8 months. The detector used a spark chamber to track  $e^+/e^-$  pairs and an energy calorimeter consisting of CsI scintillator (see figure 1.3). COS-B was sensitive to  $\gamma$ -rays with energies in the 30 MeV - 5 GeV range and had an effective area of  $50 \text{ cm}^2$  (about the size of a human palm) at 400 MeV. The scientific objectives of the SAS-2 and COS-B missions included the study of the spectrum and distribution of Galactic  $\gamma$ -rays, the study of known point sources, and the search for new point sources. One of the best known results of the COS-B detector was the 2CG catalog of point sources (see Figure 1.4). A total of 25 point sources were reported, including extragalactic (Quasar 3C273) and Galactic sources [142].

## 1.2 A revolution in space

Our understanding of complex phenomena occurring in the Universe depends not only on the quantity, but also on the diversity and complementarity of the information that we collect with our instruments. In astronomy, this often means combining data from different parts of the electromagnetic spectrum. For this reason, NASA proposed the concept of *Great Observatories*, a series of four satellites that would study the Universe over many different wavelengths. The first observatory, and probably the best-known, is the Hubble Space Telescope (HST). Launched in 1990, Hubble can observe the Universe at ultraviolet, visual, and near-infrared wavelengths. The second of NASA's Great Observatories was the Compton Gamma Ray Observatory (CGRO), a satellite carrying 4  $\gamma$ -ray experiments designed to study the high-energy Universe. At 17 tons, the CGRO was

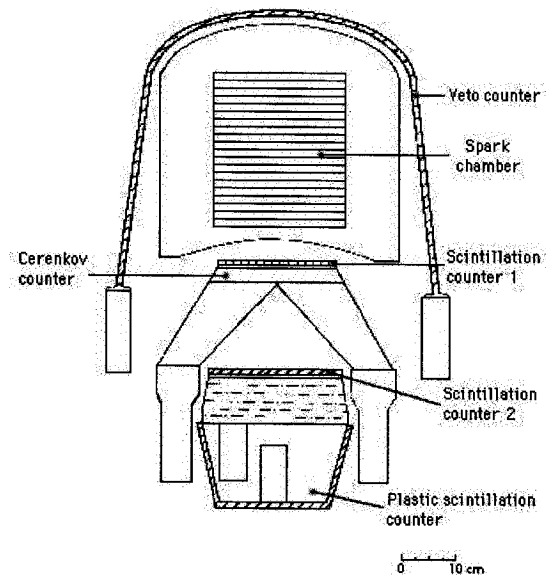


Figure 1.3: Diagram of the  $\gamma$ -ray detector on COS-B. (NASA's HEASARC)

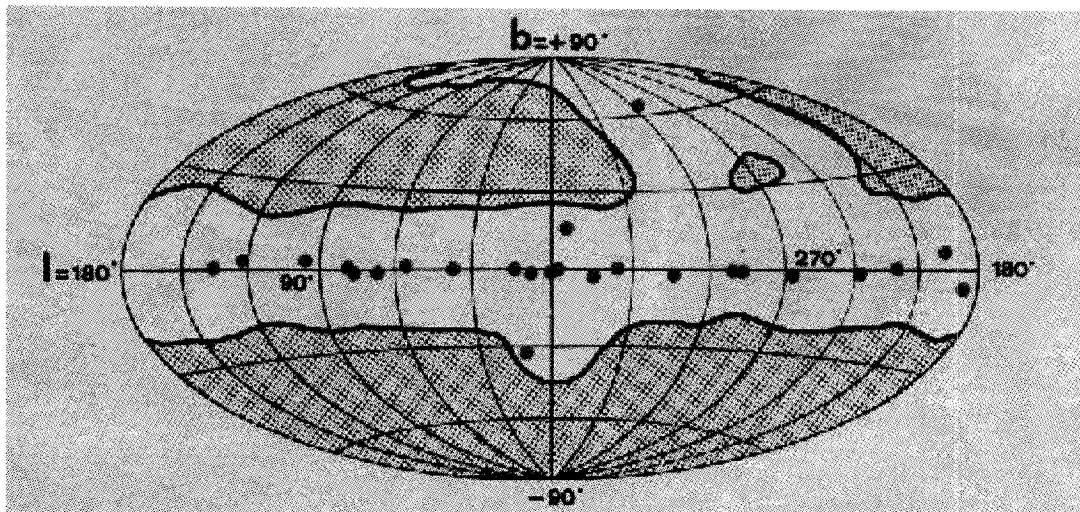


Figure 1.4: 2CG catalog of point sources detected by the COS-B telescope [142].

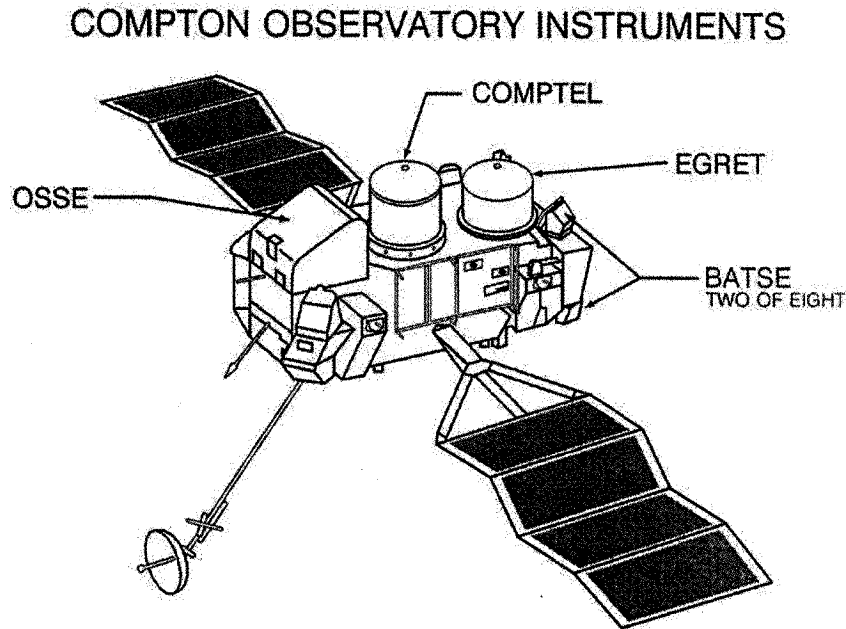


Figure 1.5: CGRO instruments: Burst And Transient Source Experiment (BATSE), the Oriented Scintillation Spectrometer Experiment (OSSE), the imaging Compton Telescope (COMPTEL), and the Energetic Gamma Ray Experiment Telescope (EGRET).

the heaviest astrophysical payload ever flown at the time of its launch on April 5, 1991. The mission was terminated on June 4, 2000 and the satellite was deorbited, re-entered into the Earth's atmosphere, and plunged into the Pacific Ocean approximately 4000 km southeast of Hawaii. The CGRO revolutionized the field of high-energy astrophysics (see next section). The third of NASA's Great Observatories is the Chandra X-Ray Observatory (CXO), launched in 1999, and the last of the series, launched on August 25 2004, is the Spitzer Space Telescope, sensitive to infrared photons in the 3–180 micron range.

### 1.2.1 The Compton Gamma Ray Observatory

The CGRO carried 4  $\gamma$ -ray experiments, covering an energy range from 20 keV to  $\sim 30$  GeV [94]. Figure 1.5 shows a diagram of the satellite with labels indicating the location of the different experiments.

- The Burst And Transient Source Experiment (BATSE) was an all-sky monitor used for the detection and localization of GRBs and outbursts from sources over the entire sky. Each corner of the satellite was equipped with a detector, and differences in count rates among separate detectors were used to reconstruct the direction of events. Each detector was composed of 2 NaI(Tl) scintillation crystals: one opti-

## 2704 BATSE Gamma-Ray Bursts

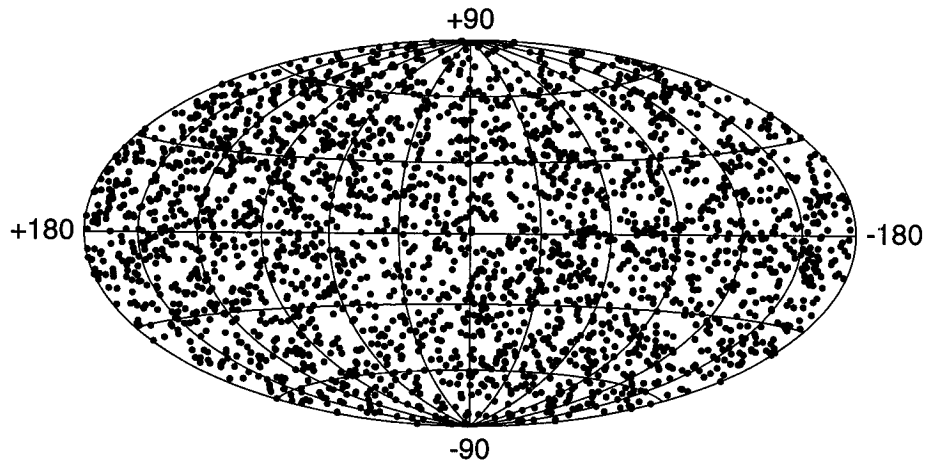


Figure 1.6: Distribution of GRBs detected by BATSE, in Galactic coordinates. Taken from [119]

mized for sensitivity and directional response, and the other optimized for energy coverage and energy resolution. The energy range covered by BATSE was from 20 keV to 20 MeV. BATSE observations of 2704 cosmic GRBs revealed an isotropic angular distribution (see figure 1.6), providing the first indication of the extragalactic origin of GRBs [119].

- The Oriented Scintillation Spectrometer Experiment (OSSE) consisted of four NaI-CsI phoswich scintillation detectors, sensitive to energies from 50 keV to 10 MeV. Amongst other results, OSSE produced a map of Galactic 511 keV positron annihilation line emission [125].
- The imaging Compton Telescope (COMPTEL) used the Compton scatter effect to produce maps of the  $\gamma$ -ray sky in the 0.8 to 30 MeV energy range. The top layer of the detector was made of a low-Z liquid scintillator (NE 213A) and the lower layer was composed of several blocks of NaI(Tl) scintillator. The energy and direction of the primary  $\gamma$ -rays were determined by measuring the energy and interaction

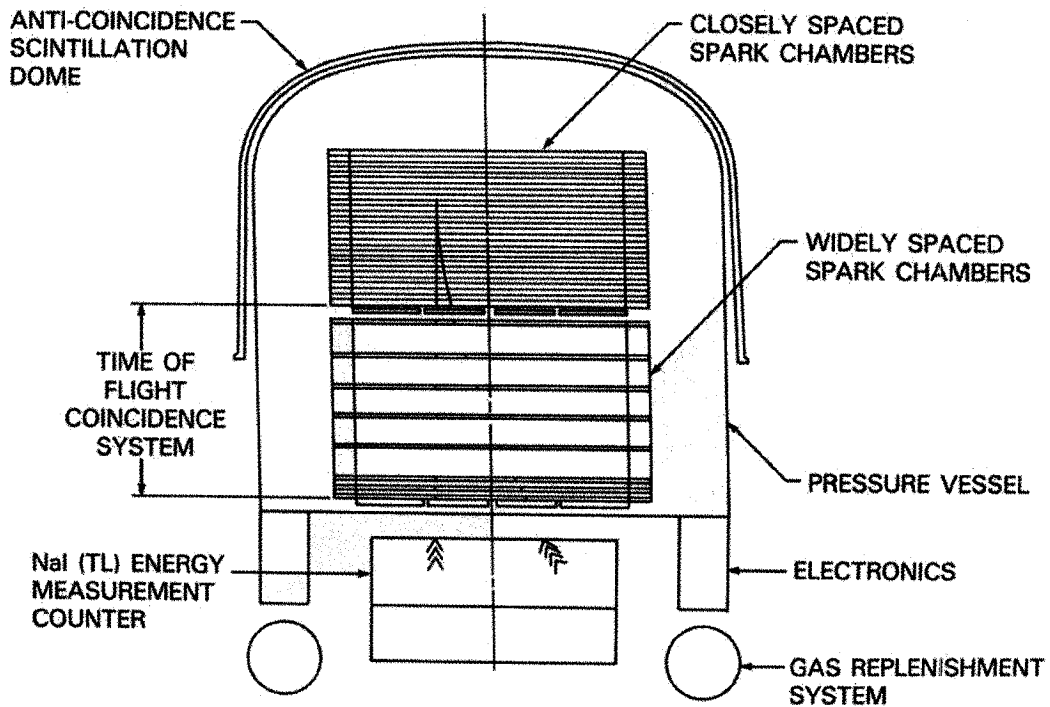


Figure 1.7: Schematic of the EGRET instrument.

position of the recoil electron in the top layer, and the total energy deposited in the lower layer.

- The Energetic Gamma-Ray Experiment Telescope (EGRET) covered the highest and broadest energy range, from about 20 MeV to about 30 GeV [87, 147]. EGRET used technologies very similar to those used by previous space instruments, notably SAS-2 and COS-B. EGRET used a multilevel spark chamber interspersed with thin layers of tantalum and a calorimeter made of NaI(Tl) (see figure 1.7). The effective area was approximately  $1500 \text{ cm}^2$  between 200 MeV and 1 GeV, about 30 times larger than SAS-2's effective area. EGRET had a wide field of view of  $\sim 0.5 \text{ sr}$ , with an angular resolution of  $\sim 0.5^\circ$  at 10 GeV.

The EGRET experiment was an astounding success. Besides producing the first map of cosmic  $\gamma$ -rays above 100 MeV, EGRET detected a large number of sources ( $\sim 270$ ), including GRBs, solar flares, 6  $\gamma$ -ray pulsars, and more than 60 Active Galactic Nuclei (AGN) of the blazar class. Furthermore, the third EGRET catalog [73] contained  $\sim 170$  unidentified objects which have yet to be identified with counterparts at other wavelengths

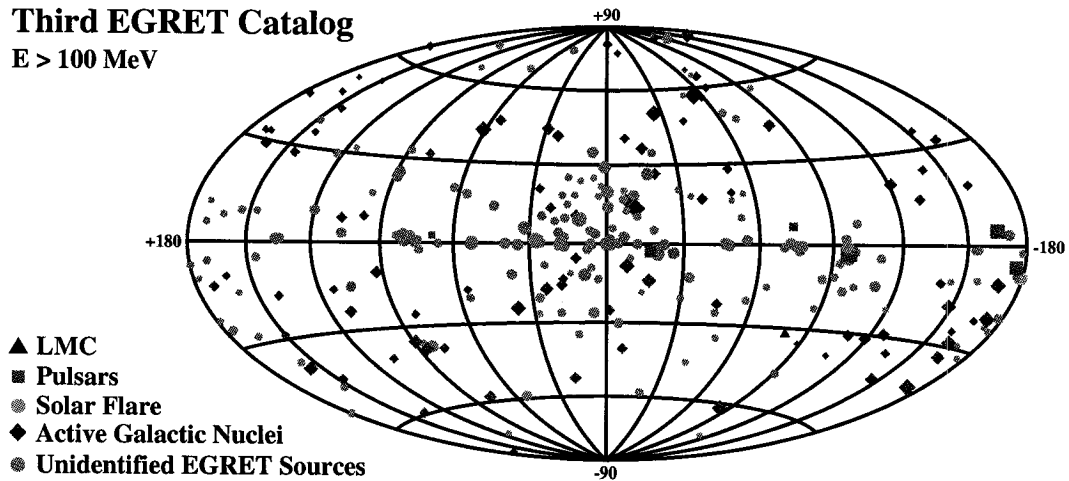


Figure 1.8: The third EGRET catalog all-sky map, in Galactic coordinates. Taken from [73].

(see figure 1.8).

### 1.3 Future satellites

Following in the footsteps of EGRET, two satellites are going to continue the exploration of the  $\gamma$ -ray Universe: AGILE and GLAST. The *Astro-rivelatore Gamma a Immagini LEggero* (AGILE) [145] satellite is designed to detect and image  $\gamma$ -rays in the 30 MeV–50 GeV energy range and hard X-rays in the 10–40 keV energy range. The spark chamber found on previous generations of satellites will be replaced with silicon plane detectors, a technology developed by high energy physicists working at particle accelerators. Although the sensitivity of the detector will be comparable to that of EGRET, the angular resolution will be much better ( $\sim 5' - 20'$  for intense sources) and the field of view will be quite large ( $\sim 3 \text{ sr}$ ). In addition, the small deadtime ( $\lesssim 200 \mu\text{s}$ ) and excellent absolute time tagging resolution of near  $1 \mu\text{s}$  will allow AGILE to study millisecond pulsars. AGILE is due for launch by the Italian Space Agency in 2005 and will be the only satellite sensitive to  $\gamma$ -rays above 30 MeV during the period 2005–2007.

The Gamma-ray Large Area Space Telescope (GLAST) [58] is NASA's next generation  $\gamma$ -ray satellite. The Large Area Telescope (LAT) is GLAST's main instrument and uses technologies similar to that of AGILE. GLAST will have a much larger effective area ( $8000 \text{ cm}^2$  versus  $1500 \text{ cm}^2$  for EGRET) and will cover an energy range from 20 MeV to 300 GeV, although above 100 GeV there will be very few statistics. GLAST is due for launch in 2007.

## 1.4 Ground-based detectors

Except at a few wavelengths, such as in the visible spectrum and at radio frequencies, electromagnetic radiation from space is unable to reach the surface of the Earth.  $\gamma$ -rays are no exception, and for this reason direct detection of  $\gamma$ -rays have been made by instruments on board rockets, balloons, or satellites. The radiation length for high energy  $\gamma$ -rays in air is  $\sim 37 \text{ g cm}^{-2}$ . Given an atmospheric depth at sea level of  $1033 \text{ g cm}^{-2}$ , the atmosphere is  $\sim 28$  radiation lengths thick, which is comparable to the attenuation produced by  $\sim 20$  cm of lead.

From a ground-based perspective,  $\gamma$ -ray astronomy is the offspring of the prominent field of cosmic ray research. Cosmic rays were discovered almost 100 years ago (1912) by Victor Hess [76] during a series of balloon flights where he measured the ionization of air at different altitudes. Instead of decreasing with altitude, the ionization increased with altitude, indicating that the source of this penetrating radiation was extra-terrestrial. In 1934, Bruno Rossi noticed coincidences between several counters placed in a horizontal plane, indicating the arrival of groups of particles at the same time. These events were studied in detail by Pierre Auger and collaborators and became known as Extensive Air Showers (EAS). It was realized that the primary particles responsible for these showers were of very high energy (higher than what could be produced in man-made accelerators) and large arrays of counters were built around the world. Even today, scientific experiments like the Pierre Auger project are building gigantic arrays of particle detectors to study primary particles with energy  $> 10^{20}$  eV.

Even though Cherenkov radiation was discovered in the 1930's, it was not until 1948 that Blackett suggested that a small fraction of the light of the night sky should be from Cherenkov radiation produced by cosmic rays [17]. Shortly after this publication, Galbraith and Jelley built the first Atmospheric Cherenkov Telescope (ACT) and detected Cherenkov pulses [57] in coincidence with charged particles from EAS. Many developments followed in various countries, notably in Ireland, the U.S.S.R., and the United States. In 1960, Cocconi suggested that protons could be accelerated to high energies in the Crab Nebula. Nuclear collisions would produce neutral pions which would decay to  $\gamma$ -rays. Being unaffected by Galactic magnetic fields, some of these  $\gamma$ -rays would reach the Earth. Even though the predicted fluxes were too optimistic, these predictions effectively launched the field of ground-based  $\gamma$ -ray astronomy. As we shall see in the next section, cosmic  $\gamma$ -rays interact with atoms in the atmosphere and produce EAS that can be detected on the ground. It took nearly two decades for the experimental techniques to reach a mature stage of development and the first convincing detections were reported by the Whipple group in 1989 [152]. Ground-based  $\gamma$ -ray astronomy became firmly estab-

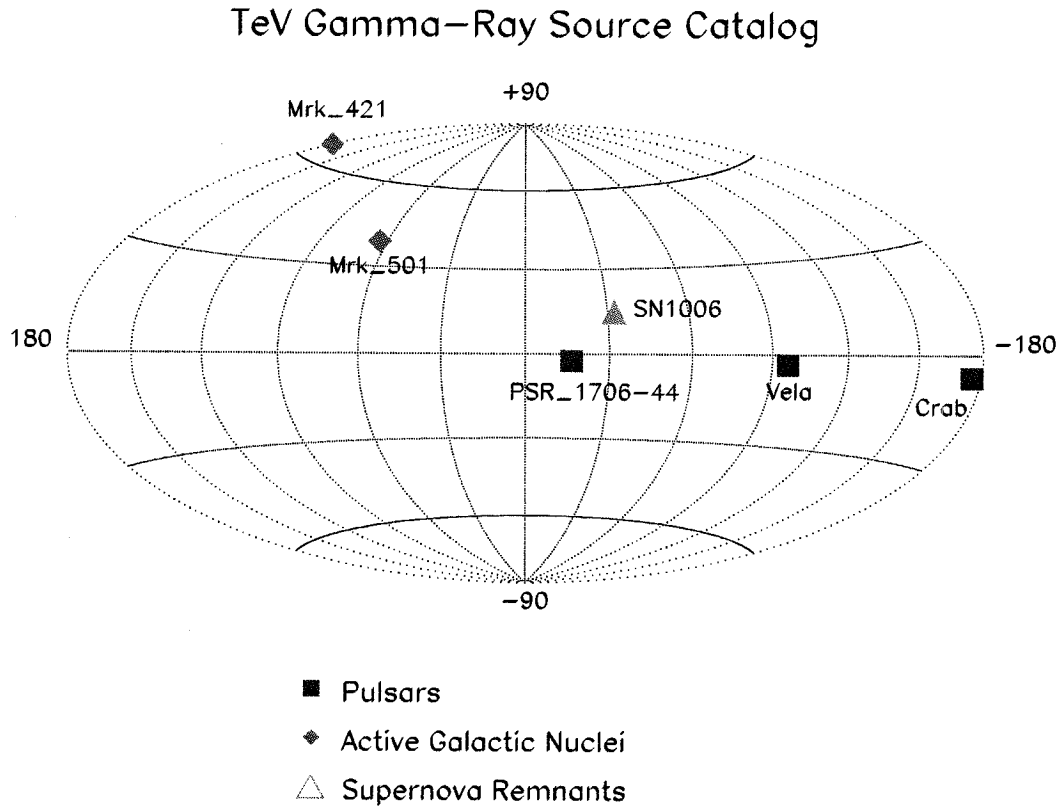


Figure 1.9: Sky map of point sources detected with a good statistical significance at energies above 250 GeV by ground-based detectors (Year 2000).

lished as a science in the 1990's, and by the year 2000, 6 sources had been detected with good statistical significance (see figure 1.9).

### 1.4.1 Extensive Air Showers and Cherenkov radiation

The physics of the interaction of high energy photons with matter (in the present case, the atmosphere) is fairly well understood (see for example [123]). A high energy photon interacts with an air molecule in the upper atmosphere and produces an  $e^+/e^-$  pair which initiates an electromagnetic cascade. Photons are created by Bremsstrahlung and subsequent  $e^+/e^-$  pairs are created by the photons. The number of particles in the cascade grows exponentially until the mean particle energy falls below the critical energy  $E_c$  (83 MeV in air), when ionization loss becomes more important than pair creation and Bremsstrahlung. Thus, the number of particles in the cascade rapidly reaches a maximum, called *shower max*, after which it gradually declines as shown in figure 1.10. Only the most energetic  $\gamma$ -rays ( $E > 100$  TeV) produce enough particles to be detected at

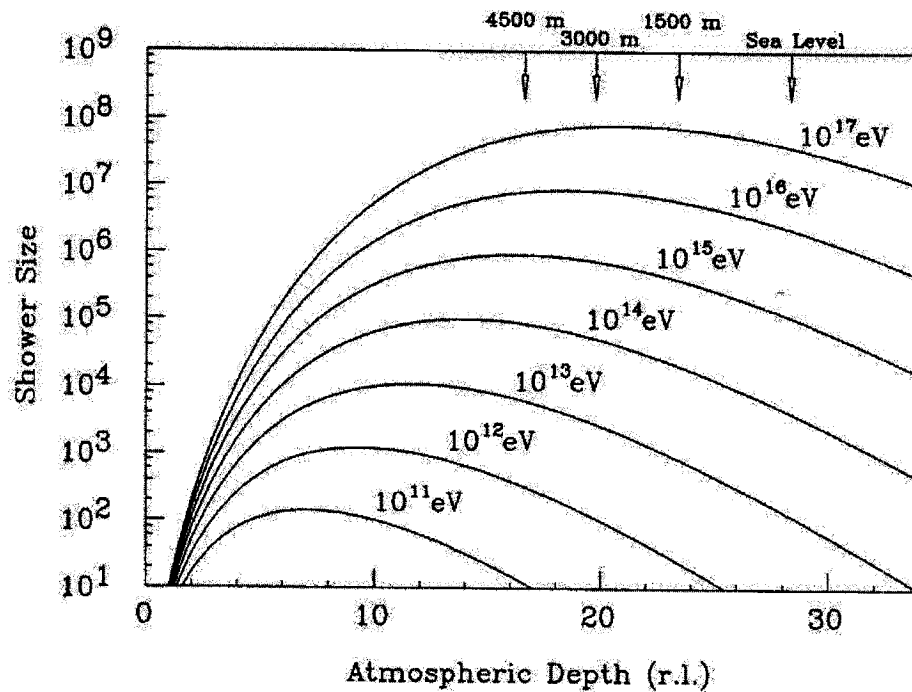


Figure 1.10: Total number of particles in air showers initiated by  $\gamma$ -rays of different energies as a function of depth in the atmosphere. The depth is defined by the number of radiation lengths (r.l.), which is  $\sim 37 \text{ g cm}^{-2}$  in air at STP. Taken from [113].

sea level; this explains why particle detectors are built at high altitude. The lateral development of EAS is the result of Coulomb scattering of the electrons as they propagate through the atmosphere. The lateral spread is given by the Molière radius which defines the containment radius for 90% of the total energy of the shower ( $\sim 75$  meters for a 100 GeV photon).

The relativistic particles produced by EAS are beamed along their trajectories and so retain the directionality of the original  $\gamma$ -ray. The shower front is quite thin ( $\sim 1$  m at the center) and the lateral distribution extends to radii larger than 100 m. Thus, by measuring the arrival time of the charged particles at different positions on the ground, one can determine the arrival direction of the  $\gamma$ -ray. For ground-based detectors, the effective area is defined by the spread of the EAS, not by the size of the individual detectors. Consequently, it is possible to achieve an extremely large collection area simply by spreading a number of detectors over a large area. For example, the CASA-MIA air-shower array achieved a detector area of  $230000 \text{ m}^2$  using 1089 scintillation detectors placed on a grid with intercounter spacing of 15 meters [22].

Another critical property of EAS is the production of Cherenkov photons by rela-

tivistic charged particles. The Cherenkov effect was discovered in 1934 by Pavel A. Cherenkov [33], and the theoretical interpretation was given by Frank and Tamm [55] (all three were later rewarded for their work with the 1958 Nobel Prize in physics). When charged particles move faster than the speed of light in air (or any other dielectric medium), the electromagnetic fields add coherently to form a shock front (see figure 1.11). This is the electromagnetic analog of a *sonic boom*. The opening angle  $\Theta_c$  of the Cherenkov cone at wavelength  $\lambda$  is given by:

$$\cos \Theta_c = \frac{1}{\beta n(\lambda)}, \beta > \frac{1}{n(\lambda)}, \quad (1.1)$$

where  $\beta = v/c$  is the particle's velocity (expressed as a fraction of the speed of light) and  $n(\lambda)$  is the index of refraction which may depend on the emission wavelength. The number of photons emitted per unit path length  $dx$  by a particle of charge  $ze$  is given by:

$$\frac{d^2N}{dx d\lambda} = \frac{(2\pi ze)^2}{hc\lambda^2} \left( 1 - \frac{1}{\beta^2 n^2(\lambda)} \right). \quad (1.2)$$

The radiation is mostly in the ultraviolet and blue regions of the electromagnetic spectrum and can easily propagate through the atmosphere to reach detectors located on the ground, typically 1000–2000 meters above sea level. Given that the refractive index  $n$  of the air at ground level and STP is 1.000273, the Cherenkov radiation energy threshold for electrons and positrons with energy  $m_e c^2 / (1 - \beta^2)^{1/2}$  is  $\sim 21$  MeV. Thus, for electrons with values of  $\beta \sim 1$ , the Cherenkov angle is  $\Theta_c \sim 1.3^\circ$ . Relativistic particles in the EAS produce Cherenkov radiation at all depths, and the total number of Cherenkov photons reaching the ground is proportional to the total number of  $e^+/e^-$  pairs produced in the shower. Hence, the atmosphere acts as a calorimeter, and the total Cherenkov light yield is proportional to the energy of the primary particle (see figure 1.12). The radius of the Cherenkov light pool on the ground is  $\sim 120$ – $150$  meters and the wavefront is relatively flat with a thickness of  $\sim 1$  meter (3–5 ns thick).

Hadronic cosmic rays also initiate EAS which are similar in many respects to those produced by  $\gamma$ -rays. Unfortunately, the flux of cosmic rays is much higher than the flux from  $\gamma$ -ray sources and constitutes a daunting source of background for ground-based  $\gamma$ -ray telescopes. For example, the integral flux of cosmic ray particles above 1 TeV in a circular angular bin of  $0.5^\circ$  is 400 times larger than the integral flux of  $\gamma$ -rays from the Crab Nebula above 1 TeV [113]. The main differences between hadronic and  $\gamma$ -ray induced EAS are in their compositions and morphologies. Gamma-ray induced showers are composed almost exclusively of  $e^+/e^-$  pairs, while hadronic showers produce copious

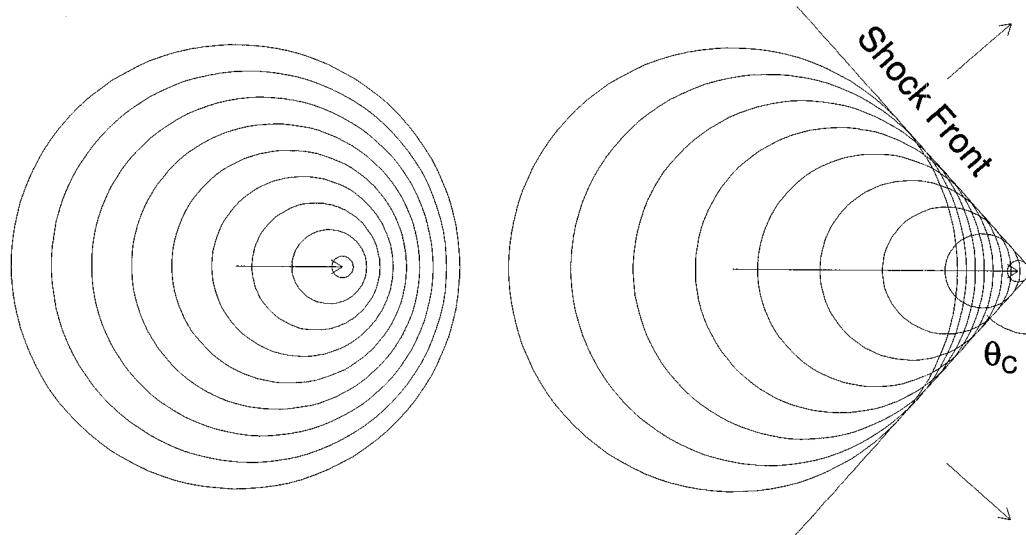


Figure 1.11: Cherenkov radiation shock front. Spherical wavefronts emanate from a moving charged particle at the phase velocity of light,  $c/n$ . The particle on the left is moving at half the phase velocity, whereas the particle on the right moves at  $1.33c/n$  and emits Cherenkov radiation. The Cherenkov angle shown here ( $41^\circ$ ) corresponds to the case of highly relativistic particles in water; in air the opening angle of the Cherenkov cone is closer to  $1^\circ$ . Taken from [118]

amounts of pions ( $\pi^{\pm,0}$ ), muons ( $\mu^\pm$ ), and  $e^+/e^-$  pairs. In addition, the secondary nucleons usually have larger transverse momentum than the  $e^+/e^-$  pairs produced in  $\gamma$ -ray initiated EAS. Hadronic showers also produce Cherenkov radiation, but subtle differences in the light density and timing distributions can be used by ground-based Cherenkov detectors to reject hadronic events. Figure 1.13 shows the lateral density profiles of Cherenkov photons on the ground for a 50 GeV  $\gamma$ -ray and 200 GeV proton initiated EAS. The nucleonic cascades created in hadronic showers can initiate their own sub-showers which result in more irregular Cherenkov density profiles. These irregularities are also seen in the timing profiles as shown in figure 1.14. Ground-based telescopes make use of these differences in the timing and density profiles to reject hadronic events and improve their sensitivities.

Two different classes of ACT are used to study  $\gamma$ -ray sources: wavefront samplers, and imagers (IACT). Wavefront samplers use an array of mirrors to measure the lateral density and timing profile of the Cherenkov light pool; STACEE is such a detector and details of the technique are given in subsequent chapters. Imagers have typically used a single mirror with a pixelated camera to form an image of the EAS development. The shape of the Cherenkov image is used to differentiate between  $\gamma$ -ray and hadron induced EAS. As shown in figure 1.15,  $\gamma$ -ray showers tend to have an elliptical shape and point toward the

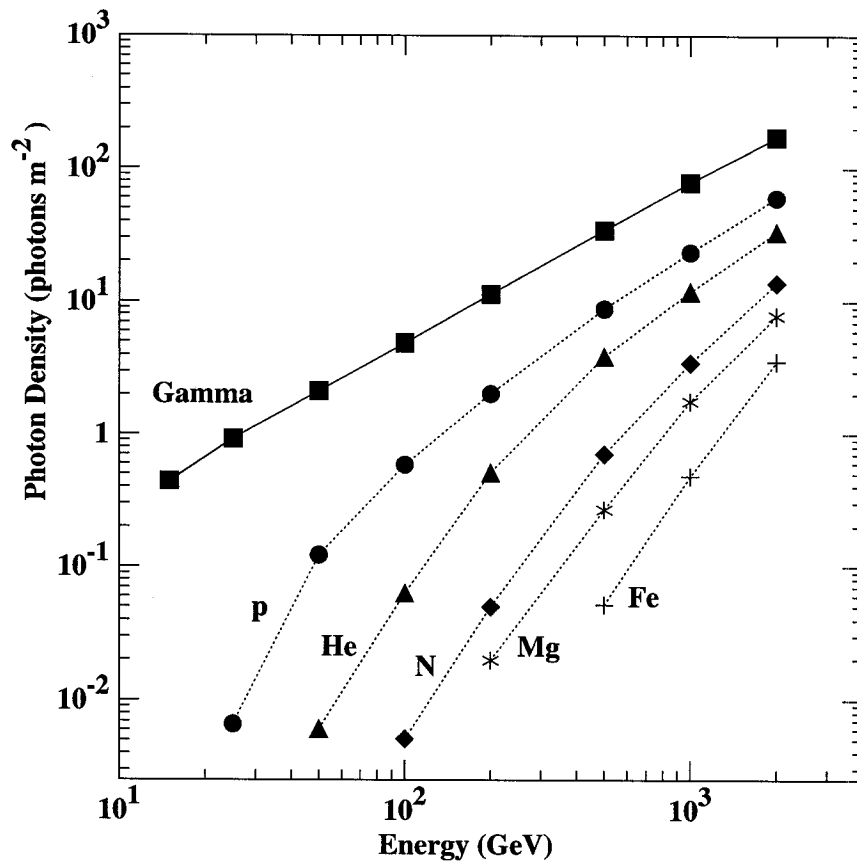


Figure 1.12: Cherenkov light yield as a function of energy and composition at an altitude of  $\sim 3$  km. The density is calculated using the photons landing within 125 meters from the shower axis. Only photons with wavelengths between 300 and 550 nm and landing within 10 ns of the peak arrival time are included. Taken from [113].

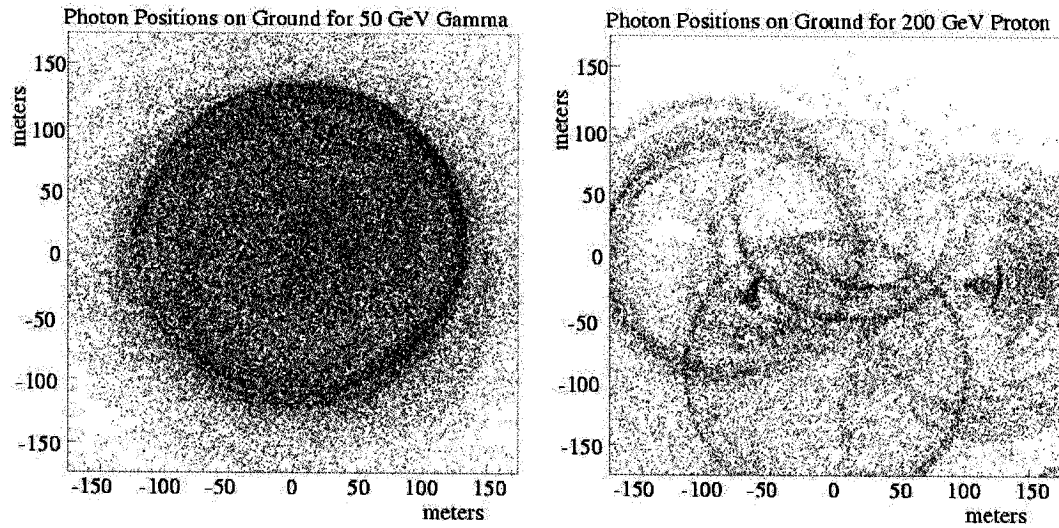


Figure 1.13: Lateral density profile of Cherenkov photons produced by a 50 GeV  $\gamma$ -ray (left) and 200 GeV proton (right) initiated EAS.

center of the camera, while hadronic EAS have irregular shape. The imaging technique was used successfully by many telescopes; in particular the Whipple, CAT, HEGRA, and CANGAROO atmospheric telescopes. Energy thresholds as low as 250 GeV were achieved by these telescopes, but this is still well above the range accessible by satellites. The new generation of telescopes (VERITAS, H.E.S.S., MAGIC, CANGAROO-III) now use up to 4 large (10–17 meters) telescopes to get stereoscopic images of the EAS which dramatically improve the sensitivity of the detectors. In addition, the larger effective areas of these instruments will help bridge the energy gap between satellites and the previous generation of ground-based instruments.

### Simulated Shower Front Timing Profiles

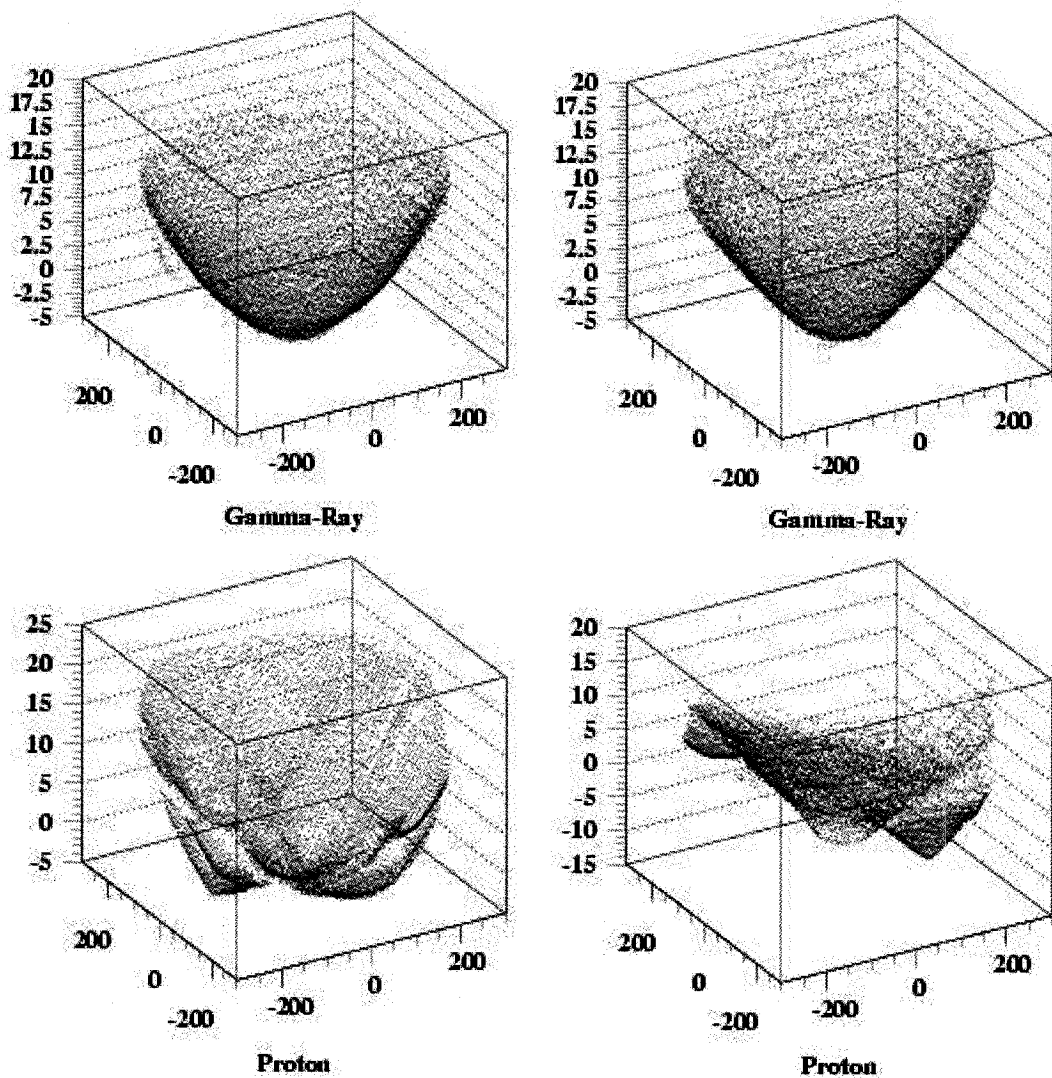


Figure 1.14: Lateral timing profiles for representative  $\gamma$ -ray and proton showers. The horizontal axes are position on the ground in meters, while the vertical axis is the arrival time of the Cherenkov photons in ns.

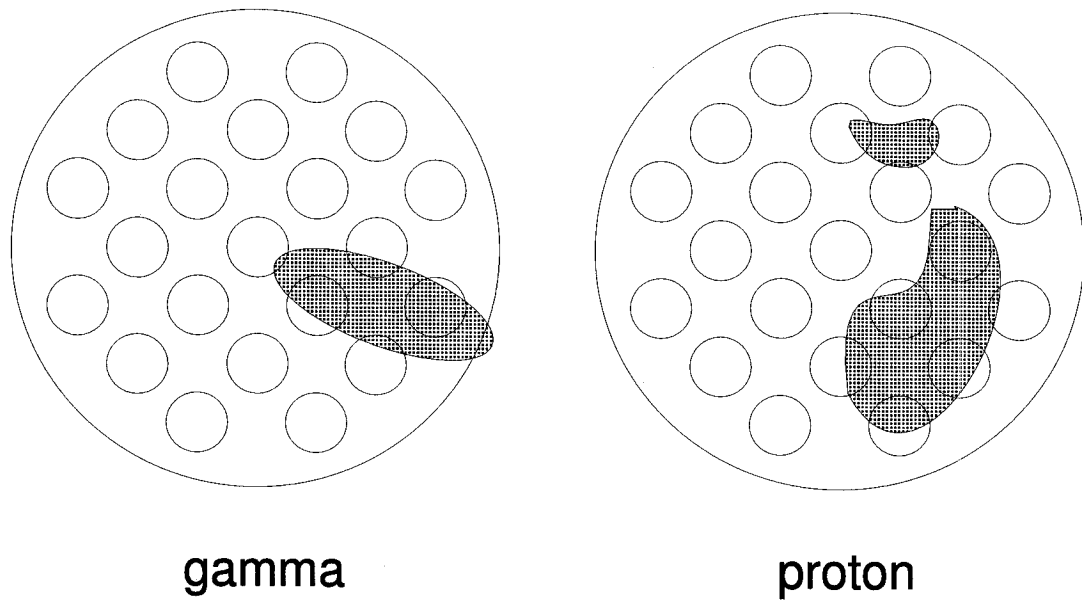


Figure 1.15: Schematic of Cherenkov images in the focal plane of an imaging Cherenkov telescope. Left:  $\gamma$ -ray images have an approximately elliptical shape and point towards the center of the camera. Right: proton images have irregular shapes. Taken from [113].

# Chapter 2

## Gamma-rays from the Crab

The Crab is a plerion-type<sup>1</sup> supernova remnant [153] located at a distance of about 2 kpc ( $\sim 6000$  light-years) in the constellation of Taurus [148]. The visual magnitudes of the nebula and pulsar (PSR 0531+21) are respectively +8.4 and +16, well below what the human eye can see<sup>2</sup>. The Crab pulsar is approximately 10 km in diameter and rotates 30 times per second. In the optical band, the Crab Nebula has an elliptical shape  $6 \times 4$  arcminutes across (see figure 2.1). The Crab Nebula has been detected over a very broad range of energies, from radio frequencies, to TeV  $\gamma$ -rays. Unlike the nebula, the pulsar has never been detected convincingly at TeV energies. It is said that the Crab Nebula and its pulsar are the most studied objects in astrophysics.

### 2.1 A brief biography of the Crab

Interpretations of historical records link the Crab supernova remnant to the supernova explosion of A.D. 1054 [34]. According to Chinese and Japanese observations, the *guest star* appeared twice as bright as Venus and could even be seen in the day time for approximately 3 weeks. The radiation from the supernova explosion eventually dimmed and the star disappeared from sight approximately 2 years later and was not observed for nearly 700 years. The first rediscovery of the supernova remnant was made by the English physician and amateur astronomer John Bevis, in 1731 (see figure 2.2 for a reproduction of his personal star atlas). Several years later on the night of August 28, 1758 the French astronomer Charles Messier independently rediscovered the supernova remnant while following the comet of that year, comet 1758 De La Nux. Here is an extract from Messier's

---

<sup>1</sup>Most supernova remnants have shell morphologies, but some, like the Crab Nebula are filled with emitting material at all wavelengths; these are called Plerions.

<sup>2</sup>The unaided night-adapted human eye can see down to magnitude +6.

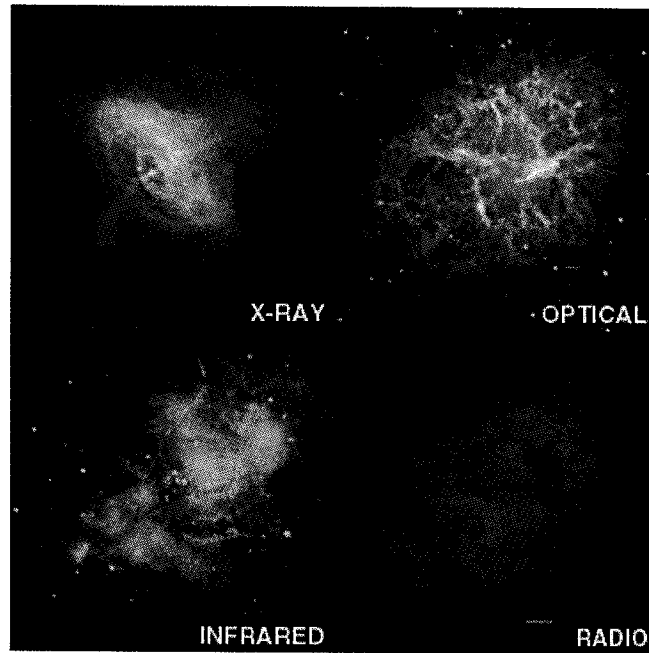


Figure 2.1: Multi-wavelength images of the Crab Nebula (images not to scale). The nebula appears most compact in X-rays and largest in the radio. The X-ray nebula shown in the Chandra image is about 40% as large as the optical nebula, which is in turn about 80% as large as the radio image.

first catalog:

The Comet of 1758, on August 28, 1758, was between the horns of Taurus. I discovered above the southern horn, and little distant from the star Zeta of that constellation, a whitish light, elongated in the form of the light of a candle, which didn't contain any star. This light was almost the same as that of the Comet which I observed at that time; yet it was a bit more vivid, more white and a bit more elongated than that of the Comet which to me had always appeared almost round in its coma, without the appearance of a tail or beard. On September 12 of the same year, I determined the position of this nebula, its right ascension is 80d 0' 33", and its declination 21d 45' 27" north. This nebula is placed [printed] on the chart of the route of the Comet of 1758. *Mémoires de l'Académie for 1771, p. 435-436 (first Messier catalog).*

This supernova remnant became the first object in Messier's famous catalog and is now known as M1. In 1848, William Parsons, third Earl of Rosse, was the first one to refer to it as the Crab Nebula, after he published a drawing of the nebula in 1844 (see figure 2.3).

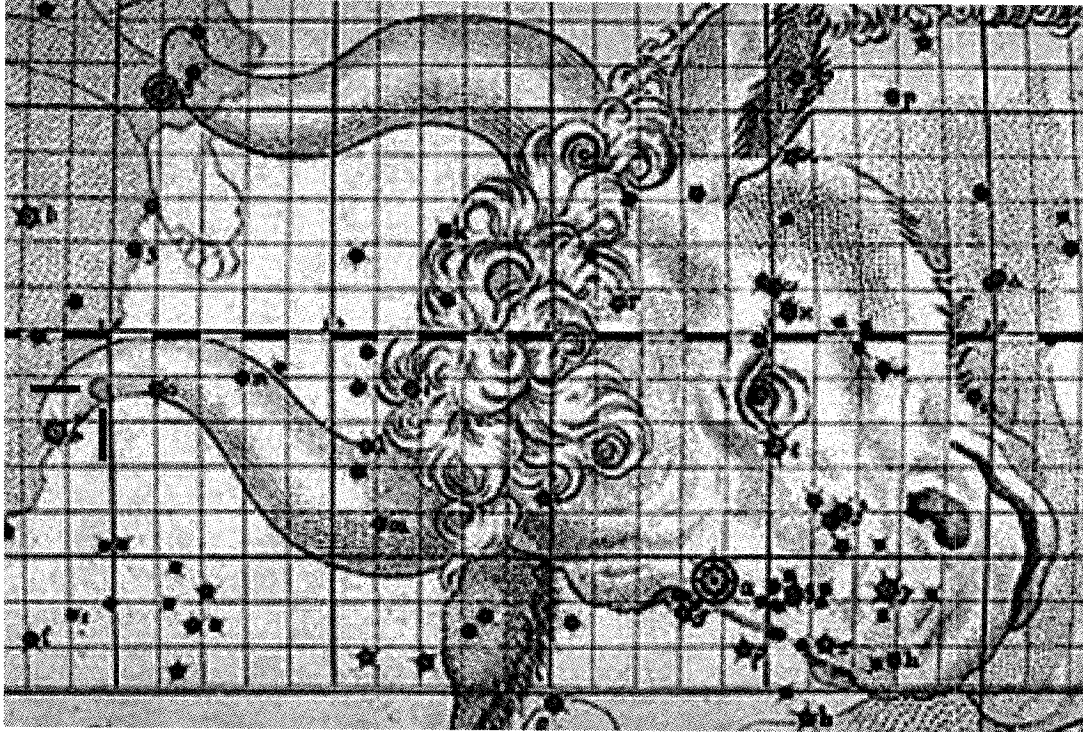


Figure 2.2: The first star chart showing the Crab Nebula, M1, drawn by John Bevis, who discovered it in 1731. M1 is the faintly painted nebula slightly upper-right (NE) of Zeta, at the tip of the lower (southern) horn of Taurus the Bull. Taken from <http://www.klima-luft.de/steinicke/ngcic/persons/bevis.htm>



Figure 2.3: Drawing of the Crab Nebula by William Parsons, the third Earl of Rosse. This drawing gave rise to the name "Crab Nebula". It was created using the 36-inch reflector at Birr Castle about 1844.

Spectroscopic studies of the Crab Nebula undertaken in 1919 [135] showed that the light from the nebula was made of two major components: bright lines which formed a complex web of filaments with an emission spectrum like that of gaseous nebulae, and a bluish diffuse background which had a continuous spectrum and was strongest toward the center of the nebula. In order to understand what was powering the nebula, astronomers started searching for the central star. Two stars appeared closer to the center and were examined by Minkowski [104] and Baade [14] in 1942. One of the stars was identified as a type F star, too cool to produce high levels of UV, and the other star showed a continuous spectrum without recognizable emission lines, making it difficult to classify. The second star became the favorite candidate as the source of energy for the nebula but its nature would remain a mystery for almost 30 years. Another piece was added to the puzzle in 1949 when the Crab was detected as a strong radio source [19]. The radio flux density was so large that it could not be explained by thermal processes. In 1953, Shklovsky [138] interpreted the continuous spectrum of the Crab Nebula as synchrotron radiation. Subsequent measurements of the polarization of radio and optical emission confirmed Shklovsky's hypothesis [45, 115]. Even though synchrotron radiation explained the nonthermal spectrum, the origin of the relativistic electrons that gave rise to the radiation remained a fundamental difficulty, and remains poorly understood.

In 1967, a few months before the discovery of radio pulsars by Hewish and Bell [78], Franco Pacini showed that a rapidly rotating neutron star with a dipole magnetic field would convert its rotational energy into electromagnetic radiation [120]. Pacini showed that a rotating neutron star could provide the luminosity of the Crab Nebula for its entire lifetime. Shortly after the discovery of radio pulses by Staelin and Reifenstein [140] from the central star previously identified by Minkowski and Baade, Thomas Gold argued that pulsars were actually rotating neutron stars [60]. His theory was confirmed [61] and the long-standing puzzle was solved when the period of the Crab pulsar was shown to be increasing with time, implying a spin-down which could power the nebula [130].

## 2.2 High energy emission from the nebula

Shortly after it was shown that the continuous spectrum of the Crab Nebula was synchrotron radiation, Robert Gould [64] predicted that high energy  $\gamma$ -rays would be produced in the nebula by the inverse Compton (IC) process. As the name implies, it is the electrons that lose energy rather than the photons. The low energy *seed* photons are boosted to GeV-TeV energies by interacting with high energy electrons accelerated in the termination shock of the pulsar wind [129, 89]. The first convincing detection of the Crab

Nebula in the  $\gamma$ -ray regime by a ground-based detector was made in 1989 by the Whipple collaboration [152] when they reported a TeV signal ( $>0.7$  TeV) at the  $9\sigma$  level. The Crab Nebula has now been detected by more than 10 groups, from 60 GeV [42] to 80 TeV [2].

The transport of energy from the pulsar wind and accompanying magnetic fields to the nebula has been modeled using magnetohydrodynamic (MHD) approximations [89]. Even though these models assume spherical symmetry (the Crab Nebula has an oblate shape) they successfully describe the general characteristics of the synchrotron nebula. Figure 2.4 shows the nonthermal spectrum of the Crab Nebula which extends over 21 decades in energy. The IC spectrum appears to gradually steepen from  $\alpha \sim 2$  at  $E \sim 100$  GeV, where the spectrum is defined by  $dN/dE \propto E^{-\alpha}$ , to  $\alpha \sim 2.5 - 2.6$  at  $E \sim 1$  TeV, which corresponds to the energy range covered by STACEE. The flattening of the spectrum at lower energies has not yet been measured and this is one of the reasons for STACEE to observe the Crab Nebula. Another reason is that the flux from the Crab Nebula in the GeV-TeV range is constant in time, which makes the Crab Nebula a standard candle for  $\gamma$ -ray astrophysics and the perfect calibration source for ground-based telescopes.

### 2.3 High energy emission from the pulsar

As mentioned previously, the Crab pulsar was first discovered at radio wavelengths in 1968 [140]. The discovery of rotating neutron stars was very exciting and many groups started searching for pulsed emission at different wavelengths. A few months later, optical pulses were detected from the Crab pulsar by Cocke, Disney, and Taylor [36]<sup>3</sup>. During the same year, two X-ray detectors specially designed to detect pulsed emission were launched on board rockets [56,23] and showed that the power radiated in the X-ray region was at least 100 times that in visible light. Pulsed emission at higher energies was detected by the EGRET  $\gamma$ -ray detector from 100 MeV to  $\sim 10$  GeV with no indication of a cutoff and is well fit by a power law with an index of  $-2.05 \pm 0.04$  [112,127,49]. The pulse profile is remarkably similar across all wavelengths and shows two narrow peaks separated by  $\sim 0.4$  cycles. Figure 2.5 shows the pulse profile as formed from the data accumulated during the first three cycles of EGRET observations above 100 MeV. Ground-based detectors with much higher energy thresholds have also searched for pulsed emission, but only upper limits have been reported, indicating a strong spectral cutoff above a few  $10$ 's of GeV. The most constraining upper limit published to date is that of the CELESTE col-

<sup>3</sup>A dramatic and inspiring audio recording of their discovery was digitized and is available on the American Institute of Physics web site:<http://www.aip.org/history/mod/pulsar/pulsar1/01.html>

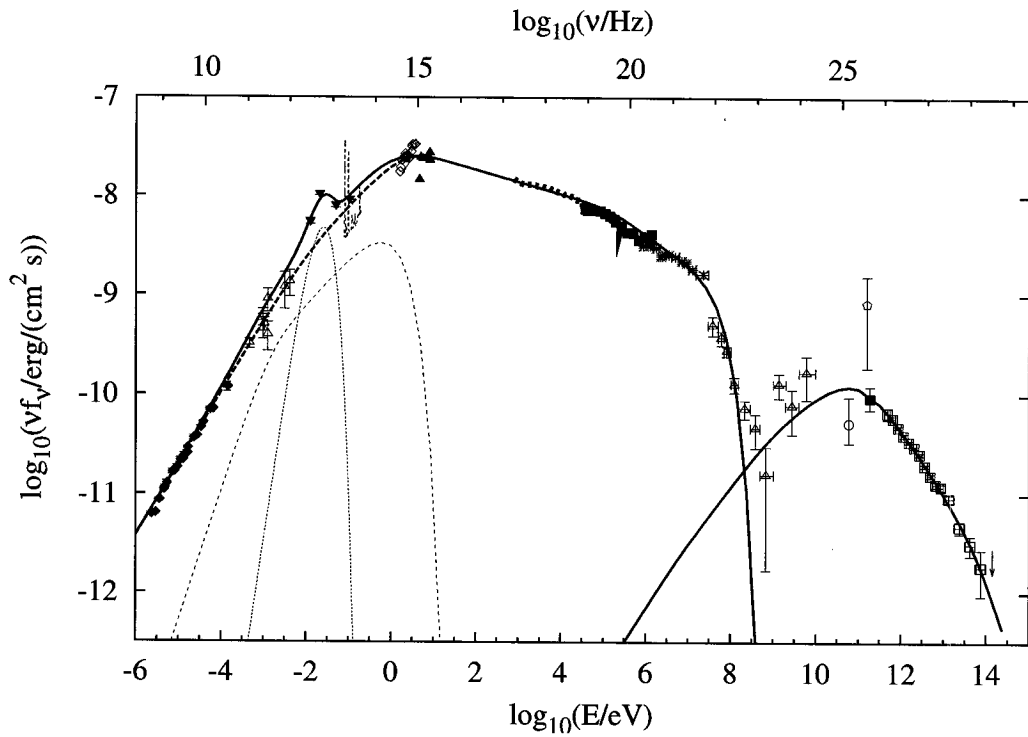


Figure 2.4: Nonthermal radiation of the Crab Nebula from radio to very high energy  $\gamma$ -rays. The solid lines correspond to the synchrotron and inverse Compton emission, as calculated in the framework of the spherically symmetric MHD wind model [89]. The dotted line is the thermal excess radiation and the dashed line is the emission at millimeter wavelengths. Taken from [2].

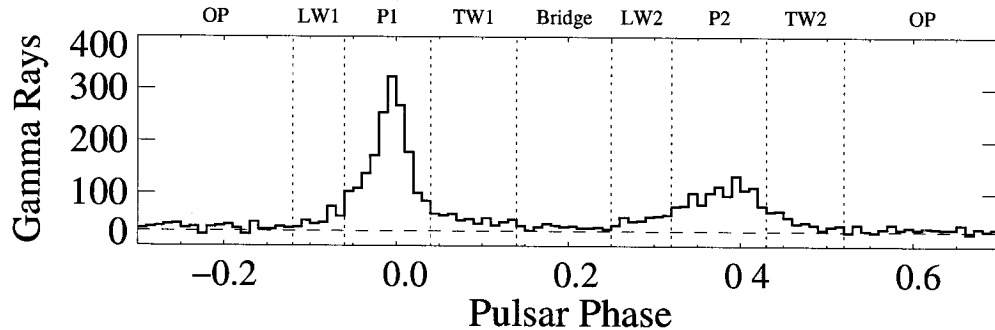


Figure 2.5: Pulse profile of the Crab pulsar formed from the data accumulated during the first three cycles of EGRET observations above 100 MeV. Adapted from [49].

laboration at 60 GeV [42]<sup>4</sup>. Figure 2.6 shows the differential flux of the Crab pulsar from  $\sim 60$  MeV to  $\sim 1$  TeV.

### 2.3.1 Pulsed emission models

The detection of pulsed  $\gamma$ -rays indicates that charged particles are accelerated to high energies in the pulsar magnetosphere, but there is still no agreement on where the acceleration occurs or on the radiation mechanisms. Two competing models (polar cap and outer gap) have been proposed to explain high energy emission and they were both derived from the idealized case of the aligned rotator model proposed by Goldreich and Julian in 1969 [63]. Both models successfully explain the EGRET results and upper limits from ground-based detectors, but predict different cutoff energies. Figure 2.7 shows a diagram of the geometry of the emission regions in the polar cap and outer gap models.

All the models assume that magnetized neutron stars are perfect conductors where there can be no net electric field in the stellar interior. Therefore, the star is polarized and must possess an interior electric field which satisfies

$$\mathbf{E} + \frac{\boldsymbol{\Omega} \times \mathbf{r}}{c} \times \mathbf{B} = \mathbf{0}. \quad (2.1)$$

The charges redistribute themselves in such a way that the Lorentz invariant  $\mathbf{E} \cdot \mathbf{B}$  vanishes in the stellar interior. Goldreich and Julian showed that a strong electric field parallel to the magnetic field lines of magnitude  $\sim 3 \times 10^{10}$  V/cm is present just outside the surface of the star and that this field is strong enough to rip electrons and ions from the surface of the neutron star and carry them into the magnetosphere. Some of the charges can escape

<sup>4</sup>The CELESTE collaboration has since revised their energy threshold to  $\sim 100$  GeV. Even with this change in threshold, their result is still the most constraining upper limit for a ground-based detector.

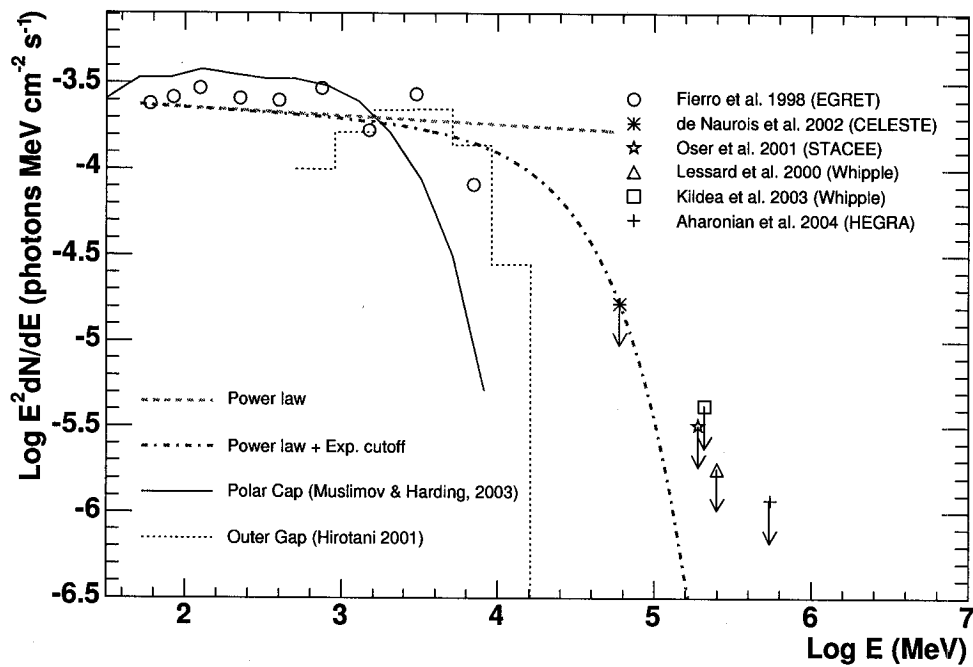


Figure 2.6: Pulsed  $\gamma$ -ray fluxes and limits for the Crab pulsar. The differential flux multiplied by  $E^2$  is plotted versus energy. The dashed line is a power law fit to the EGRET points [49]. The dot-dashed line is a power law fit with an exponential cut-off at  $E_0 = 26 \text{ GeV}$  which is constrained by the CELESTE result [42]. The solid line is a fit of the EGRET data to a Polar Cap model [107], and the dotted line is a fit to an Outer Gap model [85]. Upper limits are from the CELESTE [42], STACEE [117], WHIPPLE [98, 91], and HEGRA [2] experiments.

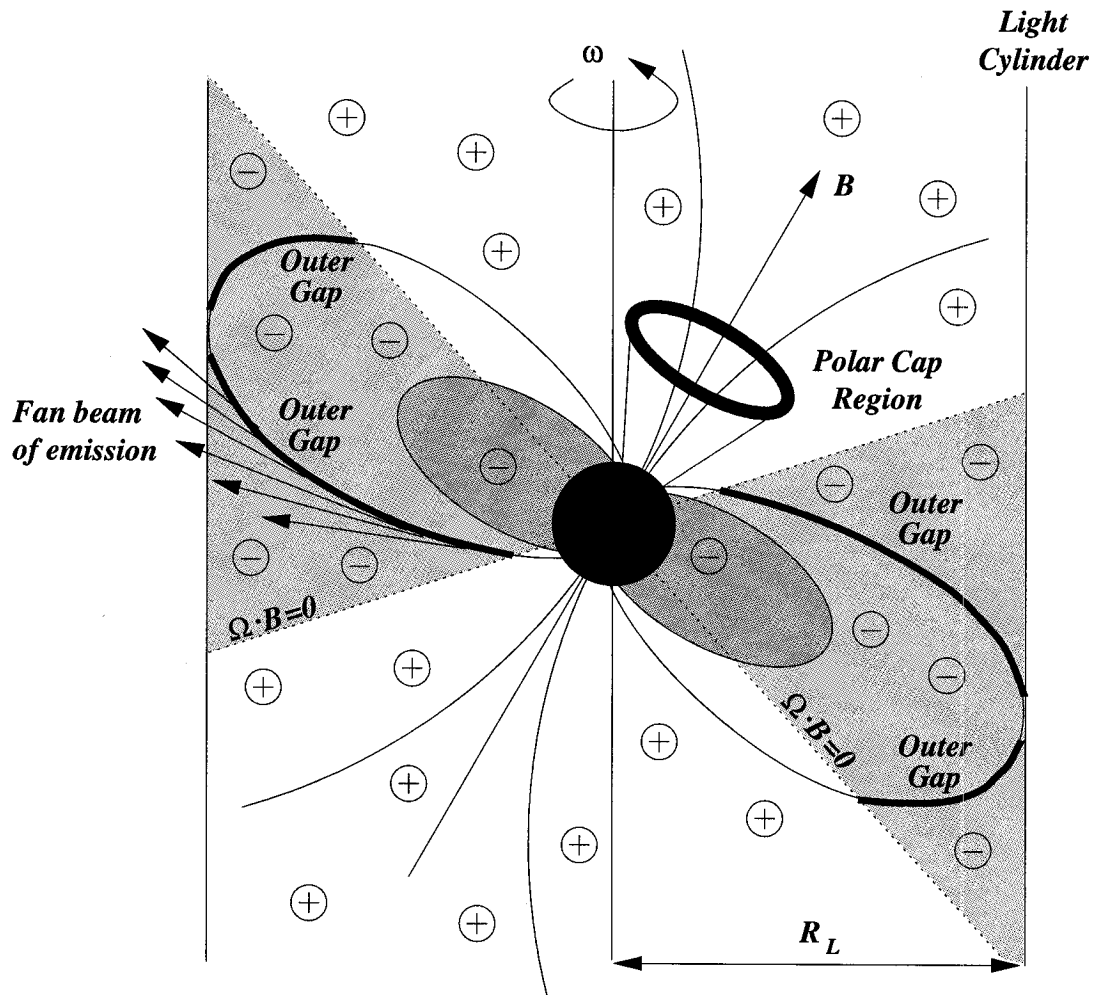


Figure 2.7: Schematic diagram of the polar cap and outer gap models showing the acceleration regions above the magnetic poles and outside the last closed magnetic field lines. The charge distribution is assumed to follow the Goldreich-Julian charge density. The dotted lines represent the null surfaces where  $\Omega \cdot B = 0$  (on this plot  $\Omega = \omega$ ). The light cylinder is the radius at which a particle co-rotating with the neutron star would move at the speed of light ( $R_L = c/\Omega$ ) [92].

the magnetosphere by following the open field lines, while others follow the closed field lines and co-rotate with the star. Assuming that the surface of the star can supply enough charge, the charged particles distribute themselves in the magnetosphere in such a way that  $\mathbf{E} \cdot \mathbf{B} = 0$ . The distribution of charges around the neutron star is known as the Goldreich-Julian charge density

$$\rho_{GJ} = \frac{\nabla \cdot \mathbf{E}}{4\pi} = \frac{-\Omega \cdot \mathbf{B}}{2\pi c[1 - |\boldsymbol{\Omega} \times \mathbf{r}|^2]}. \quad (2.2)$$

Figure 2.7 shows the distribution of charges around a neutron star as well as the null surfaces where  $(\boldsymbol{\Omega} \cdot \mathbf{B} = 0)$ . If for some reason the charge density cannot be maintained, a “gap” will be created, the electric field won’t be cancelled, and particle acceleration will occur. There are two distinct sites where a gap can form and strong electric fields may accelerate particles. This has given rise to two different models for  $\gamma$ -ray emission: the polar cap model, where the gap forms close to the magnetic pole of the neutron star, and the outer gap model, where the gap forms in the outer magnetosphere.

The polar cap model proposed by Ruderman and Sutherland invoked a vacuum gap caused by the trapping of ions in the neutron star crust, preventing the flow of positive charges along the open field lines [134]. The potential drop across the gap can accelerate electrons up to  $10^{14}$  eV in the case of the Crab pulsar, at which point pair creation limits the growth of the gap. In this model,  $\gamma$ -rays are produced by curvature radiation<sup>5</sup>. One of the problems with this model is the difficulty to produce double-peaked pulse profiles where the peaks are separated by less than 0.5 cycles, which is the case for the Crab pulsar. Modern polar cap models can now produce double-peaked pulse profile using a hollow beam of curvature radiation from a single pole of a nearly aligned rotator [38,39,71,107]. All these models predict a sharp cutoff in the  $\gamma$ -ray spectrum above  $\sim 10$  GeV due to pair creation in the strong magnetic field close to the surface of the neutron star. An interesting feature of this model is that the electromagnetic cascades produced in the accelerating region also produce synchrotron radiation which leads to pulsed emission at lower energies. Given that the pulse profile of the Crab is remarkably similar at all wavelengths, this model is very appealing.

The outer gap model was proposed as an alternative to the polar cap model which could not explain for a long time the separation between the two peaks seen in certain pulsars. The model was originally proposed by Cheng, Ho, and Ruderman in 1986 [32]

<sup>5</sup>In the very high magnetic field of the pulsar magnetosphere, an electron may be constrained to follow the path of a magnetic field line very closely, with pitch angle nearly zero. The field line will generally be curved, so that the electron will be accelerated transversely and will radiate. The radiation is closely related to synchrotron radiation. Taken from [99].

and later refined by Romani [133]. Negative charges are assumed to move out from the magnetosphere region beyond the light cylinder and leave behind a negative charge-depleted region that acts as a positively charged region and pushes the positively charge-separated plasma on the starward side of the null surface back toward the star and leaves a growing gap. This outer gap lies just outside the last closed magnetic field line and extends from the null surface out to the light cylinder. Charged particles that traverse the gap are accelerated along the magnetic field lines and emit  $\gamma$ -rays due to synchro-curvature radiation and inverse Compton scattering of the soft photon background. The size of the accelerating region is limited by the production of  $e^+/e^-$  pairs by the  $\gamma$ -rays which interact with either the magnetic field lines or, more probably, lower energy photons which are produced by thermal emission at the surface of the star or by synchrotron radiation of charged particles. A generic feature of the outer gap model is that the high energy cutoff is at much higher energies and more gradual than that of the polar cap model (see figure 2.6).

Although the next generation of instruments (MAGIC on the ground, and GLAST in space) will certainly be able to determine which model applies to the Crab, STACEE has the potential to improve the current upper limits and this is what we attempt here.

## **Part II**

### **STACEE: A ground-based detector**

# Chapter 3

## Concept

STACEE is a large-area Atmospheric Cherenkov Telescope (ACT) located at the National Solar Thermal Test Facility (NSTTF) in Albuquerque, NM (latitude 35.0°, longitude 106.5° West, altitude 1705 meters above sea level). The NSTTF, which is operated by Sandia National Laboratories for the U.S. Department of Energy, is a test facility devoted to the development of the use of solar energy. Built in the mid 1970's, the facility uses an array of 222 heliostats, each 37 m<sup>2</sup> in area, to focus sunlight onto a central receiver located on a central tower. Under ideal conditions, the heliostats can direct up to 5 MW of solar radiation onto a target 2 meters in diameter. Figure 3.1 shows an aerial view of the NSTTF facility.

One of the driving motivations of STACEE is to lower the energy threshold of ground-based telescopes and bridge the energy gap between space-based and ground-based instruments. Given the linear relationship between the energy of  $\gamma$ -rays and the Cherenkov light density (lower energy  $\gamma$ -rays produce less Cherenkov light), we want to maximize the collection power to increase the signal-to-noise ratio ( $S/N$ ). The fluctuations of the night sky, which constitute the background for ACTs, are proportional to the square root of the total number of photons collected ( $B$ ), which suggests that the signal-to-noise ratio scales with the square root of the collection power ( $S/N = S/\sqrt{B}$ ). Therefore, the energy threshold of an ACT is proportional to the reciprocal of the  $S/N$  and can be written as:

$$E_{th} \propto \sqrt{\frac{\Phi \Omega \tau}{\epsilon A}}, \quad (3.1)$$

where  $\Phi$  is the flux of night sky background photons,  $\Omega$  is the solid angle of the field of view,  $\tau$  is the integration time (or the coincidence gate width of the electronic trigger),  $\epsilon$  is the detector collection efficiency, and  $A$  the collection area. Two of these parameters have limitations set by the physical properties of EAS:  $\tau$  cannot be shorter than the duration of

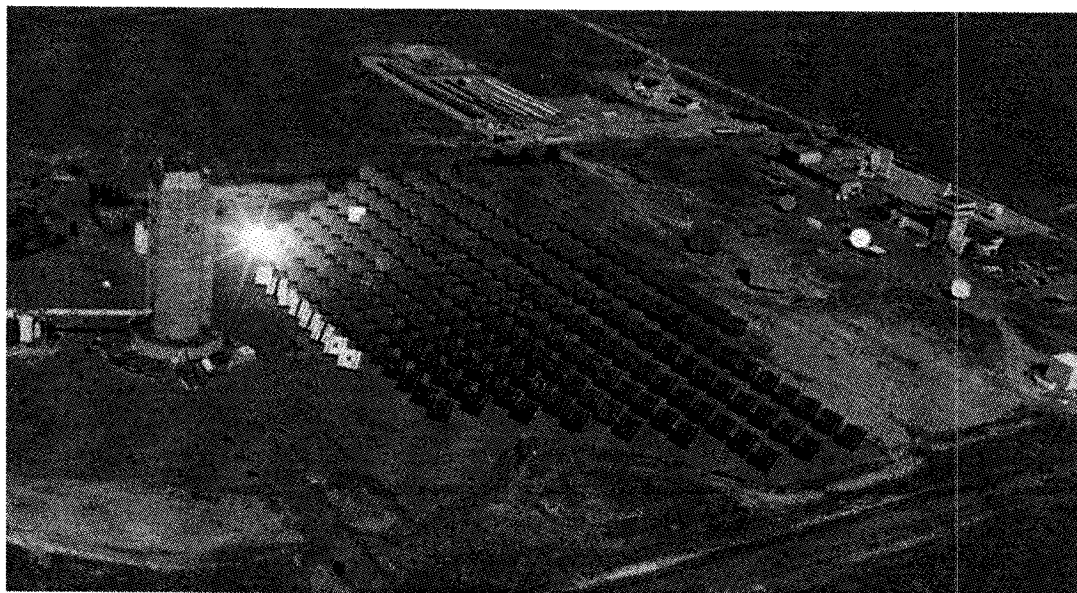


Figure 3.1: Aerial view of the National Solar Thermal Test Facility (NSTTF), Albuquerque, NM.

the Cherenkov pulses ( $\sim 5$  ns), and  $\Omega$  must be large enough to contain the full width of the EAS at shower max ( $\sim 0.5^\circ$ ). Two other parameters ( $\Phi$  and  $\epsilon$ ) have already reached a limit as most detectors are located at dark sites and use the best photo sensors available on the market. The only free parameter is the collection area ( $A$ ). It was already known in the 1980's that the best way to attain a lower energy threshold was to increase the collection area. However, building large telescopes is very expensive (e.g. the budget for construction of the VERITAS telescope array is  $\sim 13$  million dollars) as the high price of the reflectors themselves dominates the overall cost of the experiment.

The originality of the STACEE concept is to use the large collection area of the existing heliostat field at the NSTTF to collect Cherenkov light from  $\gamma$ -ray air showers at night. In fact, this idea dates back to 1982 when the same heliostats were used to reflect Cherenkov light onto a camera of photomultiplier tubes (PMTs) located on top of the central tower [37]. However, the initial concept had a number of flaws:

- Because of the large distances separating the heliostats, the time of propagation for light varied significantly from heliostat to heliostat and changed with the Earth's rotation while tracking a source. For this reason, a very large ( $\tau \gg 5$  ns) trigger coincidence gate width was required, cancelling the benefit of using a large collection area.
- The large ( $> 1$  m diameter) size of the spot of light from a given heliostat was

---

much larger than even a large PMT. A PMT would see the light from more than one heliostat, which would increase the amount of background light seen by each PMT.

The idea of using existing solar arrays was revived in 1990 by Tumay Tümer who thought of using secondary optics (a large Fresnel lens) to separate the light from each heliostat and focus it onto PMTs, with each PMT seeing only a single heliostat [149]. Fixed timing differences between heliostats caused by time of flight differences could be easily corrected by using cables of different length. The remaining problem of varying time delays caused by the rotation of the Earth could be solved by using a computer controlled delay system which solved the large trigger coincidence gate width problem. Two groups studied this concept and proceeded to build detectors: the CELESTE group used the Thémis site in the French Pyrénées [59, 121], while the STACEE group initially used the Solar Two site in Barstow, California [114] before moving to the current site at the NSTTF. The first prototype of the STACEE detector replaced the Fresnel lens with a secondary mirror and used eight heliostats [31]. In addition to CELESTE and STACEE, two other groups have build detectors using similar designs: the now defunct GRAAL group [13] operated near the city of Almeria in Spain, and the CACTUS group (formerly SOLAR-II) is currently operating at the Solar Two site [1].

The current version of the STACEE detector uses a subset of 64 heliostats, more or less uniformly distributed across the field, to track potential sources of  $\gamma$ -rays and focus the Cherenkov light on a secondary optical system which reflects the light on cameras made of PMTs. The PMTs convert the photons to analog electrical signals which are fed to a coincidence trigger system. Figure 3.2 shows an illustration of the conceptual design of STACEE.

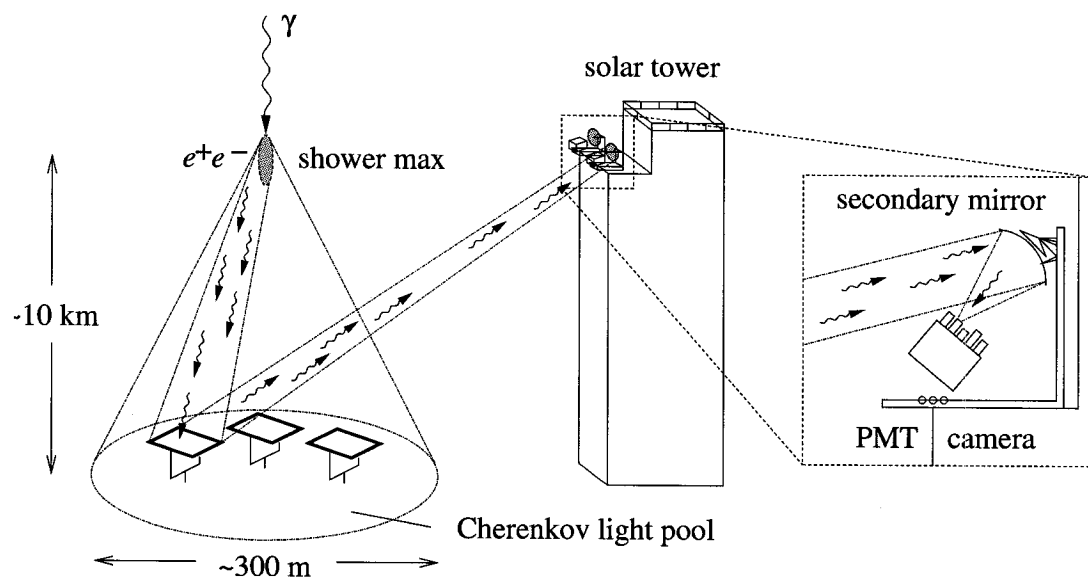


Figure 3.2: Conceptual design of the STACEE experiment.

# Chapter 4

## STACEE optics

Considerable progress has been made in the last decade to improve the sensitivity of ground-based  $\gamma$ -ray telescopes. However, the energy threshold ( $\sim 250$  GeV) of imaging telescopes hasn't decreased significantly; this can be attributed to the limited collection area of the primary mirrors ( $\sim 10$ -meter diameter) which hasn't increased except for the latest generation. The idea behind STACEE — to use the large collection area of the heliostats at the NSTTF — is a way to achieve a lower energy threshold. In the following sections we review the properties of each component of the optical system.

### 4.1 Heliostats

The STACEE heliostats are each composed of 25 individual square facets, arranged in a  $5 \times 5$  array. Each facet is four feet on a side, giving a total reflective area of  $\sim 37$  square meters per heliostat. The facets are made of two layers of glass with reflective silver between the glass layers and mounted on an adjustable metal frame with adjustment screws controlling the tilt and focus of the facets. Figure 4.1 shows a schematic diagram of an individual STACEE heliostat.

The frame which holds the facets can be rotated and tilted in azimuth and elevation by two independent motors equipped with 13-bit encoders that provide a pointing accuracy of 0.044 degrees in each direction. The calibration of the absolute pointing, or biasing, of the heliostats involves doing drift scans of a bright star [25,24]. The heliostats are pointed  $1^\circ$  ahead of the star in right ascension and stopped at this position. The PMT currents are read out as the star drifts in and out of the field of view of the heliostats and this procedure is repeated with the heliostats pointed at several different values of declination. The currents are then interpreted as a raster-scanned (or 2D map) light distribution (see figure 4.2). Using this calibration procedure we can achieve a pointing accuracy of 1 bit

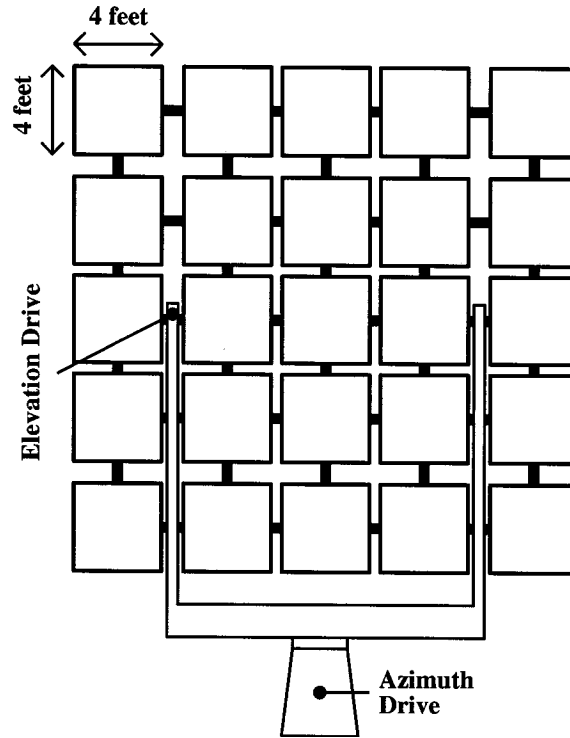


Figure 4.1: Schematic diagram of an individual STACEE heliostat.

RMS.

The number of particles produced during the development of EAS in the Earth's atmosphere reaches a maximum (shower max) at about 12.5 km above sea level ( $\sim 11$  km above the STACEE heliostats). In order to maximize the number of Cherenkov photons collected, the heliostats are pointed (or canted) to the shower max point. Figure 4.3 illustrates the concept of canting. The canting parameter is defined as the reciprocal of the height a.s.l. of the canting point. In principle, each heliostat can be assigned a different canting parameter. In the simplest configuration, called monocanting, all the heliostats track the same point and are assigned the same canting parameter ( $0.08 \text{ km}^{-1}$ ). Recently, a new canting scheme, called *paracanting*, was proposed for STACEE. A subset of 16 heliostats (out of the 64), which are uniformly distributed across the array, are pointed directly at the source (looking straight up in figure 4.3). Although this pointing scheme lowers the collection efficiency of the array, it is believed that we can get a better handle on the reconstruction of the  $\gamma$ -rays during the offline analysis and make a net gain in sensitivity.



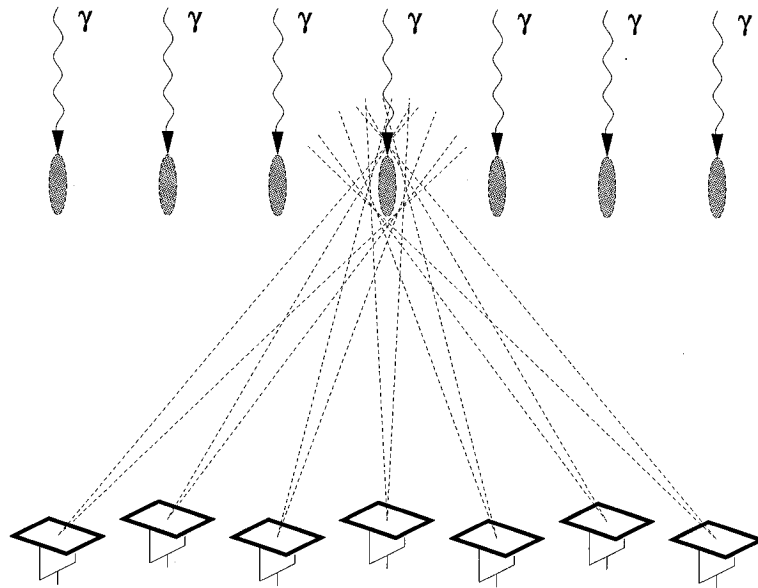


Figure 4.3: Schematic diagram illustrating the concept of convergent pointing, or canting. This pointing configuration optimizes the collection efficiency for Cerenkov photons. Taken from [136].

## 4.2 Secondary optics and cameras

The STACEE heliostats reflect light to the secondary mirrors located on the solar tower (see figure 4.4). The three secondary mirrors located on the 260-level (which is actually 160 feet above the heliostat field) are made of seven hexagonal facets, each having a spherical shape and a focal length of 2 meters. The resulting multi-faceted secondary mirror has a diameter of approximately 1.9 meters. The two secondary mirrors on the 220-level are spherical mirrors 1.1 meters in diameter, with a focal length of 1.1 meters. All the secondaries are made of front-surfaced aluminized glass, which has good reflectivity at ultraviolet wavelengths.

The role of the secondary mirrors is twofold: reduce the size of the images reflected by the heliostats ( $\sim 2$ -meter wide) to a size manageable by a single PMT (a few centimeters), and to separate these images to minimize the overlap between adjacent PMTs. Without the secondary mirrors we would need 64 huge light concentrators located at different (non-overlapping) positions on the tower, a solution which is highly impractical. Each of the 3 secondary mirrors on the 260-level collects the light from 16 heliostats that are clustered around the same region of the heliostat field. On the 220-level, each secondary mirror collects the light from 8 heliostats which are located near the front of the heliostat array. Figure 4.5 shows the 64 heliostats selected for STACEE and indicates to which cluster each heliostat belongs.

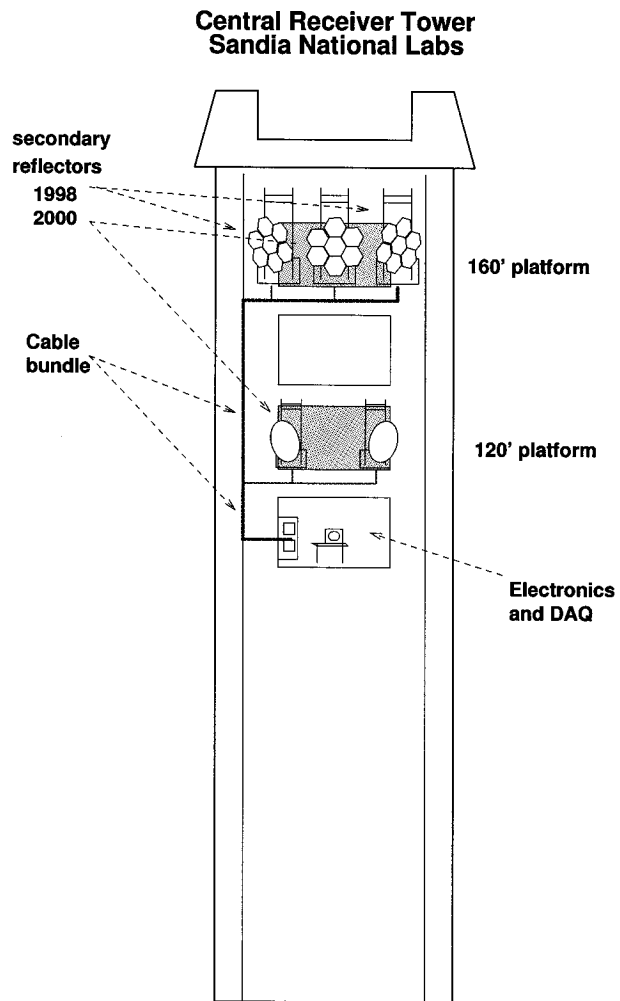


Figure 4.4: Schematic view of the solar tower indicating the location of the STACEE secondary mirrors. Taken from [136].

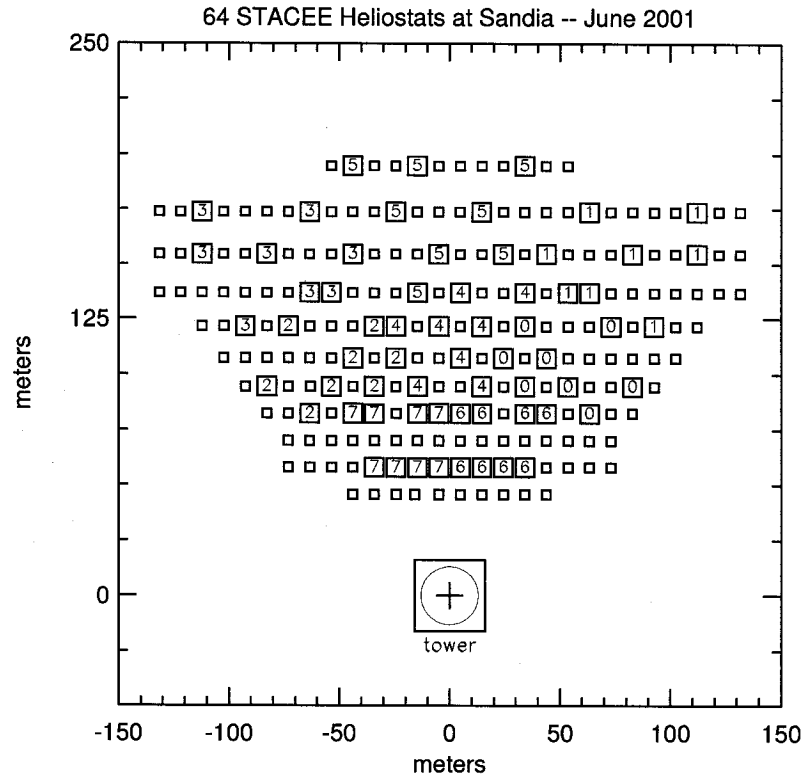


Figure 4.5: Selection of the 64 STACEE heliostats. The numbers represent the cluster to which the heliostats belong (see description of trigger system in section 5.2). Heliostats in clusters 0–5 reflect the light to the secondary mirrors located on the 260-level, while heliostats in clusters 6–7 reflect the light to the secondary mirrors on the 220-level.

The secondary mirrors reflect the light from the heliostats to the cameras (see figure 4.6) which are made of PMTs enclosed in special *cans* (see figure 4.7). The image of the heliostats in the camera plane is approximately  $15\text{ cm} \times 15\text{ cm}$ , which is much larger than the diameter of the PMTs (5 cm). Special light concentrators that were built at McGill University, called Dielectric Totally Internally Reflecting Concentrators (DTIRCs), are used to maximize the light collection efficiency and define the field of view of the PMTs. DTIRCs were introduced in 1987 [111], and were supposed to supplant the compound parabolic concentrators (Winston cones) which had been used in solar energy concentration systems and high-energy Cerenkov light detectors. DTIRCs combine front surface refraction with total internal reflection from the sidewall to achieve concentrations close to the theoretical maximum limits. When a light ray is incident on the front surface, it is refracted according to Snell's law, and then reaches the sidewall or goes straight to the far end. If the light ray is within the angular field of view of the DTIRC, it is reflected back into the DTIRC by total internal reflection, and it gets out through the exit aperture. In the case where the light ray is beyond the acceptance angle, it exits through the side profile. Figure 4.8 shows trajectories of light rays at the limit of the acceptance angle. The photons that reach the photocathode have a chance to create photoelectrons. The PMTs and DTIRCs have been extensively tested at McGill University under different lighting conditions (different incidence angles and wavelengths) and the results of these tests have been incorporated into the Monte Carlo simulation of STACEE [52]. As shown in figure 4.9, the overall throughput of the optical system, including heliostat and secondary reflectivities, DTIRC transmission, and PMT quantum efficiency, depends very much on the wavelength of the photons.

To a good approximation, the field of view of each heliostat is given by the angle subtended by the secondary mirror on the tower when viewed from that heliostat. Thus, the heliostats' fields of view range from  $0.5^\circ$  (for the most distant heliostats) to  $0.9^\circ$  (for the closest heliostats). Because the amount of night sky background light each heliostat sees varies with its field of view, it is desirable to equalize the field of views of all heliostats as much as possible. Ideally, each PMT would be matched with a custom-sized DTIRC, but it is impractical to use more than 3 different field of views for the DTIRCs. Therefore, PMTs viewing heliostats closest to the tower are matched with DTIRCs that have a field of view of  $19^\circ$ , whereas PMTs viewing the heliostats farthest from the tower are matched with DTIRCs having a field of view of  $28^\circ$ , and PMTs viewing heliostats at intermediate distances are matched with DTIRCs having a field of view of  $24^\circ$ . The effect of the DTIRC is to limit the effective diameter of the secondary mirror which modifies the field of view of the heliostat as explained above.

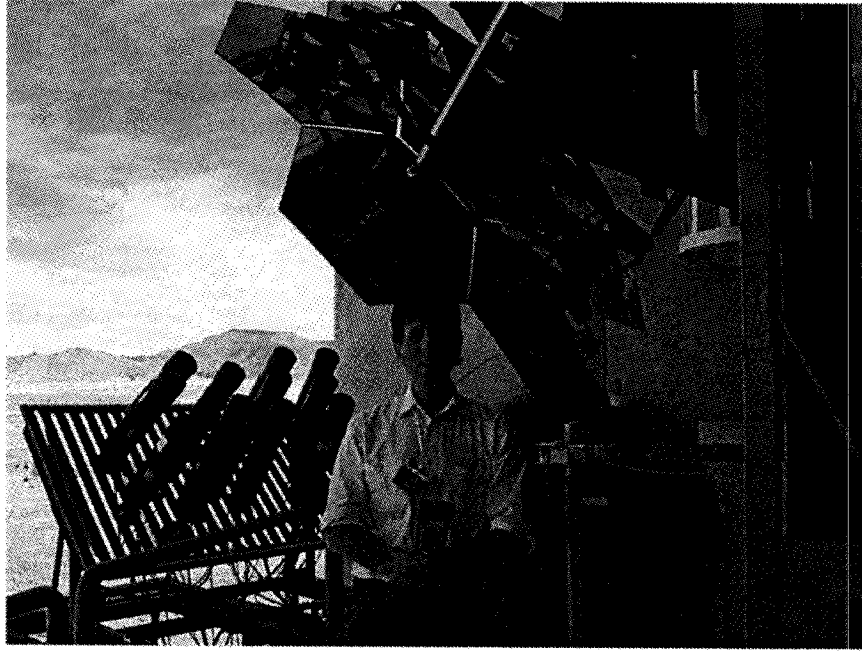


Figure 4.6: Photo of the secondary optical system on the 260-level showing the multi-faceted secondary mirror and the camera made of photomultiplier tubes. A specimen of *Homo sapiens* is shown for scale.

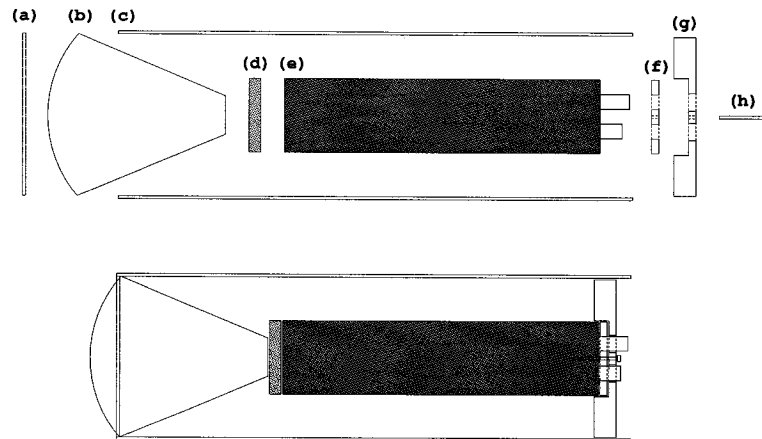


Figure 4.7: Schematic view of a STACEE PMT can assembly. List of parts: (a) retaining ring, (b) light concentrator (DTIRC), (c) aluminum can, (d) silicon optical coupling, (e) PMT, (f) pressure pad, (g) base, (h) retaining screw.

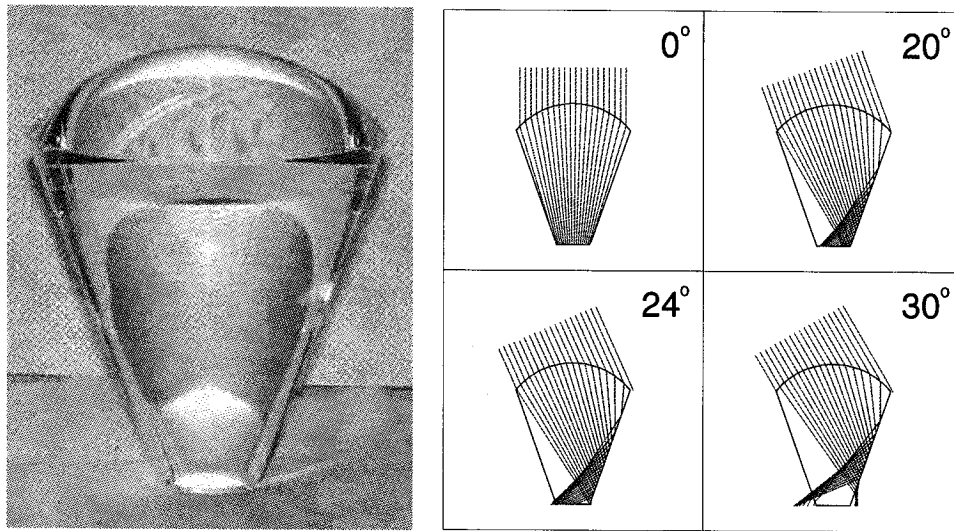


Figure 4.8: Photo of a typical DTIRC used by STACEE (left), and ray-tracing simulations for a DTIRC with a 24° field of view, at various angles of incidence.

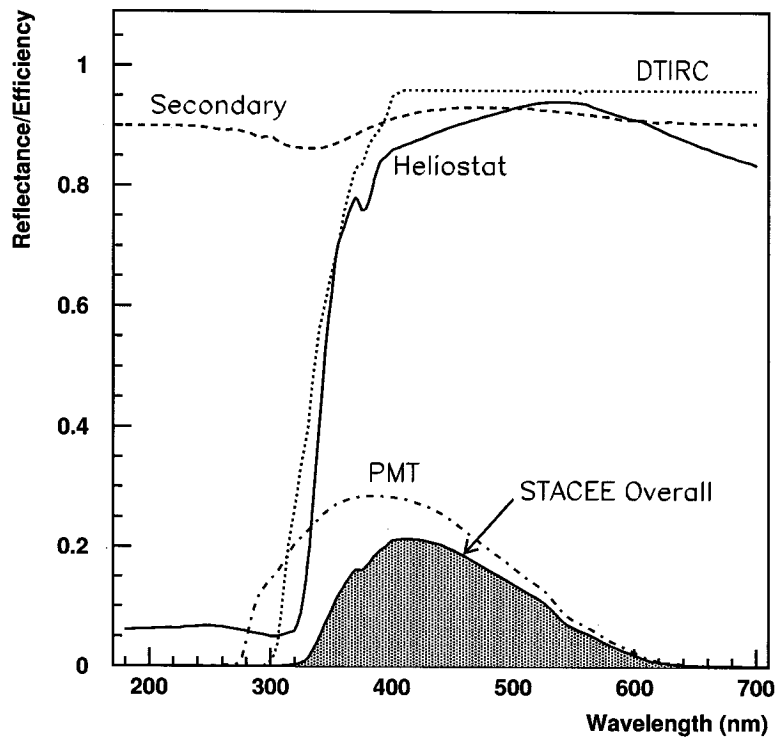


Figure 4.9: Overall throughput of the STACEE optical system as a function of wavelength, including: heliostat and secondary reflectivities, DTIRC transmission, and PMT quantum efficiency, as well as the product of these curves (hatched area). Taken from [70].

# Chapter 5

## STACEE electronics

From an electronics standpoint, STACEE is much closer to particle physics experiments than conventional optical telescopes. Even though STACEE detects photons from the visible part of the electromagnetic spectrum, the brief duration of EAS (a few ns) demands special electronics modules and techniques which are rarely seen in optical astronomy. Figure 5.1 shows a block diagram of the STACEE electronics. In the following sections we review the properties of key electronic modules: the photomultiplier tubes (PMTs), the delay and trigger module, the waveform digitizers, and the hardware used to study the Crab pulsar in the optical regime.

### 5.1 Photomultiplier tubes

The photomultiplier tubes used by STACEE are subject to strict requirements; they must be able to tolerate high levels of illumination and have a fast response time. In addition, they must have a good quantum efficiency in the wavelength range of photons produced by EAS (near-UV to blue region of the visible spectrum). The large field of view and collection area of the heliostats subject the PMTs to very large light levels; indeed, the PMTs have typical single photoelectron rates in the GHz range. For a typical discriminator threshold of  $\sim 6$  photoelectrons, the response time (or rise time) of the PMTs must be of the order of 1 ns to minimize the *pile up* of random photoelectron pulses. The type of PMT selected for STACEE was the Photonis<sup>1</sup> (model XP2282B). It has a bi-alkali photocathode with spectral sensitivity in the range 290–650 nm and a maximum sensitivity at 420 nm, with a corresponding quantum efficiency of 27%. According to the manufacturer, the rise time is typically 1.5 ns with a duration at half height of 2.2 ns. The operational gains are typically  $\sim 1.0 \times 10^5$ , which is at the low end of the range for which

---

<sup>1</sup>Complete specs available at: <http://www.photonis.com>

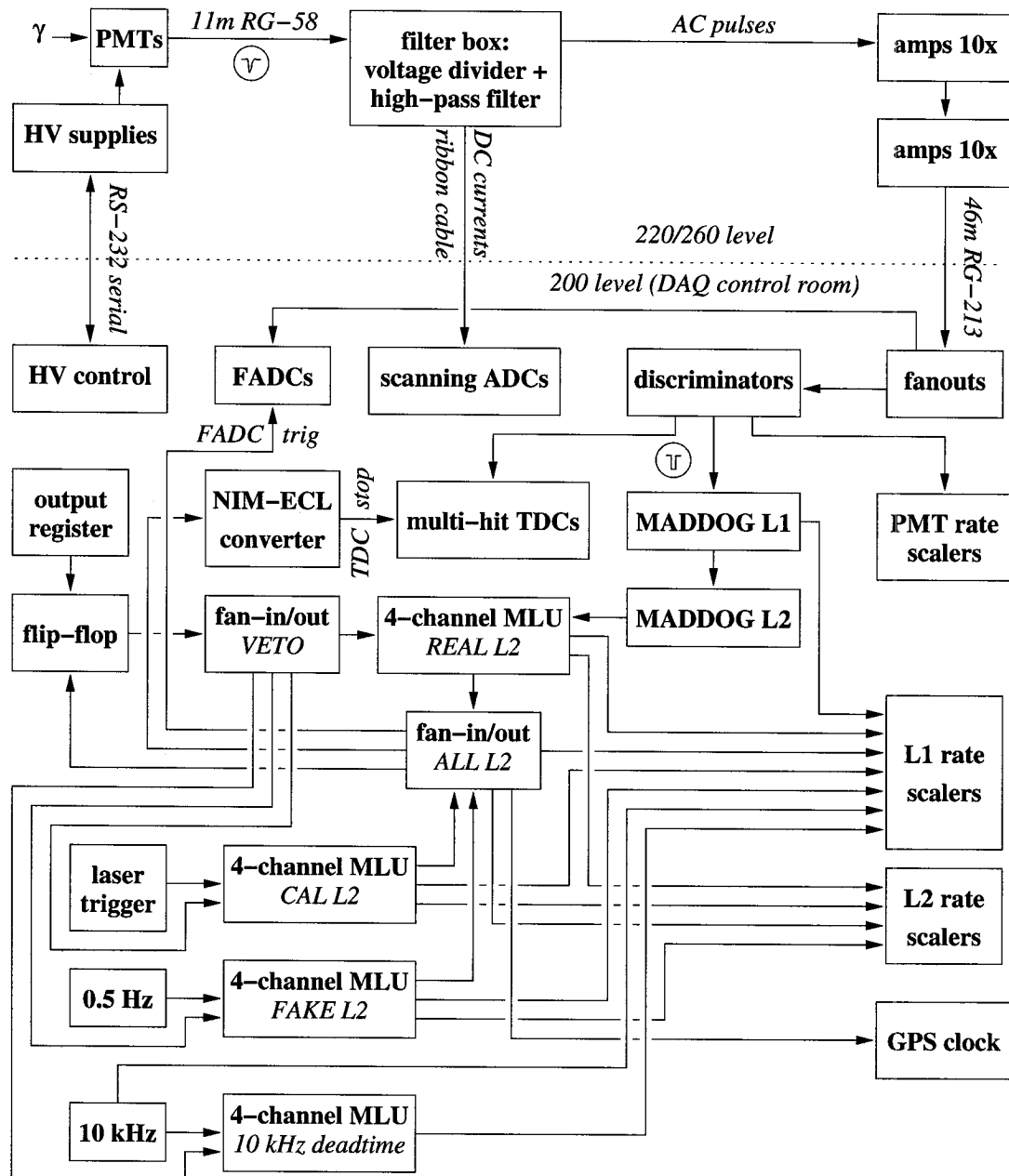


Figure 5.1: Schematic diagram of the STACEE electronics. The PMTs convert the photons to analog electrical signals which are then AC-coupled and amplified before being discriminated. The digital pulses are delayed by the trigger system (MADD OG) which sets the coincidence requirement. Acronyms: Analog-to-Digital Converter (ADC), Time-to-Digital Converter (TDC), Multiplicity Logic Unit (MLU), McGill Asynchronous Digital Delays for Observation of Gammas (MADD OG).

the PMTs were designed. We should point out that the benefits of using fast PMTs are somewhat diminished by the low-bandwidth of the electronic modules downstream of the PMTs; in particular, the Phillips 776 amplifiers and 748 fanout modules (see diagram) have a limited bandwidth of 250 MHz. In addition, the long signal cables ( $\approx 150$  meters) appreciably widen the pulses.

## 5.2 Trigger system

As mentioned in Chapter 3, STACEE samples the wavefront of EAS at 64 different locations on the ground which are separated by many light-nanoseconds. In order to retain the timing of the wavefront at the trigger level, each channel must be delayed to compensate for the different times of flight, and these delays must be dynamically adjusted as the source appears to move across the sky. Delaying signals for a fixed duration can easily be accomplished by using cables of different length, with the caveat that longer cables stretch-out and distort the pulses more than shorter cables. The real challenge is to dynamically change the delays during data acquisition. Two different approaches have been used by wavefront sampling experiments: one can dynamically change the cable lengths, or discriminate the signals, thereby converting the information in the traces to 0s and 1s, and delay these bits using a digital electronics module.

The former approach is known as the *analog trigger* method and has been used with success by the CELESTE experiment. After calculating the required delay for a particular channel, a custom-made module selects the appropriate route by linking cables of different length, effectively changing the transit time of the pulses. The delayed signals are then summed and may trigger the telescope under certain conditions. The advantage of summing the analog signals of individual channels is to increase the signal-to-noise ratio and achieve a lower energy threshold.

The second approach is used by STACEE. In this particular case, the trigger system starts downstream of the fanouts, more precisely at the discriminator modules (see figure 5.1) where the analog traces are converted to 0s and 1s (as ECL<sup>2</sup> logic signals). All 64 channels are discriminated at the same nominal discriminator threshold, which sets the minimum number of photoelectrons necessary to consider a channel *hit*. The widths of the discriminator pulses are approximately 5–6 ns long; the wider the pulse, the higher the channel deadtime. The signals come out of the discriminator modules as pulse trains of 0s and 1s, where the detailed information about the amplitude of the analog signals

<sup>2</sup>The Emitter-Coupled Logic (ECL) is a bipolar logic family used to achieve extremely high speed in integrated circuits.

has been effectively reduced to binary values. The discriminated signals then enter the delay and trigger formation system, known as *McGill Asynchronous Digital Delays for Observation of Gammas* (MADDOG), whose design is based on field-programmable gate array (FPGA) technology. A detailed description of the system is provided elsewhere [103, 126]; here we simply highlight the general features relevant to this thesis.

The array is divided into 8 clusters of 8 heliostats each. The event trigger is divided into two levels: the L1, or *cluster* trigger, sets the coincidence requirement for the channels pertaining to a given cluster; and the L2 trigger, or *global* trigger, sets the coincidence requirement between the different clusters. This division into L1 and L2 levels also corresponds to a hardware division; 8 *slave* boards delay the individual channels with a step size of 1 ns over a range of 2  $\mu$ s and generate L1 triggers, while a *master* board receives the L1 triggers and generates the L2 trigger. A slave board generates a L1 trigger when a set number of channels, called the *Local Trigger Condition* (LTC), is above threshold during a well defined coincidence window. The implementation of this logic is done using one of two modes. In *wide* mode, a L1 trigger is generated if the number of channels with at least one hit within a 24-ns interval is greater than the LTC. In *narrow* mode, the width of the coincidence window is set in firmware, and is currently set to 12 ns. Similarly, a L2 trigger is generated when a set number of clusters, called the *Global Trigger Condition* (GTC), have generated a L1 trigger. The selection of the LTC and GTC values is critical since it determines the raw sensitivity and energy threshold of the telescope.

The operating point is determined by measuring the discriminator threshold at which accidental coincidences start to dominate the event trigger rate. Figure 5.2 shows a typical rate versus threshold curve for hadronic air showers taken with a trigger configuration of LTC/GTC equal to 5/5. The upward pointing triangles represent data taken with normal (*intime*) delays, and the downward pointing triangles represent data taken with random (*scrambled*) delays. The operating point is given by extrapolating the scrambled curve to  $10^{-2}$  Hz, which would be 120–125 mV in this case. Its value is entirely determined by the background currents and the specific LTC/GTC configuration. Above this point, triggers are caused uniquely by Cherenkov light from EAS. Correlated electronic noise, such as electromagnetic discharges or electronic pick-up, is unlikely to have the right channel-to-channel delays and does not contribute to the trigger rate.

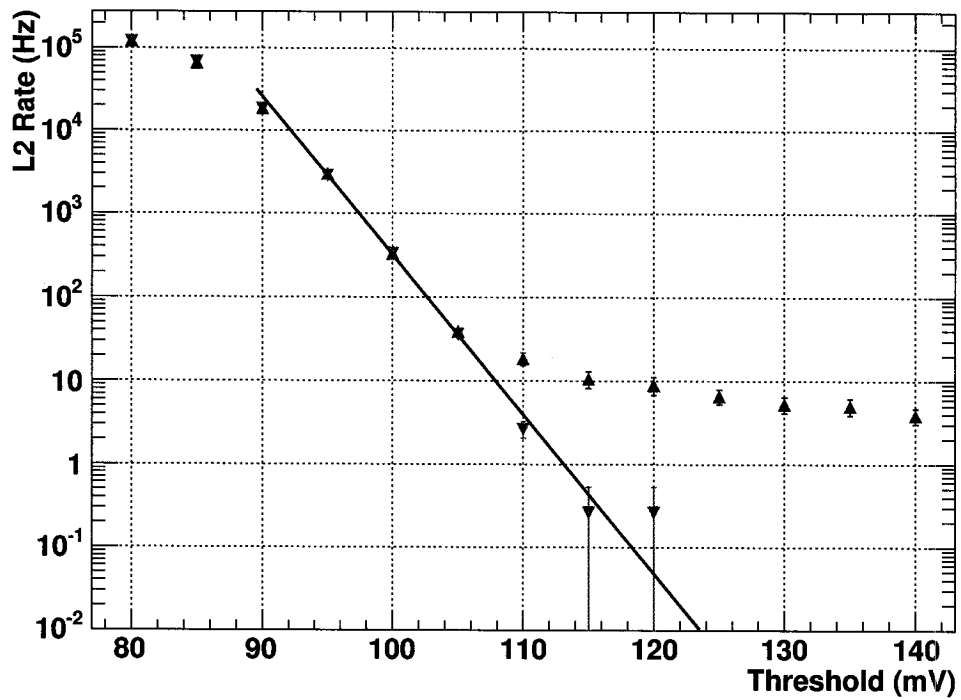


Figure 5.2: L2 trigger rate for hadronic air showers as a function of the discriminator threshold for a 5/5 LTC/GTC configuration. Upward pointing (blue) triangles: data taken with *intime* delays. Downward pointing (red) triangles: data taken with *scrambled* delays, showing the contribution of accidental coincidences produced by background photons.

### 5.3 Waveform digitizers (FADCs)

As shown in Figure 5.1, a copy of the analog signals is routed from the fanouts to the FADC<sup>3</sup> digitizers. For each triggered event, the digitized signals are stored to disk for offline analysis. The digitizer modules are produced by Acqiris<sup>4</sup> (model DC270) and have a sampling rate of 1 GSamples/s with a resolution of 8 bits. Although the full scale range of the modules can be adjusted, the 1 Volt full-scale range represented the best compromise between good resolution for small pulses and minimizing saturation problems for large pulses. For each triggered event, the FADCs record a 192-ns long trace for each of the 64 channels and calculate the pedestal and RMS of each trace using a 400-ns long window which immediately precedes the 192-ns long window. The pulse amplitude and integrated charge can be corrected on an event-by-event basis for fluctuations in the background levels. Figure 5.3 shows a sample FADC trace from a typical Cherenkov air shower.

Although the trigger system successfully rejects a large fraction of hadron induced air showers, the raw sensitivity of the telescope is barely good enough to detect strong sources like the Crab Nebula. The key to improving the sensitivity of the telescope is to use the information stored in the FADC traces. In principle, the rise time, pulse width, integrated charge, pulse decay time constant, can all be used to help identify  $\gamma$ -ray showers and improve the sensitivity of the detector.

### 5.4 Optical pulsar detection system

This purpose of this temporary system<sup>5</sup> was to demonstrate the validity of the barycentering code (see Section 8.1) and confirm the accuracy of the GPS timestamps. The system was designed to work in parallel with the  $\gamma$ -ray telescope and integrate seamlessly with the data acquisition. The idea was to add three independent channels with special electronic modules and use triggers generated by the  $\gamma$ -ray telescope to start data acquisition and provide GPS timestamps. Three additional heliostats (8E3, 8W1, 8W3) were selected for optical observations and equipped with standard PMTs and signal cables.

<sup>3</sup>FADC stands for Flash ADC, also called parallel A/D converter. This type of circuit is formed of a series of comparators, each one comparing the input signal to a unique reference voltage. The comparator outputs connect to the inputs of a priority encoder circuit, which then produces a binary output. Not only is the flash converter the simplest in terms of operational theory, but it is the most efficient of the ADC technologies in terms of speed, being limited only in comparator and gate propagation delays. *Ref:* <http://www.allaboutcircuits.com>

<sup>4</sup>Acqiris web site: <http://www.acqiris.com>

<sup>5</sup>The system was installed only for 3 months during the 2002-2003 Crab season.

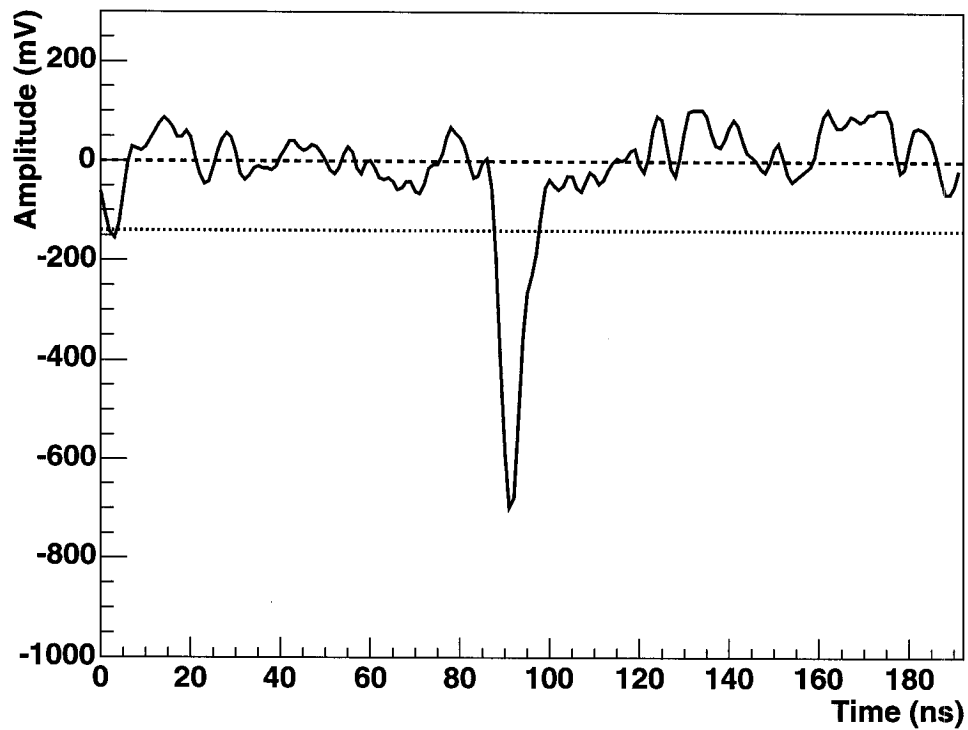


Figure 5.3: Sample FADC trace for a typical Cherenkov air shower event near  $t = 90$  ns. The dashed line indicates the pedestal value and the dotted line indicates the value of the nominal discriminator threshold. A fluctuation in the night sky background near  $t = 0$  ns was large enough to trigger the discriminator.

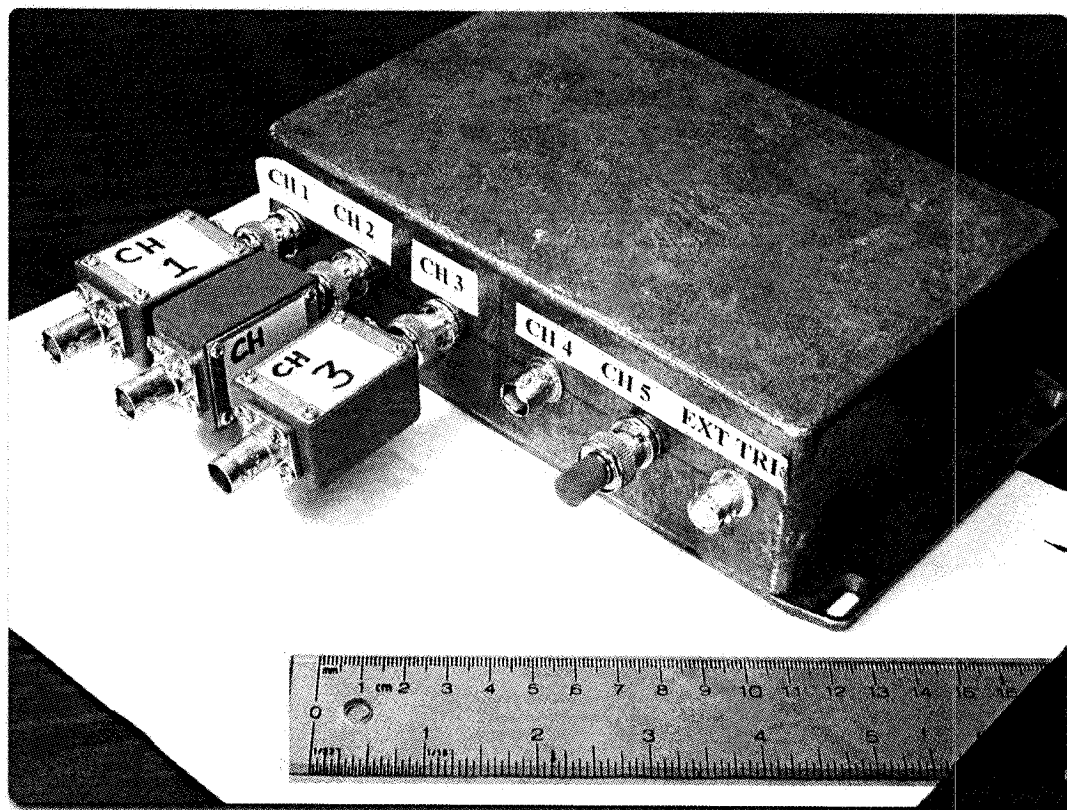


Figure 5.4: Interface module used to link the analog signals, the GPS time code generator signal, and the external trigger signal with the National Instrument digitizing card in the PC.

The analog signals from the three PMTs bypassed the standard high-pass filter modules and the 100X amplifiers; instead, the signals were filtered using custom-made band-pass filters ( $\sim 0.01 - 10^3$  Hz). Figure 5.4 shows a picture of the interface module with three band-pass filters connected to the inputs. The interface module was used to connect the special acquisition card in the PC with the three signal cables, the GPS time code generator signal (more on this below), and the external trigger signal. The band-pass filter circuit was designed to remove high frequencies (mostly radio interferences) and AC-coupled the signal to prevent slow baseline drifts. Figure 5.5 shows a diagram of the passive circuit; this combination of resistors and capacitors lets the frequencies of interest ( $\sim 30$  Hz and higher harmonics) pass through the circuit with little attenuation. The signals coming out of the interface modules were digitized using a National Instruments PCI card (NI 6034E). This particular card samples and logs data to disk at up to 200 kSamples/s with 16-bit resolution; a sampling rate of 10 kSamples/s was chosen for this project. The precision and stability of the sampling frequency were measured using the

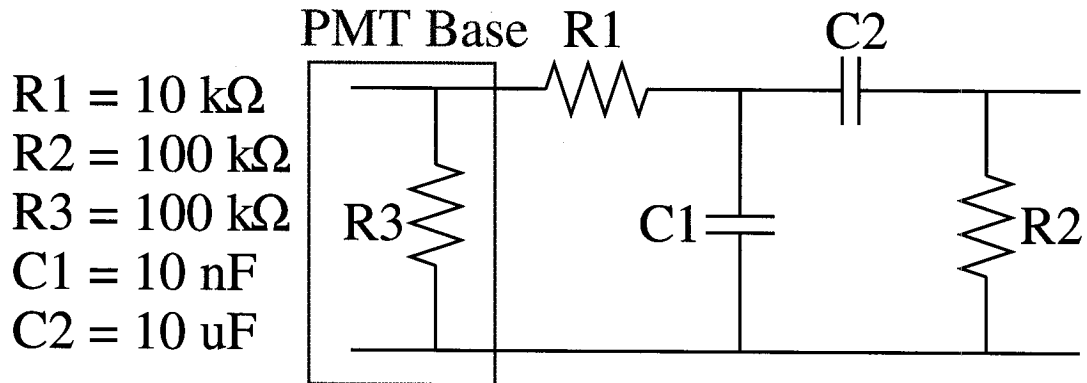


Figure 5.5: Diagram of the band-pass filter circuit used by the optical pulsar system. The first stage ( $R1/C1$ ) is a low pass filter with a -3dB point at  $\approx 1.6 \text{ kHz}$ . The second stage ( $R2/C2$ ) is a high pass filter with a -3dB point at  $\approx 0.2 \text{ Hz}$

1 kHz high precision time code generator (IRIG B) signal produced by the Datum bc637 GPS clock. The time code signal was sampled at 10 kSamples/s and the recorded trace was folded at frequencies in the range  $(1000 \pm \delta) \text{ Hz}$ . The pulse profile with the largest  $\chi^2$  in this frequency range corresponded to the effective sampling frequency of the digitizer. We found that the effective sampling frequency was 9999.986 Hz and we could not detect any drift in that value over many hours of data acquisition (in fact this value was constant for the entire optical data set). The Data Acquisition (DAQ) code was based on the Linux open-source COMEDI<sup>6</sup> driver which supports a wide a range of data acquisition cards produced by different manufacturers.

<sup>6</sup><http://www.comedi.org>

# Chapter 6

## Calibration of STACEE electronics

The calibration process consists of measuring and adjusting the parameters which determine how the electronic modules respond to different input signals. Some modules are easily calibrated, while others require more attention or need to be regularly monitored. For example, the FADC digitizers feature on-board calibrated DC levels and the calibration procedure takes only a few minutes. The PMT gains, on the other hand, are more difficult to calibrate and tend to drift with time, which calls for regular monitoring.

In this chapter, we review the calibration procedures which are unique to STACEE. These procedures make use of a special laser system (see figure 6.1) which is used to monitor the evolution of the detector's response [68, 69]. A nitrogen laser generates short duration pulses ( $\sim 4$  ns at half height) which simultaneously illuminate the 64 PMTs. The intensity of the pulses can be adjusted using neutral density filters and is monitored by photodiodes. This laser calibration system is used to measure the PMT gains, fine-tune the timing residuals, and measure the timing resolution.

### 6.1 Calibration and monitoring of the PMT gains

Unlike space-based detectors, STACEE cannot be calibrated with a beam of  $\gamma$ -rays produced by a particle accelerator. Instead, STACEE has to rely extensively on detailed Monte Carlo simulations. Of all the parameters in the Monte Carlo, the PMT gains are probably the ones which most strongly influence the predicted performance of the detector. For example, the PMT gains have a direct influence on the energy scale of reconstructed showers; when the gains are underestimated, the reconstructed energies are overestimated, and vice versa. It is crucial to measure the value of the PMT gains and to monitor their evolution, as they are known to decrease with time. Two techniques were used to measure the absolute and relative gains.

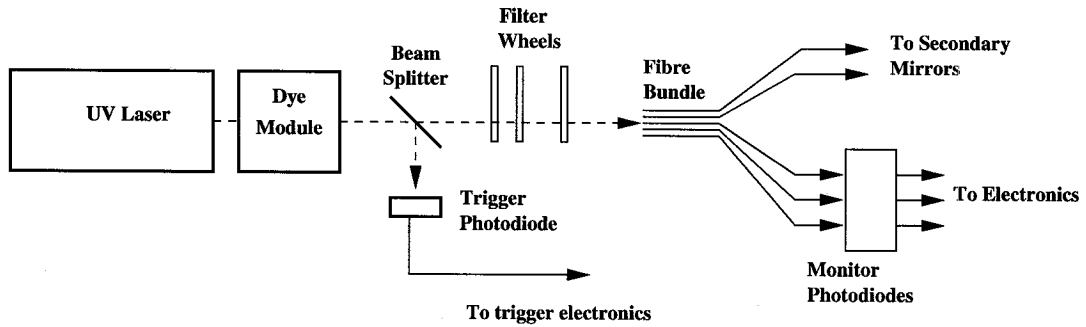


Figure 6.1: Schematic diagram of the laser calibration system. The nitrogen laser generates short duration pulses ( $\approx 4$  ns) of ultraviolet light (337 nm) which are converted to blue light (420 nm) by a stilbene dye module. A beam splitter diverts a fraction of the light to a photodiode which triggers the readout of the electronics. The remaining fraction goes through a set of neutral density filters before being routed to monitor photodiodes and the cameras on the 220 and 260 levels. From [69]

### 6.1.1 FADC Gain Inference Technique, *a.k.a.* FGIT

The absolute gains are determined by measuring the charge of a single photoelectron pulse [53]. In order to get a small number of photoelectrons with each laser pulse, the intensity of the laser is attenuated to a point where only  $\approx 1/3$  of laser shots produce one or more photoelectrons for a particular PMT. In addition, a special lens cap is used to cover the front face of the DTIRC, such that only the light from the laser can reach the photocathode. Figure 6.2 shows a sample FADC trace for a single photoelectron pulse. The number of photoelectrons produced by a single laser shot is determined by Poisson statistics. The probability of getting  $r$  photoelectrons is given by:

$$P(r) = \frac{\alpha^r e^{-\alpha}}{r!}, \quad (6.1)$$

where  $\alpha$  is the mean number of photoelectrons produced by the PMT for a single laser pulse. Once the value of  $\alpha$  is known, one can easily predict the relative number of events with 0, 1, 2, ..., photoelectrons. The technique used to determine the value of  $\alpha$  and calculate the charge of a single photoelectron is the following:

- For each laser shot, we calculate the total charge in the *background* and *signal* regions (see figure 6.2) by integrating the signal over the width of the region.
- After processing hundreds of events, we obtain distributions of pulse charges similar to the ones shown in figure 6.3.
- The *background* histogram is fitted with a Gaussian distribution and the parameters

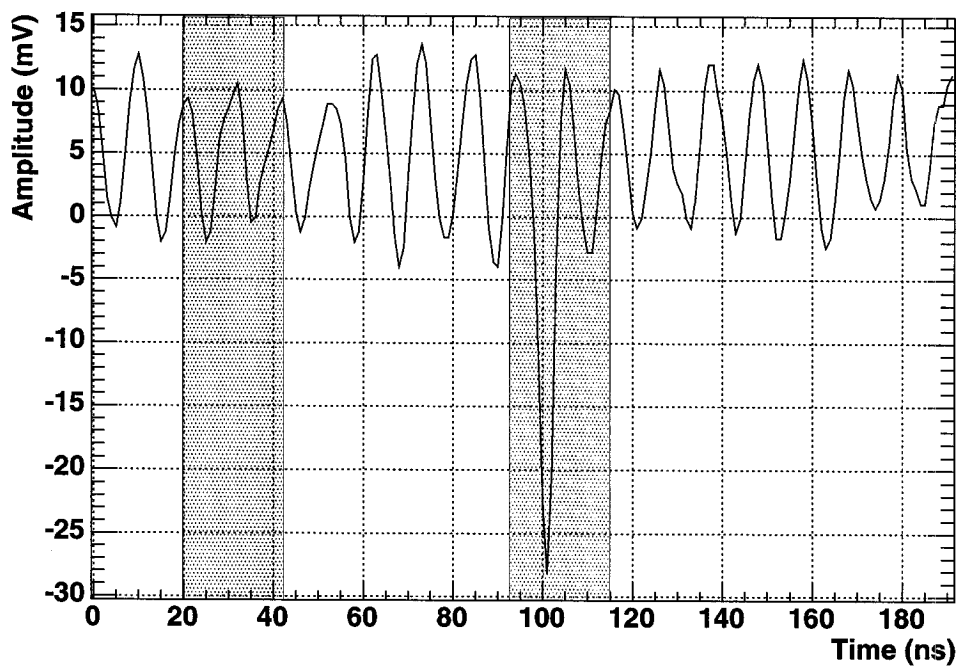


Figure 6.2: Sample FADC trace for a single photoelectron pulse. The shaded area on the left side corresponds to the *background* region. The shaded area which overlaps with the photoelectron pulse is the *signal* region (same width as the background region). The sinusoidal signal is produced by RF interference.

of the fit  $(A_b, \mu, \sigma)$ <sup>1</sup> are used to calculate  $\alpha$ . By construction, the *background* region does not receive any light from the laser and the average charge should essentially be 0 pC. The mean and width of the *background* distribution should be equal to the mean and width of the *signal* distribution when 0 photoelectrons are produced; the only difference between the two distributions being the normalization constants  $(A_b, A_s)$ . The ratio of these normalization constants is equal to the probability of getting  $(r = 0)$  photoelectrons, namely:

$$P(r = 0) = e^{-\alpha} = A_s/A_b \quad (6.2)$$

- The charge of an average photoelectron pulse is obtained by fitting the distribution of pulse charges from the signal region with four separate Gaussian distributions, each corresponding to events with a different number of photoelectrons (0, 1, 2, and 3 photoelectrons<sup>2</sup>). Using the value of  $\alpha$  and Poisson statistics, we can calculate the expected number of events with 1, 2, and 3 photoelectrons, which constrains the normalization factors of these distributions. In addition, the mean of each distribution is an integer multiple of the average charge of the single photoelectron pulse. This imposes serious constraints on the fit and the only free parameters are the mean and variance of the charge of a single photoelectron.

The total gain of the electronics — which includes the PMT gain, the gain of the amplifiers ( $\sim 98$ ), and the attenuation caused by the cables ( $\sim 12\%$ ) — is given by the ratio of the average photoelectron charge to the charge of the electron ( $1.6 \times 10^{-19}C$ ). For the example shown in figure 6.3, the total gain of the electronics is  $1.06 \times 10^7$ , which corresponds to a PMT gain of  $\sim 1.2 \times 10^5$ . The FGIT method is robust but tedious, as measuring the gains for all 64 channels takes hours. For this reason, the FGIT method is used to measure the absolute gains for a subset of channels in conjunction with another method which measures the relative gains of all channels.

### 6.1.2 Monitoring the gains with $\sigma^2/I$ method

As mentioned in the previous section, a different method is used to measure the relative PMT gains [67]. Both methods make use of Poisson statistics and FADC traces to calculate the gains. This new method is called  $\sigma^2/I$  for reasons which will soon become clear.

<sup>1</sup> $A_b$  is the normalization constant,  $\mu$  is the mean, and  $\sigma$  is the standard deviation of the Gaussian distribution.

<sup>2</sup>The number of events with more than 3 photoelectrons is negligible and we have confirmed that adding a fifth Gaussian distribution does not improve the result of the fit.

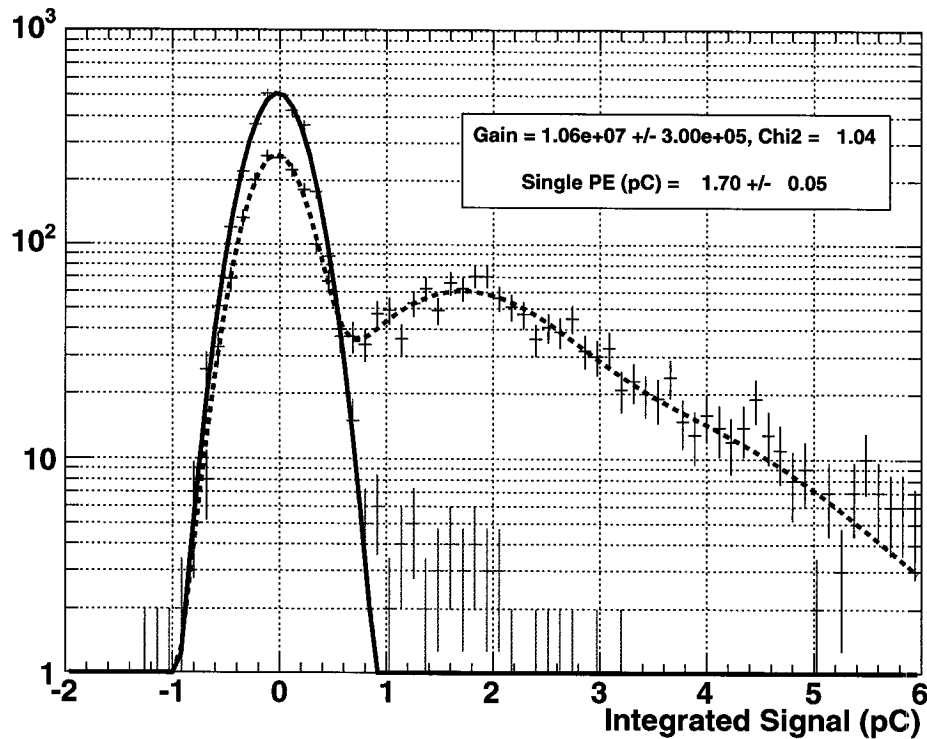


Figure 6.3: Distributions of pulse charges for the *background* (red markers and solid line) and *signal* (black markers and dashed line) regions. The *background* distribution is fitted with a Gaussian distribution, while the *signal* distribution is fitted with four Gaussian distributions whose normalization factors are set by Poisson statistics (see text for details) and whose means are separated by the average charge of a single photoelectron.

Consider an ideal PMT which produces photoelectron pulses at a rate  $R$ . The current measured at the base of the PMT is given by

$$I = GeR, \quad (6.3)$$

where  $G$  is the PMT gain and  $e$  the electron charge. One could argue that the fluctuations of the current ought to be proportional to the square root of the rate  $R$  since they are driven by Poisson fluctuations in the arrival of photons. Given that the voltage measured by the FADC is directly proportional to the current, the RMS of the voltage can be expressed as

$$\sigma \propto Ge\sqrt{R}. \quad (6.4)$$

A simple manipulation of the last two equations shows the relationship between the variance of the FADC trace ( $\sigma^2$ ), the PMT current, and the PMT gain; namely that

$$\sigma^2/I \propto G. \quad (6.5)$$

Figure 6.4 shows the relationship between  $\sigma^2$  and  $I$  for 4 typical channels. The slope of the fits is used to compare the relative gains and can be combined with the FGIT results to get the absolute gains for all channels. With thousands of FADC traces and hundreds of current measurements per run, this technique is extremely valuable as it provides gain measurements for *free*, i.e., we get information on the calibration of the detector in real time. We can easily monitor the evolution of the gains during the season and increase the high voltage when the gains drop below some value.

## 6.2 Timing residuals and timing resolution

As mentioned in section 5.2, the discriminated pulses must be delayed to account for differences in the times of flight. Even though the positions of the heliostats and secondary mirrors were surveyed with great precision (resolution of  $\sim 1$  cm), the transit time of the photoelectrons and discriminated pulses through the cables and electronic modules vary slightly from channel to channel ( $\leq 5$  ns). These small variations are caused by differences in cable length and intrinsic channel-to-channel differences caused by the manufacturing processes of the electronic modules (e.g., although the tap delay lines used by the trigger module are separated on average by 1 ns, the actual specifications indicates that they can be separated by at least 0.5 ns and at most by 1.5 ns). Even though 5 ns appears to be small (if not negligible), this is quite large compared to the shower front

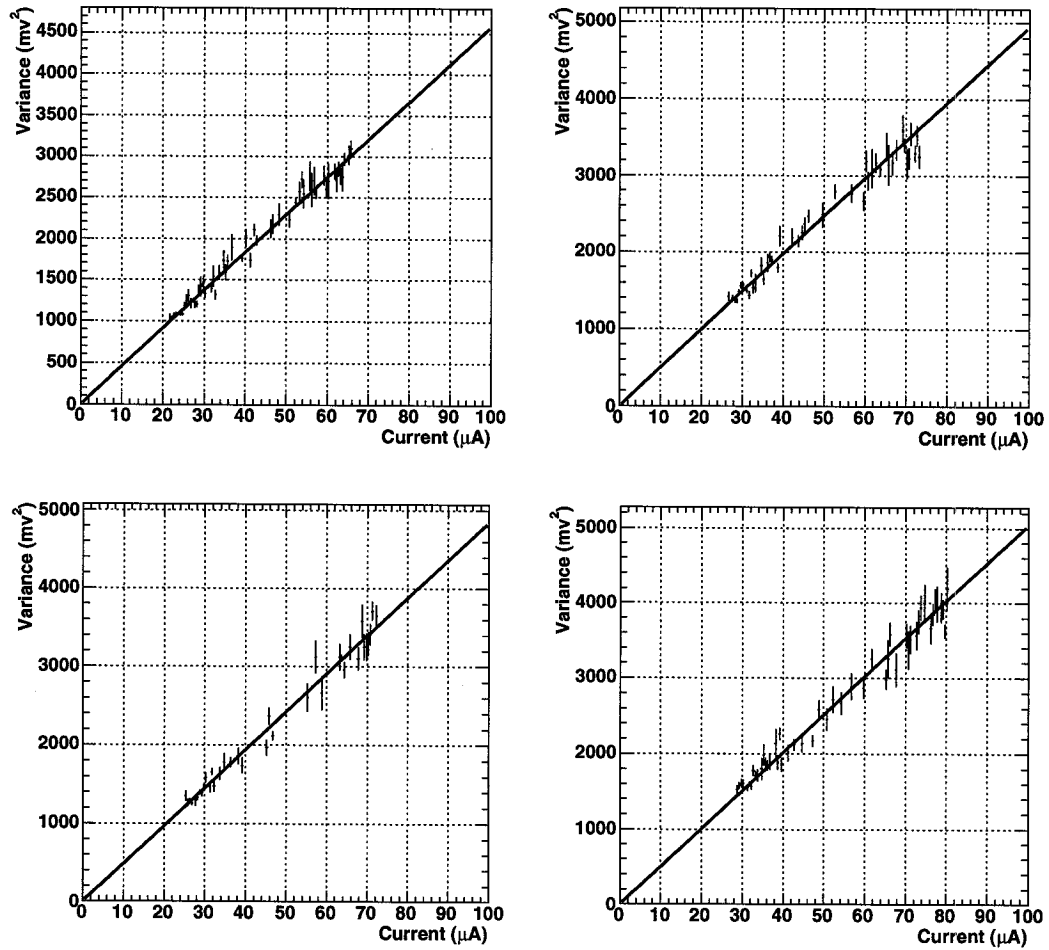


Figure 6.4: Plot of variance of FADC samples versus currents for four typical channels.

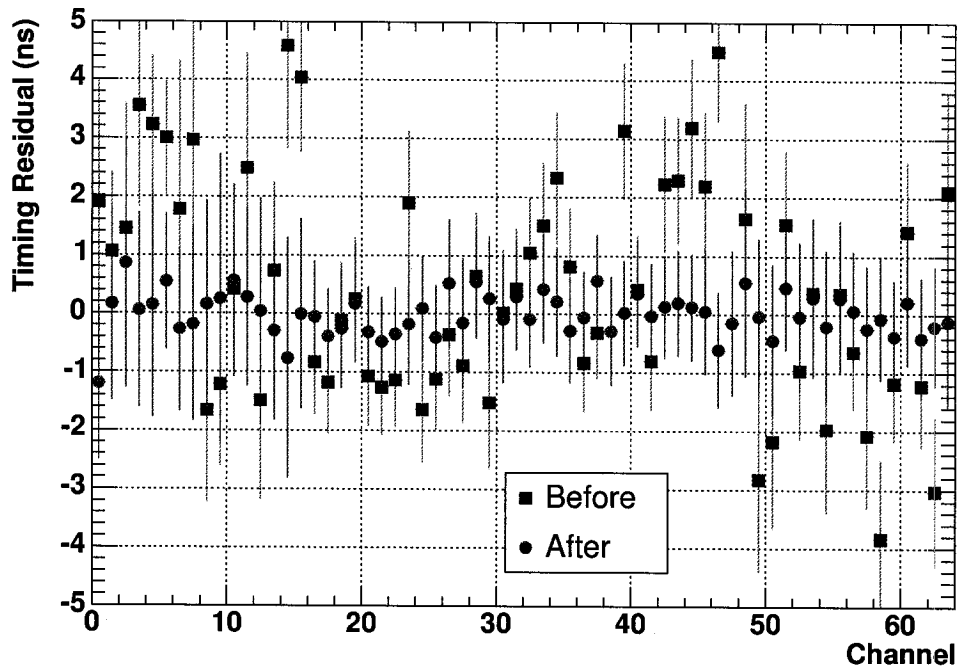


Figure 6.5: Timing residuals before (squares) and after (circles) the calibration procedure. The error bars represent the RMS values.

size. Moreover, preliminary Monte Carlo studies indicate that small timing differences between  $\gamma$ -ray and hadronic EAS can be used to improve the sensitivity of the detector. For this reason, we need to measure the timing differences as precisely as we can and account for them when setting the delays.

The laser system is used to measure these small channel-to-channel timing differences, or *timing residuals*, by simultaneously illuminating the 64 channels with large pulses. The arrival time of the pulse on each channel is compared to the mean arrival time for all channels; for an ideal system, these times should all be equal. Figure 6.5 shows the timing residuals before and after the calibration procedure. These timing residuals need to be measured each time an electronics module is replaced. Luckily, the detector is relatively stable and we rarely have to replace modules.

Equally important as the timing residuals, the timing resolution describes the accuracy with which one can reconstruct the arrival time of Cherenkov pulses. According to simulations,  $\gamma$ -ray events look more spherical than hadronic showers (see figure 1.14) and one could hope to differentiate the two types of events by looking at the *sphericity* of the wavefront. For example, the  $\chi^2$  value of a spherical fit to the wavefront could be used as a cut parameter. The procedure used to measure the timing resolution after corrections

for amplitude dependent pulse slewing is beyond the scope of this thesis [54], but the results are relevant and are summarized in figure 6.6. Except for the lowest background level (closed circle), which is never seen in real data (we had to use the lens cap to keep the PMT current below  $10\mu A$ ), the timing resolution clearly depends on the pulse amplitude and background level; the larger the pulse amplitude and the lower the background level, the better the timing resolution. The following arguments help understand why this should be.

- Figure 6.7 shows that the leading edge of a large pulse is sharper than for a small pulse. Conceptually, an infinitely large pulse would have an infinitely sharp edge, and background fluctuations would not change the time at which the pulse crosses the discriminator threshold. Conversely, the *slope* of a pulse just above the discriminator threshold can change significantly under the influence of background fluctuations. This explains why the timing resolution degrades for small pulse amplitudes.
- Intuitively, one would also expect the timing resolution to degrade as the background levels increase, especially for small pulses which are more distorted by the background fluctuations. The larger the background level, the higher the probability that a random fluctuation would happen just before the pulse and *push* it above threshold, giving the impression of an early hit time.

Multiple datasets similar to the one shown in figure 6.6 were analyzed and parameterized, which allows us to calculate the timing resolution for each pulse above threshold in the STACEE dataset.

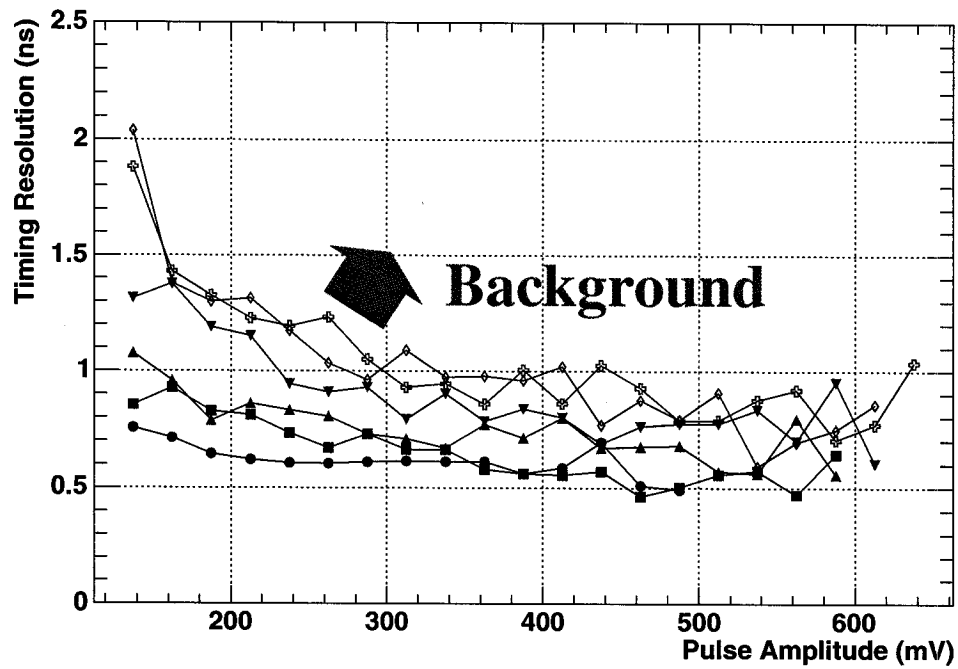


Figure 6.6: Timing resolution of a typical FADC channel as a function of the pulse amplitude and the background level. Each data file (represented by a different symbol) was taken with a different background level of illumination. The red arrow indicates that as the background levels get larger the data points move upward, which signifies a degradation of the timing resolution. Error bars not drawn for clarity reasons. Symbols by increasing order of background level: ●■▲▼◆.

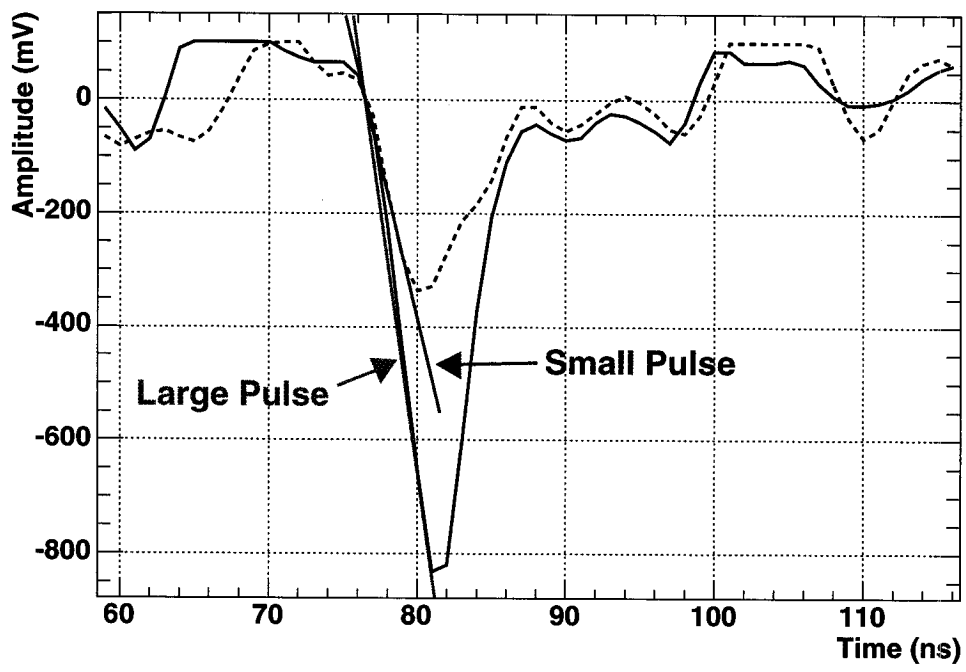


Figure 6.7: Comparison of the rise time for small and large pulses.

# Chapter 7

## Data reduction package: PASSO

For each event, the DAQ harvests data from the electronic modules and stores the information to disk using formats specific to each module. Although compact, these formats need to be decoded before the data can be interpreted. This process can be tedious, as some modules use arcane formats. A special software tool (PASSO) was created to decode the raw data and present the user with a calibrated data product. PASSO calculates relevant quantities such as the total charge collected by each channel, the arrival time of the Cherenkov photons on the heliostats, the reconstructed direction of the wavefront, etc. Although the details of the procedures used to calculate these quantities are beyond the scope of this thesis, we highlight some important aspects of event analysis in the next section. In the last section, we review in greater detail the most crucial procedure in PASSO: the correction of the field brightness, also known as *padding*.

### 7.1 Event analysis

In this section we review the analysis procedures used by PASSO to extract meaningful information from the data. STACEE data files are made of two types of events: the *environmental* events, which are read out twice per second and contain information on the PMT currents and rates; and the *triggered* events, which are produced by EAS. The environmental events are used exclusively to determine the  $\sigma^2/I$  ratios and monitor the stability of the PMT gains (see section 6.1.2). The analysis of triggered events can be done solely by decoding the information contained in the FADC traces. Figure 7.1 shows a typical FADC trace with several annotations which highlight important aspects of the analysis. The following list is a step-by-step guide which explains how the events are analyzed.

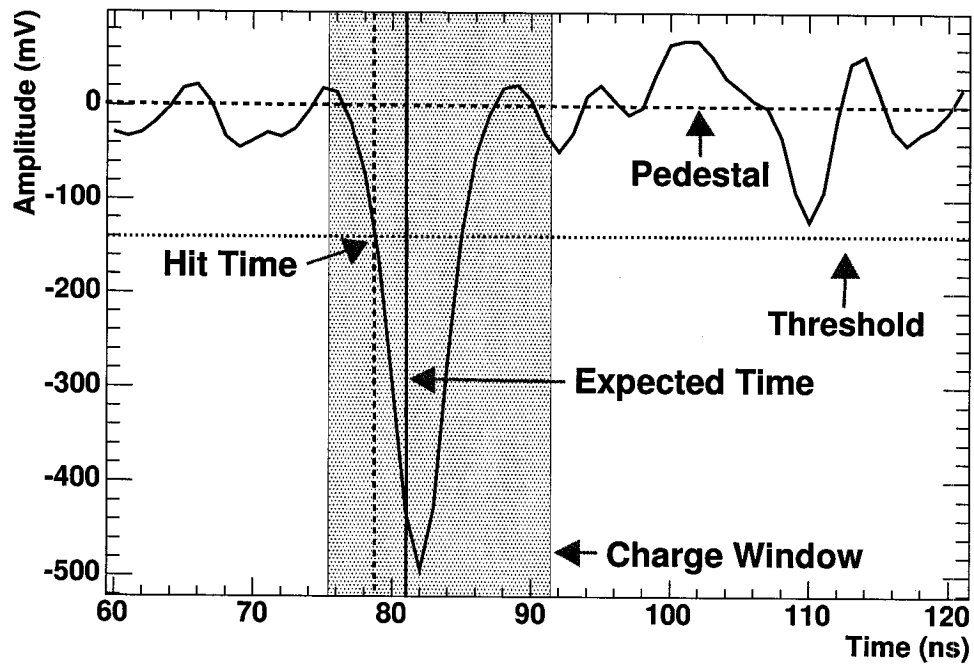


Figure 7.1: Sample FADC trace for a triggered event. Horizontal dashed line: pedestal value which is calculated on a event-by-event basis. Horizontal dotted line: nominal discriminator threshold. Vertical dashed line: time at which the pulse crossed the discriminator threshold. Vertical solid line: position where the pulse should have crossed the discriminator threshold for a spherical wavefront originating at the heliostat canting point. Shaded area: 16-ns window starting 6 ns before the expected arrival time which defines the region where the integrated charge is calculated.

1. The FADC traces with their respective pedestals and RMS values are decoded and converted to mV using the calibration parameters. Even though the signals from the PMTs are AC coupled, night sky background fluctuations on timescales of order  $1 \mu\text{s}$  can shift the baseline of the FADC traces up or down by a few mV. As mentioned in section 5.3, the pedestals and RMS values are calculated for each event and all the physical quantities extracted from the FADC traces are calculated with respect to the pedestal values.
2. The FADC traces are padded to equalize the field brightness of the ON/OFF runs. This process is discussed in detail in the next section.
3. The FADC traces are discriminated at a threshold 10 mV larger than the nominal discriminator thresholds; *e.g.*, for a typical nominal threshold of -140 mV, the analysis is done at -150 mV. A *hit* is produced each time the amplitude of the trace drops below the discriminator threshold. The position of the hit, or its arrival time, is calculated with respect to the beginning of the trace.
4. Using the programmed delays we calculate the position in the FADC traces where a spherical wavefront originating at the heliostat canting point would arrive. This position is referred to as the *dead reckoned* position.
5. We define a 16-ns wide *intime* window (not shown in figure 7.1) symmetrically centered on the dead reckoned position. The hits within this window ( $\pm 8$  ns) are considered to be intime and their properties are used during the subsequent reconstruction of the wavefront; the hits falling outside this window are discarded for the rest of the analysis.
6. For each of the 64 channels, we calculate the arrival time of the Cherenkov light on the corresponding heliostats. These arrival times are then used to reconstruct the direction of the EAS assuming a spherical wavefront.
7. Finally, the total charge deposited on each channel is calculated by integrating the signal over a 16-ns window which starts 6 ns before the expected arrival time.

## 7.2 Field brightness correction

During the 2000-2001 season, we observed Markarian 421, a famous BL Lac AGN originally detected at TeV energies by the Whipple group in 1992 [124]. We quickly realized

that the PMT currents were larger in the direction of Markarian 421 than in the corresponding OFF fields. The excess in the currents was coming from the bright star HD 95934 (magnitude 6.16 in the B band), which is within a few arcminutes of Markarian 421, well within the STACEE field of view. Some of the extra photons coming from the star arrive at the same time as sub-threshold events and therefore promote them and create a fake signal. This promotion effect was studied by observing a star (HIP 80460) with a magnitude and declination comparable to HD 95934 [20]. We discovered that for a raw excess rate of  $\sim 7$  events per minute on Markarian 421,  $\sim 2$  events per minute resulted from the promotion effect.

A systematic study of event promotion was undertaken in 2003. Three stars of different magnitudes (HIP 89279, 21 Com, and  $\iota$  CrB) were observed using the standard ON/OFF procedure. Notice that none of the ON and OFF fields contain any source of  $\gamma$ -rays; the triggered events are purely hadronic in nature. Figure 7.2 shows the relationship between the average excess event rate and the characteristic current difference between the ON and OFF fields. As the plot suggests, if we could equalize the currents (or the FADC variances as indicated in section 6.1.2) of the ON and OFF fields we would cancel out the promotion effect. As the excess event rate varies from run to run due to differences in the sky conditions, one would like to account for event promotion on a run-by-run basis. The driving motivation of this study was to find the optimal method to equalize the field brightness of the ON and OFF fields.

A simple way to correct the field brightness would be to add the background noise (which we automatically get from the early part of the trace that does not contain Cherenkov light) from the ON run to the OFF run, and vice versa. Mathematically, this can be written as:

$$\sigma_{ON}^2 + \sigma_{Noise(OFF)}^2 = \sigma_{OFF}^2 + \sigma_{Noise(ON)}^2. \quad (7.1)$$

The only drawback to this method is that it requires raising the analysis threshold of the detector by an excessively large value. A better way to equalize the field brightness would be to add noise only to the dimmest of the two fields to get its variance to match the variance of the brightness field. For a source where the ON field is brighter than the OFF field, the previous equation becomes:

$$\sigma_{ON}^2 = \sigma_{OFF}^2 + \sigma_{Noise}^2. \quad (7.2)$$

This correction procedure is applied on a channel-by-channel basis since the field of view of each channel is slightly different. Given that the differences in field brightness differ from source to source and span a considerable range, we built a library of noise traces with

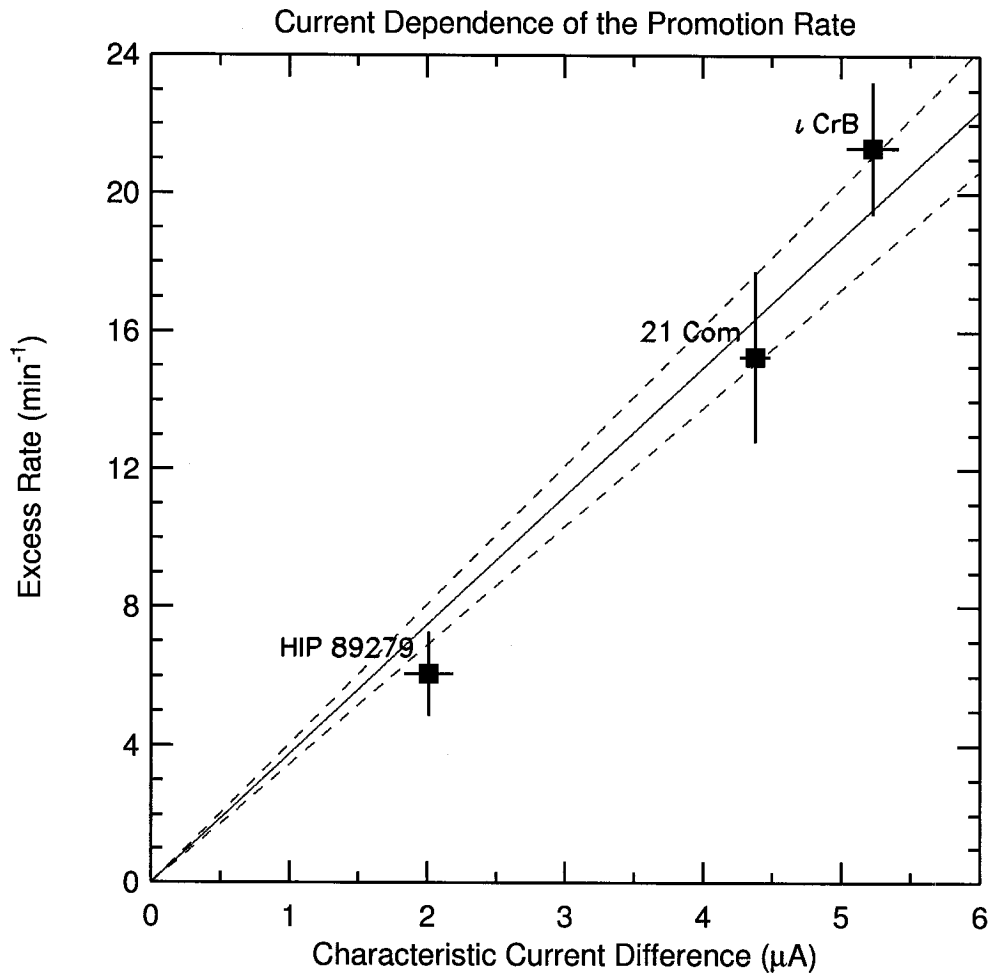


Figure 7.2: Excess event rate as a function of the characteristic current difference for ON/OFF observations of stars. Solid line: linear fit to the data. Dashed lines:  $\pm 1\sigma$  error on the slope.

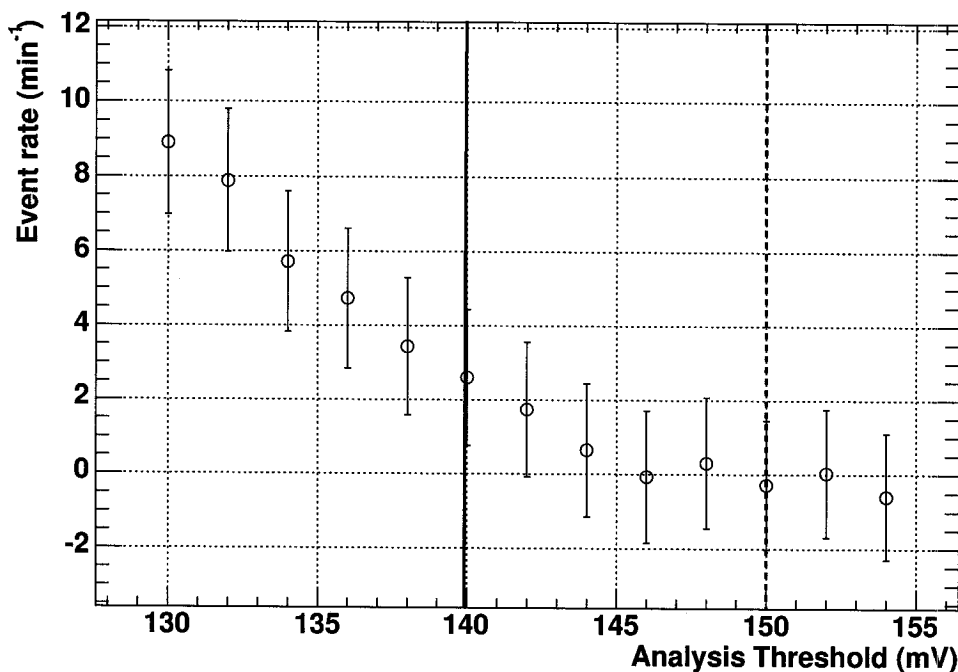


Figure 7.3: Excess event rate as a function of the analysis threshold for padded data for the star  $\iota$  CrB. Solid line: nominal threshold. Dashed line: analysis threshold (nominal + 10 mV).

different variances. Using a LED as a source of background light, we recorded thousands of FADC traces over a large range of background intensities.

Given that we can only add noise to the FADC traces during the analysis, we cannot recover the events that would have passed the trigger requirements had the additional noise been present at the time of the acquisition. For this reason, the analysis threshold has to be raised after correcting the field brightness to remove this initial bias. We empirically determined that raising the discriminator threshold by 10 mV above the nominal value was sufficient to remove any bias in the data. This procedure was tested on star data and figure 7.3 shows the excess event rate as a function of the analysis threshold for data taken on  $\iota$  CrB, a star with current differences larger than any other STACEE source. The very last step of the padding procedure is to reimpose the trigger using the same LTC/GTC conditions as the ones used during the acquisition. After discriminating the FADC traces (see previous section) we simply count the number of intime hits in each of the 8 clusters. If the number of clusters with at least LTC hits is equal or greater than GTC, the event is considered valid, otherwise the event is rejected.

# Chapter 8

## Pulsar timing tools

In October of 1632, Galileo Galilei (1564–1642) received the visit of the Inquisitor of Florence, Italy, who summoned him to appear before the Inquisition in Rome. According to the Catholic Church, Galileo was guilty of heresy for his views on the Copernican theory. In his book titled *“Dialogue Concerning the Two Chief World Systems”*, Galileo argued in favor of the Copernican idea and ridiculed the Catholic Church’s position. Galileo was eventually sentenced to house arrest for life<sup>1</sup>...

Thanks to Copernicus and in spite of the persecution demonstrated in the case of Galilei, we’ve known for almost 400 years that the Earth is not a unique central body, but one of the bodies orbiting the Sun. The distance of the Earth to celestial objects is constantly changing and being modulated by our motion around the Sun. Pulses emitted from a pulsar will reach the Earth after the Sun when the Earth is farthest from the pulsar; six months later, the pulses will reach the Earth before the Sun. The only way to study pulsars over long periods of time (longer than a few minutes) is to take into account the position of the Earth with respect to the center of the solar system. The ideas of the Copernican revolution become essential in analysing pulsar data!

### 8.1 Epoch folding and barycentering

When searching for periodicities in time series data, a large variety of methods with different statistical properties is available. For low to moderate signal-to-noise ratios, the epoch folding method is often used to search for coherent signals. This method is particularly well suited for unevenly sampled data, which is the case for STACEE.

As mentioned at the beginning of this chapter, the motion of the Earth around the Sun creates a Doppler-like shift which needs to be accounted for. This correction is known

---

<sup>1</sup>See “The Galileo Project” at <http://galileo.rice.edu> for more details on Galileo’s life.

as *barycentering* and consists in converting the arrival time of photons on Earth to arrival times at the solar system barycenter<sup>2</sup>. This is a standard procedure in astronomy and is described in detail in [18]. The implementation of the barycentering procedure was done using the JPL Planetary and Lunar Ephemeris DE200 package [108].

Each month, the period, period derivative, and phase of the Crab Pulsar are determined with extreme accuracy from radio observations using the Jodrell Bank radio telescope [100]. Using the monthly ephemerides, we can easily calculate the phase of each time-stamped STACEE event and build the pulse profile.

## 8.2 Validation of the technique

The barycentering and epoch folding techniques were thoroughly tested using data from two different telescopes: the CELESTE  $\gamma$ -ray telescope [42], and the Arecibo radio telescope.

David Smith and Denis Dumora of the CELESTE collaboration graciously offered a subset of their optical data obtained on the Crab Pulsar. The observations of the Crab Pulsar in the optical regime were done to confirm the validity of their barycentering code. The data was sampled at 2 kHz for a duration of  $\sim 17$  minutes and their pulse profile is shown in Figure 8.1. As expected, the main pulse and interpulse are aligned at phase 0 and 0.4 respectively (see Figure 10.9 for comparison with the Hubble Space Telescope pulse profile). The STACEE barycentering and epoch folding programs were applied to the same data and the resulting pulse profile is shown in Figure 8.2. The STACEE and CELESTE pulse profiles are identical, which constitutes the first evidence that our barycentering and epoch folding programs are working.

Thanks to Jason Hessels and Scott Ransom of the pulsar group at McGill University, we were also able to test our analysis code on two radio pulsars: PSR J2021+3651 [131, 132, 77] and PSR 1639+36 [97]. PSR J2021+3651 is a young and energetic Vela-like pulsar coincident with the EGRET  $\gamma$ -ray source GeV 2020+3658 with a spin period of  $\sim 104$  ms. The data were obtained using the Wideband Arecibo Pulsar Processor (WAPP) at 1.4 GHz with 100 MHz of bandwidth. Figure 8.3 shows the pulse profile produced by our analysis programs. This profile is consistent with the pulse profiles reported in [131], providing a second confirmation that our analysis procedure is working.

The last of the three pulsars was PSR 1639+36, a rapidly rotating 10-ms pulsar in the globular cluster M13 (NGC 6205), originally discovered by Kulkarni et al. [97]. Recent

---

<sup>2</sup>The barycenter is the center of mass of two or more bodies which are orbiting each other, and is the point around which both of them orbit.

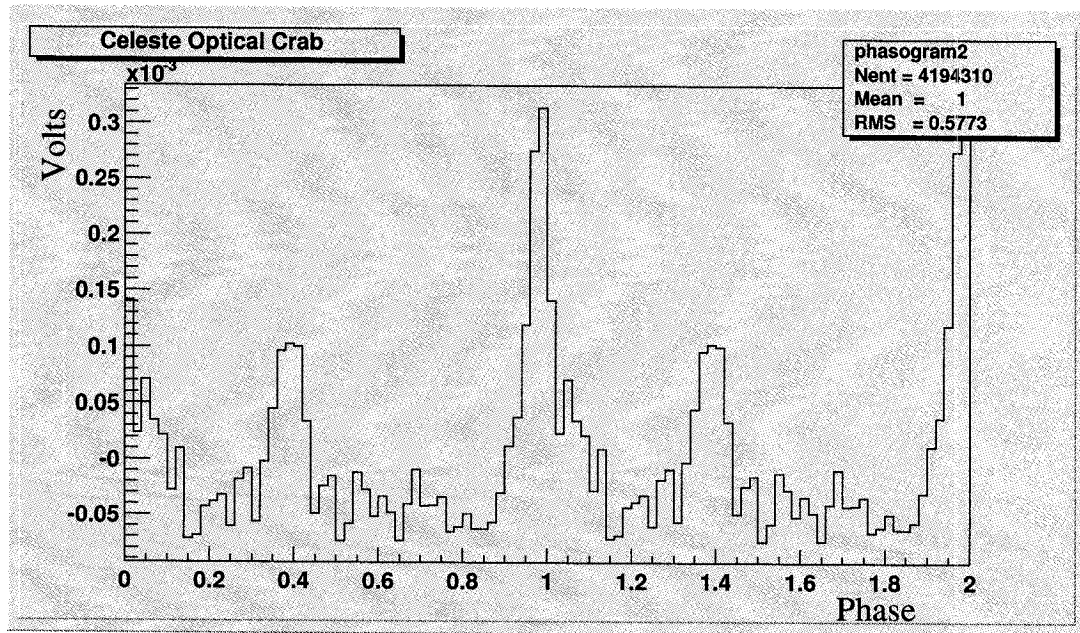


Figure 8.1: Pulse profile of the Crab Pulsar in the optical regime as measured by the CELESTE collaboration. Two complete pulse periods are shown for clarity.

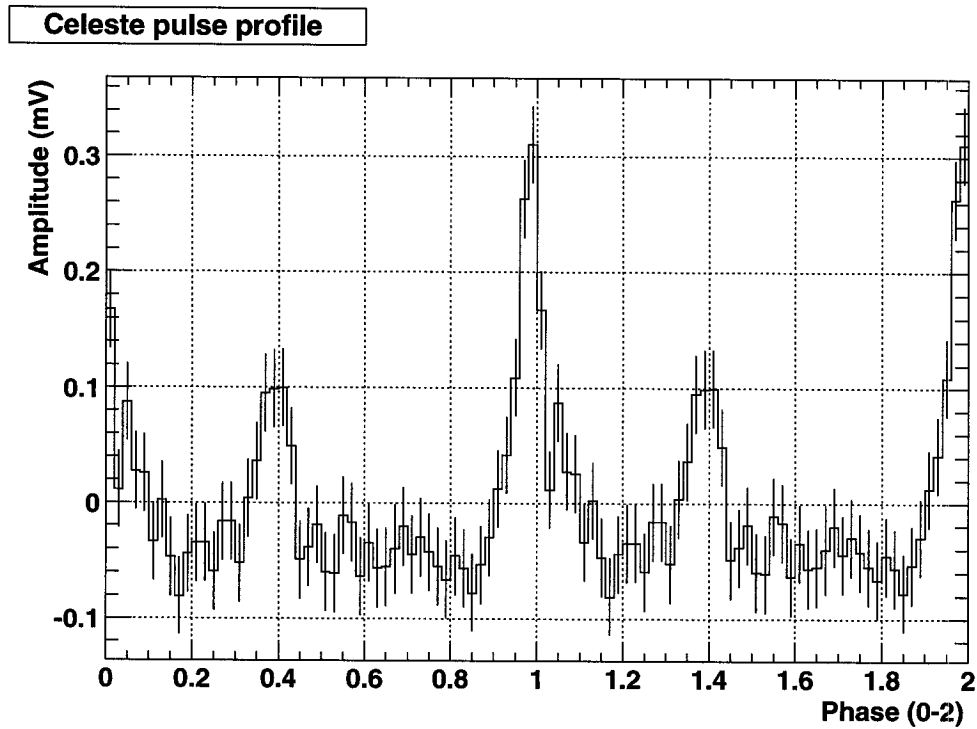


Figure 8.2: Pulse profile of the Crab Pulsar using the STACEE barycentering and epoch folding programs on CELESTE data.

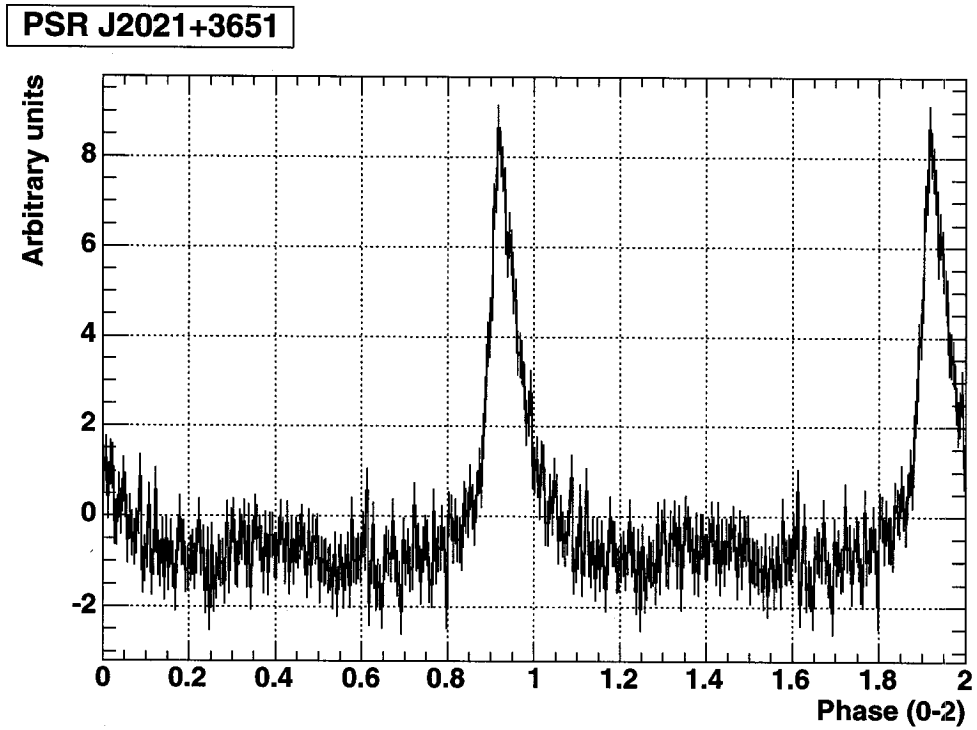


Figure 8.3: Pulse profile of pulsar PSR J2021+3651 using the STACEE analysis programs. This pulse profile is consistent with the pulse profile reported in [131].

data were obtained by Jason Hessels using the WAPP on Arecibo at 1.175 GHz. Figure 8.4 shows the pulse profile as calculated using STACEE's barycentering code. The top plot shows the narrow double-peak pulse which clearly stands out above the background noise. This pulse profile is identical to the pulse profile calculated by Jason Hessels<sup>3</sup>. The lower plot shows the pulse profile as a function of time (the duration of the run was 3.8 ks). For rapidly rotating pulsars like PSR 1639+36, the pulse would rapidly get out of phase if the barycentering code was not working properly. As an example, figure 8.5 shows what happens to the pulse profile when the barycentering correction is not applied. Even though the signal-to-noise ratio of this pulsar is large, if one assumes that the earth is not moving with respect to the barycenter it becomes impossible to detect this pulsar after a few minutes. The lower plot clearly shows that the phase of the pulse rapidly drifts off. By counting the number of *wraps* one can estimate the total delay of the pulse over the observation period. Given that the number of wraps is  $\sim 14$ , and the pulsar's period is 10 ms, this corresponds to a time delay of only 140 ms over more than one hour of observation!

The analysis of these three pulsars confirms without any doubt the validity of our barycentering and epoch folding code. This provides another demonstration that Copernicus was indeed correct!

---

<sup>3</sup>Personal communication.

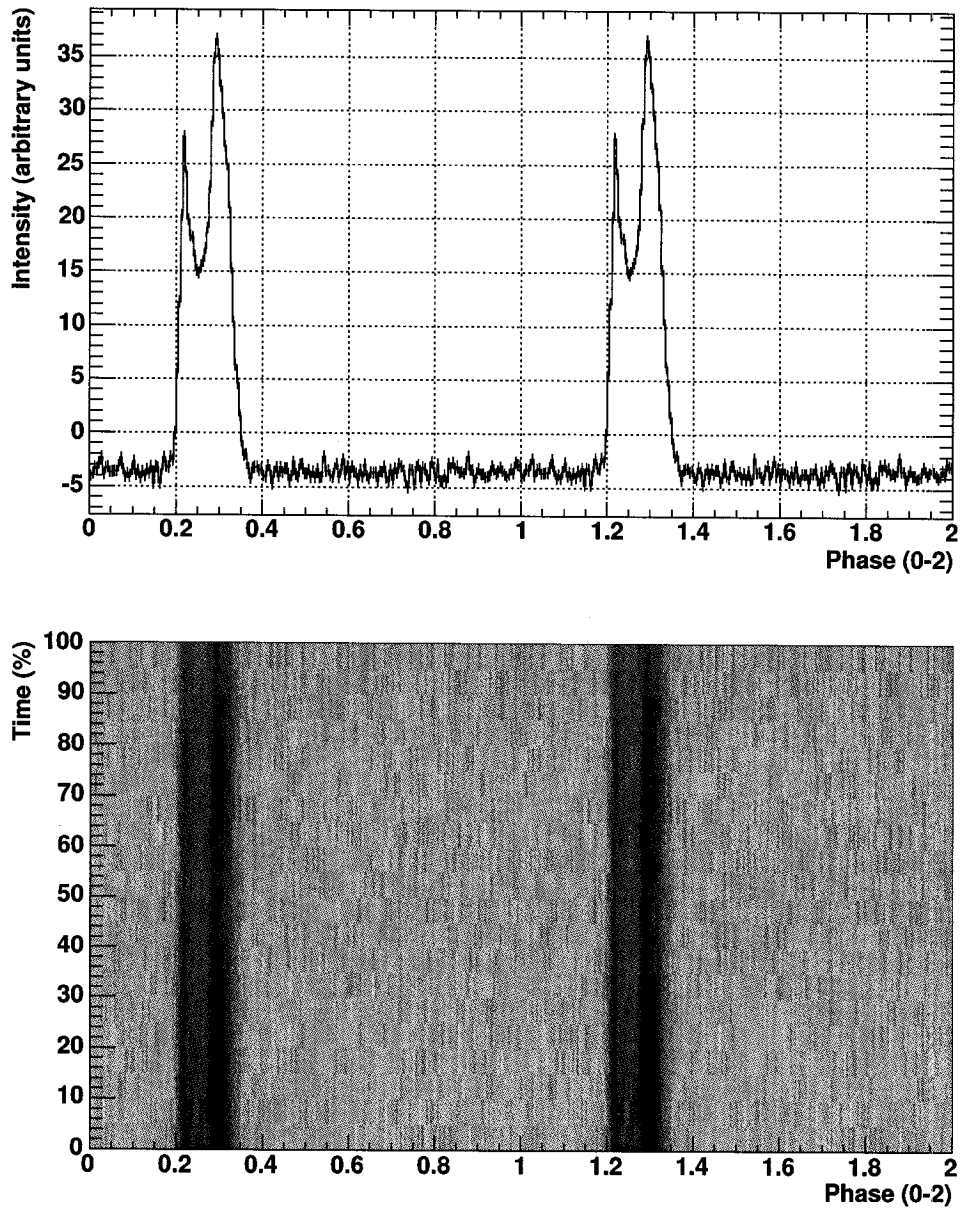


Figure 8.4: The top plot shows the average pulse profile for PSR 1639+36 after barycentering. The lower plot shows the pulse profile versus time as a fraction of the duration of the run (3.8 ks).

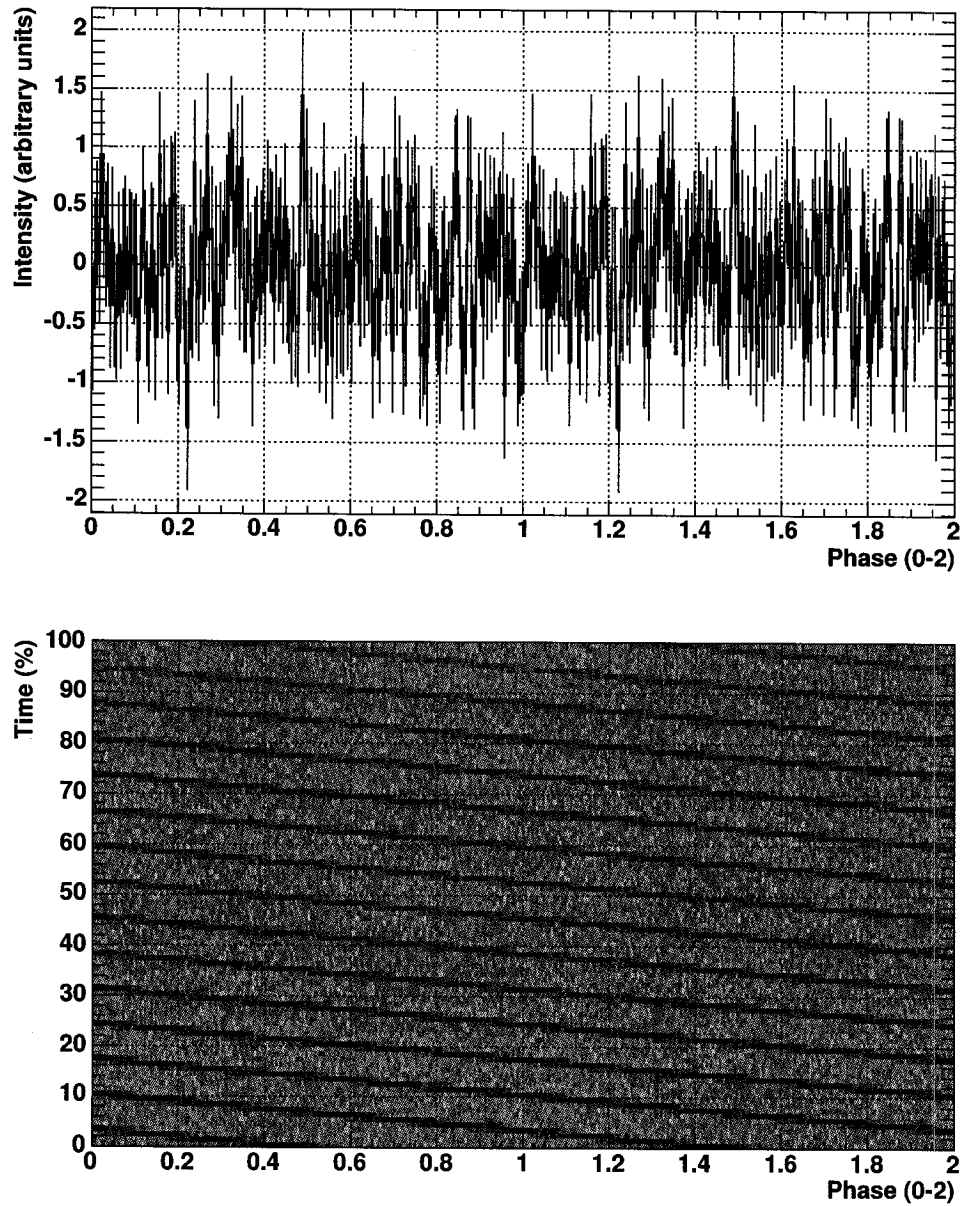


Figure 8.5: Pulse profile for pulsar PSR 1639+36 without the barycentering correction. The top plot shows the average pulse profile and the lower plot shows the pulse profile versus time as a fraction of the duration of the run (3.8 ks).

# Chapter 9

## Data quality cuts

After much development, the STACEE telescope reached a relatively stable configuration with the addition of the FADC system. Although different pointing schemes were used, the trigger configuration remained the same for the last two seasons. In addition, much progress was made in detecting and fixing problems early on, minimizing the amount of data corrupted by hardware and software failures. Unfortunately, external factors, such as the weather and other atmospheric perturbations, had a direct impact on the quality of the data. Special quality cuts were used to remove corrupted sections from the analysis. These cuts were grouped into two categories: detector malfunctions and atmospheric instabilities.

### 9.1 Detector malfunction cuts

A sophisticated online monitoring system was used to keep the heliostat and DAQ operators informed about the state of the detector. For example, if one of the FADC crates failed, a visual display would indicate that something went wrong with the FADC system. Within seconds, the DAQ operator could respond to the alert and take the appropriate measures to rectify the problem. The information about the state of the detector was recorded to disk, which made it possible for offline programs to automatically cut out bad sections from the data. A list of standard cuts is given in Table 9.1.

### 9.2 Atmospheric instability cuts

The atmosphere is an integral part of the detector, and as such, it must remain stable for the duration of the acquisition. Unstable conditions can easily bias the data and artificially

HELIO cut	<p>The positioning of each heliostat is controlled by two independent motors; for 64 heliostats, this represents 128 possible points of failure. Heliostats with tracking problems can seriously compromise the quality of the data; not only do they decrease the sensitivity of the detector (loss of Cherenkov photons), but a change in field brightness (by pointing at a different region of the sky) can change the cluster rates significantly and produce accidental triggers. The status of each heliostat is recorded every 20 seconds and this information is used to apply a tracking cut. If any heliostat was more than 2 bits off (<math>\sim 0.1</math> degrees) in any direction (azimuth or elevation), the cut program removes this 20-second section from the analysis.</p>
STACQ cut	<p>The software driver provided with the Acqiris digitizers was not designed to support the high trigger rate of STACEE. For standard operating systems' (e.g. Linux or Windows), the latency to respond to interrupts can be as large as 30 ms, which is larger than the smallest event interval for STACEE (<math>\sim 20</math> ms). A customized real time Linux driver was written by the STACEE collaboration to support higher trigger rates. Driver errors causing missed events or abnormal termination are infrequent, but occur. Given that the event reconstruction relies almost exclusively on the FADC traces, sections with missing events are removed from the analysis.</p>
HV cut	<p>The PMT currents are continuously monitored by an online system which can automatically shut down the high voltage supply in case of a current surge to preserve the integrity of the PMTs. Current surges are usually caused by clouds or airplanes passing through the field of view. Sections where the high voltage supply was turned off are removed from the analysis.</p>

Table 9.1: List of standard cuts used to remove sections affected by software or hardware failures.

produce a false signal or cancel a genuine signal. The brightness of the night sky background and atmospheric attenuation have a direct impact on the individual tube currents, which in turn affect the cluster rates and the global trigger rate. Since STACEE needs data from both the ON and OFF fields for background subtraction, the atmospheric conditions must remain stable on a time scale longer than the duration of an ON–OFF pair. In the following sections, we describe methods used to detect unstable atmospheric conditions.

### 9.2.1 Clouds and transient disturbances

Clouds passing through the field of view are the main source of atmospheric instabilities. Low altitude clouds not only block the Cherenkov photons produced by EAS, they also scatter the light pollution from the Albuquerque metropolitan area into the field of view of the telescope. This leads to short time scale variations (seconds to minutes) of the PMT currents and cluster rates. Given that the value of the break point in the rate versus threshold curve depends on the cluster rates, there is a chance that the break point will move above the operating point — which is only a few mVs higher than the breakpoint — and produce accidental triggers which might not be removed during the offline analysis. Luckily, clouds can be easily detected by looking at the time evolution of the cluster rates.

Figure 9.1 shows the cluster rates (L1 rates) for a pair affected by clouds. The cluster rates of the OFF run (blue lines) indicate the passage of a big cloud through the field of view during the first half of the run and a smaller cloud during the last 200 seconds. Sharp spikes in the cluster rates also indicate the passage of airplanes through the field of view. The atmospheric conditions were clearly unstable and this pair was cut out from the analysis.

Visual inspection of the cluster rates for the entire data set is sufficient to identify bad pairs, or pairs which are partially corrupted by the passage of clouds through the field of view. Bad pairs are manually cut out from the analysis while partially corrupted pairs are sliced using a special program (L1 cut program). The L1 cut program is used only after applying the detector malfunction cuts since heliostat malfunctions can also produce cluster rate fluctuations.

### 9.2.2 Frost and water condensation

The onset of water condensation (dew formation), or frost formation at lower temperatures, on the surface of heliostat facets is an insidious problem for STACEE since it cannot be easily detected. The only infallible way to detect it is by inspecting the heliostat array at regular intervals during a night of observation, which is rarely possible.

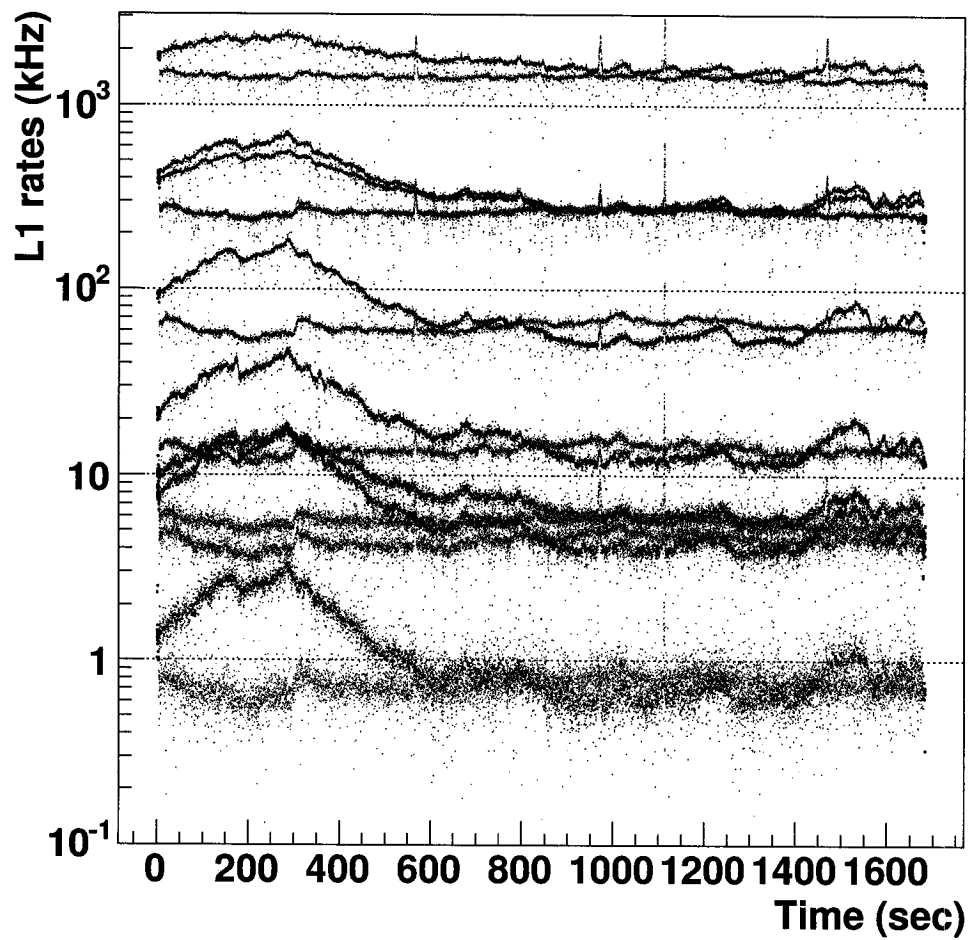


Figure 9.1: Effect of clouds passing through the field of view of STACEE. Unstable cluster rates (L1 rates) indicate changing atmospheric conditions. The red lines corresponds to the cluster rates of the ON run, while the blue lines corresponds to the OFF run. This pair of runs was manually removed from the analysis chain.

The temperature to which air needs to be cooled in order for condensation to begin to form is called the dew point temperature. A small weather station installed on the roof of the heliostat control room continuously monitors the ambient temperature and the dew point temperature. When the difference between these two temperatures drops below 10 degrees centigrade, there is a good chance of condensation <sup>1</sup>. Data taken under these circumstances are suspicious and generally discarded. Frost, on the other hand, is formed by sublimation - water vapor moving directly to solid ice. Frost is formed when the dew point is near or below freezing and the temperature of the air falls to within a few degrees of the dew point.

Water condensation and frost formation on the heliostat facets scatter the incident light and significantly reduce the collection efficiency. This drop in efficiency is not necessarily accompanied by a change in PMT currents or cluster rates as light from random parts of the sky is scattered in the field of view of the telescope. Still, this reduction in collection efficiency has a direct impact on the trigger rate of the detector and the DAQ operator can notice a monotonic drop in the L2 rate during the onset of condensation or frost formation. Figure 9.2 shows the effect of frost formation on the trigger rate of STACEE for the night of January 19, 2004. Needless to say, the data taken under these conditions were discarded.

---

<sup>1</sup>This 10-degree temperature difference is empirical, but appears to work reasonably well for STACEE.

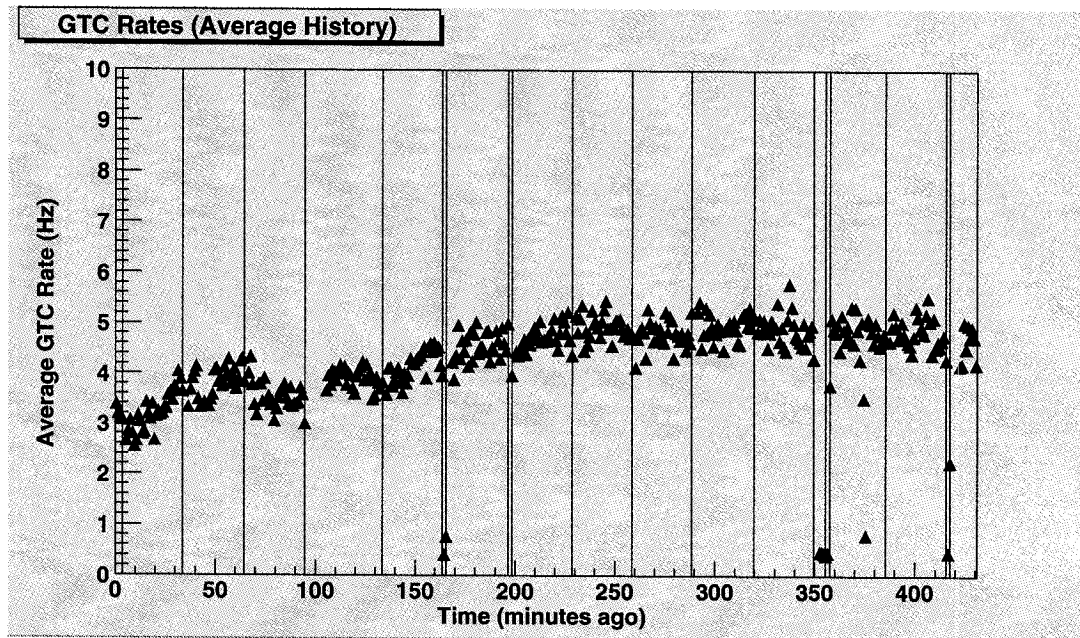


Figure 9.2: A monotonic decrease of the trigger rate (GTC rate) caused by the formation of frost on the heliostat facets (the most recent points are on left). The presence of frost was confirmed by the DAQ operator.

# Chapter 10

## Detector simulation and expected performance

Ground-based experiments like STACEE measure a few simple quantities: the arrival time and density of photons at each heliostat, and the average event rate (trigger rate). Other experiments, sensitive to different parts of the electromagnetic spectrum, use a variety of techniques — hence, they usually measure different quantities — to study the same astronomical objects. Our knowledge of the physical processes at play often comes from combining information obtained at different wavelengths. This requires standard measurement units. The quantities measured by STACEE must be converted into energies (GeV), differential flux ( $cm^{-2}s^{-1}GeV^{-1}$ ), etc... The conversion of an excess rate into an integral flux requires detailed knowledge about the detector response. Contrary to space-based instruments, which can be meticulously calibrated at particle accelerator laboratories, the response of STACEE cannot be measured in a controlled environment. We have to rely to a great extent on Monte Carlo simulations.

In this chapter we present the simulation programs used to simulate the response of the STACEE detector and some cross-checks of the detector performance. The simulation chain is made up of three programs: `CORSIKA`, which generates Extensive Air Showers (EAS), `sandfield`, which propagates the Cherenkov photons through the optical system, and `elec`, which simulates the response of the electronics.

### 10.1 The `CORSIKA` air-shower simulation

The first step of the simulation process is the production of EAS for various types of particles, e.g., *protons* ( $p$ ),  $^4\text{He}$  nuclei, and  $\gamma$ -rays. STACEE uses the `CORSIKA` [74] simulation package which was initially developed for the KASCADE experiment [44].

CORSIKA offers a choice of different interaction models used in particle physics. For high energy hadronic interactions ( $E > 80$  GeV), six models are available: DPMJET [128], HDPM [28], NEXUS [46], QGSJET [86], SIBYLL [50], and VENUS [154]. STACEE operates in the lower region of the energy range covered by these models, where the physics is relatively well known and the differences between models is small. We decided to use the QGSJET model for high energy hadronic interactions and the GHEISHA [47] model for low energy hadronic interactions. Electrons, positrons, and  $\gamma$ -rays are simulated by the Electron Gamma Shower code EGS4 [110].

CORSIKA tracks particles through the atmosphere until they interact with air nuclei or decay. CORSIKA supports 20 predefined atmospheric profiles as well as two customizable profiles. The predefined profiles are available for four world-wide locations: central Europe (measured above Stuttgart), the South pole, Malargüe (Argentina), and the US. Seasonal profiles are available for the first three locations, but only the US standard atmosphere is available for the US [150]. At the time the simulations were done, only Linsley's parameterization of the US standard atmosphere was available [79]; a new parameterization is now available for comparative studies [88]. The atmosphere is an integral part of our detector and it is essential to understand the effect of different atmospheric conditions on the Cherenkov yield. Monte Carlo studies indicate that seasonal variations at mid-latitude (primarily due to density profile differences) lead to differences in Cherenkov yield of the order of 15–20% [15] — the winter and summer profiles having respectively the highest and lowest Cherenkov yields. Given that the Crab season typically starts in late October and ends in February — a period where the differences in atmospheric profiles are certainly less marked than the differences between the winter and summer profiles — we estimate the systematic error on the Cherenkov yield to be  $\sim 10\%$  for STACEE.

A special STACEE output module is used to save the information regarding the Cherenkov photons. Wavelength-independent losses due to mirror reflectivities and quantum efficiencies are handled within CORSIKA to reduce file size.

## 10.2 The sandfield optical simulation

Simulated Cherenkov photons produced in EAS terminate their course on a horizontal plane  $\sim 30$  meters above the heliostat array. The cores of these EAS are uniformly scattered on a circular plane perpendicular to the trajectory of the primary particle to reflect the uniform spatial distribution of real EAS. The radius of the scattering region is adjustable and each EAS can be scattered multiple times. By reusing the same EAS we significantly reduce the amount of CPU time required by the simulation process. By keeping the num-

ber of scatters to a small value (typically 5) we avoid introducing correlations in triggered events.

After correcting the wave-vectors of the individual photons for the shift in core landing position, `sandfield` determines which photons interact with the STACEE heliostats. Individual heliostats are modeled as 25 square parabolic facets. The alignment of each facet is given a small random jitter to reflect imperfections in the real heliostats [84]. `sandfield` also applies a wavelength-dependent cut to reproduce the reflectivity of the heliostats (see figure 4.9).

Photons reflected by the heliostats are then ray-traced to the secondary mirrors. Some of these photons hit the camera box, which is a significant source of occultation for some channels. `sandfield` then calculates where the remaining photons intersect the plane of the secondary mirrors, which are modeled as spherical mirrors with a diameter of 1.9 meters on the 260 level, or 1.1 meters on the 220 level. Figure 10.1 shows the distribution of photons in the plane of the North secondary mirror for 3 channels located at different distances from the tower. The width of the light distribution scales with the distance from the tower. The occultation from the camera box is more important for heliostats closer to the tower, with the exception of the south camera channels which use a different camera design and are not affected by occultation.

Before reflecting the photons into the PMTs, `sandfield` applies another wavelength-dependent cut to reproduce the reflectivities of the secondary mirrors and the quantum efficiencies of the PMTs. Some of the reflected photons enter the DTIRCs, at which point a lookup table is used to determine those which get converted into photoelectrons. A list of photoelectrons with their arrival times at the DTIRCs is finally written out to disk for input into `elec`.

### 10.3 The `elec` electronics simulation

The simulation of the STACEE electronics response is the most complex part of the simulation process. After reading the list of photoelectrons produced by `sandfield`, `elec` filters out events which don't have a chance to trigger the detector. Since we scatter the EAS over large areas, many of these events have a very small number of photoelectrons. If the total number of photoelectrons produced on all channels is not sufficient to trigger a single PMT, the event is thrown away. This removes a significant fraction of events and saves a significant amount of CPU time. Analog waveforms are built for the remaining events which are likely to trigger the detector. The *signal* part of the trace is built using the list of photoelectrons produced by `sandfield`. Each photoelectron produces an

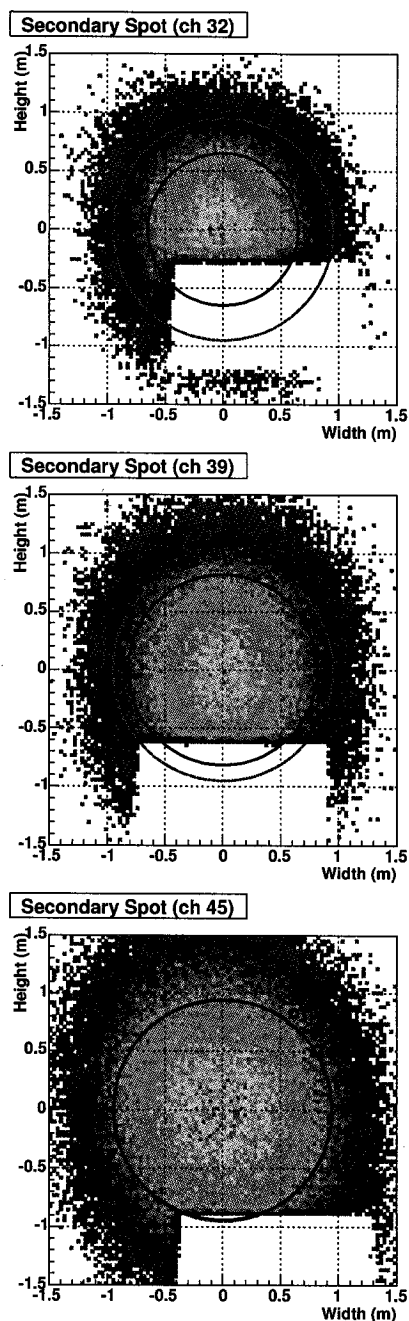


Figure 10.1: Distribution of photons in the plane of the North secondary mirror for 3 different channels (32–39–45). The source of photons was located at the Crab transit point ( $Az = 180^\circ$ ,  $El = 77.1^\circ$ ). The angular size of the source was  $0.5^\circ$ , which is approximately the same size as a typical EAS. The red circles indicate the size of the secondary mirror and the black circles indicate the area seen by each channel after accounting for the opening angle of different DTIRC sizes.

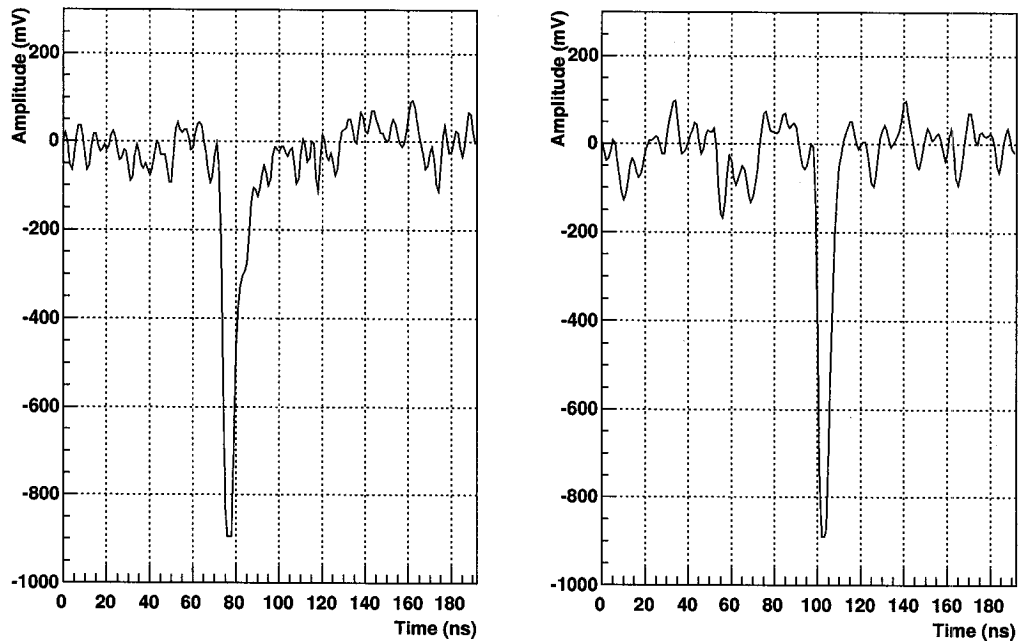


Figure 10.2: Left: Real trace from a typical channel. Right: Trace generated by `elec`.

electron cascade in the photomultiplier tube which produces a photoelectron pulse with charge  $Ge$ , where  $G$  is the gain of the photomultiplier tube. The pulse shape is given by:

$$f(t) = A(\alpha t)^{1.5} \exp[-(0.1\alpha t)^2], \quad (10.1)$$

where  $A$  is a scaling factor defined by the photomultiplier gains, and  $\alpha$  is an empirical factor used to vary the pulse shape. The photoelectron pulses are added together to form the *signal* trace. The *background* trace, which corresponds to the contribution of the night sky background, is built by converting the currents into expected rates for each channel. RF noise can also be added to the *background* trace if desired. `elec` then combines the *signal* and *background* traces. Figure 10.2 shows a typical trace generated by `elec` together with a real trace.

The traces are then discriminated and a detailed simulation of the trigger system checks if the event satisfies the trigger conditions. If the event triggers the detector, `elec` saves the information about the event using the same format as real data produced by the DAQ.

Hour Angle (HA)	Azimuth (degrees)	Elevation (degrees)
-3	96.0	48.8
-2	108.3	60.8
-1	130.6	71.6
0	180.0	77.1
+1	229.4	71.6
+2	251.7	60.8
+3	264.0	48.8

Table 10.1: Hour angle, azimuth, and elevation of the arrival directions for air showers simulated with CORSIKA. A complete set of showers ( $p$ ,  ${}^4\text{He}$ ,  $\gamma$ ) was simulated for each point.

## 10.4 Simulation parameters

The first stage of the simulation process is the generation of hadronic and  $\gamma$ -ray showers using the CORSIKA package as explained in section 10.1. Complete sets of EAS were generated for a number of points along the trajectory of the Crab. These points were equally spaced in hour angle (HA); the azimuth and elevation of each point is given in Table 10.1.

In the case of hadronic showers, only  $p$  and  ${}^4\text{He}$  nuclei were simulated; heavier nuclei account for a negligible fraction of the trigger rate. The incoming directions were scattered uniformly in solid angle to reproduce the isotropic nature of cosmic rays. The angular radius was  $2.5^\circ$ , which was large enough to extend to the region where the probability of an event triggering the detector becomes negligible. The primary energy spectra for  $p$  and  ${}^4\text{He}$  were obtained from recent experimental data [82]. Figure 10.3 shows the differential energy spectra of hadronic cosmic rays. A power-law fit gives the spectral index and absolute normalization for each flavor of cosmic rays. The spectral indices for  $p$  and  ${}^4\text{He}$  nuclei were  $-2.71$  and  $-2.65$  respectively.

Similarly,  $\gamma$ -ray EAS were generated at discrete energies and for a power-law spectrum ( $\alpha = -2.4$ ). Showers generated at discrete energies were used to calculate the response of the detector and showers generated on a power-law spectrum were used to investigate possible  $\gamma$  / hadron cuts.

As mentioned on section 10.2, the cores of EAS were scattered on a disk perpendicular to the arrival direction of the primary particles. Since particles generated in hadronic EAS usually have larger transverse momentum  $P_T$  than particles in  $\gamma$ -ray EAS, the size of the light pool on the ground is larger (but less uniform) and hadronic events can trigger the detector at greater distances from the center of the array. For this reason, we used a

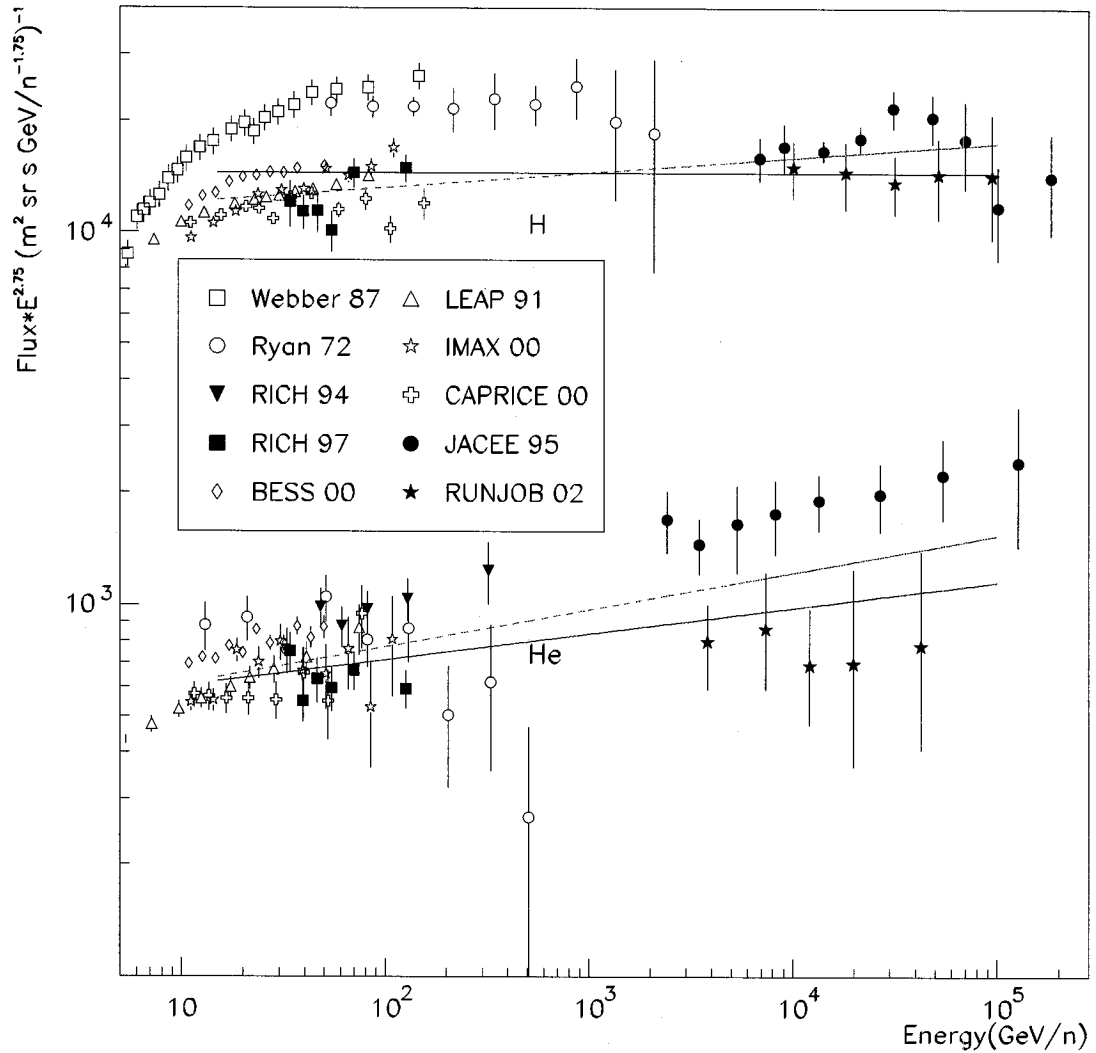


Figure 10.3: Differential energy spectra for  $p$  and  ${}^4\text{He}$  cosmic rays. The dashed red line is the fit used for all the simulations of hadronic showers in CORSIKA. This line is a power-law fit and the spectral index for  $p$  and  ${}^4\text{He}$  nuclei is  $-2.71$  and  $-2.65$  respectively. The fit also gives the absolute normalization of the differential spectra used to predict the trigger rate of the detector.

scattering radius of 400 meters for hadrons and 200–250 meters for  $\gamma$ -rays. Figure 10.4 shows the distributions of core positions for simulated  $\gamma$ -rays and protons. Two different canting schemes were used for the simulations: monocanting and paracanting. The former scheme was the standard configuration for the data taken during the 2002-2003 season and the latter was used during the 2003-2004 season.

As mentioned in Section 10.3, the amplitude of the photoelectron pulses depends on the PMT gains. The gains were calculated directly from the data — using the  $\sigma^2/I$  method presented in Section 6.1.2 — and we used an average value for all 64 channels. The PMT currents depend very much on the position of the source in the sky. The currents are generally lower when the source rises in the east and get larger when the source sets over Albuquerque (main source of light pollution). We calculated the average currents from the data for each channel at the hour angle positions where we generated the simulations. Other free parameters in `elec`; e.g., attenuation factor along the cables, amplifier gains, discriminator pulse width, etc., were set to values measured at the site.

## 10.5 Effective areas and energy thresholds

Using the simulation parameters mentioned above we ran complete sets of simulations for different points along the trajectory of the Crab. We used discrete  $\gamma$ -ray energies from 30 GeV to 10 TeV and calculated the trigger probability at each energy bin. The effective area as a function of energy and hour angle ( $HA$ ) is given by

$$A_{\text{eff}}(E, HA) = \pi R_{\text{scatter}}^2 P(E, HA), \quad (10.2)$$

where  $R_{\text{scatter}}$  is the scattering radius as explained in section 10.2 (typically 200 – 250 meters) and  $P(E, HA)$  is the probability for an event to trigger the detector (the ratio of the number of triggered events to the number of simulated events). Figure 10.5 shows the results of a simulation for monocanted heliostats using a wide mode trigger configuration and a 150 mV discriminator threshold. This particular configuration was used for a subset of the data taken during the 2002-2003 season.

Effective area curves for different detector configurations show a number of generic features. The sensitivity of the detector to low energy  $\gamma$ -rays depends strongly on the source position. As the source moves away from its transit point to lower elevation, the effective area drops quickly, especially below  $\sim 200$  GeV. At lower elevations, a larger fraction of Cherenkov photons are scattered and absorbed in the atmosphere — due to the greater path length for interactions. Angular projection effects increase the size of the

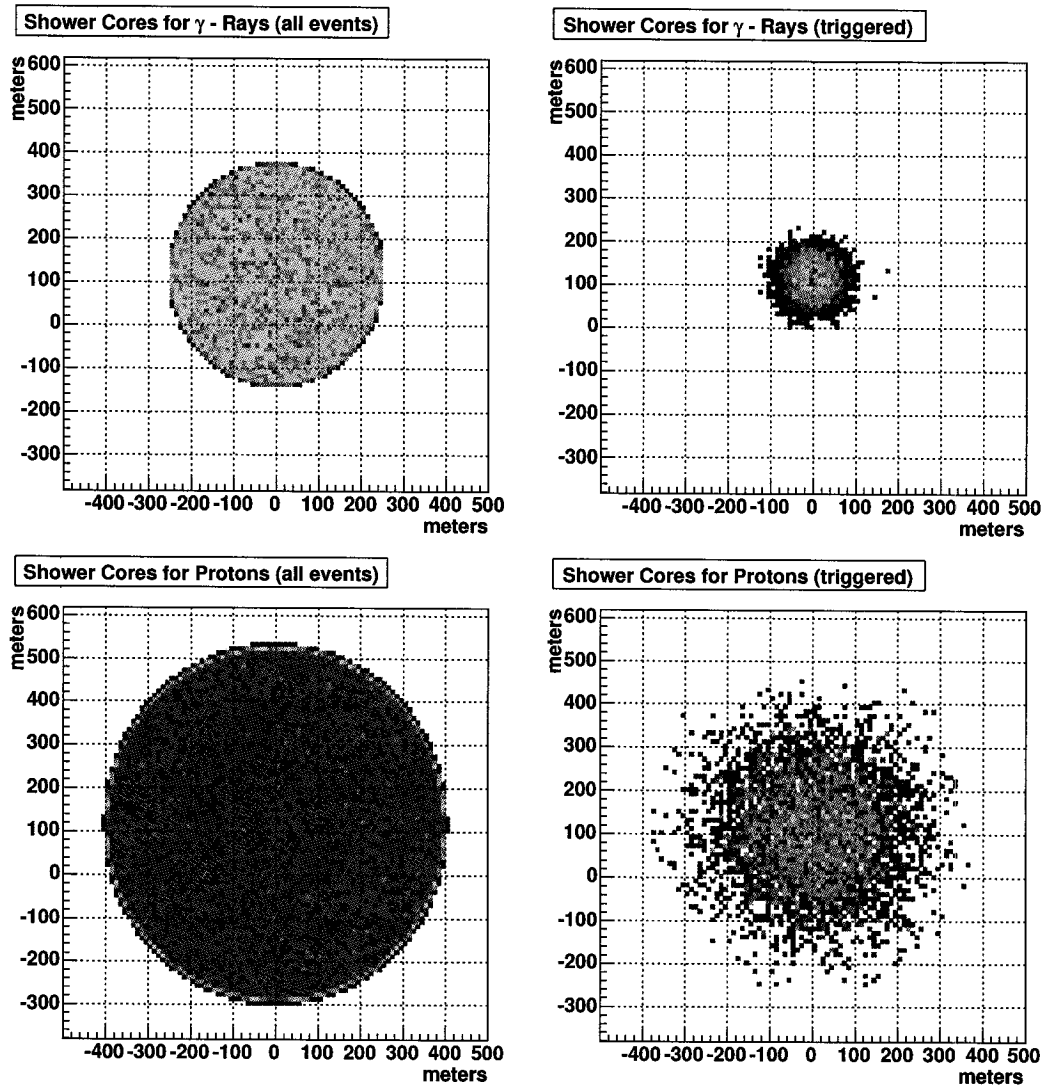


Figure 10.4: Distribution of core positions for simulated  $\gamma$ -rays and protons. The left column shows the distributions for all the events in the simulation. The right column shows the distributions for events that triggered the detector.

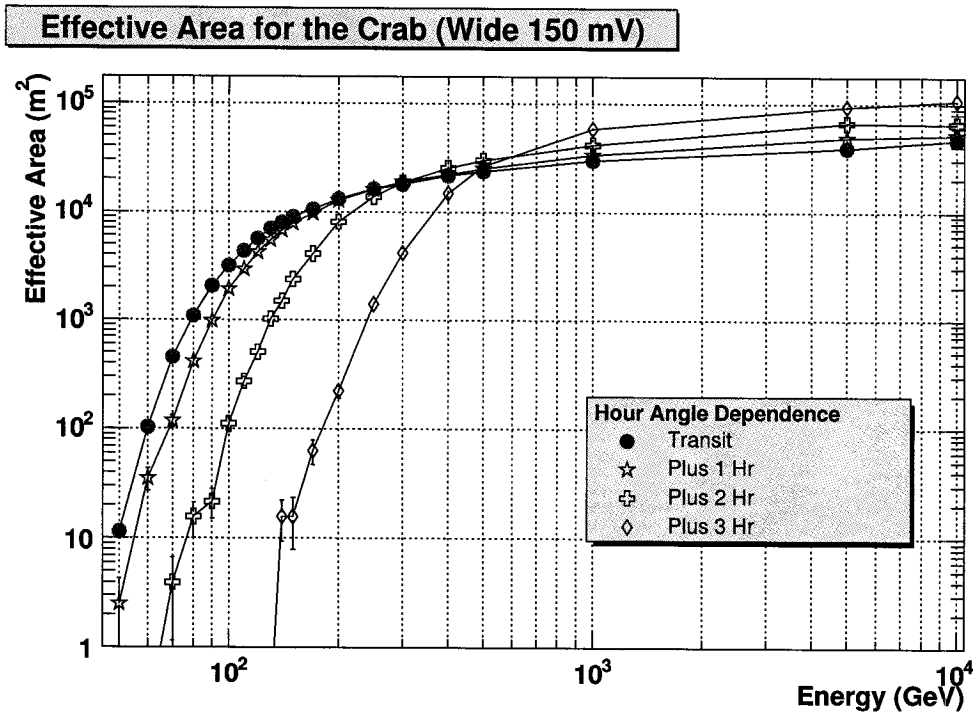


Figure 10.5: Effective area curves of the detector for different positions along the trajectory of the Crab. The configuration of detector for this simulation was: monocanted heliostats, wide mode trigger, 150 mV discriminator threshold. The lines join the points and are meant to guide the eye only.

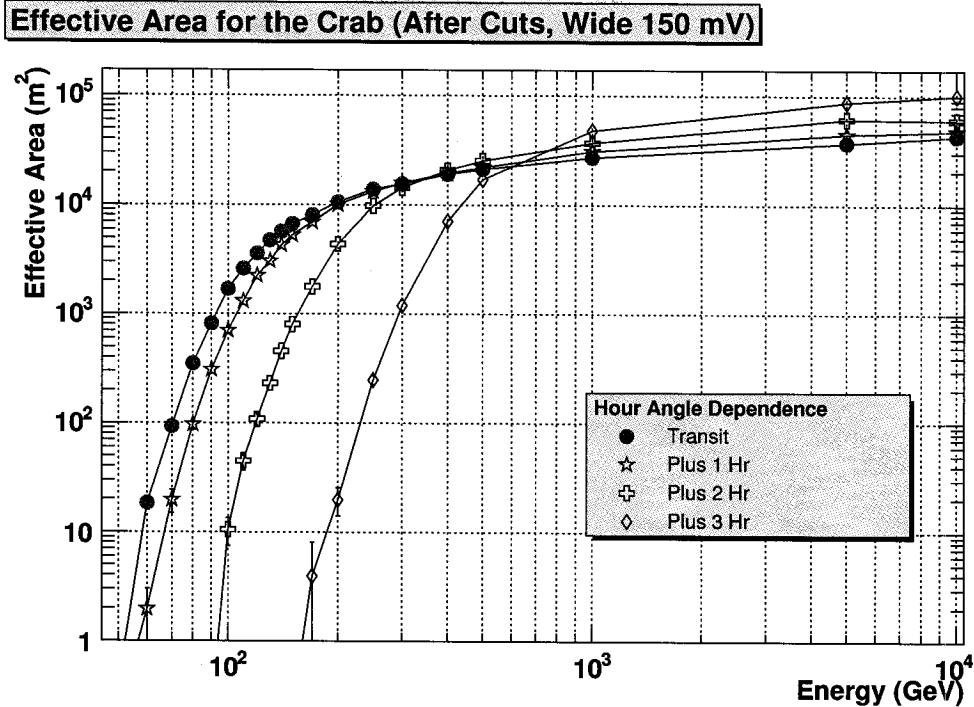


Figure 10.6: Effect of the analysis procedure on the effective areas. The data produced by the simulation was padded to equalize the field brightnesses. The analysis threshold was raised by 10 mV, and a tighter trigger was reimposed.

light pool on the ground, but decrease the density of photons. For low energy  $\gamma$ -rays the density becomes insufficient to trigger the detector. This emphasizes the importance of acquiring as much data as possible when the source is close to transit. Above  $\sim 500$  GeV the opposite effect is seen; the lower the elevation of the source, the larger the effective area. Even though the density of Cherenkov photons is less, it is still above the trigger threshold and the larger light pool compensates for the loss in density; hence the net effect is to increase the effective area.

The effective areas shown in Figure 10.5 correspond to what we would get at the raw trigger level, i.e., the events that get written out to disk by the acquisition system. We expect the effective areas to be different after the data go through the complete analysis chain (see Chapter 7 for more details). Padding the data, raising the analysis threshold, and reimposing a tighter trigger window change the trigger probability  $P(E, HA)$ , especially at low energies. Figure 10.6 shows the effective areas for the same detector configuration after processing the data with the standard analysis programs. The dominant effect is to decrease the effective areas at low energies.

These effective areas are valid for sources with the same declination (same trajectory

on the sky) and field brightness as the Crab. However, the energy threshold and overall sensitivity of the detector depend on the energy spectrum of the source. The definition of the energy threshold for detectors like STACEE is rather arbitrary. Ideally, the effective area of the detector would be a step function

$$A_{\text{eff}}(E) = \begin{cases} 0 & \text{if } E < E_{\text{thr}} \\ A & \text{if } E \geq E_{\text{thr}} \end{cases} \quad (10.3)$$

where the energy threshold would be given by  $E_{\text{thr}}$ . As shown in Figure 10.6, the effective areas do not cutoff sharply and we cannot unambiguously determine the energy threshold. Here we follow the convention used in previous STACEE publications [117, 21, 137]: the energy threshold is defined as the energy at which the differential trigger rate reaches a maximum. The differential trigger rate is obtained by folding the effective area with the source energy spectrum. For the Crab Nebula we use the same spectral index ( $dN/dE \sim E^{-2.4}$ ) that was used for STACEE-32 [117].

Figure 10.7 shows the convolution of the effective area curves with an  $E^{-2.4}$  power law spectrum. When the source is at transit, the peak rate per unit energy occurs at an energy around 140 GeV although there is sensitivity below 100 GeV. The expected trigger rates are obtained by calculating the area under these curves. Not only does the energy threshold increase with hour angle, but the trigger rate drops abruptly. The detector sensitivity below 100 GeV is zero for hour angles greater than one hour.

The overall response of the detector is obtained by weighting the different effective areas by the amount of time spent in each configuration. The result of this weighting procedure is presented in section 12.1 where we calculate the integral flux for the Crab Nebula.

## 10.6 Cosmic ray event trigger rate

Predictions from different parts of the simulation programs can be compared to real data and provide cross-checks to give us confidence in the simulation process. In this section, we compare the predicted cosmic ray event rate with real data. The trigger rate is given by

$$\text{Trig Rate} = \pi R_{\text{scatter}}^2 \Omega P \Phi, \quad (10.4)$$

where  $R$  is the radius used to scatter the core of the EAS in `sandfield`,  $\Omega$  is the solid angle on the sky,  $P$  is the probability to trigger the detector, and  $\Phi$  is the integral flux of cosmic rays above some low energy  $E_0$  (the probability to trigger the detector at  $E_0$  is

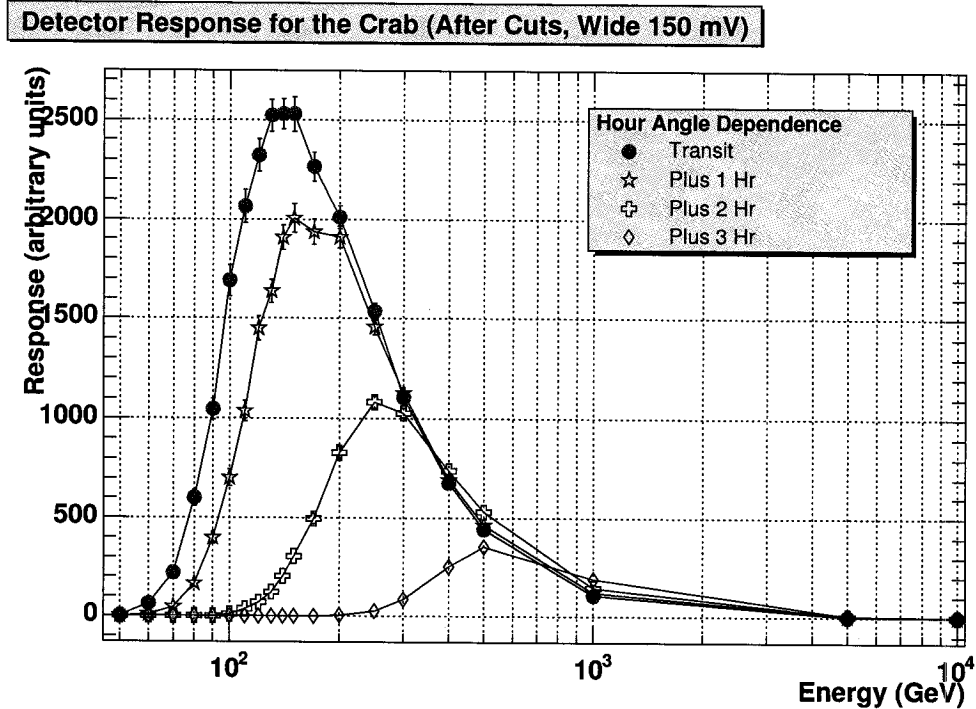


Figure 10.7: Differential  $\gamma$ -ray trigger rate as a function of energy for an  $E^{-2.4}$  power law spectrum.

negligible). Table 10.2 shows the predicted trigger rates and real rates measured during the 2003-2004 season. The agreement between simulations and real data is good, with the predicted trigger rate being slightly lower than the real trigger rate. Given the complexity of STACEE, this result gives confidence in the simulation chain.

## 10.7 Optical Crab Pulsar simulations

In the energy range covered by STACEE, the Crab Nebula is the strongest steady source of  $\gamma$ -rays. It is the perfect source for calibrating and testing the response of the instrument.

HA	$p$ (Hz)	${}^4\text{He}$ (Hz)	Total (Hz)	Real Rate (Hz)
0	$3.85 \pm 0.05$	$1.81 \pm 0.09$	$5.67 \pm 0.10$	$5.91 \pm 0.09$
+1	$3.9 \pm 0.1$	$1.70 \pm 0.09$	$5.6 \pm 0.1$	$5.73 \pm 0.07$
+2	$3.4 \pm 0.1$	$1.43 \pm 0.07$	$4.8 \pm 0.1$	$5.33 \pm 0.08$

Table 10.2: Predicted trigger rates compared to real data for different source positions. The real rates were calculated by grouping all the data from the 2003-2004 season in hour angle (HA) bins.

As mentioned in Section 2.3, the Crab Pulsar is visible in every region of the electromagnetic spectrum, from the radio to EGRET energies, but has evaded detection at higher energies. Theoretical models predict  $\gamma$ -ray emission at energies above the EGRET range and one of the scientific motivations of STACEE is to search for pulsed emission from the Crab Pulsar. Contrary to space-based detectors which detect  $\gamma$ -rays via the  $e^+/e^-$  pair creation process, atmospheric Cherenkov telescopes like STACEE collect Cherenkov light produced by air showers. The optical system used by STACEE is sensitive to photons with wavelengths between  $\sim 300$  nm and  $\sim 700$  nm. The large collection area of the heliostats can be used to study sources in the optical band. Although the angular resolution of the detector is poor, the timing resolution is excellent, which means that the detector can be used to study variable sources. The Crab Pulsar is the perfect candidate for such studies. Not only is the Crab Pulsar bright in the optical, but we can collect optical and Cherenkov data at the same time. Detecting the Crab Pulsar in the optical using the same GPS timestamps as Cherenkov events would confirm that the timing and barycentering procedure used by STACEE is working as expected. This would also give credence to our upper limit if we are unsuccessful in detecting a pulsed  $\gamma$ -ray signal. A description of the special hardware used for this test was presented in Section 5.4; here we present results from the simulation of the optics and electronics.

### 10.7.1 Optical photons from the Crab Pulsar

The first step of the simulation process is to create a source of photons with the same characteristics as real photons from the Crab Pulsar; it must be a point source with the same energy spectrum, timing properties (pulse profile), frequency (approximately 30 Hertz), and flux. The energy spectrum of the Crab Pulsar was measured by several groups in the optical and UV bands [122,109,65,139,29,62,51]. We used the spectrum presented in [139] because it covers both the UV and optical (see Figure 10.8). The UV data was obtained with the Space Telescope Imaging Spectrograph on board the Hubble Space Telescope and the optical data are from the Nordic Optical Telescope. The lower spectrum in figure 10.8 corresponds to what is seen from the ground — except for the UV part — and this is what we used for the simulation of the source. The pulse profile was measured with the High Speed Photometer on board the Hubble Space Telescope between 400 and 700 nm [122]. Figure 10.9 shows the pulse profile used for our simulation. Using the energy spectrum and pulse profile we generated photons having the same characteristics as the Crab Pulsar for a number of points along the trajectory of the Crab.

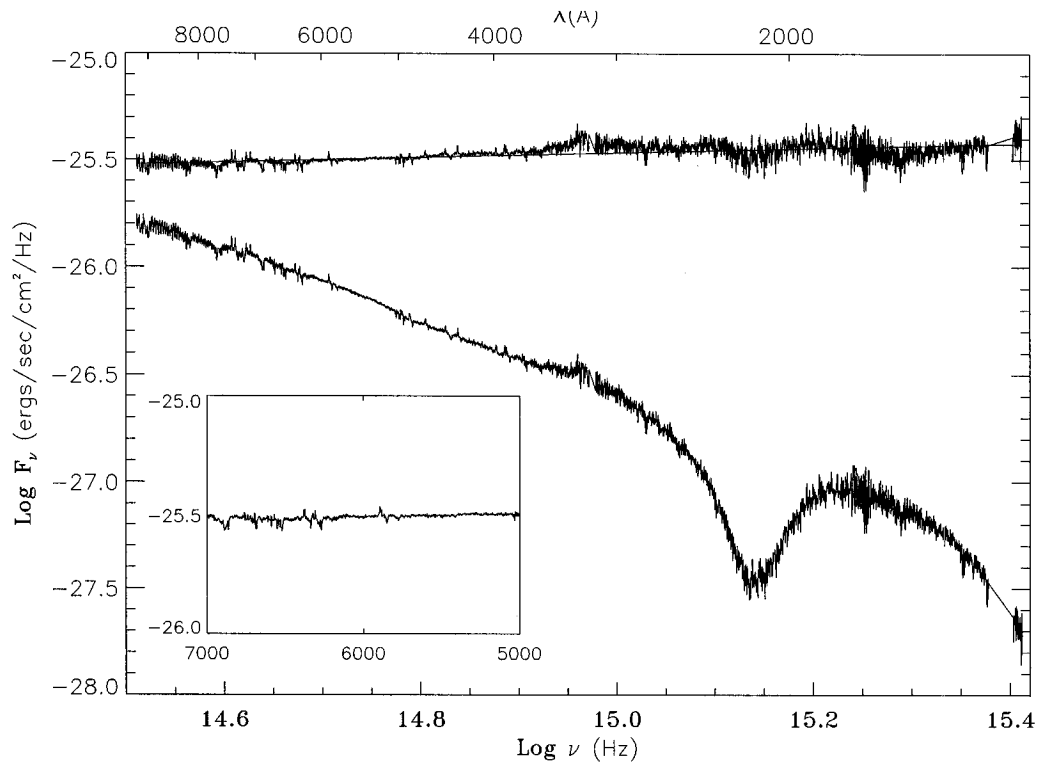


Figure 10.8: Spectrum of the Crab Pulsar in the UV and optical. The lower spectrum shows the flux-calibrated spectrum without dereddening. Starlight passing through intervening dust clouds becomes reddened as the blue light is removed. The interstellar reddening causes stars to appear redder than their effective temperatures would otherwise imply. Fortunately, it is possible to detect this change and correct for it (upper curve) [30]. The insert shows a blowup of the dereddened spectrum from 5000 to 7000 Å. Figure taken from [139].

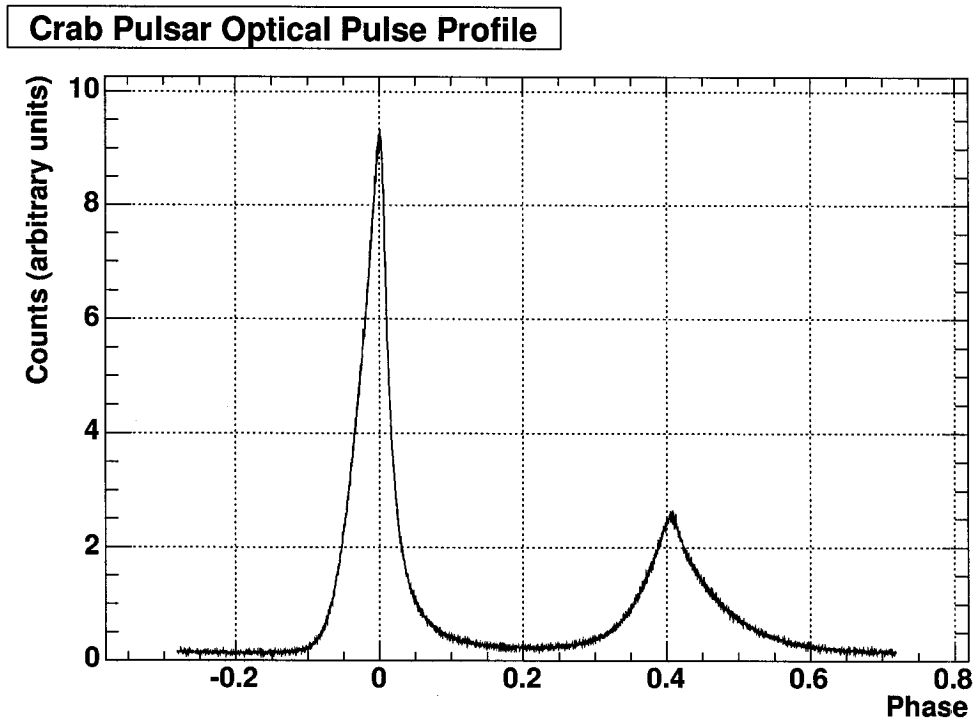


Figure 10.9: Pulse profile of the Crab Pulsar in the optical band (400–700 nm). The measurement was made using the High Speed Photometer on board the Hubble Space Telescope [122].

### 10.7.2 Optical response

In this section we study the throughput of the optical system. The procedure is very similar to the procedure used for EAS. The optical simulation package `sandfield` is used to generate the photons and propagate them through the optical system. When used in this mode, `sandfield` simulates only individual heliostats and uses a much smaller scattering radius (10 meters). We want to calculate the effective areas of the 3 heliostats (channels 64–65–66) used to collect data as a function of the source hour angle ( $HA$ ). The effective area is defined as

$$A_{\text{eff}}(HA) = \pi R_{\text{scatter}}^2 P(HA), \quad (10.5)$$

where  $R_{\text{scatter}}$  is the scattering radius and  $P(HA)$  is the probability for a photon to produce a photoelectron at the photocathode of the PMT. Figure 10.10 shows the results for a simulation of a point source of photons located at the Crab transit point ( $Az = 180^\circ$ ,  $El = 77.1^\circ$ ). The upper left plot shows the spectrum of simulated photons (grey histogram), and the distribution of photons that produced photoelectrons (red histogram). The ratio of the number of entries in the red histogram to the number of entries in the grey histogram gives the probability  $P(HA)$ . The lower left plot shows the distribution of photons in the plane of the secondary mirror. The red circle represents the size of the secondary mirror. The “void” in the lower left corner of the plot results from occultation by the camera box. The lower right plot shows the distribution of photons in the plane of the DTIRC front face. The red circle represents the size of the DTIRC aperture. Figure 10.11 shows the effective areas of the three heliostats as a function of the source hour angle.

### 10.7.3 Electronics response

Using the effective areas calculated in the previous section and the optical flux of the Crab Pulsar we can calculate the signals produced at the base of the PMTs. Before being recorded by the DAQ, these signals go through different filters used to remove undesirable frequencies. Figure 5.5 shows a diagram of the circuit used to process the signals. We used GNUCAP [40] to simulate the response of the circuit (see Appendix D for code) which is shown in Figure 10.12. The upper left plot confirms that the circuit is a bandpass filter; low frequencies below  $10^{-2}$  Hz and high frequencies above  $10^3$  Hz are cut out. The lower plots show the *real* and *imaginary* Fourier coefficients. We can calculate the effect of the filters by convolving the impulse response of the filters with the pulse profile. When working in frequency-space, we simply multiply the FFT of the pulse profile with

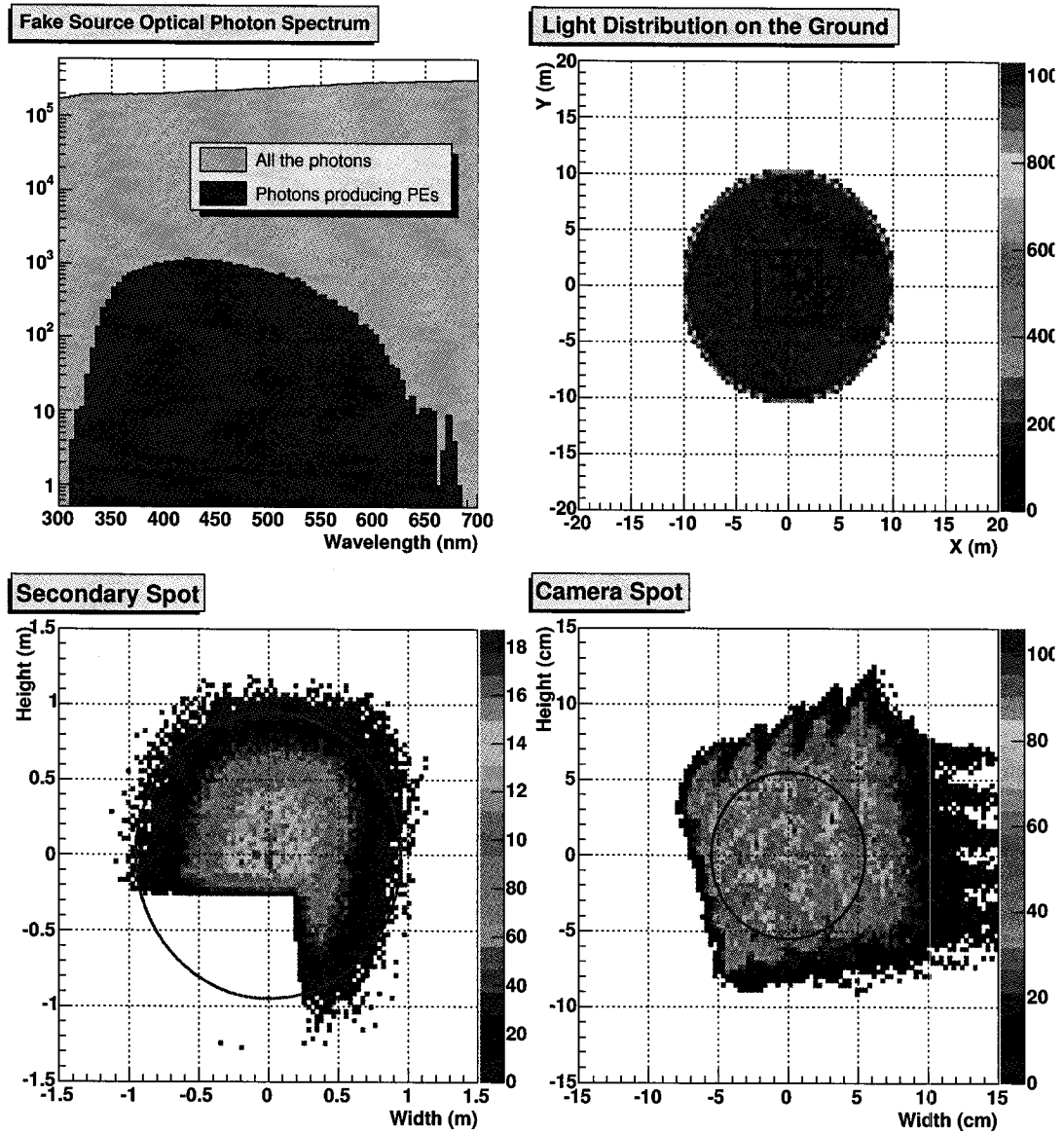


Figure 10.10: Results from the simulation of the optical system for channel 66 (8W3). The source of photons was located at the Crab transit point ( $Az = 180^\circ$ ,  $El = 77.1^\circ$ ). The upper left plot shows the spectrum of simulated photons (grey histogram), and the distribution of photons that produced photoelectrons (red histogram). The ratio of the number of entries in the red histogram to the number of entries in the grey histogram gives the probability  $P(HA)$ . The upper right plot shows the distribution of light on the ground (only photons falling within 10 m have been retained). The square at the center represents the approximate size of a heliostat. The lower left plot shows the distribution of photons in the plane of the secondary mirror. The red circle represents the size of the secondary mirror. Photons falling outside this circle are lost. The void in the lower left corner of the plot results from occultation by the camera box. The lower right plot shows the distribution of photons in the plane of the DTIRC front face. The red circle represents the size of the DTIRC aperture.

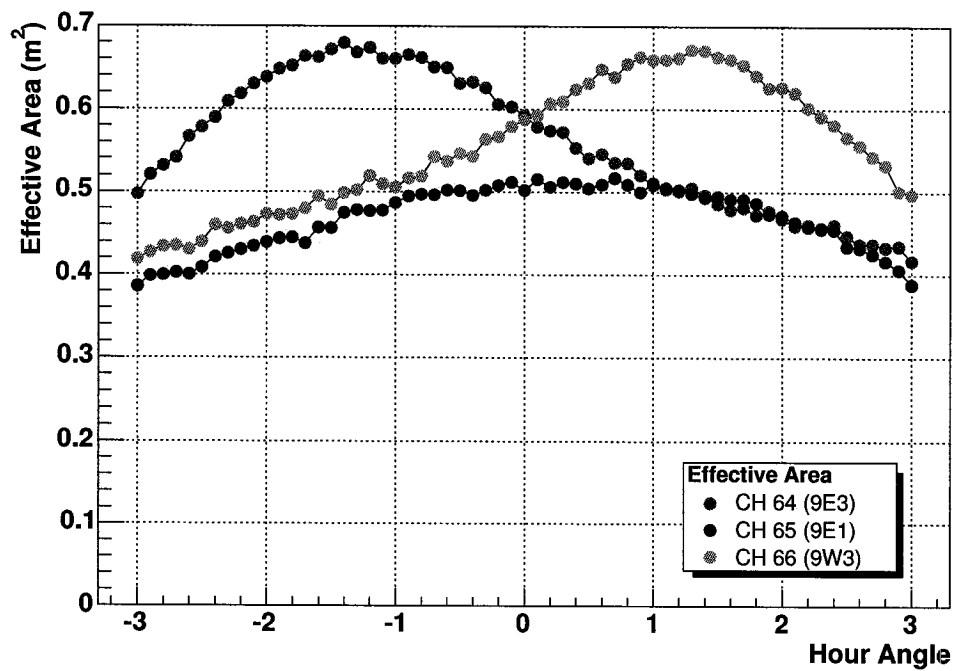


Figure 10.11: Effective areas of the 3 channels used for the optical pulsar search as a function of the source hour angle.

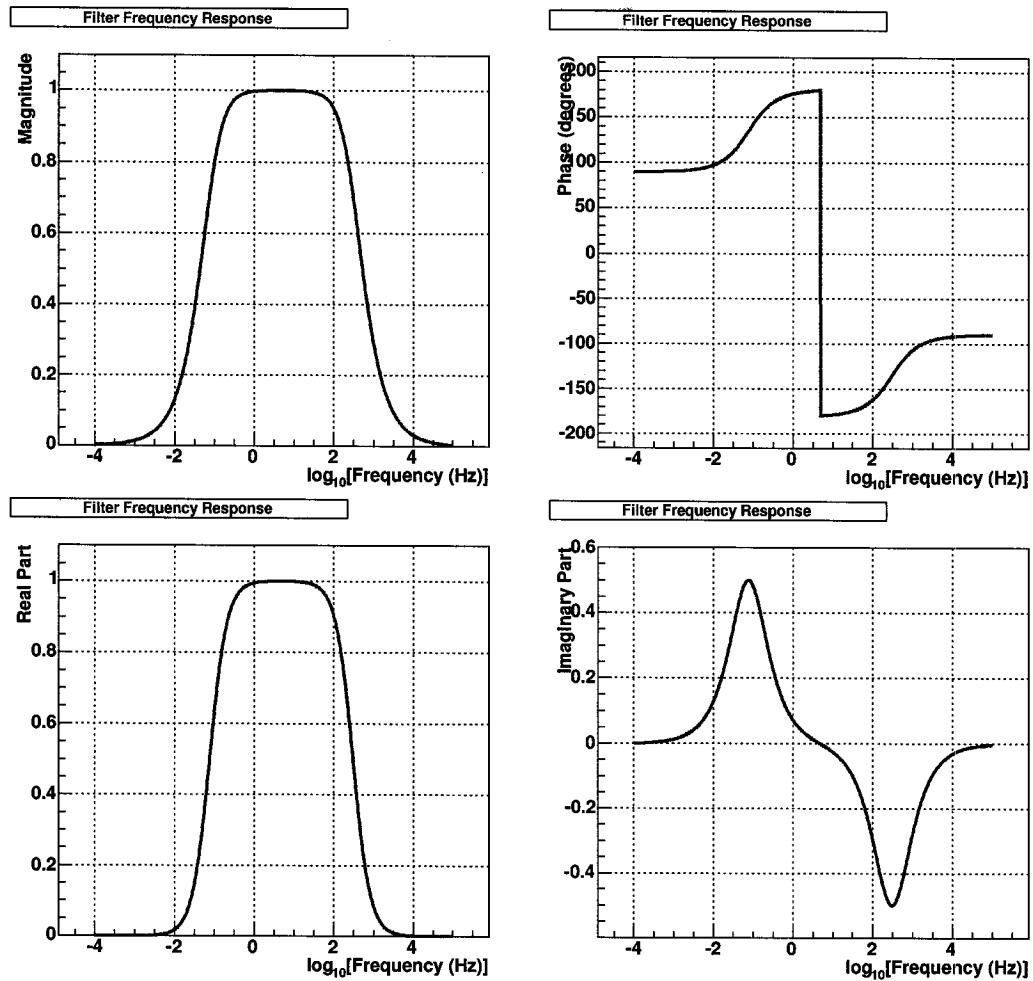


Figure 10.12: Frequency-domain response of the filter circuit. The upper plots show the *magnitude* and *phase* components. The lower plots show the *real* and *imaginary* components.

the Fourier coefficients of the filters. We then calculate the inverse FFT to get the filtered pulse profile in the time-domain. Figure 10.13 shows some characteristics of the expected pulse profile before and after the filters<sup>1</sup>. The left plot shows the power spectrum of the pulse profile. As expected, the fundamental harmonic of the pulse profile is  $\sim 30$  Hz. The right plot shows the pulse profiles for two complete periods. The filtered signal is AC coupled and the phase is slightly shifted ( $\sim 2^\circ$ ). At this stage of the simulation, the signal is background-free; we consider the effects of the night sky background and light pollution on the pulse profile in Chapter 11.

<sup>1</sup>We assume that the impedance of the system is the same with or without the filters. This is not the case in reality, but it makes it easier to visualize the effects of the filters on the frequency content and pulse shape.

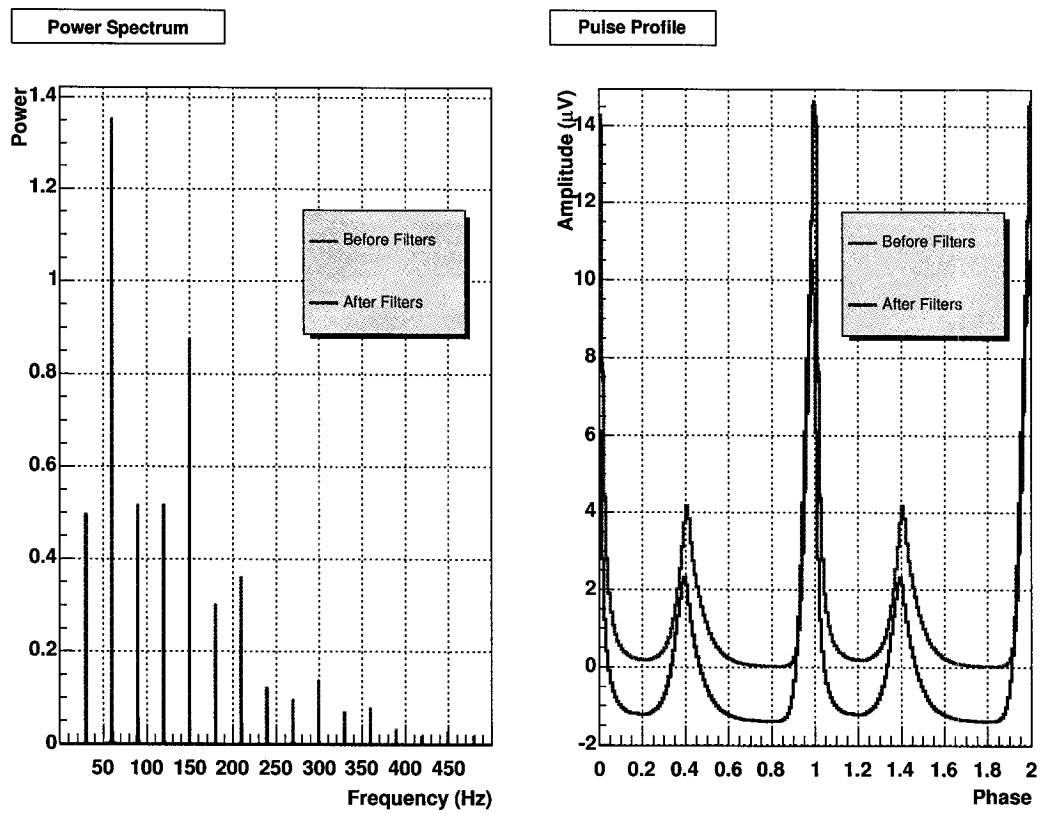


Figure 10.13: Power spectra and pulse profiles before and after the filters.

## **Part III**

### **Data set and analysis**

# Chapter 11

## Optical data set

The electronics and data acquisition system for the optical pulsar were installed at the beginning of December 2002. A total of about 7 hours was obtained on the Crab pulsar between December 9, 2002 and February 22, 2003. A detailed list of the individual data runs is presented in Appendix A.

The large collection area of the heliostats, combined with their large field of view ( $0.6^\circ - 1.0^\circ$ ), is a clear advantage when collecting Cherenkov photons produced by low energy  $\gamma$ -ray showers. For point sources in the optical band, however, the prospects are not nearly as good. The problem lies in the size of the field of view and the lack of any imaging capability. For traditional telescopes equipped with multi-pixel cameras, each pixel sees a unique region of the field of view. The light from a point source can be collected by a single pixel, easily separating the signal of interest from the background surrounding it. Conversely, each element (heliostat-pmt) of STACEE is a single pixel; the photons from the point source *and* from the background cannot be differentiated. This translates into a poor signal-to-noise ratio for optical observations. Using results from the optical simulations presented in Section 10.7 and measured PMT currents, we can estimate the signal-to-noise ratio, which is given by:

$$SNR = \frac{S_{\text{rate}}}{\sqrt{B_{\text{rate}}}}, \quad (11.1)$$

where  $S_{\text{rate}}$  is the rate of photoelectrons produced by the source, and  $B_{\text{rate}}$  is the background rate of photoelectrons. The simulations indicate that we should get on average  $\sim 3800$  photoelectrons per second from the Crab pulsar, while the background current on a typical STACEE channel is  $\sim 30\mu A$ . Given that the PMT gains for the optical channels were decreased by 50% ( $0.5 \times 10^5$  versus  $1.0 \times 10^5$ ), a background current of  $\approx 15\mu A$  is expected, which corresponds to  $1.9 \times 10^9$  photoelectrons per second. This translates into

a signal-to-noise ratio of

$$SNR = \frac{3800}{\sqrt{1.9 \times 10^9}} = 87 \times 10^{-3}. \quad (11.2)$$

The background noise dominates the signal and a deep exposure is required to detect pulsed emission. The significance of a detection (in units of sigmas) as a function of time is given by:

$$Significance = SNR * \sqrt{t}. \quad (11.3)$$

Based on this equation, a 5-sigma detection is expected in  $\approx 1$  hour. This is valid only if the background noise is random, i.e., the background noise is made of transient disturbances with a statistically random time distribution.

## 11.1 Properties of the background noise

The noise present in the data is made of two components: electronic noise, and noise inherent to the signal that's being measured — photons from the night sky background and local sources of light pollution. The electronic noise should be dominated by AC pickup from the power lines at 60 Hz (and higher harmonics). These frequencies could be harmful since the harmonics of the Crab pulsar are close to the AC harmonics; hence, the electronic noise could interfere directly with the pulsed signal from the Crab pulsar. Figure 11.1 shows a sample trace of the electronic noise (the PMT was covered to prevent noise from the night sky background) with its frequency content. The trace is  $\sim 200$  ms long with a peak-to-peak amplitude of  $\sim 300\mu V$ . The power spectrum shows a strong peak around 60 Hz and higher harmonics. The effect of the electronic noise on the pulse profile can be investigated by folding the trace at the Crab pulsar frequency. Figure 11.2 shows the resulting pulse profile for 28 minutes of integration time ( $2^{24}$  samples). Given that the Crab pulsar frequency is  $\sim 30$  Hz, it is not surprising to see that the 60 Hz AC pickup does not completely cancel out. After folding, the peak-to-peak amplitude is reduced to  $\sim 0.4\mu V$ , which is much smaller than the amplitude of the expected signal from the Crab Pulsar ( $\approx 10\mu V$ ). This result indicates that electronic noise is not an obstacle to the detection of optical pulsations from the Crab Pulsar.

Photons from the night sky background and local sources of light pollution constitute the dominant sources of background noise. Assuming that the background noise is well-behaved, i.e., the average intensity is constant in time, we can estimate the amplitude of the fluctuations. Using the numbers presented in the previous section, we get  $\sim 2 \times 10^5$  photoelectron pulses per sample (for a sampling rate of 10 kHz), which corresponds to

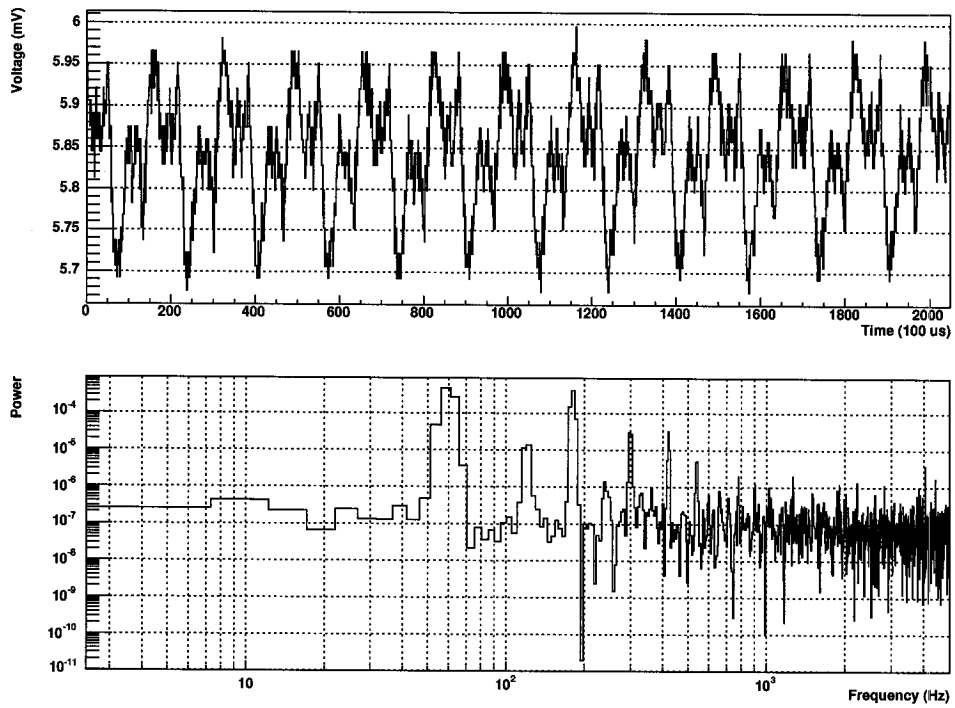


Figure 11.1: Sample trace of electronic noise with its frequency content. The trace is  $\sim 200$  ms long with a sampling rate of 10 kHz.

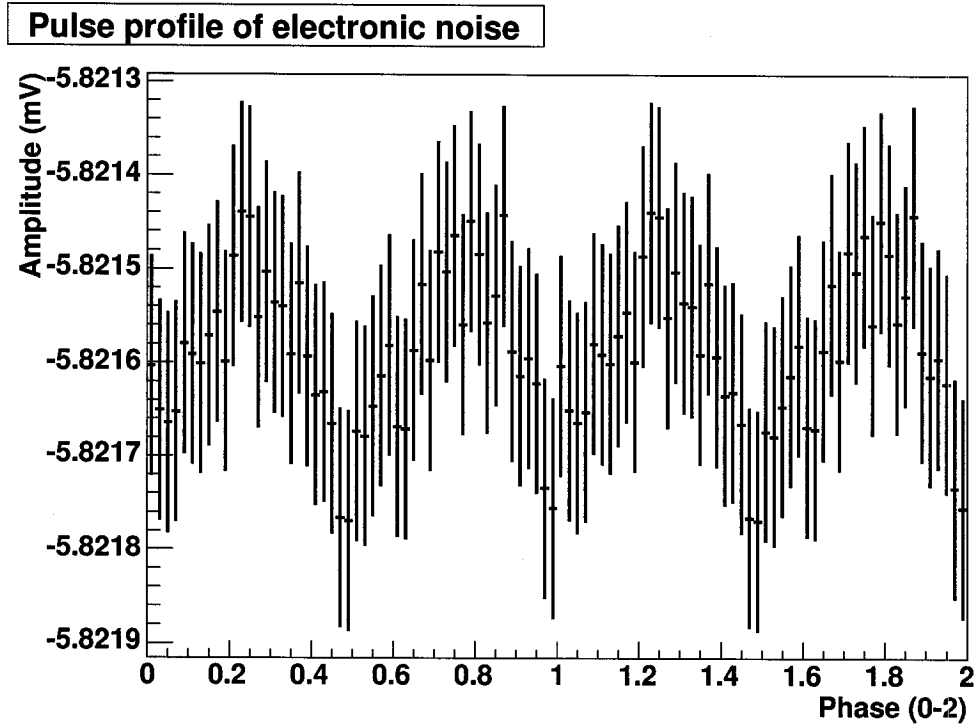


Figure 11.2: Pulse profile of electronic noise after folding 28 minutes of data using the Crab Pulsar frequency.

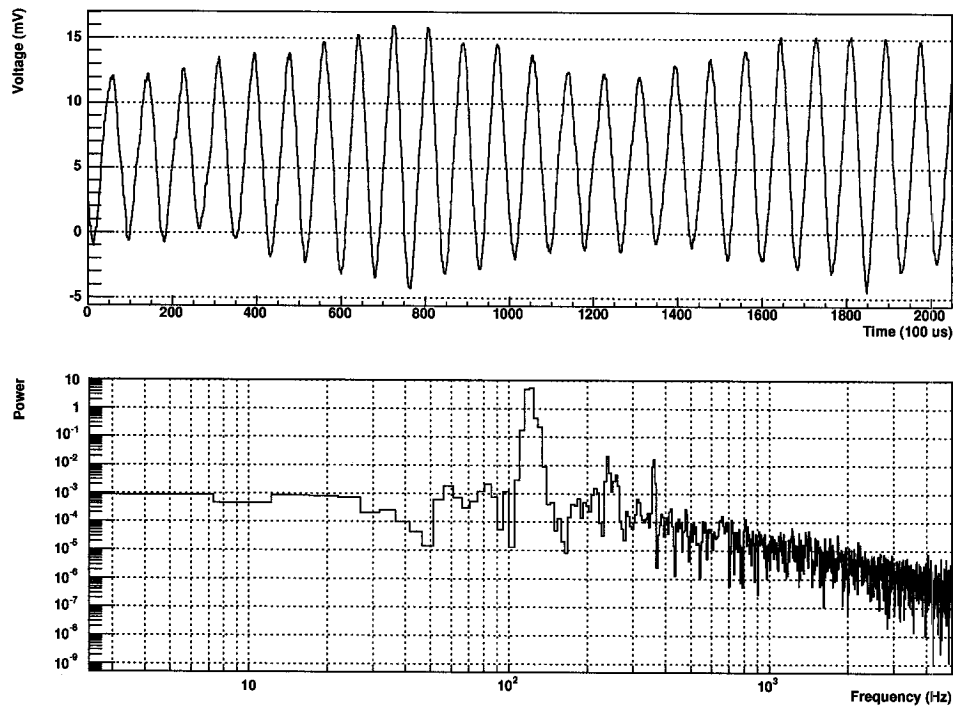


Figure 11.3: Sample trace and frequency content of the background noise when the PMTs are exposed to the night sky.

fluctuations of  $\pm \sim 450$  photoelectron pulses. Converting this number to a current and multiplying by the effective impedance of the circuit ( $\sim 50000$  Ohms) gives an amplitude of  $\approx 2$  mV. Figure 11.3 shows a sample trace of the background noise when the PMTs are exposed to the night sky. The modulated sinusoidal signal is very different from the random fluctuations that were expected. The main peak in the power spectrum indicates that the frequency of the signal is 120 Hz, which corresponds to the frequency of optical emission from gas lamps. It is regrettable that these lamps have now become ubiquitous around the STACEE site. The peak-to-peak amplitude of the wave is approximately 10 times larger than the amplitude of the expected fluctuations, and 100 times larger than the amplitude of the electronic noise. Figure 11.4 shows the pulse profile of the background noise after folding 28 minutes of data at the Crab pulsar frequency. The peak-to-peak amplitude of the pulse profile is  $\sim 25\mu V$ , which is very large compared to the expected signal from the Crab Pulsar. There are two ways to minimize the effect of the background noise on the pulse profile: fold the data for a longer period of time, or use a digital notch-filter to remove the noise at 120 Hz.

We devised a simple simulation to investigate the first option. A sinusoidal signal at 120 Hz was folded at the Crab pulsar frequency and the amplitude of the pulse profile was

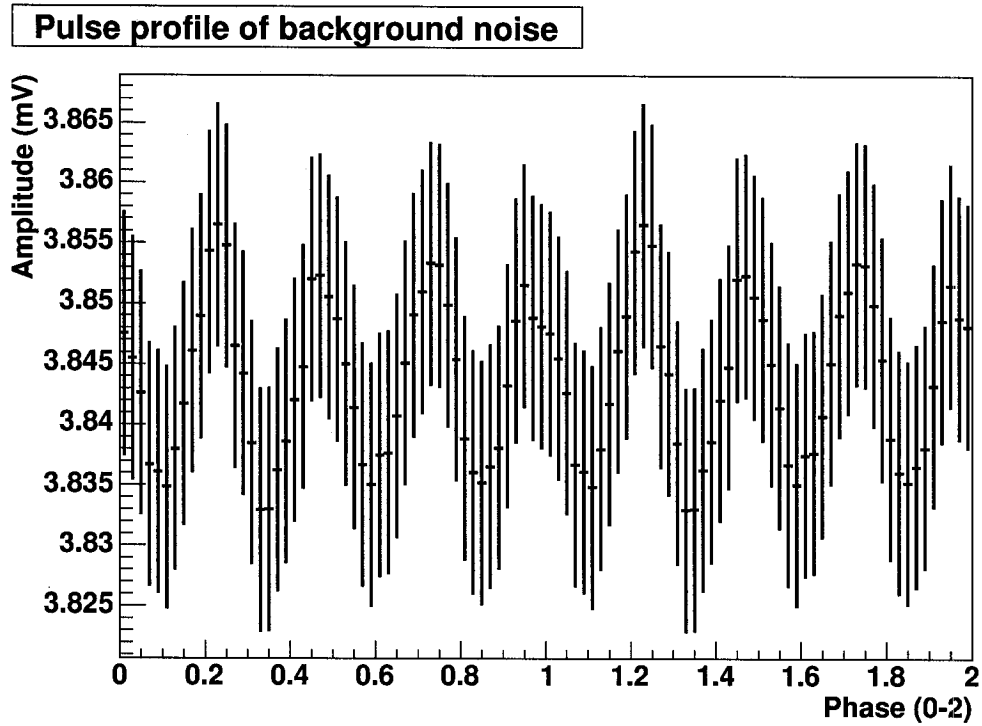


Figure 11.4: Pulse profile of background noise (including electronic noise) after folding 28 minutes of data using the Crab Pulsar frequency. The peak-to-peak amplitude is  $\sim 25\mu V$ .

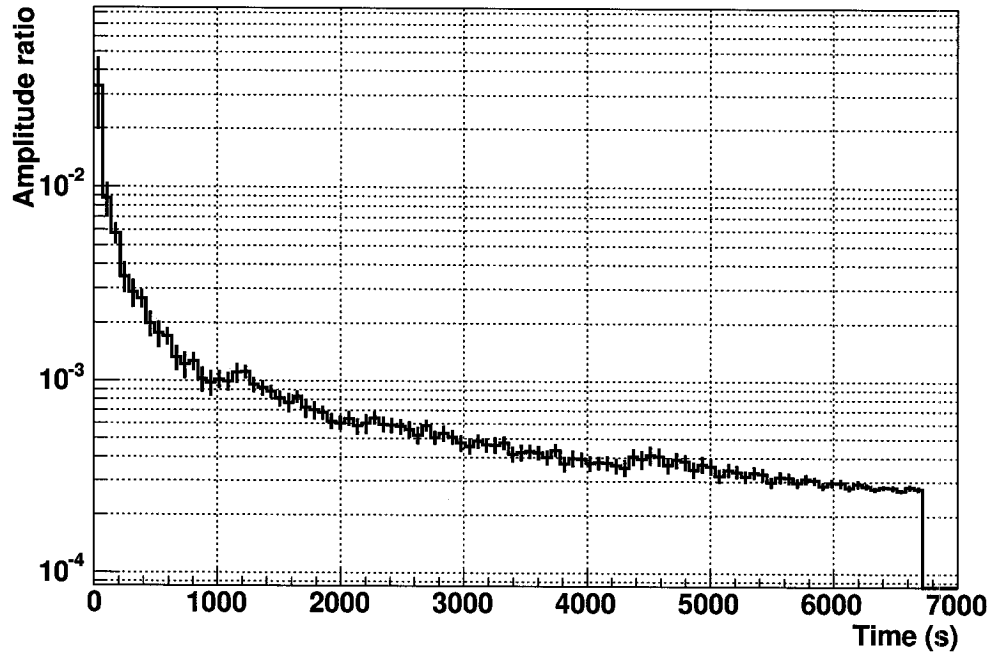


Figure 11.5: Amplitude of the folded pulse profile divided by the amplitude of the original sinusoidal signal as a function of time. The sinusoidal signal had a frequency of 120 Hz and was folded at the Crab pulsar frequency.

measured as a function of time. Figure 11.5 shows the ratio of the amplitude of the pulse profile to the initial amplitude as a function of total integration time. At first, the ratio drops rapidly before reaching a pseudo-asymptotic value. It appears that it would take many hours (probably close to 10 hours) to reduce the amplitude of the pulse profile by a factor of  $10^4$ , which is the required value to reduce the amplitude of the background noise from  $20\text{ mV}$  to  $2\text{ }\mu\text{V}$ . This simulation is a best case scenario and it would probably take longer with real data. For this reason we decided to use digital signal processing (DSP) to remove the background noise at 120 Hz.

## 11.2 Digital filtering

Digital signal processing is a rich subject with applications in a multitude of disciplines. The concepts and theory of DSP are covered in many textbooks (see for example the books from Oppenheim [116], Lyons [102], or Lynn [101]) and we invite the reader to consult one of these books to get accustomed with the techniques presented in this thesis.

A digital filter designed to remove a specific frequency from a signal is called a *notch-*

*filter*. There are different ways to design and implement such a filter; we decided to use the z-transform to create an infinite impulse response filter (IIR). The output of a IIR filter not only depends on past input values, but it also depends on past output values. We opted for a simple design with pairs of complex conjugate zeros and poles. The filter's  $H(z)$  transfer function is given by:

$$H(z) = \frac{[z - e^{j\theta}][z - e^{-j\theta}]}{[z - re^{j\theta}][z - re^{-j\theta}]}, \quad (11.4)$$

where  $\theta$  is the frequency (in radians) to be rejected, and  $r$  is the radius of the z-plane pole used to set the width (-3 dB) of the notch. The filter's frequency response is given by:

$$H(w) = \frac{[\cos(2w) - 2\cos(\theta)\cos(w) + 1] + j[\sin(2w) - 2\cos(\theta)\sin(w)]}{[\cos(2w) - 2r\cos(\theta)\cos(w) + r^2] + j[\sin(2w) - 2r\cos(\theta)\sin(w)]}. \quad (11.5)$$

Figure 11.6 shows the filter's response for a sampling rate of 10 kHz with a 5 Hz rejection band centered at 120 Hz. The gain of the filter is unity for all frequencies, except at 120 Hz, where the signal is completely suppressed. The recursive formula for this type of filter is given by:

$$y[n] = 2rAy[n-1] - r^2y[n-2] + x[n] - 2Ax[n-1] + x[n-2], \quad (11.6)$$

where  $x$  and  $y$  correspond to the input and output values of the filter, and  $A$  is the cosine of the frequency to be cut. This filter is easy to implement in the time domain and is relatively fast.

### 11.3 Predicted pulse profile

In Section 10.7 we calculated the expected pulse profile for the Crab Pulsar in a noise-free environment. It is instructive to study the effect of the notch-filter on the pulse profile before adding background noise. Given that the fourth harmonic of the Crab pulsar is almost exactly 120 Hz, we can expect the pulse profile to be significantly affected by removing this frequency. Figure 11.7 shows the pulse profiles before and after filtering the signal with a notch-filter at 120 Hz. Indeed, the pulse profile looks quite different after removing the fourth harmonic; the main pulse and interpulse are not as sharp, and ripples of significant amplitude cover the entire period of the pulse profile.

Instead of parameterizing the complex background noise present in the data, we decided to use real data as a source of background noise for the simulation. Some of the

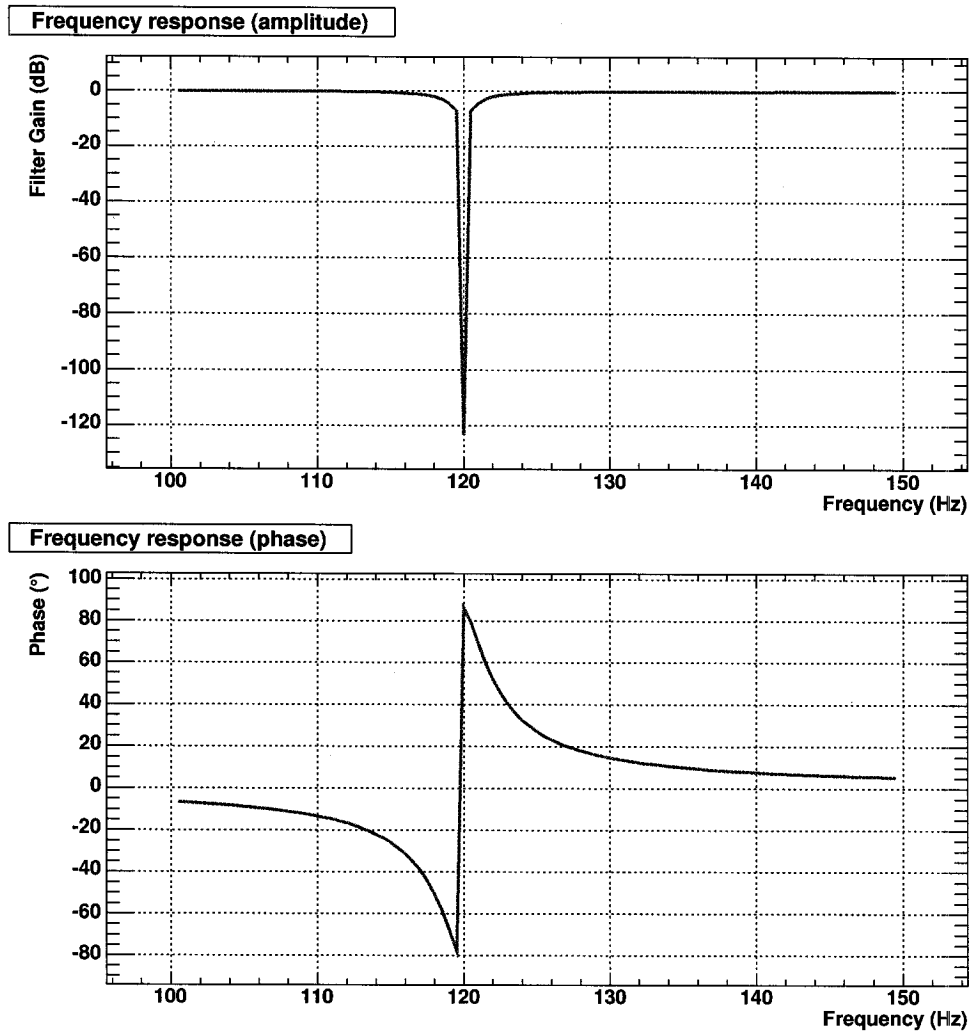


Figure 11.6: Frequency response of the notch-filter used to remove the background noise at 120 Hz.

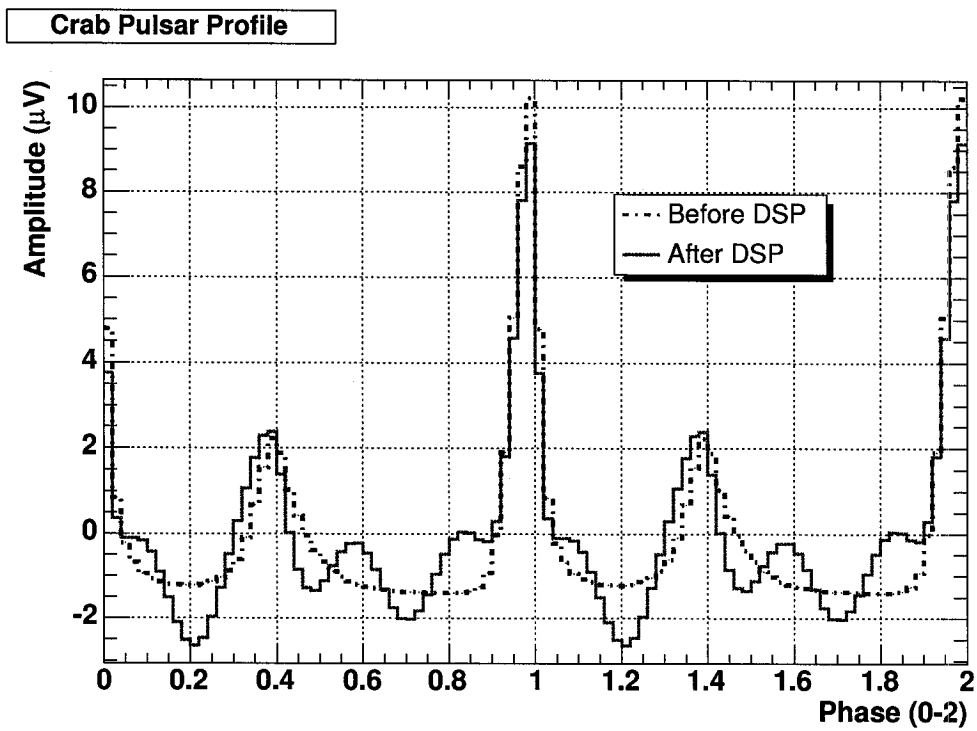


Figure 11.7: Predicted pulse profile for the Crab pulsar before (dash-dot) and after (solid line) filtering the signal (no background noise) with a notch-filter at 120 Hz.

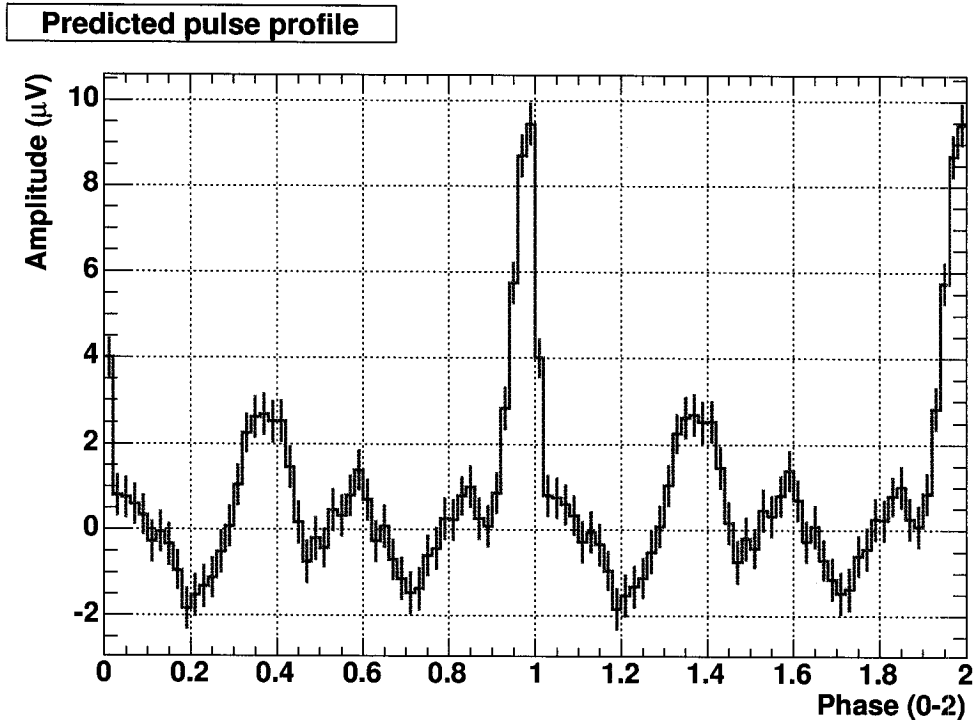


Figure 11.8: Predicted pulse profile after combining the simulated signal with real background noise and filtering the resulting trace with a notch-filter at 120 Hz.

optical data was collected with the heliostats pointing at the Crab OFF field. The field brightness (i.e. PMT currents) for the ON and OFF fields are nearly identical, which makes the OFF field an ideal source of background noise for the simulation. The exposure time of the simulation was comparable to the total livetime of the real data. Figure 11.8 shows the pulse profile after combining the simulated signal with real background noise and filtering the resulting trace using a notch-filter at 120 Hz.

## 11.4 Analysis results

The analysis of the optical data is now relatively simple. First, data corrupted by cloudy sky conditions were removed from the analysis. Only one run was affected by this problem; all the other runs were taken under clear, stable sky conditions. Another run was affected by a bright pulsating light source near the STACEE site and was discarded from the analysis. For reasons which are still not clear, the third channel ceased functioning after a few nights and this channel was excluded from the analysis. The signal traces from the first 2 channels were combined to reduce the statistical errors. After filtering the signal trace with the notch-filter at 120 Hz, each sample of the trace was barycentered and

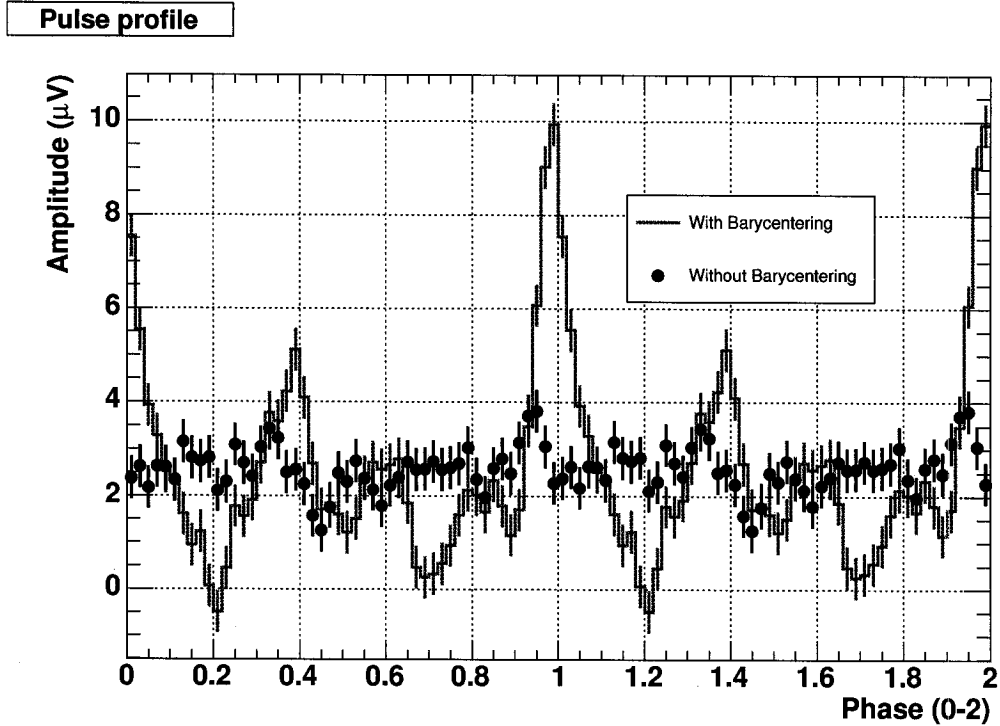


Figure 11.9: Pulse profile of the Crab pulsar in the optical band. The traces of the first 2 channels were combined to reduce the statistical errors. The resulting trace was filtered using a notch-filter at 120 Hz, and each sample was barycentered (solid line) — or not (filled circles) — and folded at the Crab pulsar frequency.

folded at the Crab Pulsar frequency.

Figure 11.9 shows the final pulse profile for the optical data, with and without the barycentering correction. The similarity between the simulated pulse profile and the real pulse profile is remarkably good, both in phase and amplitude, providing strong circumstantial evidence that STACEE detects pulsed emission from the Crab pulsar in the optical band. This result confirms that the GPS clock is accurate and that the barycentering procedure is working. We can now search with confidence for pulsed emission from the Crab pulsar in  $\gamma$ -ray data.

# Chapter 12

## Gamma-ray data set

In the energy range covered by STACEE, the  $\gamma$ -ray emission from the Crab is expected to be dominated by DC emission from the nebula, although pulsed emission from the pulsar might also be detected below 100 GeV. The analysis techniques used for DC and pulsed emission are different and will be described in the following two sections.

### 12.1 Nebula analysis

Because of the low signal-to-noise and angular resolution of wavefront samplers like STACEE, the rate of  $\gamma$ -ray events can only be determined by making observations in ON-OFF pairs. Each observation of the source is immediately preceded or followed by the observation of an OFF field separated in RA by 30 minutes (standard duration of a STACEE *run*), ensuring that the background observation follows the same trajectory in azimuth and elevation as the observation of the source. Both parts of the pair are treated equally and the same analysis procedure is applied to them. The first step of the procedure is to run the data reduction package (PASSO) on the data. This is done automatically as soon as the data is available. Differences in the ON-OFF field brightness are corrected as explained in section 7.2, and a more selective trigger is applied (*trigger reimposition*). The second step is to apply standard quality cuts to the data (see chapter 9). Sections of the data that are affected by detector malfunctions or unstable atmospheric conditions are removed from the analysis.

Here we analyze the data from two consecutive seasons, namely the 2002-2003 and 2003-2004 seasons. We first calculate the excess event rates for each season before combining the results to provide better statistics for the calculation of the integrated flux.

### 12.1.1 2002-2003 season

The final version of the detector (64 channels, each equipped with an FADC channel) was put in place shortly before the 2002-2003 season, just in time for the Crab season. Getting data on the Crab early in the season was critical since we knew we would not be able to observe it during the best part of the season. The planet Saturn was going to pass in front of the Crab during the December and January campaigns. This rare and spectacular event happens only every 30 years. Although the exact time when Saturn would pass in front of the Crab was during the night of January 4-5 2003, its brightness (magnitude of -0.4) was large enough that its presence in our field of view would damage the PMTs. The observing campaign on the Crab was interrupted between December 14, 2002 and January 27, 2003. For STACEE this event was unfortunate, but other scientists had a great opportunity to study Saturn's moon Titan. Using NASA's Chandra X-ray Observatory, astronomers were able to use the X-ray shadow cast by Titan to study the extent of its atmosphere [105].

A total of 49 ON-OFF pairs were taken on the Crab (see Table B.1 for detailed information). Out of these 49 pairs, 12 pairs were manually removed because of unstable L1 rates (see chapter 9), and 3 pairs were affected by frost. This left us with 34 pairs, totalling some 47231 seconds (13.1 hours) of ON-source observing. The heliostats were monocanted and used a canting parameter of  $0.08 \text{ km}^{-1}$ . Halfway through the season the configuration of the trigger system was changed from narrow mode to wide mode; 11 pairs were taken in narrow mode and 23 pairs in wide mode. Our simulation of the instrument response and calculation of the flux from the Crab Nebula take this change into account. The trigger requirement was set to  $\text{LTC/GTC} = 5/5$  for the entire season and the PMT thresholds varied between 140 mV and 170 mV. Table 12.1 shows how much data survived each quality cut. The cuts were applied sequentially. It is unfortunate that 16% of the data was lost to STACQ cuts since this is the only quality cut that we have complete control over. Three pairs were taken with at least one of the Acqiris crates missing (due to a crash), but even after taking these 3 pairs out, the STACQ cut still represents 6%. After the HELIO and L1 cuts we are left with 27903 seconds (7.8 hours) of ON-source data. The quality cuts removed 41% of the data.

After correcting for differences in the ON-OFF field brightness and imposing a more selective trigger, the observed excess of ON-OFF events was +3.22 sigmas, at an excess event rate of  $3.5 \pm 1.1 \text{ min}^{-1}$  (see Table 12.3).

Quality Cut	Time Remaining (seconds)	Fraction Remaining (% of raw)
RAW (No cuts)	47231.10	100
STACQ	39662.21	84
HELIO	31115.52	66
HV	31115.52	66
L1	27903.33	59

Table 12.1: Effect of quality cuts on the livetime of 2002-2003 dataset. The cuts were applied in sequential order. See chapter 9 for more details on each cut.

### 12.1.2 2003-2004 season

The configuration of the detector was changed again prior to the start of the Crab season for 2003-2004. The canting scheme of the heliostats was changed from monocanting to paracanting (see section 4.1) in the expectation of getting better  $\gamma$  / hadron rejection using sophisticated template methods during the offline analysis [136]. Assumptions about the real throughput of the detector are now known to be incorrect and this method cannot be used without introducing some biases in the data. Until we get a better understanding of the channel to channel throughput variations we won't be able to take full advantage of this promising canting scheme. In the paracanting configuration, 16 heliostats have a canting parameter of 0.0, which means that they point at a source at infinity instead of pointing at shower max. This reduces their collection efficiency for Cherenkov light, which not only reduces the effective area of the detector but also increases the energy threshold.

The early part of the season for 2003-2004 was devoted almost exclusively to the BL Lac object 3C66A [26]. The Crab was given second priority and a total of 63 pairs was taken during the season. The weather was notoriously uncooperative; we manually removed 17 unstable pairs and lost 11 pairs to frost. We rejected 3 pairs taken in a different canting configuration. This left us with 32 pairs totalling 46349 seconds (12.9 hours). The configuration of the trigger was LTC/GTC = 5/5 for the entire season and the discriminator threshold was set to 140 mV. Table 12.2 shows the effect of quality cuts on the livetime. STACQ cuts removed 14% of the data, and heliostat malfunctions cost us an additional 24%. As shown in Table 12.3 the observed excess of ON-OFF events was +2.56 sigmas, at an excess event rate of  $2.6 \pm 1.0 \text{ min}^{-1}$ .

Quality Cut	Time Remaining (seconds)	Fraction Remaining (% of raw)
RAW (No cuts)	46349.30	100
STACQ	39727.57	86
HELIO and HV	28614.64	62
L1	26731.77	58

Table 12.2: Effect of quality cuts on the livetime of 2003-2004 dataset. The cuts are applied in sequential order.

Year	$t_{ON}$ (s)	$t_{OFF}$ (s)	$N_{ON}$	$N_{OFF}$	$\sigma$	Rate ( $\text{min}^{-1}$ )
2002-2003	27903.33	27918.90	131596	130023	3.22	$3.5 \pm 1.1$
2003-2004	26731.77	26687.05	106454	105101	2.56	$2.6 \pm 1.0$
Total	54635.09	54605.86	238050	235124	4.07	$3.1 \pm 0.8$

Table 12.3: Results of the Crab analysis after correcting the ON-OFF field brightness and imposing a more selective trigger. For both seasons the integrated livetime for the ON and OFF fields is shown, along with the total number of events which passed the cuts, the significances and event rate in events per minute.

### 12.1.3 Integral Flux Results

In this section we convert the excess event rate to an integral flux measurement at the appropriate energy. The first step of the process is to calculate the overall detector response. We demonstrated in Section 10.5 that the response of the detector depends on a large number of factors. Each pair was taken under different conditions: different source position, different heliostat and trigger configurations. In principle we should extract a set of parameter values for the simulation chain and carefully model each pair before combining the simulation results to get the overall detector response. However, we don't have enough statistics in a given pair to get good estimates for the parameter values. Instead, we group pairs taken under similar conditions. We did complete sets of simulations (CORSIKA - sandfield- ELEC - PASS0) for each group and combined the results by weighing each group by the amount of data acquired in that configuration.

Figure 12.1 shows the overall response of the detector for  $\gamma$ -rays. The upper plot shows the effective area of the detector as a function of  $\gamma$ -ray energy. The red dots correspond to the detector response at the trigger level, i.e., before correcting the ON-OFF field brightness and imposing a more selective trigger. The blue squares correspond to the detector response after processing the data with the offline analysis software. This is the effective area curve that we use for the calculation of the integrated flux. The lower plot shows the differential trigger rate for  $\gamma$ -rays for a simulated Crab spectrum ( $\alpha = -2.4$ ).

The energy threshold of the detector (energy where the differential trigger rate is maximal) at the trigger level was 150 GeV and 185 GeV after processing the data offline.

The integral flux is defined as the total  $\gamma$ -ray flux above the energy threshold  $E_{thr}$  of the detector and can be derived from the differential flux by

$$I(E > E_{thr}) = \int_{E_{thr}}^{\infty} dE \frac{dN}{dE}. \quad (12.1)$$

As mentioned in Section 10.5 the differential flux is assumed to be a power law spectrum of the form

$$\frac{dN}{dE} = C \left( \frac{E}{100 \text{ GeV}} \right)^{-2.4} \text{ photons cm}^{-2} \text{ s}^{-1} \text{ GeV}^{-1}, \quad (12.2)$$

where  $C$  is a normalization constant that we want to calculate. This can be accomplished by using the total trigger rate of the detector for  $\gamma$ -rays, which is given by

$$R_{\gamma} = \int_0^{\infty} dE \frac{dN}{dE} A(E). \quad (12.3)$$

Substituting Equation 12.2 for  $dN/dE$  and using the effective area curve shown in Figure 12.1 gives us:

$$R_{\gamma} = \int_0^{\infty} dE C E^{-2.4} A(E) = 6.29 \times 10^9 C. \quad (12.4)$$

As shown in Table 12.3, the average excess event rate was  $0.05 \pm 0.01$  Hz. Using this rate and Equation 12.4 we can solve for  $C$ . The differential flux spectrum becomes

$$\frac{dN}{dE} = (8.1 \pm 2.0) \times 10^{-12} \left( \frac{E}{100 \text{ GeV}} \right)^{-2.4} \text{ photons cm}^{-2} \text{ s}^{-1} \text{ GeV}^{-1}. \quad (12.5)$$

The integral flux is obtained by integrating this differential flux above the energy threshold of 185 GeV. This gives us:

$$I(E > 185 \text{ GeV}) = (2.5 \pm 0.6) \times 10^{-10} \text{ photons cm}^{-2} \text{ s}^{-1}. \quad (12.6)$$

It should be noted that the error here is only statistical. The systematic error is calculated in the next section.

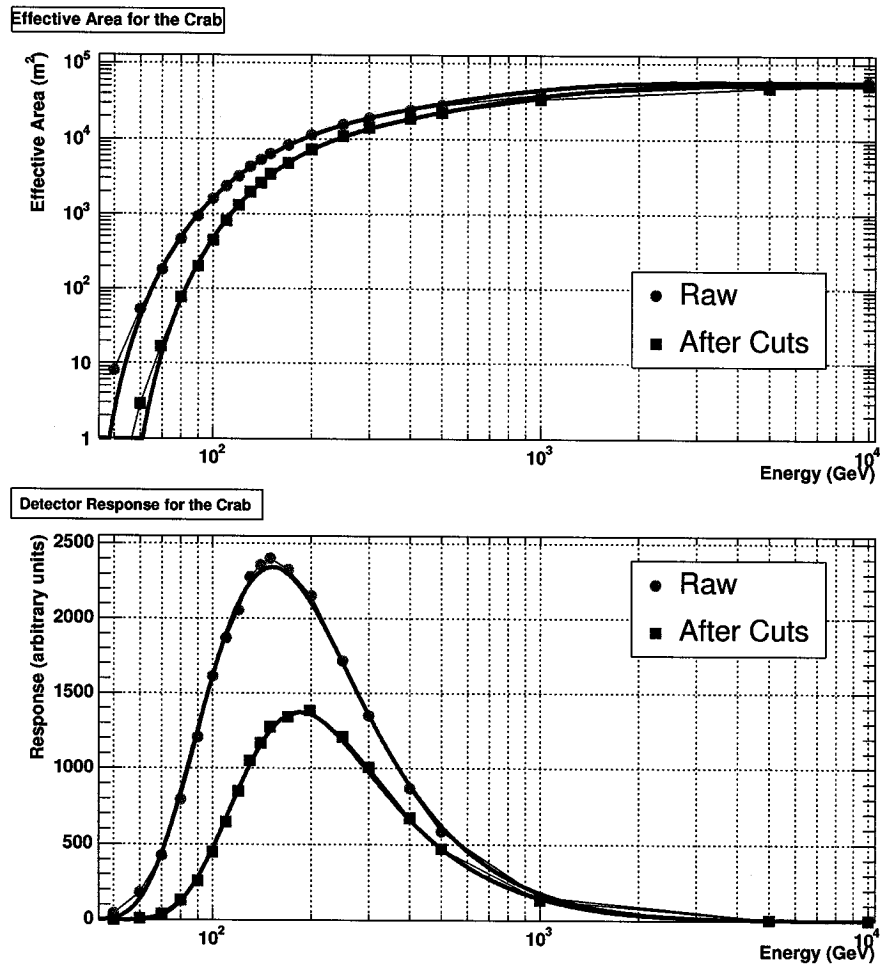


Figure 12.1: Overall detector response for  $\gamma$ -rays. The upper plot shows the effective area of the detector as a function of  $\gamma$ -ray energy. The red dots correspond to the detector response at the trigger level, while the blue squares result from processing the data with the offline analysis software. The lower plot shows the differential trigger rate for  $\gamma$ -rays for a simulated Crab spectrum ( $\alpha = -2.4$ ).

### 12.1.4 Estimating the systematic errors

The error bars on the effective area and detector response curves shown in figure 12.1 include only statistical errors from the air shower simulations. However, a number of systematic errors on the measurements of the detector calibration and characterization (e.g., reflectivity and transmission curves, phototube gains, etc.) also affect the detector throughput, and constitute sources of errors in the energy threshold of the flux measurement.

We showed in chapter 1 that  $\gamma$ -ray showers of different energies are very similar in all their properties (overall timing profile and lateral distribution of Cherenkov light), differing only in the Cherenkov yield on the ground (see also [118, 136]). For example, a 100 GeV shower where one-quarter of the photons are randomly thrown away closely resembles a 75 GeV  $\gamma$ -ray shower.

The calorimetric nature of Cherenkov light for  $\gamma$ -ray showers greatly simplifies the systematic error analysis, as errors in the detector throughput change the effective energy scale of the experiment. Scott Oser demonstrated that the effective area  $A_{eff}(E)$  is related to the nominal effective area via [118]:

$$A_{eff}(E) = A_{nom}(\beta E), \quad (12.7)$$

where  $\beta$  is the ratio of the true throughput of the detector to the nominal throughput. Systematic uncertainties can be combined and expressed in terms of some error on  $\beta$

$$\beta = 1 \pm \Delta\beta, \quad (12.8)$$

where  $\Delta\beta$  is the uncertainty in the throughput. For a source with a power law spectrum (e.g. the Crab Nebula), the differential trigger rate is proportional to  $A(E)E^{-\alpha}$ , which becomes

$$A(E)E^{-\alpha} \longrightarrow A(\beta E)E^{-\alpha}. \quad (12.9)$$

As mentioned previously in section 10.5, the energy threshold ( $E_{thr}$ ) of the experiment is defined as the energy at which the differential trigger rate reaches a maximum. If we define  $E' = \beta E$ , one must maximize

$$A(E')E'^{-\alpha}\beta^\alpha. \quad (12.10)$$

Since  $\beta^\alpha$  is simply a constant, the differential trigger rate is maximized at the original

energy threshold  $E' = E_{thr-org}$ . Since  $E' = \beta E$ , it follows that :

$$E_{thr-new} = \frac{E'}{\beta} = \frac{E_{thr-org}}{\beta} \approx E_{thr-org}(1 \pm \Delta\beta). \quad (12.11)$$

This shows that the fractional uncertainty of the spectral energy threshold is equal to  $\Delta\beta$ . In addition, by replacing  $A(E)$  with  $A(\beta E)$  and  $E_{thr}$  with  $E_{thr}/\beta$  in the calculation of the integrated flux, one can show that  $\beta$  cancels out of the calculation and that

$$I(E > E_{thr-org}) = I(E > E_{thr-new} = E_{thr-org}/\beta). \quad (12.12)$$

Therefore, the integral flux above the energy threshold for a power law spectrum is completely insensitive to the energy calibration. Changing the throughput parameter  $\beta$  does not change the integral flux value, but it does change the value at which that flux is quoted.

The estimation of  $\Delta\beta$  is achieved by combining the various uncertainties in the throughput of the detector and adding them in quadrature, assuming that they are uncorrelated. Here is a description and estimate for each of the relevant sources of error:

1. **Cherenkov production:** The uncertainty in the amount of Cherenkov light produced by  $\gamma$ -ray showers of a given energy is estimated by comparing the results from two different air shower simulation programs. We compared Cherenkov lateral density profiles generated with EGS4 (CORSIKA) and another air shower simulation package (MOCCA [80]) and found that CORSIKA produced approximately 5% more Cherenkov light for  $\gamma$ -ray initiated showers [83]. The estimated error is thus 5%.
2. **Atmospheric attenuation:** As mentioned in section 10.1, seasonal variations in the atmospheric profile affect the Cherenkov yield and we estimate an uncertainty of 10% for STACEE.
3. **Heliostat reflectivity:** Given that the heliostat facets are back-silvered we don't expect long-term changes in their reflectivity. A laboratory measurement of the overall reflectivity was estimated to be accurate to 10% [118].
4. **Secondary reflectivity:** The reflectivity of the secondary mirrors is measured with a reflectometer every month. It differs from mirror to mirror, or even from facet to facet by less than  $\sim 5\%$ .
5. **Quantum efficiency and PMT gains:** According to the specifications from the manufacturer, the channel-to-channel uncertainty on the quantum efficiency is  $\sim 10\%$

Cherenkov production	5%
Atmospheric attenuation	10%
Heliostat reflectivity	10%
Secondary reflectivity	5%
Quantum efficiency and PMT gains	18%
Optical alignment	7%
Total uncertainty ( $\Delta\beta$ )	19%

Table 12.4: Sources of systematic errors in the energy scale.

[118]. Similarly, the systematic error of the different gain measurement procedures (see section 6.1) is  $\sim 15\%$ . Both estimates are conservative. When combined, this gives a systematic error of 18%.

6. **Optical alignment:** This category regroups the systematic errors on the alignment of the heliostats (mis-biasing) and the PMT cans in the camera plane. As mentioned in section 4.1, the regular alignment of the heliostats using drift scans of stars, keeps them within 2 bits of optimal bias. The uncertainty on the heliostat biases introduces an error of 5% on the collection efficiency [136]. Similarly, ray-trace simulations of the alignment of the PMT cans in the camera plane suggest a systematic error of 5% on the collection efficiency. Combining these errors gives an uncertainty of 7%.

Table 12.4 summarizes the systematic errors that go into determining  $\Delta\beta$ . We therefore conclude that the energy threshold for the STACEE observations of the Crab Nebula during the 2002-2003 and 2003-2004 seasons was:

$$E_{thr} = 185(1 \pm \Delta\beta) \approx 185 \pm 35 \text{ GeV}. \quad (12.13)$$

There is one source of systematic error that affects the flux directly: the assumed spectral slope  $\alpha$  of the Crab Nebula's spectrum. Above 300 GeV, the spectral index is near -2.5. Predictions of inverse Compton models indicate that the spectrum should vary from -2 near 60 GeV, to -2.3 or -2.4 at 200 GeV. Previous studies done for STACEE-32 calculated integral fluxes assuming spectral indices in the range -2.2 and -2.6. These studies showed variations in the energy threshold and integral flux of only  $\pm 10$  GeV and 2% respectively [118]. These errors are much smaller than the systematic error on the energy scale and can safely be ignored.

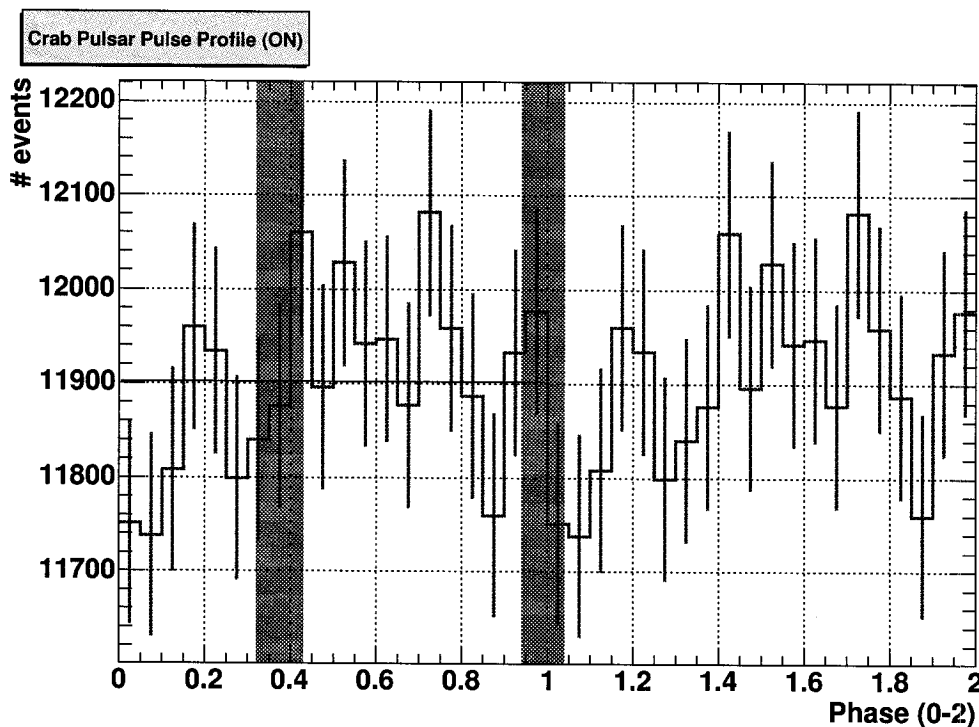


Figure 12.2: Pulse profile for the Crab pulsar. The shaded regions indicate the range of phases where pulsed emission was detected by EGRET. Two periods are shown for clarity.

## 12.2 $\gamma$ -ray pulsar analysis

In this section we search the data for evidence of pulsed emission from the Crab pulsar. We selected events using the same criteria that were used to calculate the integral flux in Section 12.1.3. The barycentering package was used to calculate the phase of the events that passed the time and event cuts (trigger reimposition) and to construct the phasegram (pulse profile). We used the Crab pulsar ephemeris from the Jodrell Bank Crab Pulsar Timing Results Ephemeris [100]. This monthly catalog provides extremely accurate information on the Crab pulsar period, period derivative, and arrival time of the main radio pulse at the barycenter of the solar system. Figure 12.2 shows the resulting pulse profile. The abscissa shows two complete periods of the pulse profile (0-2). The shaded regions indicate the range of phases where pulsed emission was detected by EGRET [49]. The phase intervals of the main peak and interpulse are  $0.94 - 1.04$  and  $0.32 - 0.43$  respectively. The ordinate shows the number of events in each bin with the corresponding error bar. A straight line was fitted to the first period (0 - 1.0) to indicate the average value of the pulse profile.

Some features are present in the phasegram but given the size of the error bars these

features are likely consistent with statistical fluctuations. A statistical test is required to determine if this pulse profile is consistent with a flat distribution. Three tests are used frequently in the literature, the Pearson's  $\chi^2$ -test, the  $Z_m^2$ -test [27], and the H-test [41]. The H-test is independent of binning as it uses the phase of each data point. The H-test was also shown to have a very good power against most light curve shapes encountered in X-ray and  $\gamma$ -ray astronomy. For these reasons we decided to use this test for the analysis of STACEE data. The H statistic is given by:

$$H = \text{maximum}_{1 \leq m \leq 20} (Z_m^2 - 4m + 4) \quad (12.14)$$

where  $Z_m^2$  is given by:

$$Z_m^2 = 2n \sum_{k=1}^m (\hat{\alpha}_k^2 + \hat{\beta}_k^2) \quad (12.15)$$

and

$$\hat{\alpha}_k^2 = \frac{1}{n} \sum_{i=1}^n \cos(2\pi k \phi_i) \quad (12.16)$$

$$\hat{\beta}_k^2 = \frac{1}{n} \sum_{i=1}^n \sin(2\pi k \phi_i) \quad (12.17)$$

for  $n$  points with phases  $\phi_i$  between 0 and 1.

The significance of a detection can be calculated using the probability distribution of H under uniformity which is given by

$$\text{Prob}(H > h) = a e^{-bh}. \quad (12.18)$$

For large  $n$ , which is the case here,  $a \approx 1.0$  and  $b \rightarrow 0.398$ . The H value calculated for the STACEE data is 4.18, which corresponds to a probability of 18.7% (i.e., for uniformly distributed data, we would expect the H value to be 18.7% of the time larger than 4.18). This probability is rather large, which indicates that the features in the pulse profile are consistent with statistical fluctuations. We conclude that the pulse profile is consistent with a uniform distribution in phase.

Having established that we have not detected pulsed emission from the pulsar we can calculate an upper limit on the pulsed fraction of the total observed excess. Although we could set upper limits for any phase of the pulse profile, it makes sense to use the phases where pulsations have been observed by other instruments at other wavelengths. EGRET detected pulsations in two intervals; the first one corresponding to the radio main pulse at phase 0.94-0.04, and the second one corresponding to the radio interpulse at

# of events in ON interval	49889
# of events in OFF interval	188165
Significance for pulsed region	$-0.52 \sigma$
Upper limit (90%)	204 counts above background, $UL = 7.0\%$ DC
Upper limit (99.9%)	480 counts above background, $UL = 16.4\%$ DC

Table 12.5: Results of search for pulsed emission from the Crab pulsar. The upper limits are given as a fraction of the integral flux.

phase 0.32-0.43 [49]. Using the number of events in the ON intervals and the number of events falling outside that range we can calculate an upper limit using the method of Helene (see Appendix C). The resulting upper limit on the pulsed fraction for a confidence level of 99.9% is 16.4% of the total  $\gamma$ -ray excess. This corresponds to an integrated flux  $(0.4 \pm 0.1) \times 10^{-10} \text{ photons cm}^{-2} \text{ s}^{-1}$ . Table 12.5 shows the number of ON and OFF events and the corresponding upper limits for different confidence levels.

# Chapter 13

## Summary of results and conclusions

The first ground-based instrument that detected the Crab Nebula below 200 GeV was the STACEE-32 detector [117]. This earlier version of STACEE used 32 heliostats (versus 64 for the current version), and therefore had a smaller effective area than that of the version presented here. Adding 32 heliostats helped gain sensitivity below 100 GeV and lower the *raw* energy threshold of the detector substantially (150 GeV for the current version versus 190 GeV for STACEE-32). The addition of FADCs was a crucial update that helped us understand and correct for the effect of promotion caused by the presence of bright stars in the field of view of the detector. Here we report an integral flux for the Crab Nebula and an upper limit on pulsed emission from the pulsar at the *effective* energy threshold of the detector; that is, after correcting for differences in the ON-OFF field brightness and imposing a more selective trigger. As shown in section 10.5, the net effect of this procedure is to increase the energy threshold of the detector by  $\sim 35$  GeV. Table 13.1 summarizes the results, and figure 13.1 shows the STACEE integral flux result which is consistent with the previous result obtained by STACEE-32 and with a continuation of the power law spectrum seen at higher energies. The upper limit on pulsed emission is also consistent with the limit calculated by STACEE-32, but unfortunately, neither the polar cap model, nor the outer gap model is excluded by this new upper limit. Even though pulsed emission from the Crab pulsar in the optical band has been detected by countless experiments, its detection by STACEE is an important result that demonstrates the accuracy of our barycentering and epoch folding analysis tools. Moreover, it shows that the timestamping procedure is correct and that we have a good understanding of the optical throughput of the detector.

Total significance of detection	+4.07 $\sigma$
Energy threshold ( $E_{thr}$ )	185 $\pm$ 35 GeV
Integral flux above $E_{thr}$ ( $photons\ cm^{-2}\ s^{-1}$ )	$(2.5 \pm 0.6) \times 10^{-10}$
Pulsed fraction upper limit (90%)	7.0% DC
Pulsed fraction upper limit (99.9%)	16.4% DC
Pulsar flux limit (99.9%) ( $photons\ cm^{-2}\ s^{-1}$ )	$< (0.4 \pm 0.1) \times 10^{-10}$

Table 13.1: Summary of STACEE results for the Crab Nebula and pulsar.

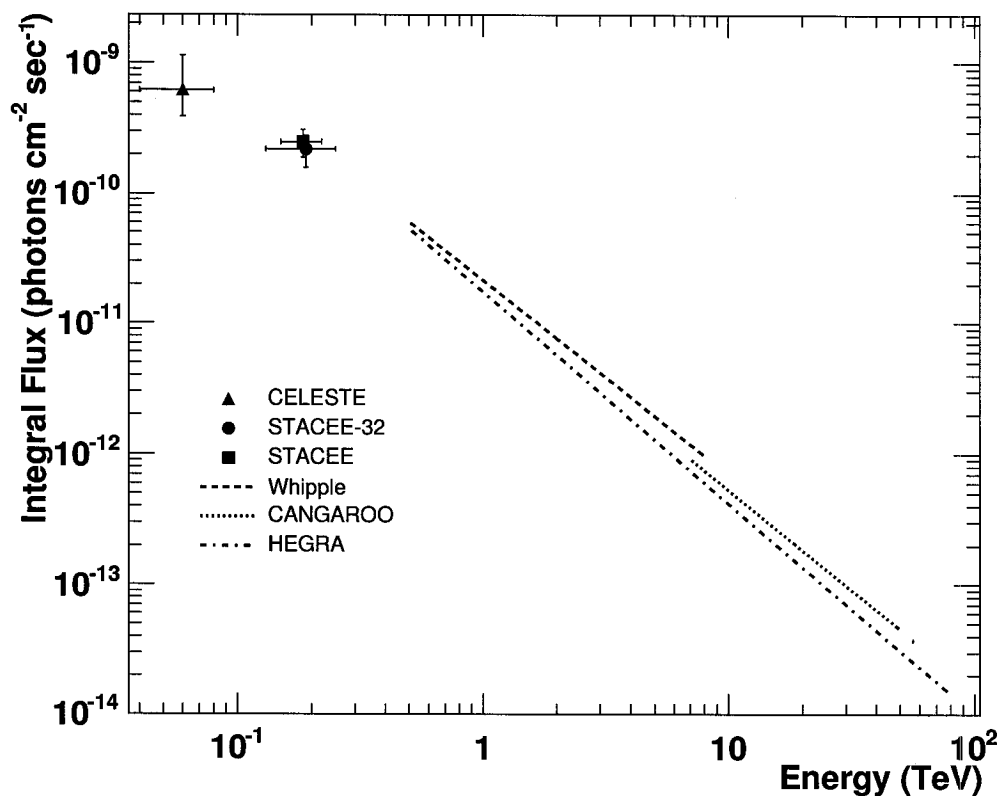


Figure 13.1: STACEE integral flux result for the Crab Nebula shown with measurements from other experiments: CELESTE [42], STACEE-32 [117], Whipple [81], CANGAROO [144], and HEGRA [2].

## 13.1 Future directions for STACEE

As mentioned previously, the *raw* energy threshold of STACEE for a source with a Crab-like spectrum and a declination of  $\sim 20^\circ$  is  $\sim 150$  GeV, which is well above the design goal of 50 GeV. It appears that the initial studies underestimated the contribution of light pollution from the city of Albuquerque and from the Kirkland Air Force Base to the background currents. The number of bright light sources has dramatically increased in the vicinity of the STACEE site over the years and this is hurting the experiment. In principle, the distinctive *yellow glow* of sodium lamps could be taken out using bandpass filters. We have recently experimented with SCHOTT BG1 and BG3 filters and have seen a decrease of 75% in the background currents. This allowed us to run at a much lower operating point, but it is still not clear how the filters affect the sensitivity of the detector. Observations of the Crab Nebula later this year and simulations will shed some light on this problem.

Besides using filters, the only other way to lower the energy threshold of STACEE would be to replace the digital trigger system with a CELESTE-like analog trigger. Even with an analog trigger, it is unlikely that the effective energy threshold would be much below 100 GeV. However, the increased sensitivity below 50 GeV would allow us to search for pulsed emission from known  $\gamma$ -ray pulsars (EGRET detected 6  $\gamma$ -ray pulsars above 100 MeV [146]) and from millisecond pulsars [72]. Although PSR 1951+32 is the weakest of the known  $\gamma$ -ray pulsars, it is the best candidate for emission above 10 GeV as its hard spectrum ( $\alpha = -1.8$ ) does not show any sign of a cutoff at EGRET energies. Moreover, its declination makes it a perfect target for STACEE. Recent studies of high-energy emission from millisecond pulsars predict that the curvature radiation spectrum may peak in power around 10 GeV. These objects could possibly be detected by STACEE if the digital trigger were to be replaced with an analog trigger. The detection of a single  $\gamma$ -ray pulsar by STACEE would be a major scientific contribution.

The sensitivity of STACEE is also lower than what was initially predicted. The addition of heliostats did increase the effective area (and sensitivity) of the detector, but the gain was marginal. Even though the hardware trigger rejects a large fraction of cosmic ray events, offline cuts are necessary to improve the hadron rejection. Recently, a remarkable technique was used with success by the CELESTE collaboration [66]. This technique, which uses timing and pulse shape information from the FADC traces, increased the sensitivity of CELESTE by a factor of 4. Given the similarity between CELESTE and STACEE, this technique could very well work for STACEE.

## 13.2 Ground-based revolution

The new generation of ground-based  $\gamma$ -ray instruments (H.E.S.S., CANGAROO-III, VERITAS, MAGIC) is now operational (some instruments will become operational within the next year) and a flurry of new results (mostly from H.E.S.S.) is taking the whole field of astrophysics by surprise. The H.E.S.S. experiment (a system of four 13 m IACTs in a square of 120 m side, located in Namibia), started operating in June 2002 with one telescope, and the last telescope was added to the array in December 2003. Here is a summary of recent results from the H.E.S.S. collaboration:

- Detection of the high-frequency peaked BL Lac PKS 2155–304 at redshift  $z = 0.117$ , the second most distant object detected at TeV energies (1ES 1426+428 has a redshift  $z = 0.129$ ) [8].
- Detection of a point-like source coincident within  $1'$  of Sagittarius A\* [6].
- Detection of high-energy particle acceleration in SNR RX J1713.7–3946 [12]. For the first time in the history of ground-based  $\gamma$ -ray astrophysics, the detection of celestial  $\gamma$ -ray source could be based not only on positional coincidence, but also on image morphology. The overall shell structure closely matched that seen in X-rays.
- Detection of the composite SNR G 0.9+0.1, the weakest source ever detected at TeV energies (2% of the flux from the Crab Nebula above 200 GeV). This source was serendipitously discovered while observing the Galactic Center. The  $\gamma$ -ray emission appears to originate in the plerionic core of the remnant, rather than the shell.
- H.E.S.S. observations around the position of PSR B1706–44 revealed no evidence for  $\gamma$ -ray emission in the TeV range at the pulsar position or at the radio arc which corresponds to the supernova remnant G 343.1–2.3 [9]. The reported upper limits correspond to 8% of the flux from an earlier detection by the CANGAROO experiment [90].
- Another upper limit was reported for the young shell-type supernova remnant SN1006 [10], which is a factor of 10 lower than previously published fluxes from CANGAROO-I [143].
- A sensitive survey (at a flux sensitivity of 3% of the Crab Nebula flux) of the inner part of the Milky Way revealed a population of 8 previously unknown sources of very high-energy  $\gamma$ -rays [3]. At least 2 have no known radio or X-ray counterparts.

- Discovery of extended very high-energy  $\gamma$ -ray emission from the asymmetric pulsar wind nebula in MSH 15-52 [4]. The morphology coincides with the diffuse pulsar wind nebula as observed at X-ray energies.
- Discovery of very high-energy  $\gamma$ -rays from the high-frequency peaked BL Lac PKS 2005–489 [11], the second blazar detected in the Southern Hemisphere.
- Serendipitous discovery of an unidentified extended TeV  $\gamma$ -ray source close to the Galactic plane (HESS J1303–631) [5]. This source has no counterpart at other wavelengths.
- Detection of TeV  $\gamma$ -ray emission from the shell-type supernova remnant RX J0852.0–4622 [7]. This source is the second shell-type SNR to be resolved at TeV energies. More data are required to distinguish between electronic and hadronic acceleration scenarios.

These results are remarkable and the number of sources of high-energy  $\gamma$ -rays is rapidly increasing. From 6 sources in 2000 (see figure 1.9), the high-energy catalog counts well over 20 sources today (see figure 13.2). The next years promise to be exciting as MAGIC and VERITAS come online and start exploring the Northern sky. Considering that the sensitivity of these new ground-based instruments is much larger than that of wavefront samplers like STACEE (H.E.S.S. detects the Crab Nebula at the  $5\sigma$  level in 30 seconds, versus many hours for STACEE), and that they have a comparable energy threshold, wavefront samplers aren't competitive anymore and are essentially at the end of their useful lifetime. STACEE will likely continue running for one more year, before shutting down permanently.

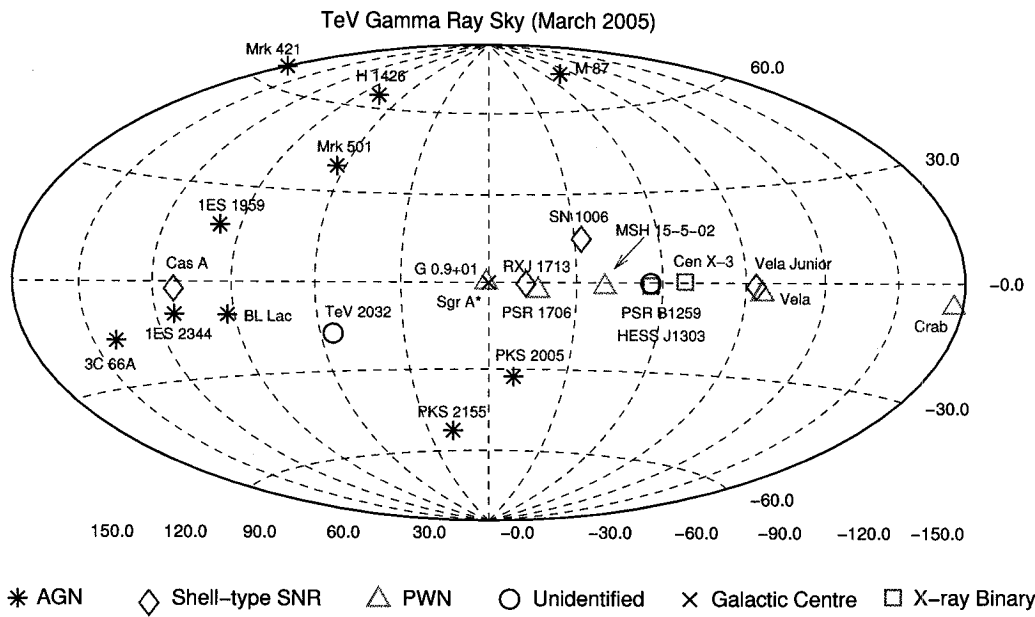


Figure 13.2: Sky map of point sources detected with a good statistical significance at energies above 250 GeV by ground-based detectors (March 2005).

# Appendix A

## Optical data set

The next table contains a detailed list of all the runs taken during the optical pulsar campaign. This includes calibration as well as test runs.

Runlog summary for optical pulsar campaign				
PSR <sup>a</sup>	VMEDAQ <sup>b</sup>	UT Date	Dur.	Remarks
21	9983	2002-12-09	1'	Fake, no HV
22	9984	2002-12-09	8'	Fake, no HV
23	9992	2002-12-09	8'	Fake, no HV
24	10020	2002-12-09	10'	Fake, HV on. Lens Cap on
25	10027	2002-12-09	5'	Crab ON
26	10034	2002-12-09	30'	Fake, no HV, timer calibration run
27	10035	2002-12-09	30'	Fake, no HV, timer calibration run
10036	10036	2002-12-12	28'	Crab ON , Clouds, cut fro analysis
10037	10037	2002-12-12	28'	Crab OFF
10038	10038	2002-12-12	28'	Crab ON CORRUPTED, LOST!
10039	10039	2002-12-12	28'	Crab OFF MISSED FIRST EVENT
10048	10048	2002-12-13	28'	Crab ON,
10049	10049	2002-12-13	28'	Crab OFF
10050	10050	2002-12-13	20'	Crab ON
10051	10051	2002-12-13	20'	Crab OFF
10053	10053	2002-12-13	5'	Zenith
10056	10056	2002-12-13	28'	Mrk 421 ON
10057	10057	2002-12-13	28'	Mrk 421 OFF
10058	10058	2002-12-13	28'	Mrk 421 ON
10064	10064	2002-12-14	5'	Crab ON
10065	10065	2002-12-14	5'	Crab ON
10066	10066	2002-12-14	5'	Crab ON
10067	10067	2002-12-14	5'	Crab ON
10068	10068	2002-12-14	5'	Crab ON
10069	10069	2002-12-14	5'	Crab ON
10070	10070	2002-12-14	5'	Crab ON
10073	10073	2002-12-14	28'	Mrk 421 OFF

*continued on next page*

continued from previous page

PSR <sup>a</sup>	VMEDAQ <sup>b</sup>	UT Date	Dur.	Remarks
10074	10074	2002-12-14	28'	Mrk 421 ON
10075	10075	2002-12-14	20'	Mrk 421 OFF
10076	10076	2002-12-14	20'	Mrk 421 ON MISSED FIRST EVENT
20000	—	2003-01-30	5'	Test run with GPS timecode signal
20001	—	2003-01-30	28'	Test run with GPS timecode signal
20002	—	2003-01-30	1'	Bogus run to test HV...
20003	—	2003-01-30	1'	Bogus run to test HV...
20004	—	2003-01-30	1'	Bogus run to test HV...
10685	10685	2003-01-30	28'	Crab ON
10688	10688	2003-01-30	28'	Crab ON
20005	—	2003-01-30	1'	Bogus run to test HV...
10733	10733	2003-01-30	28'	Crab ON First Fake Event?
10736	10736	2003-01-30	28'	Crab ON
10737	10738	2003-01-30	28'	Crab ON
10738	10739	2003-01-30	28'	Crab OFF First Fake Event?
20006	—	2003-02-01	1'	Swapping filter 2 and 3...
20007	—	2003-02-01	1'	Return to original configuration...
20008	—	2003-02-01	1'	Testing channel 3
20009	—	2003-02-01	1'	Testing channel 3
20010	—	2003-02-01	1'	Testing channel 3
20011	—	2003-02-01	1'	Testing channel 3 HV OFF...
20012	—	2003-02-01	1'	Testing channel 3 HV OFF...
20013	—	2003-02-01	1'	Testing channel 3 HV OFF...
20014	—	2003-02-01	1'	Testing channel 3 HV ON...
20015	—	2003-02-01	1'	Testing channel 3 HV ON...OFF
10761	10761	2003-02-01	28'	Crab ON
10763	10763	2003-02-01	28'	Crab ON
10765	10765	2003-02-01	28'	Crab ON
10840	10840	2003-02-04	28'	Crab ON
10842	10842	2003-02-04	28'	Crab ON
10844	10844	2003-02-04	28'	Crab ON
10952	10952	2003-02-22	28'	Crab ON Cut, bright light at 1 Hz
10955	10955	2003-02-22	28'	Crab ON

Table A.1: Runlog summary for optical pulsar campaign. *a*: number of the run assigned by the optical pulsar DAQ. *b*: Number of the run assigned by VMEDAQ.

## Appendix B

### List of pairs and analysis results

Listing of pairs for the 2002-2003 season

Pair	$t_{ON}$ (s)	$t_{OFF}$ (s)	$N_{ON}$	$N_{OFF}$	$\sigma$	Remarks
9470 - 9469	0.00	0.00	0	0	0.00	<i>f</i>
9472 - 9471	0.00	0.00	0	0	0.00	<i>a</i>
9496 - 9495	1346.31	1346.91	6273	6168	0.97	
9498 - 9497	1419.91	1417.85	7982	7801	1.35	
9500 - 9499	385.87	384.58	2149	2219	-1.17	
9501 - 9499	196.70	196.35	1140	1123	0.31	
9526 - 9525	0.00	0.00	0	0	0.00	<i>b</i>
9528 - 9527	0.00	0.00	0	0	0.00	<i>b</i>
9531 - 9530	0.00	0.08	0	0	0.00	<i>b</i>
9543 - 9542	0.00	0.00	0	0	0.00	<i>c, d</i>
9545 - 9544	0.00	0.00	0	0	0.00	<i>c, d</i>
9547 - 9546	0.00	0.00	0	0	0.00	<i>b, d</i>
9549 - 9548	0.00	0.00	0	0	0.00	<i>b, d</i>
9551 - 9550	0.00	0.00	0	0	0.00	<i>b, d</i>
9589 - 9588	0.00	0.00	0	0	0.00	<i>c</i>
9609 - 9608	0.00	0.00	0	0	0.00	<i>a</i>
9611 - 9610	0.00	0.00	0	0	0.00	<i>a</i>
9673 - 9675	1321.08	1316.29	7172	7157	-0.09	
9722 - 9721	751.73	751.82	3818	3900	-0.93	
9811 - 9813	0.00	0.00	0	0	0.00	<i>b</i>
9831 - 9832	1477.35	1475.79	6700	6527	1.44	
9834 - 9836	0.00	0.00	0	0	0.00	<i>b</i>
9903 - 9902	1189.12	1185.87	6467	6323	1.12	
9935 - 9934	0.00	0.00	0	0	0.00	<i>f</i>
9936 - 9937	0.00	0.00	0	0	0.00	<i>b</i>
10025 - 10026	0.00	0.00	0	0	0.00	<i>b</i>
10036 - 10037	0.00	0.00	0	0	0.00	<i>b</i>
10038 - 10039	0.00	0.00	0	0	0.00	<i>b</i>

*continued on next page*

continued from previous page

Pair	$t_{ON}$ (s)	$t_{OFF}$ (s)	$N_{ON}$	$N_{OFF}$	$\sigma$	Remarks
10048 - 10049	1353.43	1361.20	5817	5666	1.72	
10050 - 10051	1060.67	1061.60	3922	4020	-1.06	<i>d</i>
10579 - 10580	1072.99	1076.06	5708	5664	0.56	
10582 - 10583	861.57	864.53	4276	4194	1.05	
10603 - 10604	1441.49	1444.86	7069	6999	0.73	
10605 - 10606	1363.61	1370.26	6681	6540	1.51	
10610 - 10611	1471.03	1479.45	6425	6313	1.31	
10686 - 10687	1483.28	1483.23	6593	6592	0.01	
10688 - 10689	1510.17	1509.82	5800	5762	0.34	
10733 - 10735	0.00	0.00	0	0	0.00	<i>f</i>
10736 - 10737	0.00	0.00	0	0	0.00	<i>f</i>
10738 - 10739	0.00	0.00	0	0	0.00	<i>f</i>
10760 - 10759	598.92	595.75	3195	3008	2.17	<i>d</i>
10761 - 10762	1268.82	1267.54	6417	6276	1.19	
10763 - 10764	468.13	468.14	2284	2228	0.83	
10765 - 10766	1456.48	1453.89	6023	5990	0.20	
10840 - 10841	1450.24	1451.02	7278	7161	1.01	
10842 - 10843	1466.96	1464.69	6789	6688	0.78	
10844 - 10845	1487.49	1491.30	5618	5704	-0.67	
10952 - 10953	0.00	0.00	0	0	0.00	<i>f</i>
10955 - 10956	0.00	0.00	0	0	0.00	<i>f</i>

Table B.1: Listing of pairs for the 2002-2003 season. *a*: missing FADC data, *b*: manually removed, *c*: frost, *d*: non-standard duration, *e*: monocanted, *f*: standard quality cuts (see chapter 9).

Listing of pairs for the 2003-2004 season

Pair	$t_{ON}$ (s)	$t_{OFF}$ (s)	$N_{ON}$	$N_{OFF}$	$\sigma$	Remarks
12586 - 12587	1487.52	1484.30	6369	6339	0.14	
12622 - 12621	0.00	0.00	0	0	0.00	<i>b</i>
12636 - 12637	0.00	0.00	0	0	0.00	<i>e</i>
12639 - 12640	1499.72	1496.15	5529	5347	1.62	
12700 - 12701	0.00	0.00	0	0	0.00	<i>a</i>
12730 - 12731	1514.25	1511.45	6270	6266	-0.07	
12732 - 12733	1425.28	1417.87	5912	5824	0.53	
12756 - 12755	0.00	0.00	0	0	0.00	<i>c</i>
12757 - 12758	0.00	0.00	0	0	0.00	<i>c</i>
12759 - 12760	0.00	0.00	0	0	0.00	<i>c</i>
12788 - 12790	547.93	548.81	2373	2261	1.70	
12791 - 12793	776.92	773.77	3030	3187	-2.15	
12792 - 12793	288.89	287.69	1120	1092	0.50	
12836 - 12837	0.00	0.00	0	0	0.00	<i>f</i>
12838 - 12839	0.00	0.00	0	0	0.00	<i>f</i>
12858 - 12857	1396.33	1388.23	5975	5961	-0.19	
12859 - 12860	1403.12	1399.73	5686	5614	0.55	
12861 - 12862	1481.60	1481.31	5889	5761	1.18	
12880 - 12881	1271.72	1272.23	5239	5159	0.81	
12882 - 12883	0.00	0.00	0	0	0.00	<i>f</i>
12884 - 12885	0.00	0.00	0	0	0.00	<i>f</i>
12904 - 12905	0.00	0.00	0	0	0.00	<i>f</i>
12906 - 12907	0.00	0.00	0	0	0.00	<i>f</i>
12927 - 12928	1495.90	1490.45	6124	5949	1.39	
12929 - 12930	0.00	0.00	0	0	0.00	<i>b</i>
12942 - 12943	0.00	0.00	0	0	0.00	<i>b</i>
12944 - 12945	1493.81	1491.24	5723	5588	1.18	
12954 - 12955	1527.41	1523.00	5394	5310	0.66	
13040 - 13038	1023.08	1019.95	3970	3945	0.14	
13054 - 13053	0.00	0.00	0	0	0.00	<i>b</i>
13056 - 13055	0.00	0.00	0	0	0.00	<i>b</i>
13058 - 13059	0.00	0.00	0	0	0.00	<i>b</i>
13107 - 13106	876.50	875.94	3304	3355	-0.65	
13108 - 13109	0.00	0.00	0	0	0.00	<i>b</i>
13118 - 13117	0.00	0.00	0	0	0.00	<i>b</i>
13141 - 13140	0.00	0.00	0	0	0.00	<i>b</i>
13142 - 13143	0.00	0.00	0	0	0.00	<i>b</i>
13144 - 13145	0.00	0.00	0	0	0.00	<i>b</i>
13201 - 13202	0.00	0.00	0	0	0.00	<i>f</i>
13203 - 13204	592.62	593.13	2204	2218	-0.18	<i>d</i>
13223 - 13222	0.00	0.00	0	0	0.00	<i>e</i>

continued on next page

continued from previous page

Pair	$t_{ON}$ (s)	$t_{OFF}$ (s)	$N_{ON}$	$N_{OFF}$	$\sigma$	Remarks
3225 - 13224	0.00	0.00	0	0	0.00	<i>e</i>
13249 - 13248	0.00	0.00	0	0	0.00	<i>c</i>
13253 - 13252	0.00	0.00	0	0	0.00	<i>c</i>
13254 - 13255	0.00	0.00	0	0	0.00	<i>c</i>
13256 - 13258	0.00	0.00	0	0	0.00	<i>c</i>
13273 - 13272	0.00	0.00	0	0	0.00	<i>b</i>
13275 - 13274	1273.30	1278.61	4499	4444	0.78	
13277 - 13276	0.00	0.00	0	0	0.00	<i>b</i>
13301 - 13300	0.00	0.00	0	0	0.00	<i>c</i>
13303 - 13304	0.00	0.00	0	0	0.00	<i>c</i>
13306 - 13307	0.00	0.00	0	0	0.00	<i>c</i>
13308 - 13309	0.00	0.00	0	0	0.00	<i>c</i>
13326 - 13327	1442.75	1440.10	6044	5971	0.57	
13328 - 13329	1278.63	1274.94	5454	5364	0.71	
13457 - 13458	595.97	595.18	2216	2185	0.42	
13459 - 13460	1433.68	1436.81	5419	5268	1.57	
13495 - 13496	0.00	0.00	0	0	0.00	<i>b</i>
13497 - 13498	0.00	0.00	0	0	0.00	<i>b</i>
13520 - 13521	604.84	606.17	2711	2693	0.33	
13522 - 13523	0.00	0.00	0	0	0.00	<i>f</i>
13548 - 13549	0.00	0.00	0	0	0.00	<i>b</i>
13574 - 13575	0.00	0.00	0	0	0.00	<i>b</i>

Table B.2: Listing of pairs for the 2003-2004 season. *a*: missing FADC data, *b*: manually removed, *c*: frost, *d*: non-standard duration, *e*: mxonocanted, *f*: standard quality cuts (see chapter 9).

# Appendix C

## Upper limits using the method of Helene

Most sources in the field of high energy astrophysics are relatively dim and difficult to detect. Although the detection of a new source is always exciting, the non-detection of a source can be very useful for constraining different theoretical models. This requires calculating an upper limit on the flux from the source. In the field of pulsar astronomy the method of Helene [75] is used to calculate upper limits. Here our goal is not to explain the method but to show how we solved the equations using simple computer programs.

For experiments like STACEE with large number of events, Gaussian statistics apply and we need to solve Equations 6 and 7 in [75]. The probability density function (p.d.f)  $g(a)$  is given by

$$g(a) = N \frac{e^{-(a-\bar{a})^2/2\sigma^2}}{\sqrt{2\pi}\sigma}, \quad (\text{C.1})$$

where  $N$  is a normalization parameter, and  $\bar{a}$  is equal to the number of counts in the signal region minus the number of expected counts from the background. For the specific case of the Crab pulsar, we expect to get a signal in two regions of the pulse profile (see Figure 12.2). The rest of the period (off pulse region) is used to estimate the background in the signal region. The parameter  $\sigma$  is the standard deviation of the signal region given by  $\sigma^2 = \sigma_B^2 + C$ , where  $\sigma_B^2$  is the variance of the expected background and  $C$  is the variance on the number of counts in the signal region.

The first step is to calculate the normalization factor  $N$  such that

$$\int_0^\infty g(a) da = 1. \quad (\text{C.2})$$

Using the exact expression for  $g(a)$  we have

$$\frac{1}{N} = \frac{1}{\sqrt{2\pi}\sigma} \int_0^\infty da e^{-(a-\bar{a})^2/2\sigma^2}. \quad (\text{C.3})$$

We can simplify the expression by a simple change of variable. We get

$$\frac{1}{N} = \frac{1}{\sqrt{\pi}} \int_{\frac{-\bar{a}}{\sqrt{2}\sigma}}^{\infty} dx e^{-x^2} = \frac{1}{2} \operatorname{erfc}\left(\frac{-\bar{a}}{\sqrt{2}\sigma}\right). \quad (\text{C.4})$$

where we recognize the famous complementary error function  $\operatorname{erfc}(X)$ . After calculating  $\bar{a}$  and  $\sigma$  we can calculate the complementary error function to solve for  $N$ .

Once we have the normalization factor we can calculate the upper limit by solving this equation,

$$\alpha = \int_A^{\infty} g(a) da, \quad (\text{C.5})$$

which gives the probability of having an  $a$  value greater than  $A$ . The significance level is given by  $(1 - \alpha) \cdot 100\%$ .

Again, substituting the full expression for  $g(a)$  and using a simple change of variable we get

$$\alpha = \frac{N}{2} \operatorname{erfc}\left(\frac{A - \bar{a}}{\sqrt{2}\sigma}\right) \quad (\text{C.6})$$

The upper limit can easily be calculated by inverting the complementary error function.

# Appendix D

## GNUCAP code

This is the GNUCAP code used to simulate the response of the RC circuit shown in Figure 5.5. See the GNUCAP web site for instructions on how to use this package [40].

Optical Crab Pulsar RC circuit

```
*****
* Components in the circuit
*****
* Capacitors
C1 2 0 10n
C2 2 3 10u
* Resistors
R1 1 2 10k
R2 3 0 100k
R3 1 0 100k

*****
* Description of the current source..
* The DC current is set to 20 uA
* The AC current is set to 0.1 mA
*****
Iin 1 0 dc 20u ac 0.1m

*****
* Do a DC analysis. We sweep the current from 2uA to
* 20uA in 1 uA steps and measure the voltage at the
* 3 nodes.
*****

.print dc V(1) V(2) V(3)
.dc Iin 2u 20u 1u
```

```
*****
* Do a AC analysis. We sweep the input frequency from
* 0.01 Hz to 100 kHz using 100 steps per decade. We
* measure the voltage and currents at different nodes
*****
*.print ac I(Iin) I(R3) I(R1) V(1) V(2) V(3)
.print ac I(Iin) VM(3) VP(3) VR(3) VI(3)
.ac Decade 100 0.0001 100k >FilterResponse.dat
```

```
.end
```

```
*vin 1 0 pulse (0 1) ac 1
*.tran 0.1 7.0
*.print tran v(2) i(vin)
*.AC dec 10 .01 10
*.plot tran v(2) i(vin)
*.plot ac vdb(2) xlog
*.print ac vdb(2) xlog
*.print ac v(1)
```

# Bibliography

- [1] UC Davis ACT CACTUS. <http://ucdcms.ucdavis.edu/solar2/index.html>.
- [2] F. Aharonian, A. Akhperjanian, M. Beilicke, K. Bernlöhr, H.-G. Börst, H. Bojahr, O. Bolz, T. Coarasa, J. L. Contreras, J. Cortina, S. Denninghoff, M. V. Fonseca, M. Girma, N. Götting, G. Heinzelmann, G. Hermann, A. Heusler, W. Hofmann, D. Horns, I. Jung, R. Kankanyan, M. Kestel, A. Kohnle, A. Konopelko, D. Kranich, H. Lampeitl, M. Lopez, E. Lorenz, F. Lucarelli, O. Mang, D. Mazin, H. Meyer, R. Mirzoyan, A. Moralejo, E. Oña-Wilhelmi, M. Panter, A. Plyasheshnikov, G. Pühlhofer, R. de los Reyes, W. Rhode, J. Ripken, G. Rowell, V. Sahakian, M. Samorski, M. Schilling, M. Siems, D. Sobzynska, W. Stamm, M. Tluczykont, V. Vitale, H. J. Völk, C. A. Wiedner, and W. Wittek. The Crab Nebula and Pulsar between 500 GeV and 80 TeV: Observations with the HEGRA Stereoscopic Air Cerenkov Telescopes. *ApJ*, 614:897–913, October 2004.
- [3] F. Aharonian, A. G. Akhperjanian, K.-M. Aye, A. R. Bazer-Bachi, M. Beilicke, W. Benbow, D. Berge, P. Berghaus, K. Bernlöhr, C. Boisson, O. Bolz, C. Borgmeier, I. Braun, F. Breitling, A. M. Brown, J. B. Gordo, P. M. Chadwick, L.-M. Chounet, R. Cornils, L. Costamante, B. Degrange, A. Djannati-Ataï, L. O. Drury, G. Dubus, T. Ergin, P. Espigat, F. Feinstein, P. Fleury, G. Fontaine, S. Funk, Y. A. Gallant, B. Giebels, S. Gillessen, P. Goret, C. Hadjichristidis, M. Hauser, G. Heinzelmann, G. Henri, G. Hermann, J. A. Hinton, W. Hofmann, M. Holleran, D. Horns, O. C. de Jager, I. Jung, B. Khélifi, N. Komin, A. Konopelko, I. J. Latham, R. Le Gallou, A. Lemièrre, M. Lemoine, N. Leroy, T. Lohse, A. Marcowith, C. Masterson, T. J. L. McComb, M. de Naurois, S. J. Nolan, A. Noutsos, K. J. Orford, J. L. Osborne, M. Ouchrif, M. Panter, G. Pelletier, S. Pita, G. Pühlhofer, M. Punch, B. C. Raubenheimer, M. Raue, J. Raux, S. M. Rayner, I. Redondo, A. Reimer, O. Reimer, J. Ripken, L. Rob, L. Rolland, G. Rowell, V. Sahakian, L. Saugé, S. Schlenker, R. Schlickeiser, C. Schuster, U. Schwanke, M. Siewert, H. Sol, R. Steenkamp, C. Stegmann, J.-P. Tavernet, R. Terrier, C. G. Théoret, M. Tluczykont, D. J. van der Walt, G. Vasileiadis, C. Venter, P. Vincent, B. Visser, H. J. Völk, and S. J. Wagner. A New Population of Very High Energy Gamma-Ray Sources in the Milky Way. *Science*, 307:1938–1942, March 2005.
- [4] F. Aharonian, A. G. Akhperjanian, K.-M. Aye, A. R. Bazer-Bachi, M. Beilicke, W. Benbow, D. Berge, P. Berghaus, K. Bernlöhr, C. Boisson, O. Bolz, I. Braun, F. Breitling, A. M. Brown, J. Bussons Gordo, P. M. Chadwick, L.-M. Chounet, R. Cornils, L. Costamante, B. Degrange, A. Djannati-Ataï, L. O’C. Drury,

- G. Dubus, D. Emmanoulopoulos, P. Espigat, F. Feinstein, P. Fleury, G. Fontaine, Y. Fuchs, S. Funk, Y. A. Gallant, B. Giebels, S. Gillessen, J. F. Glicenstein, P. Goret, C. Hadjichristidis, M. Hauser, G. Heinzelmann, G. Henri, G. Hermann, J. A. Hinton, W. Hofmann, M. Holleran, D. Horns, O. C. de Jager, B. Khélifi, N. Komin, A. Konopelko, I. J. Latham, R. Le Gallou, A. Lemièrre, M. Lemoine-Goumard, N. Leroy, T. Lohse, O. Martineau-Huynh, A. Marcowith, C. Masterson, T. J. L. McComb, M. de Naurois, S. J. Nolan, A. Noutsos, K. J. Orford, J. L. Osborne, M. Ouchrif, M. Panter, G. Pelletier, S. Pita, G. Pühlhofer, M. Punch, B. C. Raubenheimer, M. Raue, J. Raux, S. M. Rayner, I. Redondo, A. Reimer, O. Reimer, J. Ripken, L. Rob, L. Rolland, G. Rowell, V. Sahakian, L. Saugé, S. Schlenker, R. Schlickeiser, C. Schuster, U. Schwanke, M. Siewert, H. Sol, R. Steenkamp, C. Stegmann, J.-P. Tavernet, R. Terrier, C. G. Théoret, M. Tluczykont, G. Vasileiadis, C. Venter, P. Vincent, H. J. Völk, and S. J. Wagner. Discovery of extended VHE gamma-ray emission from the asymmetric pulsar wind nebula in MSH 15-52 with HESS. *Astronomy & Astrophysics*, 435:L17–L20, May 2005.
- [5] F. Aharonian, A. G. Akhperjanian, K.-M. Aye, A. R. Bazer-Bachi, M. Beilicke, W. Benbow, D. Berge, P. Berghaus, K. Bernlöhr, C. Boisson, O. Bolz, I. Braun, F. Breitling, A. M. Brown, J. Bussons Gordo, P. M. Chadwick, L.-M. Chounet, R. Cornils, L. Costamante, B. Degrange, A. Djannati-Ataï, L. O’C. Drury, G. Dubus, D. Emmanoulopoulos, P. Espigat, F. Feinstein, P. Fleury, G. Fontaine, Y. Fuchs, S. Funk, Y. A. Gallant, B. Giebels, S. Gillessen, J. F. Glicenstein, P. Goret, C. Hadjichristidis, M. Hauser, G. Heinzelmann, G. Henri, G. Hermann, J. A. Hinton, W. Hofmann, M. Holleran, D. Horns, O. C. de Jager, B. Khélifi, N. Komin, A. Konopelko, I. J. Latham, R. Le Gallou, A. Lemièrre, M. Lemoine-Goumard, N. Leroy, T. Lohse, O. Martineau-Huynh, A. Marcowith, C. Masterson, T. J. L. McComb, M. de Naurois, S. J. Nolan, A. Noutsos, K. J. Orford, J. L. Osborne, M. Ouchrif, M. Panter, G. Pelletier, S. Pita, G. Pühlhofer, M. Punch, B. C. Raubenheimer, M. Raue, J. Raux, S. M. Rayner, I. Redondo, A. Reimer, O. Reimer, J. Ripken, L. Rob, L. Rolland, G. Rowell, V. Sahakian, L. Saugé, S. Schlenker, R. Schlickeiser, C. Schuster, U. Schwanke, M. Siewert, H. Sol, R. Steenkamp, C. Stegmann, J.-P. Tavernet, R. Terrier, C. G. Théoret, M. Tluczykont, G. Vasileiadis, C. Venter, P. Vincent, H. J. Völk, and S. J. Wagner. Serendipitous discovery of the unidentified extended TeV gamma-ray source HESS J1303–631. *Astronomy & Astrophysics*, 2005.
- [6] F. Aharonian, A. G. Akhperjanian, K.-M. Aye, A. R. Bazer-Bachi, M. Beilicke, W. Benbow, D. Berge, P. Berghaus, K. Bernlöhr, O. Bolz, C. Boisson, C. Borgmeier, F. Breitling, A. M. Brown, J. Bussons Gordo, P. M. Chadwick, V. R. Chitnis, L.-M. Chounet, R. Cornils, L. Costamante, B. Degrange, A. Djannati-Ataï, L. O’C. Drury, T. Ergin, P. Espigat, F. Feinstein, P. Fleury, G. Fontaine, S. Funk, Y. Gallant, B. Giebels, S. Gillessen, P. Goret, J. Guy, C. Hadjichristidis, M. Hauser, G. Heinzelmann, G. Henri, G. Hermann, J. A. Hinton, W. Hofmann, M. Holleran, D. Horns, O. C. de Jager, I. Jung, B. Khélifi, N. Komin, A. Konopelko, I. J. Latham, R. Le Gallou, M. Lemoine, A. Lemièrre, N. Leroy, T. Lohse, A. Marcowith, C. Mas-

- tersson, T. J. L. McComb, M. de Naurois, S. J. Nolan, A. Noutsos, K. J. Orford, J. L. Osborne, M. Ouchrif, M. Panter, G. Pelletier, S. Pita, M. Pohl, G. Pühlhofer, M. Punch, B. C. Raubenheimer, M. Raue, J. Raux, S. M. Rayner, I. Redondo, A. Reimer, O. Reimer, J. Ripken, M. Rivoal, L. Rob, L. Rolland, G. Rowell, V. Sahakian, L. Saugé, S. Schlenker, R. Schlickeiser, C. Schuster, U. Schwanke, M. Siewert, H. Sol, R. Steenkamp, C. Stegmann, J.-P. Tavernet, C. G. Théoret, M. Tluczykont, D. J. van der Walt, G. Vasileiadis, P. Vincent, B. Visser, H. J. Völk, and S. J. Wagner. Very high energy gamma rays from the direction of Sagittarius A\*. *Astronomy & Astrophysics*, 425:L13–L17, October 2004.
- [7] F. Aharonian, A. G. Akhperjanian, K.-M. Aye, A. R. Bazer-Bachi, M. Beilicke, W. Benbow, D. Berge, P. Berghaus, K. Bernlöhr, O. Bolz, C. Boisson, C. Borgmeier, F. Breitling, A. M. Brown, J. Bussons Gordo, P. M. Chadwick, V. R. Chitnis, L.-M. Chounet, R. Cornils, L. Costamante, B. Degrange, A. Djannati-Ataï, L. O’C. Drury, T. Ergin, P. Espigat, F. Feinstein, P. Fleury, G. Fontaine, S. Funk, Y. Gallant, B. Giebels, S. Gillessen, P. Goret, J. Guy, C. Hadjichristidis, M. Hauser, G. Heinzlmann, G. Henri, G. Hermann, J. A. Hinton, W. Hofmann, M. Holleran, D. Horns, O. C. de Jager, I. Jung, B. Khélifi, N. Komin, A. Konopelko, I. J. Latham, R. Le Gallou, M. Lemoine, A. Lemièrre, N. Leroy, T. Lohse, A. Marcowith, C. Masterson, T. J. L. McComb, M. de Naurois, S. J. Nolan, A. Noutsos, K. J. Orford, J. L. Osborne, M. Ouchrif, M. Panter, G. Pelletier, S. Pita, M. Pohl, G. Pühlhofer, M. Punch, B. C. Raubenheimer, M. Raue, J. Raux, S. M. Rayner, I. Redondo, A. Reimer, O. Reimer, J. Ripken, M. Rivoal, L. Rob, L. Rolland, G. Rowell, V. Sahakian, L. Saugé, S. Schlenker, R. Schlickeiser, C. Schuster, U. Schwanke, M. Siewert, H. Sol, R. Steenkamp, C. Stegmann, J.-P. Tavernet, C. G. Théoret, M. Tluczykont, D. J. van der Walt, G. Vasileiadis, P. Vincent, B. Visser, H. J. Völk, and S. J. Wagner. Detection of TeV gamma-ray emission from the shell-type supernova remnant RX J0852.0–4622 with H.E.S.S. *Astronomy & Astrophysics*, 2005.
- [8] F. Aharonian, A.G. Akhperjanian, K.-M. Aye, A.R. Bazer-Bachi, M. Beilicke, W. Benbow, D. Berge, P. Berghaus, K. Bernlöhr, O. Bolz, C. Boisson, C. Borgmeier, F. Breitling, A.M. Brown, J. Bussons Gordo, P.M. Chadwick, V.R. Chitnis, L.-M. Chounet, R. Cornils, L. Costamante, B. Degrange, A. Djannati-Ataï, L.O’C. Drury, T. Ergin, P. Espigat, F. Feinstein, P. Fleury, G. Fontaine, S. Funk, Y.A. Gallant, B. Giebels, S. Gillessen, P. Goret, J. Guy, C. Hadjichristidis, M. Hauser, G. Heinzlmann, G. Henri, G. Hermann, J.A. Hinton, W. Hofmann, M. Holleran, D. Horns, O.C. de Jager, I. Jung, B. Khélifi, Nu. Komin, A. Konopelko, I.J. Latham, R. Le Gallou, M. Lemoine, A. Lemièrre, N. Leroy, T. Lohse, A. Marcowith, C. Masterson, T.J.L. McComb, M. de Naurois, S.J. Nolan, A. Noutsos, K.J. Orford, J.L. Osborne, M. Ouchrif, M. Panter, G. Pelletier, S. Pita, M. Pohl, G. Pühlhofer, M. Punch, B.C. Raubenheimer, M. Raue, J. Raux, S.M. Rayner, I. Redondo, A. Reimer, O. Reimer, J. Ripken, M. Rivoal, L. Rob, L. Rolland, G. Rowell, V. Sahakian, L. Saugé, S. Schlenker, R. Schlickeiser, C. Schuster, U. Schwanke, M. Siewert, H. Sol, R. Steenkamp, C. Stegmann, J.-P. Tavernet, C.G. Théoret, M. Tluczykont, D.J. van der Walt, G. Vasileiadis, P. Vincent, B. Visser,

- H.J. Völk, and S.J. Wagner. H.E.S.S. Observations of PKS 2155–304. *Astronomy & Astrophysics*, 2005.
- [9] F. Aharonian, A.G. Akhperjanian, K.-M. Aye, A.R. Bazer-Bachi, M. Beilicke, W. Benbow, D. Berge, P. Berghaus, K. Bernlöhr, O. Bolz, C. Boisson, C. Borgmeier, F. Breitling, A.M. Brown, J. Bussons Gordo, P.M. Chadwick, V.R. Chitnis, L.-M. Chounet, R. Cornils, L. Costamante, B. Degrange, A. Djannati-Ataï, L.O’C. Drury, T. Ergin, P. Espigat, F. Feinstein, P. Fleury, G. Fontaine, S. Funk, Y.A. Gallant, B. Giebels, S. Gillessen, P. Goret, J. Guy, C. Hadjichristidis, M. Hauser, G. Heinzlmann, G. Henri, G. Hermann, J.A. Hinton, W. Hofmann, M. Holleran, D. Horns, O.C. de Jager, I. Jung, B. Khélifi, Nu. Komin, A. Konopelko, I.J. Latham, R. Le Gallou, M. Lemoine, A. Lemièrre, N. Leroy, T. Lohse, A. Marcowith, C. Masterson, T.J.L. McComb, M. de Naurois, S.J. Nolan, A. Noutsos, K.J. Orford, J.L. Osborne, M. Ouchrif, M. Panter, G. Pelletier, S. Pita, M. Pohl, G. Pühlhofer, M. Punch, B.C. Raubenheimer, M. Raue, J. Raux, S.M. Rayner, I. Redondo, A. Reimer, O. Reimer, J. Ripken, M. Rivoal, L. Rob, L. Rolland, G. Rowell, V. Sahakian, L. Saugé, S. Schlenker, R. Schlickeiser, C. Schuster, U. Schwanke, M. Siewert, H. Sol, R. Steenkamp, C. Stegmann, J.-P. Tavernet, C.G. Théoret, M. Tluczykont, D.J. van der Walt, G. Vasileiadis, P. Vincent, B. Visser, H.J. Völk, and S.J. Wagner. Search for TeV emission from the region around PRS B1706–44. *Astronomy & Astrophysics*, 2005.
- [10] F. Aharonian, A.G. Akhperjanian, K.-M. Aye, A.R. Bazer-Bachi, M. Beilicke, W. Benbow, D. Berge, P. Berghaus, K. Bernlöhr, O. Bolz, C. Boisson, C. Borgmeier, F. Breitling, A.M. Brown, J. Bussons Gordo, P.M. Chadwick, V.R. Chitnis, L.-M. Chounet, R. Cornils, L. Costamante, B. Degrange, A. Djannati-Ataï, L.O’C. Drury, T. Ergin, P. Espigat, F. Feinstein, P. Fleury, G. Fontaine, S. Funk, Y.A. Gallant, B. Giebels, S. Gillessen, P. Goret, J. Guy, C. Hadjichristidis, M. Hauser, G. Heinzlmann, G. Henri, G. Hermann, J.A. Hinton, W. Hofmann, M. Holleran, D. Horns, O.C. de Jager, I. Jung, B. Khélifi, Nu. Komin, A. Konopelko, I.J. Latham, R. Le Gallou, M. Lemoine, A. Lemièrre, N. Leroy, T. Lohse, A. Marcowith, C. Masterson, T.J.L. McComb, M. de Naurois, S.J. Nolan, A. Noutsos, K.J. Orford, J.L. Osborne, M. Ouchrif, M. Panter, G. Pelletier, S. Pita, M. Pohl, G. Pühlhofer, M. Punch, B.C. Raubenheimer, M. Raue, J. Raux, S.M. Rayner, I. Redondo, A. Reimer, O. Reimer, J. Ripken, M. Rivoal, L. Rob, L. Rolland, G. Rowell, V. Sahakian, L. Saugé, S. Schlenker, R. Schlickeiser, C. Schuster, U. Schwanke, M. Siewert, H. Sol, R. Steenkamp, C. Stegmann, J.-P. Tavernet, C.G. Théoret, M. Tluczykont, D.J. van der Walt, G. Vasileiadis, P. Vincent, B. Visser, H.J. Völk, and S.J. Wagner. Upper limits on the SN1006 multi-TeV gamma-ray flux from H.E.S.S. observations. *Astronomy & Astrophysics*, 2005.
- [11] F. Aharonian, A.G. Akhperjanian, K.-M. Aye, A.R. Bazer-Bachi, M. Beilicke, W. Benbow, D. Berge, P. Berghaus, K. Bernlöhr, O. Bolz, C. Boisson, C. Borgmeier, F. Breitling, A.M. Brown, J. Bussons Gordo, P.M. Chadwick, V.R. Chitnis, L.-M. Chounet, R. Cornils, L. Costamante, B. Degrange, A. Djannati-Ataï, L.O’C. Drury, T. Ergin, P. Espigat, F. Feinstein, P. Fleury, G. Fontaine,

- S. Funk, Y.A. Gallant, B. Giebels, S. Gillessen, P. Goret, J. Guy, C. Hadjichristidis, M. Hauser, G. Heinzelmann, G. Henri, G. Hermann, J.A. Hinton, W. Hofmann, M. Holleran, D. Horns, O.C. de Jager, I. Jung, B. Khélifi, Nu. Komin, A. Konopelko, I.J. Latham, R. Le Gallou, M. Lemoine, A. Lemièrre, N. Leroy, T. Lohse, A. Marcowith, C. Masterson, T.J.L. McComb, M. de Naurois, S.J. Nolan, A. Noutsos, K.J. Orford, J.L. Osborne, M. Ouchrif, M. Panter, G. Pelletier, S. Pita, M. Pohl, G. Pühlhofer, M. Punch, B.C. Raubenheimer, M. Raue, J. Raux, S.M. Rayner, I. Redondo, A. Reimer, O. Reimer, J. Ripken, M. Rivoal, L. Rob, L. Rolland, G. Rowell, V. Sahakian, L. Saugé, S. Schlenker, R. Schlickeiser, C. Schuster, U. Schwanke, M. Siewert, H. Sol, R. Steenkamp, C. Stegmann, J.-P. Tavernet, C.G. Théoret, M. Tluczykont, D.J. van der Walt, G. Vasileiadis, P. Vincent, B. Visser, H.J. Völk, and S.J. Wagner. Discovery of VHE Gamma Rays from PKS 2005-489. *Astronomy & Astrophysics*, 2005.
- [12] F. A. Aharonian, A. G. Akhperjanian, K.-M. Aye, A. R. Bazer-Bachi, M. Beilicke, W. Benbow, D. Berge, P. Berghaus, K. Bernlöhr, O. Bolz, C. Boisson, C. Borgmeier, F. Breitling, A. M. Brown, J. Bussons Gordo, P. M. Chadwick, V. R. Chitnis, L.-M. Chounet, R. Cornils, L. Costamante, B. Degrange, A. Djannati-Ataï, L. O. Drury, T. Ergin, P. Espigat, F. Feinstein, P. Fleury, G. Fontaine, S. Funk, Y. A. Gallant, B. Giebels, S. Gillessen, P. Goret, J. Guy, C. Hadjichristidis, M. Hauser, G. Heinzelmann, G. Henri, G. Hermann, J. A. Hinton, W. Hofmann, M. Holleran, D. Horns, O. C. de Jager, I. Jung, B. Khélifi, N. Komin, A. Konopelko, I. J. Latham, R. Le Gallou, M. Lemoine, A. Lemièrre, N. Leroy, T. Lohse, A. Marcowith, C. Masterson, T. J. L. McComb, M. de Naurois, S. J. Nolan, A. Noutsos, K. J. Orford, J. L. Osborne, M. Ouchrif, M. Panter, G. Pelletier, S. Pita, M. Pohl, G. Pühlhofer, M. Punch, B. C. Raubenheimer, M. Raue, J. Raux, S. M. Rayner, I. Redondo, A. Reimer, O. Reimer, J. Ripken, M. Rivoal, L. Rob, L. Rolland, G. Rowell, V. Sahakian, L. Saugé, S. Schlenker, R. Schlickeiser, C. Schuster, U. Schwanke, M. Siewert, H. Sol, R. Steenkamp, C. Stegmann, J.-P. Tavernet, C. G. Théoret, M. Tluczykont, D. J. van der Walt, G. Vasileiadis, P. Vincent, B. Visser, H. J. Völk, and S. J. Wagner. High-energy particle acceleration in the shell of a supernova remnant. *Nature*, 432:75–77, November 2004.
- [13] F. Arqueros, J. Ballestrin, M. Berenguel, D. M. Borque, E. F. Camacho, M. Diaz, H.-J. Gebauer, R. Enriquez, and R. Plaga. Very high-energy gamma-ray observations of the Crab nebula and other potential sources with the GRAAL experiment. *Astroparticle Physics*, 17:293–318, June 2002.
- [14] W. Baade. The Crab Nebula. *ApJ*, 96:188–198, September 1942.
- [15] K. Bernlohr. Impact of atmospheric parameters on the atmospheric Cherenkov technique\*. *Astroparticle Physics*, 12:255–268, January 2000.
- [16] G. F. Bignami, G. Boella, J. J. Burger, B. G. Taylor, P. Keirle, J. A. Paul, H. A. Mayer-Hasselwander, E. Pfeffermann, L. Scarsi, and B. N. Swanenburg. The COS-B experiment for gamma-ray astronomy. *Space Science Instrumentation*, 1:245–268, August 1975.

- [17] P. M. S. Blackett. A possible contribution to the night sky from the cerenkov radiation emitted by cosmic rays. *Physical Society of London Gassiot Committee Report*, pages 34–+, 1948.
- [18] Richard E. Blumberg and Alexander Boksenberg. *The Astronomical Almanac for the Year 1996*. U.S. Government Printing Office, Washington, D.C, 1995, 1995.
- [19] J. G. Bolton, G. J. Stanley, and O. B. Slee. Positions of three discrete sources of Galactic radio frequency radiation. *Nature*, 164:101, 1949.
- [20] L. M. Boone. *Observations of Markarian 421 with the Solar Tower Atmospheric Cherenkov Effect Experiment*. PhD thesis, University of California, Santa Cruz, 2002.
- [21] L. M. Boone, J. A. Hinton, D. Bramel, E. Chae, C. E. Covault, P. Fortin, D. M. Gingrich, D. S. Hanna, R. Mukherjee, C. Mueller, R. A. Ong, K. Ragan, R. A. Scalzo, D. R. Schuette, C. G. Théoret, and D. A. Williams. STACEE Observations of Markarian 421 during an Extended Gamma-Ray Outburst. *ApJL*, 579:L5–L8, November 2002.
- [22] A. Borione et al. A Large air shower array to search for astrophysical sources emitting gamma-rays with energies  $\epsilon = 10^{14}$ -eV. *Nucl. Instrum. Meth.*, A346:329–352, 1994.
- [23] H. Bradt, S. Rappaport, W. Mayer, R. E. Nather, B. Warner, M. Macfarlane, and J. Kristian. X-Ray and Optical Observations of the Pulsar NP 0532 in the Crab Nebula. *Nature*, 222:728–+, 1969.
- [24] D. A. Bramel. *Drift scan analysis*, 2005. STACEE internal collaboration note 05-04.
- [25] D. A. Bramel. *Observations of the BL Lac Object 3C66A with the Solar Tower Atmospheric Cherenkov Effect Experiment*. PhD thesis, Columbia University, 2005.
- [26] D. A. Bramel, J. Carson, C. E. Covault, P. Fortin, D. M. Gingrich, D. S. Hanna, A. Jarvis, J. Kildea, T. Lindner, R. Mukherjee, C. Mueller, R. A. Ong, K. Ragan, R. A. Scalzo, D. A. Williams, and J. Zweerink. Observations of the BL Lac object 3C 66A with STACEE. *ApJ*. Accepted by ApJ.
- [27] R. Buccheri, K. Bennett, G. F. Bignami, J. B. G. M. Bloemen, V. Boriakoff, P. A. Caraveo, W. Hermsen, G. Kanbach, R. N. Manchester, J. L. Masnou, H. A. Mayer-Hasselwander, M. E. Ozel, J. A. Paul, B. Sacco, L. Scarsi, and A. W. Strong. Search for pulsed gamma-ray emission from radio pulsars in the COS-B data. *Astronomy & Astrophysics*, 128:245–251, November 1983.
- [28] J. N. Capdevielle et al. *The Karlsruhe extensive air shower simulation code CORSIKA*, 1992. Karlsruhe KfK - KfK-4998 (92/11,rec.Mar.93) 55 p.

- [29] A. Carramiñana, A. Čadež, and T. Zwitter. Optical Spectrum of Main-, Inter-, and Off-Pulse Emission from the Crab Pulsar. *ApJ*, 542:974–977, October 2000.
- [30] B. W. Carroll and D. A. Ostlie. *An introduction to modern astrophysics*. Addison-Wesley, 1996.
- [31] M. C. Chantell et al. Prototype test results of the solar tower atmospheric Cherenkov effect experiment (STACEE). *Nucl. Instrum. Meth. A*, 408:468–485, 1998.
- [32] K. S. Cheng, C. Ho, and M. Ruderman. Energetic radiation from rapidly spinning pulsars. I - Outer magnetosphere gaps. II - VELA and Crab. *ApJ*, 300:500–539, January 1986.
- [33] P. A. Cherenkov. Visible radiation produced by electrons moving in a medium with velocities exceeding that of light. *Dokl. Akad. Nauk. SSSR*, 2:451, 1934. English version in *Phys. Rev.* 52, 378 (1937).
- [34] D. H. Clark and R. F. Stephenson. *The historical supernovae*. Pergamon international library of science, technology, engineering, and social studies. Pergamon Press, 1977.
- [35] G. W. Clark, G. P. Garmire, and W. L. Kraushaar. Observation of high-energy cosmic gamma rays. *ApJ*, 153:L203+, September 1968.
- [36] W. J. Cocke, M. J. Disney, and D. J. Taylor. Discovery of Optical Signals from Pulsar NP 0532. *Nature*, 221:525–+, 1969.
- [37] S. Danaher, D. J. Fegan, N. A. Porter, T. C. Weekes, and T. Cole. Possible applications of large solar arrays in astronomy and astrophysics. *Solar Energy*, 28(4):335–343, 1982.
- [38] J. K. Daugherty and A. K. Harding. Polar CAP models of gamma-ray pulsars: Emission from single poles of nearly aligned rotators. *ApJ*, 429:325–330, July 1994.
- [39] J. K. Daugherty and A. K. Harding. Gamma-Ray Pulsars: Emission from Extended Polar CAP Cascades. *ApJ*, 458:278–+, February 1996.
- [40] Albert Davis. GNUCAP, the GNU Circuit Analysis Package. Available at <http://www.gnu.org/software/gnucap/>.
- [41] O. C. de Jager, B. C. Raubenheimer, and J. W. H. Swanepoel. A powerful test for weak periodic signals with unknown light curve shape in sparse data. *Astronomy & Astrophysics*, 221:180–190, August 1989.
- [42] M. de Naurois, J. Holder, R. Bazer-Bachi, H. Bergeret, P. Bruel, A. Cordier, G. Debais, J.-P. Dezalay, D. Dumora, E. Durand, P. Eschstruth, P. Espigat, B. Fabre, P. Fleury, N. Hérault, M. Hrabovsky, S. Incerti, R. Le Gallou, F. Münz, A. Musquère, J.-F. Olive, E. Paré, J. Québert, R. C. Rannot, T. Reposeur, L. Rob,

- P. Roy, T. Sako, P. Schovanek, D. A. Smith, P. Snabre, and A. Volte. Measurement of the Crab Flux above 60 GeV with the CELESTE Cerenkov Telescope. *ApJ*, 566:343–357, February 2002.
- [43] S. M. Derdeyn, C. H. Ehrmann, C. E. Fichtel, D. A. Kniffen, and R. W. Ross. SAS-B digitized spark chamber gamma ray telescope. *Nucl. Instr. and Methods*, 98:557–566, 1972.
- [44] P. Doll et al. The karlsruhe cosmic ray project cascade. Karlsruhe KfK - KfK-4686 (90,rec.Aug.) 73 p.
- [45] V. A. Dombrovski and M. A. Vashakidze. On the nature of the radiation of the Crab nebula. *Dokl. Akad. Nauk. SSSR*, 94, 1954.
- [46] H. J. Drescher, M. Hladik, S. Ostapchenko, T. Pierog, and K. Werner. Parton-based gribov-regge theory. *Phys. Rept.*, 350:93–289, 2001.
- [47] H. Fesefeldt. The simulation of hadronic showers: Physics and applications. PITHA-85-02.
- [48] C. E. Fichtel, R. C. Hartman, D. A. Kniffen, D. J. Thompson, G. F. Bignami, M. E. Ögüman, M. E. Özel, and T. Tümer. High-energy gamma-ray results from the second Small Astronomy Satellite. *ApJ*, 198:163–182, May 1975.
- [49] J. M. Fierro, P. F. Michelson, P. L. Nolan, and D. J. Thompson. Phase-resolved Studies of the High-Energy Gamma-Ray Emission from the Crab, Geminga, and VELA Pulsars. *ApJ*, 494:734–746, February 1998.
- [50] R. S. Fletcher, T. K. Gaisser, Paolo Lipari, and Todor Stanev. Sibyll: An event generator for simulation of high-energy cosmic ray cascades. *Phys. Rev.*, D50:5710–5731, 1994.
- [51] J. L. A. Fordham, N. Vranesevic, A. Carramiñana, R. Michel, R. Much, P. Wehinger, and S. Wyckoff. Phase-resolved Spectroscopic Imaging of the Crab Pulsar. *ApJ*, 581:485–494, December 2002.
- [52] P. Fortin. An instrument for studying the response of STACEE camera components to different lighting conditions. Master's thesis, McGill University, 2000. M.Sc. thesis.
- [53] P. Fortin. *STACEE gain measurement using FGIT*, 2000. STACEE internal collaboration note 02-07.
- [54] P. Fortin. *Timing Resolution of STACEE channels*, 2003. STACEE internal collaboration note 03-11.
- [55] I. M. Frank and I. Y. Tamm. *Dokl. Akad. Nauk. SSSR*, 14:109, 1937.
- [56] G. Fritz, R. C. Henry, J. F. Meekins, T. A. Chubb, and H. Friedman. X-ray Pulsar in the Crab Nebula. *Science*, 164:709–712, May 1969.

- [57] W. Galbraith and J. V. Jelly. *Nature*, 171:349, 1953.
- [58] N. Gehrels and P. Michelson. GLAST: the next-generation high energy gamma-ray astronomy mission. *Astroparticle Physics*, 11:277–282, June 1999.
- [59] B. Giebels et al. Prototype tests for the CELESTE solar array gamma-ray telescope. *Nucl. Instrum. Meth. A*, 412:329–341, 1998.
- [60] T. Gold. Rotating Neutron Stars as the Origin of the Pulsating Radio Sources. *Nature*, 218:731–+, 1968.
- [61] T. Gold. "Rotating Neutron Stars and the Nature of Pulsars",. *Nature*, 221:25–+, 1969.
- [62] A. Golden, A. Shearer, R. M. Redfern, G. M. Beskin, S. I. Neizvestny, V. V. Neustroev, V. L. Plokhhotnichenko, and M. Cullum. High speed phase-resolved 2-d UVB photometry of the Crab pulsar. *Astronomy & Astrophysics*, 363:617–628, November 2000.
- [63] P. Goldreich and W. H. Julian. Pulsar Electrodynamics. *ApJ*, 157:869–880, August 1969.
- [64] R. J. Gould. High-Energy Photons from the Compton-Synchrotron Process in the Crab Nebula. *Physical Review Letters*, 15:577–579, October 1965.
- [65] T. R. Gull, D. J. Lindler, D. M. Crenshaw, J. F. Dolan, S. J. Hulbert, S. B. Kraemer, P. Lundqvist, K. C. Sahu, J. Sollerman, G. Sonneborn, and B. E. Woodgate. Space Telescope Imaging Spectrograph Near-Ultraviolet Time-tagged Spectra of the Crab Pulsar. *ApJL*, 495:L51+, March 1998.
- [66] M. Hakima. *Astronomie gamma au-dessus de 30 GeV. Une nouvelle méthode d'identification des rayons gamma cosmiques a partir du sol avec le detecteur CELESTE*. PhD thesis, Ecole polytechnique, 2004.
- [67] D. Hanna. *A New Way to Monitor Phototube Gains in STACEE*, 2003. STACEE internal collaboration note 03-04.
- [68] D. Hanna and R. Mukherjee. *First Results from the STACEE Laser System*, 1999. STACEE internal collaboration note 99-02.
- [69] D. Hanna and R. Mukherjee. The laser calibration system of the STACEE ground-based gamma ray detector. *Nucl. Inst. and Methods A*, 482:271–280, April 2002.
- [70] D. S. Hanna et al. The STACEE-32 ground based gamma-ray detector. *Nucl. Instrum. Meth. A*, 491:126–151, 2002.
- [71] A. K. Harding and A. G. Muslimov. Particle Acceleration Zones above Pulsar Polar Caps: Electron and Positron Pair Formation Fronts. *ApJ*, 508:328–346, November 1998.

- [72] A. K. Harding, V. V. Usov, and A. G. Muslimov. High-Energy Emission from Millisecond Pulsars. *ApJ*, 622:531–543, March 2005.
- [73] R. C. Hartman, D. L. Bertsch, S. D. Bloom, A. W. Chen, P. Deines-Jones, J. A. Esposito, C. E. Fichtel, D. P. Friedlander, S. D. Hunter, L. M. McDonald, P. Sreekumar, D. J. Thompson, B. B. Jones, Y. C. Lin, P. F. Michelson, P. L. Nolan, W. F. Tompkins, G. Kanbach, H. A. Mayer-Hasselwander, A. Mücke, M. Pohl, O. Reimer, D. A. Kniffen, E. J. Schneid, C. von Montigny, R. Mukherjee, and B. L. Dingus. The Third EGRET Catalog of High-Energy Gamma-Ray Sources. *ApJS*, 123:79–202, July 1999.
- [74] D. Heck, J. Knapp, J.N. Capdevielle, G. Schatz, and T. Thouw. *CORSIKA: A Monte Carlo Code to Simulate Extensive Air Showers*, 1998. Forschungszentrum Karlsruhe Report FZKA 6019.
- [75] O. Helene. Upper limit of peak area. *Nucl. Instr. and Meth.*, 212:319–322, 1983.
- [76] V. F. Hess. observation of penetrating radiation in seven free balloon flights. *Phys. Zeitschr.*, 13:1084, 1912.
- [77] J. W. T. Hessels, M. S. E. Roberts, S. M. Ransom, V. M. Kaspi, R. W. Romani, C.-Y. Ng, P. C. C. Freire, and B. M. Gaensler. Observations of PSR J2021+3651 and its X-Ray Pulsar Wind Nebula G75.2+0.1. *ApJ*, 612:389–397, September 2004.
- [78] A. Hewish, S. J. Bell, J. D. Pilkington, P. F. Scott, and R. A. Collins. Observation of a Rapidly Pulsating Radio Source. *Nature*, 217:709–+, 1968.
- [79] A. M. Hillas. Proc. 19th ICRC. vol. 1, p. 155 (1985).
- [80] A. M. Hillas. Proc. 24th ICRC. vol. 1, p. 270 (1995).
- [81] A. M. Hillas, C. W. Akerlof, S. D. Biller, J. H. Buckley, D. A. Carter-Lewis, M. Catanese, M. F. Cawley, D. J. Fegan, J. P. Finley, J. A. Gaidos, F. Krennrich, R. C. Lamb, M. J. Lang, G. Mohanty, M. Punch, P. T. Reynolds, A. J. Rodgers, H. J. Rose, A. C. Rovero, M. S. Schubnell, G. H. Sembroski, G. Vacanti, T. C. Weekes, M. West, and J. Zweerink. The Spectrum of TeV Gamma Rays from the Crab Nebula. *ApJ*, 503:744–759, August 1998.
- [82] J. A. Hinton. Personal communication.
- [83] J. A. Hinton. *A comparison of the MOCCA and CORSIKA air-shower simulation codes*, 2000. STACEE internal collaboration note 00-10.
- [84] J. A. Hinton, Rim Dib, and Richard Scalzo. *Measurements of heliostat bias drift & light collection using CCD sunspots*, 2000. STACEE internal collaboration note 00-14.
- [85] K. Hirotani. Gamma-Ray Emissions from Pulsars: Spectra of the TEV Fluxes from Outer Gap Accelerators. *ApJ*, 549:495–508, March 2001.

- [86] N. N. Kalmykov, S. S. Ostapchenko, and A. I. Pavlov. Quark-gluon string model and eas simulation problems at ultra-high energies. *Nucl. Phys. Proc. Suppl.*, 52B:17–28, 1997.
- [87] G. Kanbach, D. L. Bertsch, A. Favale, C. E. Fichtel, R. C. Hartman, R. Hofstadter, E. B. Hughes, S. D. Hunter, B. W. Hughlock, D. A. Kniffen, Y. C. Lin, H. A. Mayer-Hasselwander, P. L. Nolan, K. Pinkau, H. Rothermel, E. Schneid, M. Sommer, and D. J. Thompson. The Project EGRET - Energetic Gamma-Ray Experiment Telescope - on Nasa's Gamma-Ray Observatory GRO". *Space Science Reviews*, 49:61–+, 1988.
- [88] B. Keilhauer, J. Blümer, R. Engel, H. O. Klages, and M. Risse. Impact of varying atmospheric profiles on extensive air shower observation: atmospheric density and primary mass reconstruction. *Astroparticle Physics*, 22:249–261, November 2004.
- [89] C. F. Kennel and F. V. Coroniti. Confinement of the Crab pulsar's wind by its supernova remnant. *ApJ*, 283:694–709, August 1984.
- [90] T. Kifune, T. Tanimori, S. Ogio, T. Tamura, H. Fujii, M. Fujimoto, T. Hara, N. Hayashida, S. Kabe, F. Kakimoto, Y. Matsubara, Y. Mizumoto, Y. Muraki, T. Suda, M. Teshima, T. Tsukagoshi, Y. Watase, T. Yoshikoshi, P. G. Edwards, J. R. Patterson, M. D. Roberts, G. P. Rowell, and G. J. Thornton. Very high energy gamma rays from PSR 1706-44. *ApJ*, 438:L91–L94, January 1995.
- [91] J. Kildea. A Search for Pulsed TeV Gamma-Ray Emission from the Crab Pulsar using the Whipple High Resolution GRANITE III Camera. In *Proceedings of the 28th International Cosmic Ray Conference (Tsukuba, Japan 2003)*. astro-ph/0305580.
- [92] J. Kildea. *Studies of the Crab Nebula and Pulsar at TeV Energies*. PhD thesis, University College Dublin, 2002.
- [93] R. W. Klebesadel, I. B. Strong, and R. A. Olson. Observations of gamma-ray bursts of cosmic origin. *ApJ*, 182:L85–L88, June 1973.
- [94] D. A. Kniffen. The Gamma-Ray Observatory. *New York Academy Sciences Annals*.
- [95] W. L. Kraushaar and G. W. Clark. Search for primary cosmic gamma rays with the satellite Explorer XI. *Phys. Rev. Lett.*, 8(3):106–109, 1962.
- [96] W. L. Kraushaar, G. W. Clark, G. P. Garmire, and R. Borken. High-energy cosmic gamma-ray observations from the OSO-3 satellite. *ApJ*, 177:341–363, October 1972.
- [97] S. R. Kulkarni, S. B. Anderson, T. A. Prince, and A. Wolszczan. Old pulsars in the low-density globular clusters M13 and M53. *Nature*, 349:47–49, January 1991.

- [98] R. W. Lessard, I. H. Bond, S. M. Bradbury, J. H. Buckley, A. M. Burdett, D. A. Carter-Lewis, M. Catanese, M. F. Cawley, M. D'Vali, D. J. Fegan, J. P. Finley, J. A. Gaidos, G. H. Gillanders, T. Hall, A. M. Hillas, F. Krennrich, M. J. Lang, C. Masterson, P. Moriarty, J. Quinn, H. J. Rose, F. W. Samuelson, G. H. Sembroski, R. Srinivasan, V. V. Vassiliev, and T. C. Weekes. Search for Pulsed TEV Gamma-Ray Emission from the Crab Pulsar. *ApJ*, 531:942–948, March 2000.
- [99] A. G. Lyne and F. Graham-Smith. *Pulsar astronomy*. Cambridge University Press, 1998.
- [100] A. G. Lyne, C. A. Jordan, and M. E. Roberts. *Jodrell Bank Crab Pulsar monthly ephemeris*. <http://www.jb.man.ac.uk/pulsar/crab.html>.
- [101] Paul A. Lynn and Wolfgang Fuerst. *Digital signal processing with computer applications*. John Wiley & Sons, 1997.
- [102] Richard G. Lyons. *Understanding digital signal processing*. Prentice Hall PTR, 2001.
- [103] J.P. Martin and K. Ragan. A programmable nanosecond digital delay and trigger system. *IEEE Nuclear Science Symposium*, 2000.
- [104] R. Minkowski. The Crab Nebula. *ApJ*, 96, 1942.
- [105] K. Mori, H. Tsunemi, H. Katayama, D. N. Burrows, G. P. Garmire, and A. E. Metzger. An X-Ray Measurement of Titan's Atmospheric Extent from Its Transit of the Crab Nebula. *ApJ*, 607:1065–1069, June 2004.
- [106] Phillip Morrison. On gamma-ray astronomy. *Il Nuovo Cimento*, 7(6):858–865, 1958.
- [107] A. G. Muslimov and A. K. Harding. Extended Acceleration in Slot Gaps and Pulsar High-Energy Emission. 588:430–440, May *ApJ*.
- [108] NASA. *JPL Planetary and Lunar Ephemerides*. Available via anonymous FTP from <ftp://ssd.jpl.nasa.gov/pub/eph/export/>.
- [109] F. P. Nasuti, R. Mignani, P. A. Caraveo, and G. F. Bignami. Spectrophotometry of the Crab pulsar. *Astronomy & Astrophysics*, 314:849–852, October 1996.
- [110] W. Ralph Nelson, H. Hirayama, and David W. O. Rogers. The egs4 code system. SLAC-0265.
- [111] Ning, Xiaohui and Winston, Roland and O'Gallagher, Joseph. Dielectric totally internally reflecting concentrators. *Applied Optics*, 26(2):300–305, 1997.
- [112] P. L. Nolan, Z. Arzoumanian, D. L. Bertsch, J. Chiang, C. E. Fichtel, J. M. Fierro, R. C. Hartman, S. D. Hunter, G. Kanbach, D. A. Kniffen, P. W. Kwok, Y. C. Lin, J. R. Mattox, H. A. Mayer-Hasselwander, P. F. Michelson, C. von Montigny, H. I.

- Nel, D. Nice, K. Pinkau, H. Rothermel, E. Schneid, M. Sommer, P. Sreekumar, J. H. Taylor, and D. J. Thompson. Observations of the Crab pulsar and nebula by the EGRET telescope on the Compton Gamma-Ray Observatory. *ApJ*, 409:697–704, June 1993.
- [113] R. A. Ong. Very high-energy gamma-ray astronomy. *Physics Report*, 305:93–202, 1998.
- [114] R. A. Ong, D. Bhattacharya, C. E. Covault, D. D. Dixon, D. T. Gregorich, D. S. Hanna, S. Oser, J. Québert, D. A. Smith, O. T. Tümer, and A. D. Zych. Detection of atmospheric Cherenkov radiation using solar heliostat mirrors. *Astroparticle Physics*, 5:353–365, October 1996.
- [115] J. H. Oort and T. Walraven. Polarization and composition of the Crab nebula. *Bulletin of the Astronomical Institutes of the Netherlands*, 12:285–+, May 1956.
- [116] Alan V. Oppenheim. *Digital signal processing*. Prentice Hall, 1975.
- [117] S. Oser, D. Bhattacharya, L. M. Boone, M. C. Chantell, Z. Conner, C. E. Covault, M. Dragovan, P. Fortin, D. T. Gregorich, D. S. Hanna, R. Mukherjee, R. A. Ong, K. Ragan, R. A. Scalzo, D. R. Schuette, C. G. Théoret, T. O. Tümer, D. A. Williams, and J. A. Zweerink. High-Energy Gamma-Ray Observations of the Crab Nebula and Pulsar with the Solar Tower Atmospheric Cerenkov Effect Experiment. *ApJ*, 547:949–958, February 2001.
- [118] S. M. Oser. *High energy gamma-ray observations of the Crab Nebula and Pulsar with the Solar Tower Atmospheric Cherenkov Effect Experiment*. PhD thesis, The University of Chicago, 2000.
- [119] W. S. Paciesas, C. A. Meegan, G. N. Pendleton, M. S. Briggs, C. Kouveliotou, T. M. Koshut, J. P. Lestrade, M. L. McCollough, J. J. Brainerd, J. Hakkila, W. Henze, R. D. Preece, V. Connaughton, R. M. Kippen, R. S. Mallozzi, G. J. Fishman, G. A. Richardson, and M. Sahi. The Fourth BATSE Gamma-Ray Burst Catalog (Revised). *ApJS*, 122:465–495, June 1999.
- [120] F. Pacini. Energy Emission from a Neutron Star. *Nature*, 216:567–+, 1967.
- [121] E. Paré et al. CELESTE: An atmospheric Cherenkov telescope for high energy gamma astrophysics. *Nucl. Instrum. Meth. A*, 490:71–89, 2002.
- [122] J. W. Percival, J. D. Biggs, J. F. Dolan, E. L. Robinson, M. J. Taylor, R. C. Bless, J. L. Elliot, M. J. Nelson, T. F. Ramseyer, G. W. van Citters, and E. Zhang. The Crab pulsar in the visible and ultraviolet with 20 microsecond effective time resolution. *ApJ*, 407:276–283, April 1993.
- [123] Donald Perkins. *Particle astrophysics*. Oxford master series in particle physics, astrophysics, and cosmology. Oxford university press, 2003.

- [124] M. Punch, C. W. Akerlof, M. F. Cawley, M. Chantell, D. J. Fegan, S. Fennell, J. A. Gaidos, J. Hagan, A. M. Hillas, Y. Jiang, A. D. Kerrick, R. C. Lamb, M. A. Lawrence, D. A. Lewis, D. I. Meyer, G. Mohanty, K. S. O'Flaherty, P. T. Reynolds, A. C. Rovero, M. S. Schubnell, G. Sembroski, T. C. Weekes, and C. Wilson. Detection of TeV photons from the active galaxy Markarian 421. *Nature*, 358:477–478, August 1992.
- [125] W. R. Purcell, L.-X. Cheng, D. D. Dixon, R. L. Kinzer, J. D. Kurfess, M. Leventhal, M. A. Saunders, J. G. Skibo, D. M. Smith, and J. Tueller. OSSE Mapping of Galactic 511 keV Positron Annihilation Line Emission. *ApJ*, 491:725–748, December 1997.
- [126] K. Ragan. *The Montreal digital delay system Specifications and Design*, 2003. STACEE internal collaboration note 03-01.
- [127] P. V. Ramanamurthy, D. L. Bertsch, C. E. Fichtel, G. Kanbach, D. A. Kniffen, H. A. Mayer-Hasselwander, P. L. Nolan, P. Sreekumar, and D. J. Thompson. A Long-Term Study of High-Energy Gamma-Ray Emission from the Vela, Geminga, and Crab Pulsars. *ApJ*, 450:791–+, September 1995.
- [128] J. Ranft. The dual parton model at cosmic ray energies. *Phys. Rev.*, D51:64–84, 1995.
- [129] M. J. Rees and J. E. Gunn. The origin of the magnetic field and relativistic particles in the Crab Nebula. *M.N.R.A.S.*, 167:1–12, April 1974.
- [130] D. W. Richards and J. M. Comella. The Period of Pulsar NP0532. *Nature*, 222:551–+, 1969.
- [131] M. S. E. Roberts, J. W. T. Hessels, S. M. Ransom, V. M. Kaspi, P. C. C. Freire, F. Crawford, and D. R. Lorimer. PSR J2021+3651: A Young Radio Pulsar Coincident with an Unidentified EGRET  $\gamma$ -Ray Source. *ApJL*, 577:L19–L22, September 2002.
- [132] M. S. E. Roberts, J. W. T. Hessels, S. M. Ransom, V. M. Kaspi, P. C. C. Freire, F. Crawford, and D. R. Lorimer. PSR J2021+3651: a new  $\gamma$ -ray pulsar candidate. *Advances in Space Research*, 33:577–580, 2004.
- [133] R. W. Romani. Gamma-Ray Pulsars: Radiation Processes in the Outer Magnetosphere. *ApJ*, 470:469–+, October 1996.
- [134] M. A. Ruderman and P. G. Sutherland. Theory of pulsars - Polar caps, sparks, and coherent microwave radiation. *ApJ*, 196:51–72, February 1975.
- [135] R. F. Sanford. Spectrum of the Crab Nebula. *Publications of the Astronomical society of the pacific*, 31:108–109, April 1919.
- [136] R. A. Scalzo. *Observations of the EGRET blazar W Comae with the Solar Tower Atmospheric Cherenkov Effect Experiment*. PhD thesis, University of Chicago, 2004.

- [137] R. A. Scalzo, L. M. Boone, D. Bramel, J. Carson, C. E. Covault, P. Fortin, G. Gauthier, D. M. Gingrich, D. Hanna, A. Jarvis, J. Kildea, T. Lindner, C. Mueller, R. Mukherjee, R. A. Ong, K. J. Ragan, D. A. Williams, and J. Zweerink. High-Energy Gamma-Ray Observations of W Comae with the Solar Tower Atmospheric Cerenkov Effect Experiment (STACEE). *ApJ*, 607:778–787, June 2004.
- [138] I.S. Shklovskii. On the Nature of the Crab Nebula's Optical Emission. *Doklady Akad. Nauk SSSR*, 90:983, 1953. Translated to English in "A Source Book in Astronomy & Astrophysics, 1900-1975", Harvard Univ. Press, Cambridge, MA, 1979.
- [139] J. Sollerman, P. Lundqvist, D. Lindler, R. A. Chevalier, C. Fransson, T. R. Gull, C. S. J. Pun, and G. Sonneborn. Observations of the Crab Nebula and Its Pulsar in the Far-Ultraviolet and in the Optical. *ApJ*, 537:861–874, July 2000.
- [140] D. H. Staelin and E. C. Reifenstein. Pulsating radio sources near the Crab Nebula. *Science*, 162:1481–1483, 1968.
- [141] I. B. Strong and R. W. Klebesadel. Cosmic gamma-ray bursts. *Scientific American*, 235:66–70, October 1976.
- [142] B. N. Swanenburg, K. Bennett, G. F. Bignami, R. Buccheri, P. Caraveo, W. Hermsen, G. Kanbach, G. G. Lichti, J. L. Masnou, H. A. Mayer-Hasselwander, J. A. Paul, B. Sacco, L. Scarsi, and R. D. Wills. Second COS B catalog of high-energy gamma-ray sources. *ApJ*, 243:L69–L73, January 1981.
- [143] T. Tanimori, Y. Hayami, S. Kamei, S. A. Dazeley, P. G. Edwards, S. Gunji, S. Hara, T. Hara, J. Holder, A. Kawachi, T. Kifune, R. Kita, T. Konishi, A. Masaike, Y. Matsubara, T. Matsuoka, Y. Mizumoto, M. Mori, M. Moriya, H. Muraishi, Y. Muraki, T. Naito, K. Nishijima, S. Oda, S. Ogio, J. R. Patterson, M. D. Roberts, G. P. Rowell, K. Sakurazawa, T. Sako, Y. Sato, R. Susukita, A. Suzuki, R. Suzuki, T. Tamura, G. J. Thornton, S. Yanagita, T. Yoshida, and T. Yoshikoshi. Discovery of TeV Gamma Rays from SN 1006: Further Evidence for the Supernova Remnant Origin of Cosmic Rays. *ApJL*, 497:L25+, April 1998.
- [144] T. Tanimori, K. Sakurazawa, S. A. Dazeley, P. G. Edwards, T. Hara, Y. Hayami, S. Kamei, T. Kifune, T. Konishi, Y. Matsubara, T. Matsuoka, Y. Mizumoto, A. Masaike, M. Mori, H. Muraishi, Y. Muraki, T. Naito, S. Oda, S. Ogio, T. Osaki, J. R. Patterson, M. D. Roberts, G. P. Rowell, A. Suzuki, R. Suzuki, T. Sako, T. Tamura, G. J. Thornton, R. Susukita, S. Yanagita, T. Yoshida, and T. Yoshikoshi. Detection of Gamma Rays of up to 50 TeV from the Crab Nebula. *ApJL*, 492:33–+, January 1998.
- [145] M. Tavani, G. Barbiellini, A. Argan, N. Auricchio, P. Caraveo, A. Chen, V. Cocco, E. Costa, G. di Cocco, G. Fedel, M. Feroci, M. Fiorini, T. Froyland, M. Galli, F. Gianotti, A. Giuliani, C. Labanti, I. Lapshov, P. Lipari, F. Longo, E. Massaro,

- S. Mereghetti, E. Morelli, A. Morselli, A. Pellizzoni, F. Perotti, P. Picozza, C. Pittori, C. Pontoni, M. Prest, M. Rapisarda, E. Rossi, A. Rubini, P. Soffitta, M. Trifoglio, E. Vallazza, S. Vercellone, and D. Zanello. Science with AGILE. In *AIP Conf. Proc. 587: Gamma 2001: Gamma-Ray Astrophysics*, pages 729–+, 2001.
- [146] D. J. Thompson. Gamma-ray Pulsars: Observations. In *American Institute of Physics Conference Series*, pages 103–114, 2001.
- [147] D. J. Thompson, D. L. Bertsch, C. E. Fichtel, R. C. Hartman, R. Hofstadter, E. B. Hughes, S. D. Hunter, B. W. Hughlock, G. Kanbach, D. A. Kniffen, Y. C. Lin, J. R. Mattox, H. A. Mayer-Hasselwander, C. von Montigny, P. L. Nolan, H. I. Nel, K. Pinkau, H. Rothermel, E. J. Schneid, M. Sommer, P. Sreekumar, D. Tieger, and A. H. Walker. Calibration of the Energetic Gamma-Ray Experiment Telescope (EGRET) for the Compton Gamma-Ray Observatory. *ApJS*, 86:629–656, June 1993.
- [148] V. Trimble. The Distance to the Crab Nebula and NP 0532. *PASP*, 85:579–585, October 1973.
- [149] O. T. Tümer, J. T. O’Neill, A. D. Zych, and R. S. White. A promising large area VHE gamma ray detector with excellent hadron rejection capability. *Nuclear Physics B (Proc. Suppl.)*, 14A:351–355, 1990.
- [150] U.S. Government Printing Office, Washington D.C., 1976.
- [151] T. C. Weekes. Very high energy gamma-ray astronomy. *Physics Reports*, 160:1–121, 1988.
- [152] T. C. Weekes, M. F. Cawley, D. J. Fegan, K. G. Gibbs, A. M. Hillas, P. W. Kowk, R. C. Lamb, D. A. Lewis, D. Macomb, N. A. Porter, P. T. Reynolds, and G. Vacanti. Observation of TeV gamma rays from the Crab nebula using the atmospheric Cerenkov imaging technique. *ApJ*, 1989.
- [153] K. W. Weiler and N. Panagia. Are Crab-type Supernova Remnants (Plerions) Short-lived? *Astronomy & Astrophysics*, 70:419–422, November 1978.
- [154] K. Werner. Strings, pomerons, and the venus model of hadronic interactions at ultrarelativistic energies. *Phys. Rept.*, 232:87–299, 1993.